

Microstructural Origin of Residual Stress

Submitted in partial fulfillment of the requirements

of the degree of

Doctor of Philosophy

of the

Indian Institute of Technology, Bombay, India

and

Monash University, Australia

by

Arijit Lodh

Supervisors:

Prof. Indradev Samajdar (IIT Bombay)

Prof. P. J. Guruprasad (IIT Bombay)

Prof. Christopher Hutchinson (Monash University)



*The course of study for this award was developed jointly by
Monash University, Australia and the Indian Institute of Technology, Bombay
and was given academic recognition by each of them.
The programme was administrated by The IITB-Monash Research Academy*

(2018)

Approval Sheet

The thesis entitled “*Microstructural Origin of Residual Stress*” by *Arijit Lodh* is approved for the degree of **Doctor of Philosophy**.



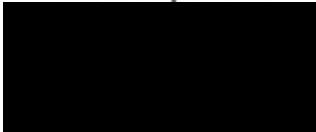
(Prof. Debalay Chakrabarti)
External Examiner



(Prof. Asim Tewari)
Internal Examiner



(Prof. Indradev Samajdar)
IITB Supervisor



(Prof. P. J. Guruprasad)
IITB Co-Supervisor



(Prof. Christopher Hutchinson)
Monash Supervisor



(Prof. Amol Gokhale)
Chairman

Date: 20th September, 2018

Place: IITB-Monash Research Academy, IIT Bombay

Declaration

I declare that this written submission represents my ideas in my own words and where others' ideas or words have been included, I have adequately cited and referenced the original sources.

I also declare that I have adhered to all principles of academic honesty and integrity and have not misrepresented or fabricated or falsified any idea/data/fact/source in my submission. I understand that any violation of the above will be cause for disciplinary action by the Institute and can also evoke penal action from the sources which have thus not been properly cited or from whom proper permission has not been taken when needed.

Notice 1

Under the Copyright Act 1968, this thesis must be used only under the normal conditions of scholarly fair dealing. In particular no results or conclusions should be extracted from it, nor should it be copied or closely paraphrased in whole or in part without the written consent of the author. Proper written acknowledgement should be made for any assistance obtained from this thesis.

Notice 2

I certify that I have made all reasonable efforts to secure copyright permissions for third-party content included in this thesis and have not knowingly added copyright content to my work without the owner's permission.



Arijit Lodh

IITB ID: 134114001

Monash ID: 25557971

Acknowledgements

I would like to gratefully and sincerely thank Prof. Indradev Samajdar and Prof PJ Guruprasad for their guidance and suggestions during my PhD work at IIT Bombay. Their constant encouragement and support from the initial to the final level enabled me to develop an understanding of this subject as well as computational skills.

I express my sincere gratitude to Prof Christopher Hutchinson for all the technical inputs, motivation and discussions on how to think and design a scientific problem during my stay at Monash University. A special mention goes to him to teach me on how to write a technical paper.

I am grateful to Prof. Alankar Alankar for helping me out in doing a part of computational work and extending the help by giving access to his computational facilities. I would like to thank Prof Chris Davies and Prof Asim Tewari for their valuable suggestions during my course of candidature as a research progress committee member.

I am thankful to every member of National Facility of Texture and OIM Lab, specially Mr. Aditya Prakash and Mr. Tawqeer Nasir. Also I am grateful to Mr Yuxiang Wu, Ms Qi Zhang, Ms Wenwen Sun for the help and support during my Monash stay. For experimental work related help, I am thankful to Mr Prakash, Ms Neelam, Mr Naik, Mr Amit and Mr Ajay for extending their help and permission to use the machines. Finally, I would like to thank all of my friends who have been involved directly or indirectly with this research work.

Finally, I would like to thank my parents and my wife for their support and constant motivation throughout the journey.

Abstract

This thesis started with a hypothesis: “the microstructural constraints, or dislocation substructures, are essential for the residual stress”. GND (geometrically necessary dislocation) density and/or in-grain misorientations were considered to represent the dislocation substructures. Residual stresses, on the other hand, were measured with multiple $\{hkl\}$ GIXRD (grazing incident X-ray diffraction), micro-Laue diffraction (for single-crystal stress measurements) and residual stress ODFs (orientation distribution function). Possible correlations between substructure and residual stress evolutions were then explored experimentally and simulated numerically (with DDD (discrete dislocation dynamics) and CPFЕ (crystal plasticity finite element)).

The main body of the thesis consists of four independent, yet interrelated, chapters. In the first of this chapter (chapter 3: *Relating Residual Stress and Substructural Evolution during Tensile Deformation of an Aluminum-Manganese Alloy*) evolution of GND density and single-crystal residual stress were shown to be orientation dependent. The patterns of experimental orientation dependence were captured effectively with DDD simulations. It thus became apparent that evolution of residual stresses, during uniaxial tensile deformation, was controlled by dislocation glide and interactions. Chapter 4 (*Microstructural Origin of Residual Stress Relief in Aluminum*) explored thermal stress relief. Direct (micro-Laue) and indirect (stress ODFs) measurements clearly established orientation dependence of the stress relief. The stress was maximum at the intermediate annealing temperature. This observation was explained with DDD: temperature dependence of residual stress relief being clearly related to a balance between dislocation glide and climb mechanisms.

Chapter 5 (*Orientation Dependent Developments in Misorientation and Residual Stress in Rolled Aluminum: The Defining Role of Dislocation Interactions*) used plane strain compression, at relatively large plastic strains, to experimentally determine the orientation dependent evolution of residual stresses and in-grain misorientation. This was captured qualitatively with CPFЕ, with assumptions of anisotropic latent hardening of the appropriate slip systems but insignificant interactions between neighboring grains. It is interesting to note that for relatively minor strains,

both single-crystal DDD and the aforementioned CPFE, captured faithfully the experimental patterns. It is thus apparent that the patterns of orientation dependent evolution in deformed microstructures, including that of the residual stresses, were determined by the behavior of the constituent single-crystals. Interactions between the neighboring grains appeared to have affected such patterns quantitatively, but did not affect the hierarchy of orientation dependence.

The last chapter (chapter 6: *Defining the Orientation Dependent Microstructure Evolution through Cyclic Deformation in an Aluminum Alloy*) explored cyclic deformation. This chapter shows orientation dependent evolution of residual stress: {001} and {111} exhibiting compressive stresses, while tensile stresses were noted for {110}. This chapter, however, remains partially complete at this point of time.

The thesis thus provides interesting insights into “*Microstructural Origin of Residual Stress*”. It shows that the stress evolution, under different deformation modes and thermal annealing, was determined by concurrent developments in dislocation substructures. This has been the real niche or novelty of the thesis.

Table of Contents

Abstract	v
Table of Contents	vii
List of Figures	ix
List of Tables	xvii
Abbreviations	xix
Chapter 1 Introduction	1
Chapter 2 Literature Review	7
2.1 Residual stress: Origin, types and measurement techniques	7
2.1.1 Measurement techniques of residual stress	10
2.1.1.1 Diffraction based methods.....	12
2.2 Plastic Deformation and dislocation substructure evolution	18
2.2.1 <i>Monotonic deformation and dislocation structure development</i>	20
2.2.2 <i>Cyclic deformation and dislocation structure development</i>	25
2.2.3 <i>Plastic deformation, dislocation structure and residual stress</i>	29
2.3 Thermal annealing of deformed material and dislocation substructure evolution.....	31
2.3.1 <i>Dislocation substructure development during thermal recovery</i>	32
2.3.2 <i>Thermal annealing, dislocation structure and residual stress</i>	34
2.4 Computational Plasticity.....	36
2.4.1 <i>Discrete dislocation dynamics simulations</i>	37
2.4.2 <i>Crystal plasticity simulations</i>	41
Chapter 3 Relating Residual Stress and Substructural Evolution during Tensile Deformation of an Aluminum-Manganese Alloy	59
3.1 Introduction.....	59

3.2 Experimental Procedure	62
3.3 Results	66
3.4 Discussion	74
3.5 Conclusions	85
Chapter 4 Microstructural Origin of Residual Stress relief in Aluminum	95
4.1 Introduction	95
4.2 Experimental Methods	97
4.3 Simulations.....	99
4.4 Simulations.....	105
4.4.1 Basic Experimental Facts	105
4.4.2 Comparison between experiments and simulations.....	114
4.5 Discussion	119
4.6 Conclusions	124
Chapter 5 Orientation Dependent Developments in Misorientation and Residual Stress in Rolled Aluminum: The Defining Role of Dislocation Interactions.....	135
5.1 Introduction	135
5.2 Experimental Details	136
5.3 Model Description	137
5.4 Results	138
5.5 Discussion and summary.....	143
Chapter 6 Defining the Orientation Dependent Microstructure Evolution through Cyclic Deformation in an Aluminum Alloy.....	147
6.1 Introduction	147
6.2 Experimental Details	148
6.3 Results and Discussion.....	149
Chapter 7 Concluding Remarks and Scope for Future Research.....	157

List of Figures

Figure 1.1: Schematic diagram showing the origin of residual stress from a ‘composite’ (a+b) material. (a) denotes the tensile extension of both the phases by $d\varepsilon$, a being harder undergoes elastic deformation while b deforms elasto-plastically. (b) Upon unloading, and under appropriate constraint, a and b will enjoy tensile and compressive residual stresses respectively. Courtesy [3].
.....2

Figure 1.2: Energy potential well and equilibrium lattice position (r_0). External energy/stress can shift the atoms from equilibrium position to r_1 or r_2 . The changed configuration can be retained, fully or in part, under appropriate constraint. And this is the source of residual strain/stress.2

Figure 1.3: Schematic representation of microstructural changes. (a) Dislocation substructures at different microstructural length scale during plastic deformation, (b) Microstructural evolution in thermal annealing. Courtesy [3].3

Figure 2.1: Origin of residual stresses from various sources. Courtesy [6]8

Figure 2.2: Development of different types of residual stress during uniaxial deformation..... 10

Figure 2.3: Development of different types of residual stress during uniaxial deformation. Courtesy [8] 13

Figure 2.4: Shift of diffraction peak in a stressed sample during the tilt of sample at an angle $\pm\alpha$. Courtesy [16] 15

Figure 2.5: Comparison between measurement techniques of laboratory X-ray diffraction and synchrotron X-ray diffraction..... 17

Figure 2.6: Development of different microstructural features in plastic deformation: (a) and (b) cell structure, (c) and (d) deformation bands, (e) and (f) shear bands. Courtesy [21]..... 19

Figure 2.7: Schematic of different deformation heterogeneities in microstructural length scale. Courtesy [6, 29]20

Figure 2.8: Schematic stress–strain $\tau(\gamma)$ and work hardening $(d\tau/d\gamma)(\tau)$ plots at three temperatures $T < 0.5T_m$. Courtesy [6, 34].....21

Figure 2.9: TEM micrograph reveals the dislocation cells and microbands in high purity iron after 80% cold reduction. Courtesy [6].	22
Figure 2.10: Figure represents the TEM micrograph of pure nickel following a reduction of 20% by cold rolling. It shows the dislocation microstructure and substructures, top part of the figure is a tracing of micrograph to demonstrate the cell block (CB) structure composed of GNBs and IDBs. The long GNBs are inclined to the rolling direction and almost parallel to the {111} slip plane. Parts of two grains are separated by a grain boundary (GB). Image is taken in longitudinal section containing the normal and rolling direction (RD). Courtesy [36].	23
Figure 2.11: Schematic of different sub microstructural features of deformed microstructure. Courtesy [47].	24
Figure 2.12: (a) Schematic representation of different regions of cyclic stress-strain curve. Courtesy [28], (b) Dislocation substructural evolution during cyclic deformation. Courtesy [59]	26
Figure 2.13: Vein structure in monocrystalline copper after cyclic loading at constant strain amplitude. Courtesy [55].	27
Figure 2.14: PSBs in fatigued copper – (a) appearance of PSBs under scanning electron microscope, (b) Transmission electron microscope image showing dislocation distribution in PSB and matrix of the same in single grain. Courtesy [61]	28
Figure 2.15: (a) Labyrinth structure formed in fatigued single crystal copper, (b) Cell structure formed at higher plastic strain in fatigued copper crystals. Courtesy [28]	29
Figure 2.16: Schematic showing recovery mechanism by dislocation annihilation; cross-section of a bent crystal containing both free (edge) dislocations and dislocations which accommodate the orientation gradient. During annealing, some dislocations anneal out by climb of opposite sign segments (encircled pairs) then the remainder rearrange into sub-grain boundaries. Courtesy [6]	32
Figure 2.17: A schematic showing substructure evolution during Recovery. Courtesy [21]	33
Figure 2.18: Schematic illustration of the substructure evolution with increasing strain and with annealing time. Courtesy [74].	34
Figure 2.19: Computational and experimental techniques for a variety of length and time scales. Courtesy [99].	37
Figure 2.20: (a) Initial dislocation structure, (b) and (c) dislocation structure developments in basal and non-basal orientations, (d) dislocation density of those orientations after same duration of simulation time. Courtesy [140].	39

Figure 2.21: Simulated and experimental GND densities for (a) (1 1 0) <0 0 1> (b) (1 1 0) <1-11>. Simulations were obtained through 2-D DDD and experimental GND densities were calculated from EBSD data. Also included are images of simulated GND and experimental orientation gradients (gradient from average orientation: as estimated from EBSD data). The latter are expected to bring out slip bands and other forms of GNDs and strain localizations. Courtesy [141].....40

Figure 2.22: Contour plots of (a) axial stress, σ_{11} , with dislocation structure superimposed on crystal, (b) GND density, and (c) Lattice rotation. Courtesy [122].....41

Figure 2.23: (i) Comparison of surface strain mapping between experimental (a) and simulation (b); (ii) Comparison of surface roughness between experimental (a) and simulation (b). Courtesy [142]42

Figure 2.24: Comparison of von Mises strain on the surface of an aluminum single crystal – left column shows experimental measurement of strain from digital image correlation, the middle column shows the simulation results using conventional visco-plastic formulation whereas the right column is calculated using a dislocation based model which considers GNDs. Courtesy [163]..44

Figure 3.1: (a) Schematic showing single-crystal stress measurement with micro-focus (~50 μm spot size) XRD and area detector. (b) Area detector image of Laue spot from the same grain before and after plastic deformation. Centroid position(s) of the spots were identified with an appropriate Matlab™ program and are shown as ‘+’. (c) From the respective centroid positions, intensity-2 θ plots were obtained and d-spacings were calculated. This exercise was repeated six times to solve strain tensors for individual grains.64

Figure 3.2: (a) Representative true stress – true strain behavior; (b) Microstructural developments at different locations of work hardening stages during tensile deformation (colors represent different orientations in inverse pole figure convention). In (b), enlarged region of ‘point 7’ shows the development of in-grain misorientations.67

Figure 3.3: (a) EBSD IPF maps of a cluster of grains for different ($\varepsilon = 0, 0.01, 0.03$ and 0.05) true strains. 1 to 3° boundaries are shown as black lines. From a single grain, of the grain cluster, evolution of orientation gradients (grain average orientation and its deviations in 0-2° scale) was also shown. (b) shows the low angle boundary (1-15°) densities (boundary length per unit area) at the corresponding strain levels.70

Figure 3.4: Correlation of Geometrically Necessary Dislocation density (ρ_{GND}) and normal residual stress (σ_{11}) and shear residual stress (σ_{13}) during each stage of tensile deformation. Y-axis includes appropriate error bars for residual stress and ρ_{GND} values. 71

Figure 3.5: For 25 grains, development of (a) normal (σ_{11}) and (b) shear (σ_{13}) residual stresses as a function of ρ_{GND} . The data is shown for first three stages of tensile deformation (imposed ϵ values are marked as respective legends). In both figures, measurement uncertainties are shown as appropriate error bars. 73

Figure 3.6: Change in Von Mises residual stress ($|\Delta \text{RS}_{\text{VonMises}}|$) as a function of change in $|\rho_{\text{GND}}|$. The data is shown for first three stages of tensile deformation. Dotted lines indicate measurement uncertainties. 74

Figure 3.7: (a) Boundary condition of OOF2 geometry; (b) OOF2 simulation showing development of residual stress; (c) Comparison of normal residual stress (σ_{11}) between experiment and simulation. 76

Figure 3.8: Development of normal (σ_{11}) residual stresses as a function of ρ_{GND} for different orientations. Measurement uncertainties are shown as appropriate error bars. 77

Figure 3.9: (a) Schematic of DDD simulation set up showing a plain strain model oriented for double slip where two slip systems are oriented at $\pm\psi_0$ from x axis, (b) Simulated stress-strain plot for the specimen during loading and unloading for three different orientations (orientations are shown as unit cells with $\{hkl\}\langle uvw \rangle$ notation at right side)..... 78

Figure 3.10: σ_{11} contours at $\epsilon_{11}=0.0225$. The data were obtained by imposing appropriate stress-strain, and then unloading, see figure 3.9b. 82

Figure 3.11: Comparison of experimental and DDD simulations, for three different orientations, showing developments in single-crystal σ_{11} as a function of normalized dislocation density (ρ_{GND}). DDD data are collated after imposing appropriate stress-strain and later by unloading (figure 3.9b and 3.10)..... 84

Figure 3.A1: (a) shows a typical (111) EBSD pole figure of a single-grain. (b) Laue diffraction spots at different goniometer tilt and rotation. The spot with highest intensity (as in figure 3.1c) was used for further processing86

Figure 4.1: (a) EBSD microstructures, combination of IPF (inverse pole figure) and IQ (image quality) maps, showing microstructural changes during annealing. (b) Fraction recrystallized and (c) hardness versus time at different annealing temperatures. (d) Brings out quantification of microstructural changes in terms GAM and GOS. (e) and (f) show the low (1-15°) and high (>15°) angle boundary density (boundary length per unit area) during annealing.107

Figure 4.2: (a) Effects of recovery on dislocation density (ρ) and residual Stress (σ_{11} component). These are shown for recovery at 573 K (for 15 and 30 minutes) using standard [45] ODF (orientation distribution function) sections of $\varphi_2 = 45^\circ, 65^\circ, 90^\circ$. (b) Evolution of dislocation density with recovery time and (c) Residual Stress (σ_{11}) versus dislocation density. (b) and (c) were taken from the respective ODFs (as in figure 4.2a), with error bars indicating the data from symmetric positions of the ideal (S {123} $\langle \bar{6}3\bar{4} \rangle$, Brass {110} $\langle \bar{1}1\bar{2} \rangle$ and Goss {110} $\langle 001 \rangle$) orientations with $\pm 15^\circ$ deviation. (d) Rate of stress relief with dislocation density as a function of recovery temperatures as estimated from slopes of figure 4.2c.111

Figure 4.3: Residual stress components of (a) σ_{11} and (b) σ_{13} as a function of annealing time. The multiple {hkl} GIXRD measurements for residual stresses were taken at different annealing temperatures. (c) Progressive stress relief for σ_{13} was used to calculate Zener–Wert–Avrami exponent (stress relaxation exponent m: see eq. (4.3)) for all three recovery temperatures.113

Figure 4.4: EBSD IQ (image quality) maps showing changes in dislocation cell or sub-grain structures. These are taken from the same grain or orientation during different recovery stages (or time periods) of 473 K annealing. They show both annihilation (‘red’ arrow) and creation (‘blue’ and ‘yellow’ arrows) of dislocation boundaries. Residual stress measurements, with micro-Laue diffraction, are taken at each stage, and the entire stress matrix was estimated.....114

Figure 4.5: GND density versus annealing time as (a) measured from EBSD and (b) simulated from DDD. The measurements were taken from regions within 5° from ideal S {123} $\langle \bar{6}3\bar{4} \rangle$, Brass

{110} < $\bar{1}12$ > and Goss {110} < 001 > orientations. The orientations are shown with their respective unit cells. 116

Figure 4.6: Residual Stress versus GND density as (a) measured experimentally from the direct observations (figure 4.4) and (b) simulated with DDD. These observations were made for three ideal orientations (as in figure 4.5). 118

Figure 4.7: Rate of stress relief with GND density ($\frac{d\sigma_{11}}{d\rho_{GND}}$) for three different orientations as a function of temperature as observed from (a) direct observations and (b) DDD simulations. ... 118

Figure 4.8: Rate of change of (a) low (1-15°) and high (>15 °) angle boundaries with annealing temperature. Rate of change of low (1-15°) angle boundaries for different (see figure 4.5) ideal orientations. The data were obtained from large area EBSD scans. 119

Figure 4.9: (a) Enlarged view of DDD simulations on substructure plus residual stress evolution during recovery. Deformed (~5% plastic strain) Goss {110} < 001 > grain was subjected to recovery at 473, 523 and 573 K. And post recovery substructure, especially the pinned dislocations, and associated residual stresses were estimated. (b) Pinned dislocation density versus recovery time for the three annealing temperature and two ideal orientations: Goss {110} < 001 > and S {123} < 634 > . (c) For these two ideal orientations, normalized glide and climb distance moved are plotted as a function of recovery temperature. 120

Figure 4.A1: Extraction of area detector data for plotting dislocation density (DD) and residual stress (RS) orientation distribution function (ODF). (a) Representation of pole figure angles (α and β) in a schematic pole figure (left side) and the goniometer angles (ω , ψ , ϕ) in XYZ coordinate system (right side). (b) Area detector (Vantec™) data (on peak profile and peak shift) were taken at different γ angles (azimuthal angle, in the anti-clockwise direction, from the diffraction plane [68]). These correspond to different positions in the measurement scheme in ψ - ϕ axes. (c) Several data points (on DD and RS) were obtained at each pole figure position (in ψ - ϕ axes), and the average values were considered for subsequent ODF calculation. 127

Figure 5.1: (a) Microtexture, in inverse pole figure (IPF) notation, evolution of rolled aluminum: as observed experimentally and simulated with crystal plasticity finite element (CPFE incorporating DRBH (dislocation reaction based hardening)). (b) Experimental ODFs (orientation distribution function) of dislocation density, residual stress (σ_{11}) and kernel average misorientation (KAM). (c) CPFE, with DRBH, simulated ODFs of σ_{11} and KAM. 139

Figure 5.2: Evolution of (a) grain orientation spread (GOS) and (b) KAM with plastic strain. These are shown for experimental and simulated (CPFE simulations with and without the dislocation reaction based hardening (DRBH)) data. Error bars indicate standard deviations from multiple EBSD scans and simulations. 140

Figure 5.3: Orientation dependent evolution of KAM, GOS and σ_{11} : as obtained experimentally and simulated with CPFE (with and without DRBH). These are shown for Goss $\{110\}\langle 001\rangle$, Cube $\{100\}\langle 001\rangle$, Copper $\{112\}\langle 111\rangle$, S $\{123\}\langle 63\bar{4}\rangle$ and Brass $\{110\}\langle \bar{1}12\rangle$ [19]. Error bars indicate standard deviations from multiple EBSD scans and simulations. 141

Figure 5.4: (a) Direct observation on microstructural evolution in split channel die plane strain compression (SCDPSC). The same microstructure was also simulated with CPFE incorporating DRBH. (b) Near boundary mesoscopic shear (NBMS) strains were measured [18] from the appropriate microstructures (both experimental and simulated): and are shown for a representative grain cluster. Average NBMS, for ~50 randomly selected grains, are plotted from the experimental and simulated grain structures. Also included is the estimated measurement uncertainty as red dotted line. (c) Residual stress evolution were measured experimentally and simulated numerically for different ideal orientations: Goss $\{110\}\langle 001\rangle$, Cube $\{100\}\langle 001\rangle$, Copper $\{112\}\langle 111\rangle$, S $\{123\}\langle 63\bar{4}\rangle$ and Brass $\{110\}\langle \bar{1}12\rangle$ [19]. 143

Figure 6.1: Flow stress versus number of cycles. These are shown for cyclic deformation with two different strain amplitudes ($\Delta\varepsilon_p$: 0.0001 and 0.0025) and three different temperatures (300, 323 and 348K)..... 149

Figure 6.2: (a) X-ray diffraction with an area detector: showing different poles or family of orientations. The latter can be represented in an inverse pole figure (IPF) as orientations with different plane normal ($\{111\}$, $\{001\}$, $\{110\}$ and $\{113\}$). (b) Intensity versus 2θ plots were

extracted from the area detector data (figure 6.2a) to show changes in peak profile and peak shift with cyclic deformation. 150

Figure 6.3: (a) $d\text{-sin}^2\psi$ stress measurements, with area detector, for the normal (σ_{11}) component of the residual stress matrix. It shows that {001} and {111} to develop compressive stresses. Tensile stresses, on the other hand, was noted in {110}. These observations, on orientation dependent residual stress evolution, were valid for all stress amplitudes and deformation temperatures. (b) Inverse pole figure representing tensile and compressive residual stresses for sample subjected to cyclic deformation at 300K ($\Delta\varepsilon_p = 0.0025$ and 1000 cycle). (a) - (b) provide a clear picture of orientation (plane normal – see figure 6.1a) dependent residual stress development 152

Figure 6.4: EBSD measured kernel average misorientation (KAM) for different plane normal (as in figure 1a). (b) EBSD estimated KAM plotted in an IPF for different cyclic deformations. (a) and (b) show a greater magnitude of orientation dependence for the higher temperatures of cyclic deformation. 153

Figure 6.5: Examples of (a) DDD simulations of single-crystal residual stress development during cyclic deformation and (b) TEM imaging showing substructure formation..... 155

List of Tables

Table 2.1: Different techniques of residual stress measurements with their measurement principle, advantages and disadvantages	11
Table 2.2: Categorization of recovery, recrystallization and grain growth, based on mechanisms and driving forces involved. Courtesy [6].	31
Table 3.1: Chemical composition (in wt% of alloying elements) of the alloy (AA3003).....	62
Table 3.2: (a) Applied stress (in MPa) versus EBSD estimated densities of geometrically necessary dislocations (ρ_{GND}), low ($1-15^\circ$, ρ_{LAGB}) and high ($15-62.8^\circ$, ρ_{HAGB}) angle grain boundaries. (b) Based on data from (a), different regimes of tensile deformation are identified.....	68
Table 3.3: Parameters used in the discrete dislocation dynamics simulations	80
Table 4.1: Chemical composition, in wt% alloying elements, of the AA1050 used in this study.	97
Table 4.2: Parameters used in the discrete dislocation dynamics simulations for recovery.....	104
Table 4.3: Average dislocation cell or sub-grain size at different annealing temperature/time. These values were measured from EBSD-IQ maps and image analysis – based on a method described elsewhere [46].....	108
Table 5.1: Chemical composition, in wt% alloying elements, of the AA1050 used in this study.	136
Table 5.2: Material parameters and hardening coefficients [50] for different junctions used in this study.	137

Abbreviations

BD	Boundary Density
CB	Cell Block
CPFE	Crystal Plasticity Finite Element
CRGO	Cold-Rolled Grain-Oriented
DD	Dislocation Density
DDD	Discrete Dislocation Dynamics
DDODF	Dislocation Density Orientation Distribution Function
DDW	Dense Dislocation Walls
DIBH	Dislocation Interaction Based Hardening
EBSD	Electron Back Scattered Diffraction
EDM	Electro-Discharge Machining
ED-XRD	Energy-Dispersive X-Ray Diffraction
fcc	Face Centered Cubic
FEG	Field Emission Gun
FEM	Finite Element Method
FWHM	Full Width at Half Maximum
GAM	Grain Average Misorientation
GIXRD	Grazing Incident X-ray Diffraction
GNB	Geometrically necessary boundaries
GND	Geometrically necessary dislocation
GOS	Grain Orientation Spread
HAGB	High angle boundary density
IDB	Incidental dislocation boundaries
IPF	Inverse Pole Figure
IQ	Image Quality
KAM	Kernel Average Misorientation
LAGB	Low angle boundary density
LB	Lamellar Boundaries

LEDS	Lower Energy Dislocation Structure
MB	Micro Bands
MRD	Material Research Diffractometer
NBMS	Near Boundary Mesoscopic Shear
ODF	Orientation Distribution Function
OOF	Object Oriented Finite-Element
PSB	Persistent Slip Band
RD	Rolling Direction
RS	Residual Stress
RSODF	Residual Stress Orientation Distribution Function
SCDPSC	Split Channel Die Plane Strain Compression
SEM	Scanning Electron Microscope
SF	Schmid Factor
SODF	Stress Orientation Distribution Function
TEM	Transmission Electron Microscopy
TF	Taylor Factor
TKD	Transmission Kikuchi Diffraction
XRD	X-ray Diffraction

Chapter 1

Introduction

From a mechanistic definition, “stress in a body, when the body is unacted by any external agency” is known as residual stress [1]. The definition of residual stress is made more metal physics oriented as “the stress in a body, which is at equilibrium with its surrounding” [2]. It is important, at this stage, to appreciate both definitions separately. Mechanistically, residual stress development can be illustrated by heterogeneous deformation of a ‘composite’ two-phase material (figure 1.1). On the other hand, residual stress can be explained from atomistic changes (figure 1.2). In equilibrium condition, the atoms stay at their minimum potential energy or at equilibrium distance r_0 . Application of any external energy (mechanical, thermal, chemical or combination of them) can shift the atoms (either at r_1 or r_2 as shown in figure 1.2) from their equilibrium position and the surrounding obstacles (such as grain boundaries, dislocations) can prohibit them to move back to equilibrium value. This creates the misfit strain inside the material: the so-called origin of residual stress. Practical implications of such stress build-up or relief are undeniable. Almost every engineering industry practices stress relief. However, its quantification, effectiveness and more significantly, understanding in relation to microstructure remain challenging. And this was the motivation for this thesis.

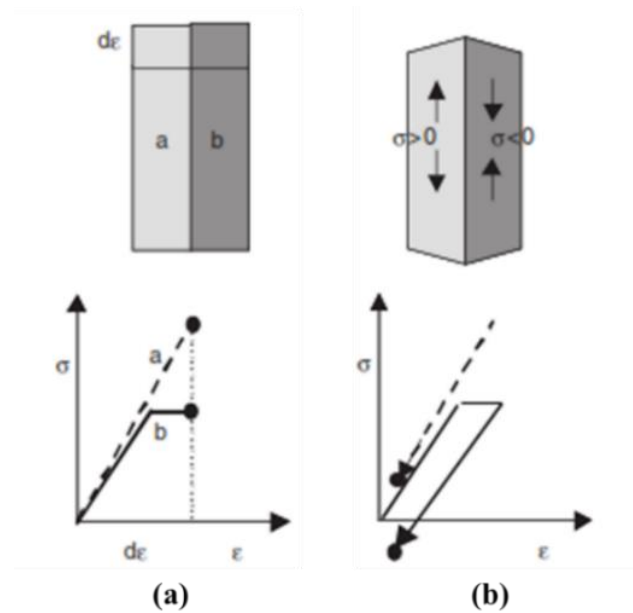


Figure 1.1: Schematic diagram showing the origin of residual stress from a ‘composite’ (a+b) material. (a) denotes the tensile extension of both the phases by $d\epsilon$, a being harder undergoes elastic deformation while b deforms elasto-plastically. (b) Upon unloading, and under appropriate constraint, a and b will enjoy tensile and compressive residual stresses respectively. Courtesy [3].

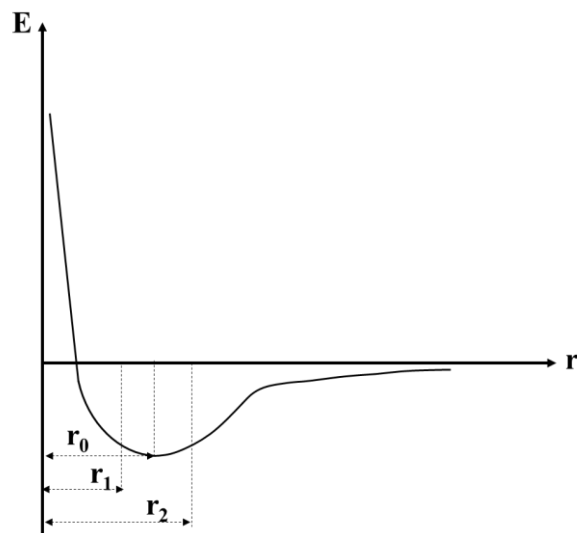


Figure 1.2: Energy potential well and equilibrium lattice position (r_0). External energy/stress can shift the atoms from equilibrium position to r_1 or r_2 . The changed configuration can be retained, fully or in part, under appropriate constraint. And this is the source of residual strain/stress.

It is important to appreciate that both mechanistic (figure 1.1) and the atomistic (figure 1.2) definitions of residual stress demand appropriate constraints. Such constraints may originate from solute atoms and vacancy clusters to dislocations and grain boundaries: the latter being more relevant to the domain of metallic materials. For example, plastic deformation [4-6] as well as thermal annealing [7-9] may significantly alter (figure 1.3) the dislocation substructures or the constraints accounting for the residual stresses. However, direct correlation between microstructure and residual stress evolution remains largely uncharted. And this is exactly what this thesis tried to explore.

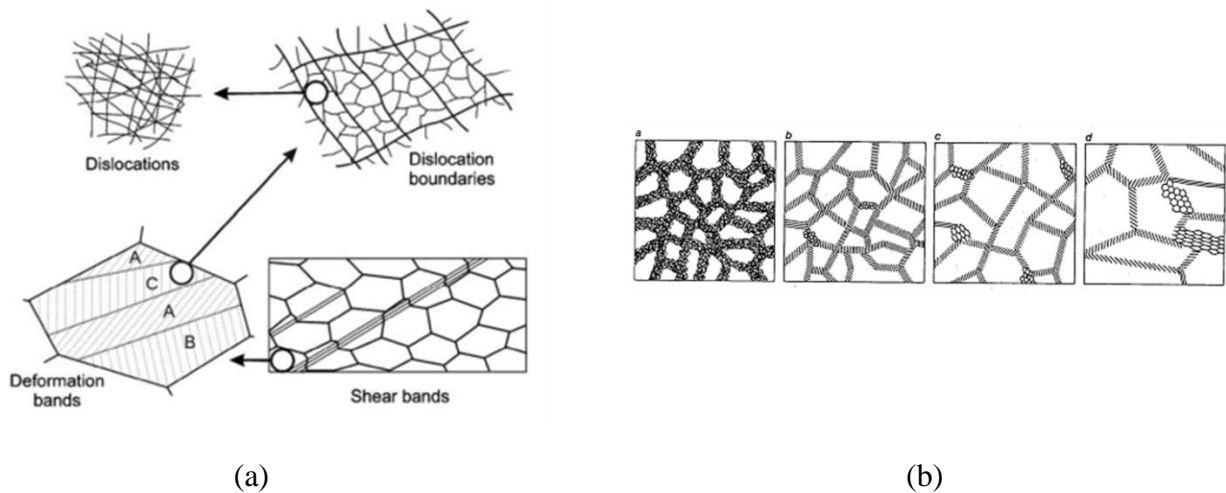


Figure 1.3: Schematic representation of microstructural changes. (a) Dislocation substructures at different microstructural length scale during plastic deformation, (b) Microstructural evolution in thermal annealing. Courtesy [3].

The thesis begins with a review of relevant literature (chapter 2). It starts with a brief discussion (chapter 2.1) on residual stress, its types and a brief description of diffraction based measurements of residual stress. In the next section (chapter 2.2 and 2.3), developments of dislocation substructures, both during plastic deformation and thermal annealing, are discussed. Chapters 2.1, 2.2 and 2.3 are important and relevant, as later in the thesis residual stress evolution is related to the substructural changes. Chapter 2.4 of the literature review deals with modelling aspects of residual stress: involving both discrete dislocation dynamics (DDD) and crystal plasticity finite

element (CPFE). It is important to point out that this thesis also used DDD and CPFE extensively, and hence a working knowledge of the relevant numerical simulations is considered necessary. Each of these sub-sections, also highlight the gaps in literature, which were then used to formulate the individual thesis chapters. The four main chapters of the thesis (chapters 3-6) and independent yet interrelated under a common theme: “*Microstructural Origin of Residual Stress*”. And these are discussed below.

Relating residual stress and substructural evolution during tensile deformation of an Aluminum-Manganese alloy (Chapter 3): Single crystal residual stress measurements (with micro-Laue diffraction) and evolution of GND (geometrically necessary dislocation) density were quantified during ex-situ tensile deformation. Experimental patterns of orientation dependent residual stress evolution were then simulated with DDD.

Microstructural Origin of Residual Stress Relief in Aluminum (Chapter 4): Direct (micro-Laue) and indirect (stress ODFs (orientation distribution function)) measures of residual stress relief were related to microstructural evolution. Orientation and temperature dependent stress relief were then linked to dislocation glide versus climb.

Orientation Dependent Developments in Misorientation and Residual Stress in Rolled Aluminum: The Defining Role of Dislocation Interactions (Chapter 5): Orientation dependent developments in residual stresses and in-grain misorientations were experimentally measured and numerically simulated (with CPFE). Combination of CPFE and DDD established that the orientation dependence originated primarily from slip systems, and associated anisotropic latent hardening.

Defining the Orientation Dependent Microstructure Evolution through Cyclic Deformation in an Aluminum Alloy (Chapter 6): This chapter remains partially complete, as additional experiments and simulations need to be completed. The chapter, however, come up with novel observation on orientation dependent residual stress evolution. It is stipulated that such reproducible measurements on tensile and compressive residual stresses can have technological implications on tailoring fatigue-resistant microstructures. And that is one of the reason that the partially completed chapter has been included in the present thesis. The author of the thesis is, however, sanguine that all pending experiments and simulating will be completed within next two months, and the final thesis will include a stand-alone (and complete) chapter 6. The last chapter (Chapter 7) summarizes the thesis and highlights the future research scopes.

References

1. Heindlhofer, K., *Evaluation of Residual Stress*. 1948: McGraw-Hill.
2. Withers, P.J. and H. Bhadeshia, *Residual stress. Part 1—measurement techniques*. Materials science and Technology, 2001. **17**(4): p. 355-365.
3. Verlinden, B., et al., *Thermo-mechanical processing of metallic materials*. Vol. 11. 2007: Elsevier.
4. Bay, B., et al., *Overview no. 96 evolution of f.c.c. deformation structures in polyslip*. Acta Metallurgica et Materialia, 1992. **40**(2): p. 205-219.
5. Bay, B., N. Hansen, and D. Kuhlmann-Wilsdorf, *Deformation structures in lightly rolled pure aluminium*. Materials Science and Engineering: A, 1989. **113**: p. 385-397.
6. Laird, C., P. Charsley, and H. Mughrabi, *Low energy dislocation structures produced by cyclic deformation*. Materials Science and Engineering, 1986. **81**: p. 433-450.
7. Humphreys, F.J. and M. Hatherly, *Recrystallization and related annealing phenomena*. 1995: Elsevier.
8. Nes, E., *Recovery revisited*. Acta Metallurgica et Materialia, 1995. **43**(6): p. 2189-2207.
9. Raabe, D., 23 - *Recovery and Recrystallization: Phenomena, Physics, Models, Simulation A2 - Laughlin, David E*, in *Physical Metallurgy (Fifth Edition)*, K. Hono, Editor. 2014, Elsevier: Oxford. p. 2291-2397.

Chapter 2

Literature Review

This section is aimed at summarizing available knowledge, from published literature, relevant to this thesis (*Microstructural Origin of Residual Stress*). This thesis used plastic deformation (both monotonic and cyclic) and thermal annealing. And then it tried to relate the concurrent evolution of residual stress and dislocation substructures. Finally, appropriate modelling and simulations were used to capture such concurrent evolution, and more importantly to bring out the underlying micro-mechanisms.

The literature review started with section 2.1: a discussion on residual stress (its origin, types and measurements). As deliberated in the introduction, the residual stresses are retained in a metallic material by the presence of dislocation substructures. Naturally, section 2.2 covered a description of plastic deformation (both monotonic and cyclic: as used in this thesis) and dislocation substructure evolution. Section 2.3, on the other hand, was focused on the dislocation substructure evolution during thermal annealing. Sections 2.1-2.3 thus covered the experimental aspects of the subsequent thesis chapters. They also summarized the gaps in literature. The final section of the literature review, section 2.4, collated information on computational plasticity: which covered the modelling tools (discrete dislocation dynamics and crystal plasticity finite element) used under this thesis.

2.1 Residual stress: Origin, types and measurement techniques

In 1913, Bragg [1] discovered the method to estimate interplanar spacing in crystalline material. Following his approach, a series of research articles were published from 1922-30 [2-4] on the possibility of residual stress determination from x-ray diffraction. With further improvements in accuracy and protocol, x-ray diffraction became a widely used technique for residual stresses measurements.

The most common definition of residual stress often coined in textbooks and journal papers suggests it is the “stress present in a body which is at equilibrium with surroundings in absence of external load” [5]. A more lucid picture is elaborated in [6], and figure 1.1, which describes the

generation of residual stress from ‘two phase composite’ material deformation. Residual stress is developed in almost all processing conditions – extending from plastic deformation (rolling, forging, uniaxial and multiaxial deformations, cyclic deformation, shot peening) to thermal or chemical processes (thermal annealing, welding, carburizing or nitriding, precipitation, phase transformation). Most of the time, this is detrimental to the material service conditions, while sometimes it has impact on the improvement of performances.

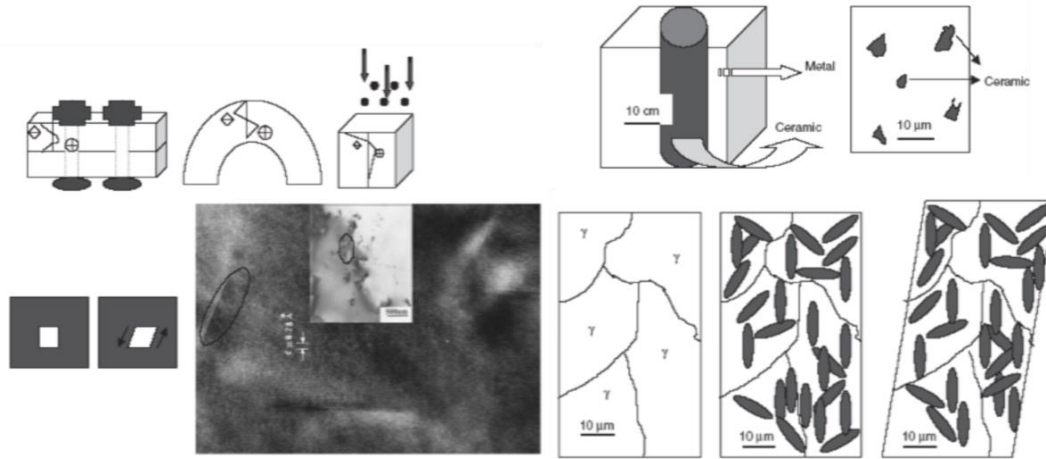


Figure 2.1: Origin of residual stresses from various sources. Courtesy [6]

Microstructurally, residual stress in a body is induced because of the misfit from interplanar spacing. This arises from different processes and gets retained inside the body because of the constraints from the surrounding. The misfit in interplanar spacing can be of chemical, mechanical, thermal or thermo-mechanically induced (figure 2.1).

In 1914, Heyn [7] pointed out that plastic deformation could lead to heterogeneous residual stress distribution. The reason was attributed to the inherent elastic and plastic anisotropy of individual grains. Further publications also supported the fact that x-ray measured residual stresses vary with crystallographic orientations. Under the lights of modern day investigations, residual stress can broadly be classified into two types based on their scale of existence [5, 6, 8, 9]: macro stress and micro stress. Micro stress is again subdivided in two categories: intergranular and intragranular residual stress. Thus the distribution of residual stress is the summation of these three types of residual stresses.

$$\sigma_{RS} = \sigma^{macro} + \sigma^{intergranular} + \sigma^{intragranular}$$

Residual stress that spans over a long distance within the material covering many grains and represents the average value of residual stress within that volume of material is known as macro stress. This is often denoted as type I residual stress or bulk residual stress (σ^I). This stress can be introduced by various manufacturing process like rolling, forging, casting, welding, thermo-mechanical treatments etc. and could be harmful to the required in-service mechanical properties. Thus this of main interest to design engineers. Mathematically, this is defined as the mean stress over the material volume of interest (V)

$$\sigma^I = \frac{1}{V} \int_V \sigma_{RS} dV \quad \text{-----}(2.1)$$

Intergranular or type II residual stress (σ^II) varies from grain-to-grain due to heterogeneity and anisotropy of each grain (for single phase materials) or due to the property difference of individual phases (for multiphase materials), and these are important as an indicator of strain hardening and damage to a material. This is calculated as the deviation from macro stress over the volume of individual crystallite (or phase) of interest

$$\sigma^{II} = \frac{1}{V} \int_V (\sigma_{RS} - \sigma^I) dV \quad \text{-----}(2.2)$$

Intragranular or type III residual stress is the local variation of residual stress inside an individual grain from its grain average residual stress. The development of type III residual stress occurs due to varying stress fields of individual dislocations, dislocation pile-ups, and other microstructural phenomena of discontinuous nature, making the grain either susceptible or resistant to damage. Thus the local development is reflected in the macroscopic outcome.

The following schematic in figure 2.2 shows the microstructural scale of all three types of stress in a material.

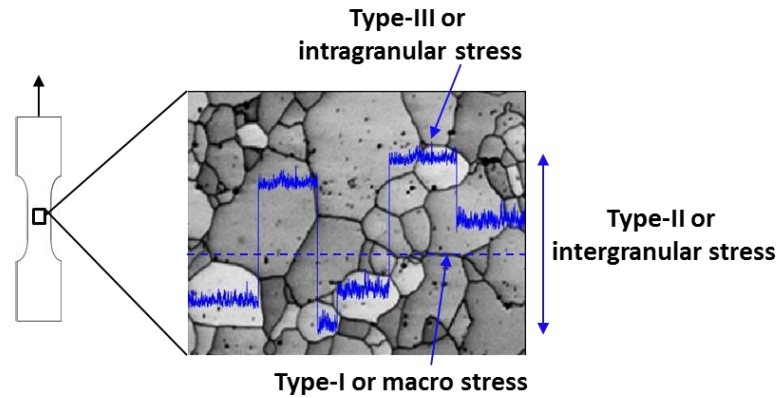


Figure 2.2: Development of different types of residual stress during uniaxial deformation

Long range strain incompatibilities act as the source of type I stress in the material. Plastic deformation (attributed to heterogeneous deformation of grains attributed to crystallographic slip and/or twinning) or temperature gradient (difference in thermal expansion coefficient) causes the modification of microstructure in individual grains. As the elastic properties vary in individual grains with orientation, the microstructural modification is not homogeneous and it varies from grain to grain. This acts as the source of type II stress. Crystal imperfections (e.g. voids, dislocations) produce due to slip or twinning which causes an internal stress field. This varies with the probe location and causes the type III stress. In any residual stress development process, all these types of stress develop simultaneously. There are many techniques to estimate residual stress in a material. The following section elaborates that.

2.1.1 Measurement techniques of residual stress

There are several techniques to measure residual stresses. Most of them are focused on measuring type I stresses. Based on their nature of measurement, these techniques can be broadly classified [6, 8-12] as (a) Mechanical methods, (b) Methods which involve material property change and (c) Diffraction techniques. As a general understanding, mechanical methods work by measuring the relaxation of stress that occurs by material removal and the other two estimates the stress by measuring some intrinsic physical property that is related to stress (e.g. magnetic response, ultrasound velocities, inter-planar spacing etc.). That is why often the first method is categorized as destructive method and the latter two as non-destructive method. As an interest to the present

thesis, the following section discusses the diffraction based stress measurement procedure with a brief outline of other methods [6, 8-11, 13] shown in table 2.1.

Table 2.1: Different techniques of residual stress measurements with their measurement principle, advantages and disadvantages

Technique	Measurement Principle	Advantage	Disadvantage
Hole drilling	Drilling a hole at the surface of the sample which allows relaxation around the hole and the lateral relaxation is measured by strain gauges fitted around the hole before making it	Fast, Easy to use and available for wide range of materials	Semi destructive method and difficult to interpret the data. Resolution of measurement is also low
Crack-compliance	Stress relaxation around a crack by strain gauge interferometry	Improved resolution of residual stress variation with depth and ability to measure both small and very large parts	Semi destructive method
Curvature	Measurement of the bending of substrate due to the deposition of a layer on it, then Stoney's equation to calculate residual stress	Easy method to estimate the stress	Mainly applicable to thin films. Accuracy is limited to measured curvature

Ultrasonic	Comparing the velocity (usually time of flight measurements are carried out to determine the velocity) between the stressed samples and an unstressed one gives the magnitude and direction of stresses present	Very quick and low cost method. Portable instruments which can give through thickness stress distribution for complex shaped structures	Limited resolution and bulk measurements over whole volume
Electrical and magnetic method	A detectable amount of change in electrical conductivity or magnetic permeability of the test piece is required compared to an unstressed material	Qualitative information can be obtained only, but a cheap and faster estimation of residual stress	Restricted to only electrically conductive or magnetic materials

2.1.1.1 Diffraction based methods

Diffraction based techniques to determine residual stresses principally measure the shift in diffraction angle (2θ). If residual stress is present inside a material, the interplanar spacing (d) changes. As per Bragg's law ($\lambda = 2d \sin \theta$), this change in interplanar spacing is reflected as shift in diffraction angle from the unstressed state value (d_0) and proportional to the magnitude of residual stress [8, 9, 14, 15]. The most important need of this method is to get the accurate value of the stress free interplanar spacing, d_0 . The most common diffraction based techniques are discussed below

X-ray diffraction

For surface residual stress measurement, X-ray diffraction is the most common and popular non-destructive technique. When the material is under stress, elastic strains are produced due to non-equilibrium shift of interatomic planes which is calculated as

$$\varepsilon = \frac{d - d_0}{d_0} = \frac{\Delta d}{d_0} \text{-----(2.3)}$$

where d and d_0 denote the interplanar spacing of the material in stressed and unstressed condition. By X-ray method, we can correlate this shift or deviation by differentiating Bragg's law $\left(\frac{\Delta d}{d_0} = -\cot \theta \Delta \theta\right)$ with residual strain which is further converted to residual stress (Hooke's law).

Figure 2.3 shows the orthogonal coordinate convention associated with X-ray diffraction. X_1 and X_2 constitute the sample surface whereas L_i defines the laboratory system. L_3 is in the normal direction to the planes whose interplanar spacing will be measured. The rotation angle (ϕ) and the tilt angle (ψ) are defined as the angle between X_1 and L_1 axes and X_3 and L_3 axes respectively. For the interplanar spacing measured from the diffraction peak for a given plane $\{hkl\}$, the strain component along L_3 can be noted as

$$\varepsilon_{33}^{\phi\psi} = \frac{d_{\phi\psi} - d_0}{d_0} \quad \text{-----(2.4)}$$

where $d_{\phi\psi}$ is the interplanar spacing at any angle (ϕ, ψ) and d_0 is the strain free or equilibrium lattice spacing.

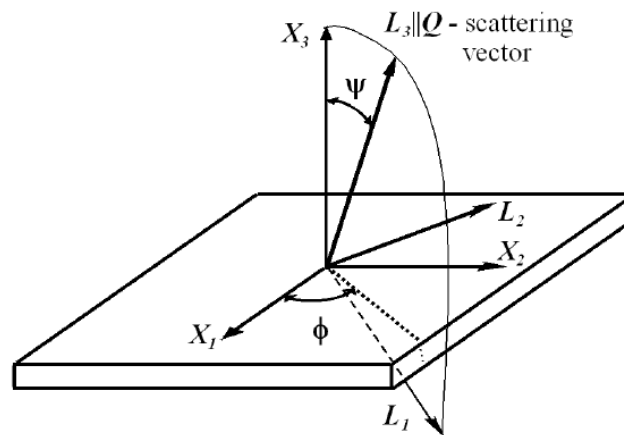


Figure 2.3: Development of different types of residual stress during uniaxial deformation. Courtesy [8]

This strain can be transformed to specimen coordinate system imposing tensor transformation [9]

$$\varepsilon_{33}^{\phi\psi} = a_{3k} a_{3l} a_{kl} \quad \text{-----(2.5)}$$

whereas a_{3k} and a_{3l} are the direction cosines and can be written as

$$a_{ik} = \begin{vmatrix} \cos \phi \cos \psi & \sin \phi \cos \psi & -\sin \psi \\ -\sin \phi & \cos \phi & 0 \\ \cos \phi \sin \psi & \sin \phi \sin \psi & \cos \psi \end{vmatrix}$$

Substituting the values in equation 2.4, it becomes [9]

$$\begin{aligned} \varepsilon_{33}^{\phi\psi} &= \frac{d_{\phi\psi} - d_0}{d_0} \\ &= \varepsilon_{11} \cos^2 \phi \sin^2 \psi + \varepsilon_{12} \sin 2\phi \sin^2 \psi + \varepsilon_{22} \sin^2 \phi \sin^2 \psi + \varepsilon_{33} \cos^2 \psi + \varepsilon_{13} \cos \phi \sin 2\psi + \varepsilon_{23} \sin \phi \sin 2\psi \end{aligned} \quad \text{-----(2.6)}$$

This equation is the fundamental equation of X-Ray strain measurement. This signifies that at least six independent reflections are needed to solve the linear equation to get full stress tensor.

To measure residual stress using XRD, there are various techniques (e.g. single angle technique, $\sin^2\psi$ method, multiple $\{hkl\}$ or grazing incidence X-ray diffraction (GIXRD)) amongst which the popular ones are $d - \sin^2\psi$ [9, 11, 14, 15] method and GIXRD for polycrystalline sample. In $d - \sin^2\psi$ method, the lattice spacing is determined for multiple ψ tilts [11]. When the sample is tilted by an angle ψ , the peak position shifts, proportional to residual stress present in material (see figure 2.4). Generally, as the depth of penetration is low in Lab-XRD, a bi-axial plane-stress condition can be assumed ignoring shear components of strain i.e. no stress present perpendicular to the free surface ($\sigma_{33}=0$) and $\sigma_{11} = \sigma_{22}$. Applying elasticity theory for isotropic solid, equation 2.4 becomes [6, 8, 9, 11, 14]

$$\varepsilon_{33}^{\phi\psi} = \frac{d_{\phi\psi} - d_0}{d_0} = \frac{1+\nu}{E} (\sigma_{11} \cos^2 \phi + \sigma_{22} \sin^2 \phi) \sin^2 \psi - \frac{\nu}{E} (\sigma_{11} + \sigma_{22}) \quad \text{-----(2.7)}$$

This is the common x-ray residual stress equation which predicts linear $d_{\phi\psi}$ vs. $\sin^2\psi$ behavior. Experimentally, the lattice spacing is measured for multiple $\pm\psi$ tilts (see figure 2.4) and the experimental data is fitted to a least square line where the slope gives the estimate for residual stress assuming the material constants E and ν and unstressed lattice spacing d_0 is known.

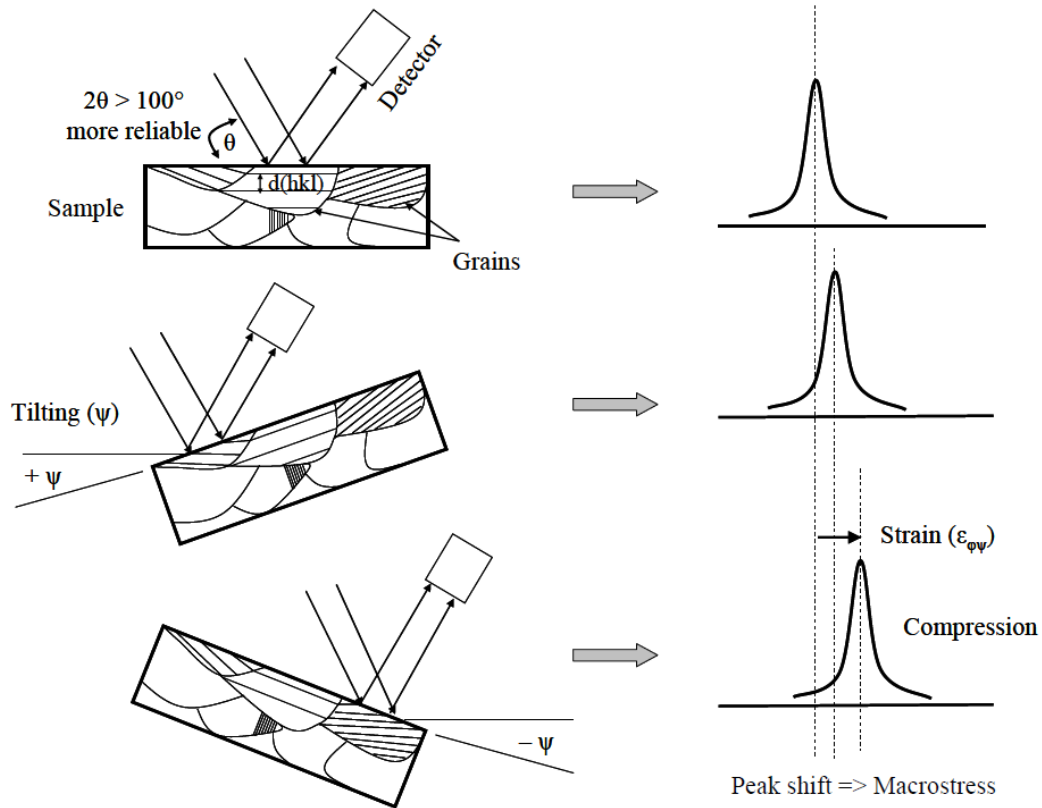


Figure 2.4: Shift of diffraction peak in a stressed sample during the tilt of sample at an angle $\pm\psi$. Courtesy [16]

The assumption of non-existence of strain components in normal direction to sample surface and shear components may not be true always as the ψ -split in the expected linear relationship shows the existence of other strain components for most of the materials. In a similar way, the lattice spacing is measured for multiple $\pm\psi$ tilts with a ϕ rotation at 0° , 45° and 90° . This helps to solve the fundamental equation with other strain components and a full stress tensor can be obtained.

Standard $\sin^2\psi$ method involves measurement of lattice spacing for a range of $\pm\psi$ tilts for a fixed diffraction angle. On the other hand, GIXRD [17-19] involves reflections for different $\{hkl\}$ or

Bragg angles. This different {hkl} offer a range of lattice spacing and ψ tilts, sufficient to solve $d_{\phi\psi}$ vs. $\sin^2\psi$ relation.

Two-tilt method is a simplified version of standard $\sin^2\psi$ method which are used for quick testing. Instead of multiple $\pm\psi$ tilts, only two tilts are used here to get the peak shift. This method is valid only for small range of peak shift. Single angle technique is another variation in class which is less sensitive than $\sin^2\psi$ method as the ψ range is restricted by the Bragg angle.

Laboratory and Synchrotron X-Ray Diffraction

Based on number of factors e.g. X-ray source, degree of accuracy, measurement speed, spacial resolution of residual stress needed etc., we can choose the laboratory X-ray diffraction (Lab-XRD) or the energy-dispersive X-ray diffraction using synchrotron radiation (ED-XRD) based on the advantages offered by each method. Lab-XRD uses low energy monochromatic beam of fixed wavelength (depending on the target material used in x-ray tube e.g. $\lambda = 1.5418 \text{ \AA}$ for Cu source) with a free choice of Bragg diffraction angle to measure residual stress. The penetration depth remains low because of beam energy which makes it suitable to measure residual stresses at surface or few micro meter in depth from surface. Also as the penetration depth is low, the interaction volume becomes small and any stress gradient present inside the material does not influence the measurement much. Contrary to this, ED-XRD uses very intense and narrow beam of high energy making it suitable for measurement at higher penetration depth (~50 mm for aluminum) with an area which can be restricted to crystallite size. It is faster in data collection than lab-XRD and whole spectrum of diffracted radiation can be recorded simultaneously. It can provide a three-dimension map of strain distribution in polycrystalline materials as well as single crystals. A schematic view of both the techniques is shown in figure 4.5.

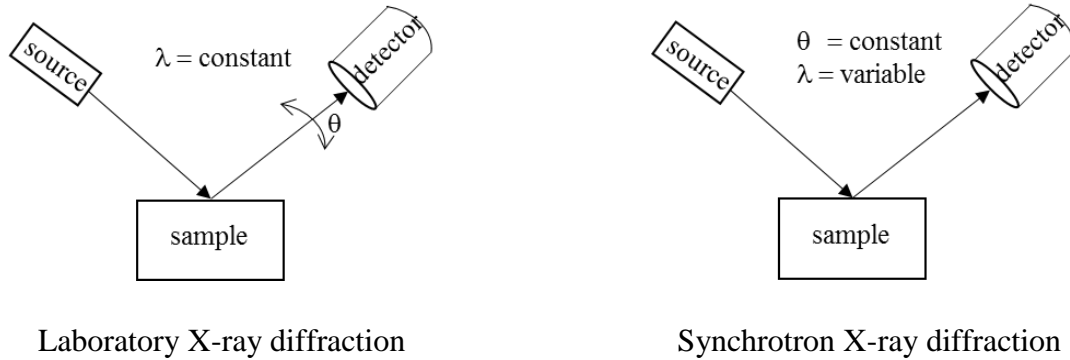


Figure 2.5: Comparison between measurement techniques of laboratory X-ray diffraction and synchrotron X-ray diffraction

Neutron Diffraction

Similar to XRD, neutron diffraction also measures elastic strain components from interplanar spacing change. A monochromatic beam of a constant wavelength is used for diffraction and peak positions from diffraction data are used to get interplanar spacing using Bragg's law [10, 20]. Then the shift compared with an unstressed state interplanar spacing yields the residual strain $\left(\varepsilon = \frac{\Delta d}{d_0} = -\cot \theta_0 \cdot \Delta \theta \right)$. These strains in three orthogonal directions of sample are converted into stresses using Hooke's law

$$\sigma_x = \frac{E}{(1+\nu)(1-2\nu)} \left\{ (1-\nu)\varepsilon_x + \nu(\varepsilon_y + \varepsilon_z) \right\} \text{-----(2.8)}$$

with similar expressions for σ_y and σ_z , where E is elastic modulus and ν is Poisson's ratio.

The following are the advantages and disadvantages of using neutron diffraction

- ✓ Due to low absorption in materials, it can be used for high penetration depths (~100 mm in aluminum) of complex shapes of material.
- ✓ Surface preparation is not required.
- ✓ Tri-axial stress state can be measured because of higher resolution.
- ✗ Laboratory based technique with high cost involved.
- ✗ Surface and near surface stress cannot be measured.

2.2 Plastic Deformation and dislocation substructure evolution

Plastic deformation is widely used in manufacturing (example: plate rolling, sheet metal forming, drawing etc.). These industrial operations show a wide variety of microstructural features. From the view point of physical metallurgy, study of deformation microstructure unfolds many unanswered questions of industrial processing. Insights of deformation have two sides: macroscopically only geometrical shape and size changes are observed. The crystal lattice needs to compensate these changes to ensure non-failure. At microstructural scale, the movement of crystallographic defects (mainly dislocations) creates the microscopic movements which accommodate this macroscopic change. As a result, the dislocation density increases: leading to the generation of characteristic dislocation substructure.

Most of the energy associated with plastic deformation is spent as heat, only ~10% of energy remains inside the material: the so-called stored energy cold work [6, 21]. And this is the basis of dislocation substructure evolution. The formation of dislocation substructure, in turn, may depend on two factors: (i) dislocation interactions typical of a crystallographic orientation (or grain) and (ii) with additional influence from near-neighbor interactions. All these [6,22-27] lead to developments of various microstructural features (see figure 2.6).

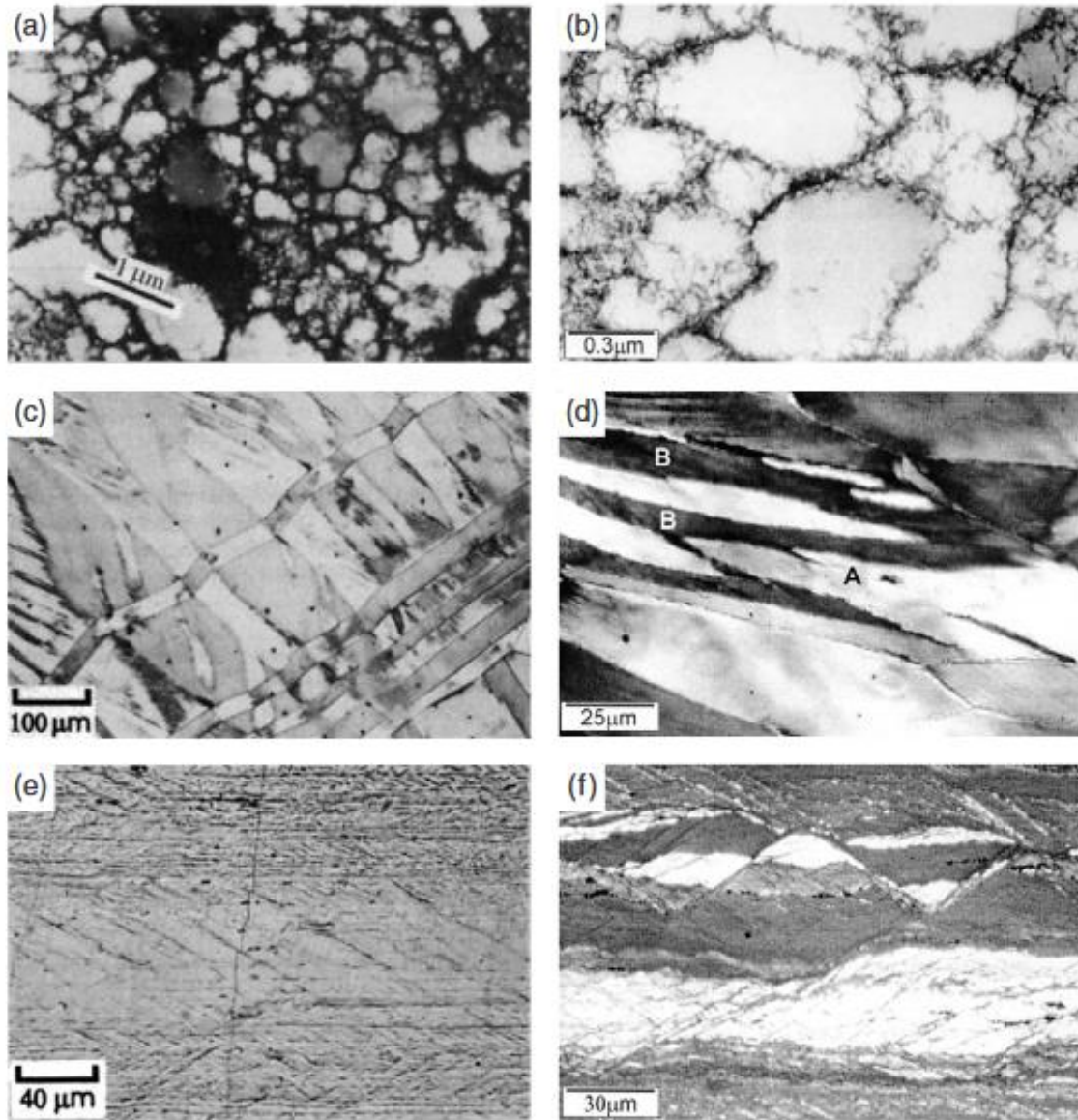


Figure 2.6: Development of different microstructural features in plastic deformation: (a) and (b) cell structure, (c) and (d) deformation bands, (e) and (f) shear bands. Courtesy [21]

The loading type in plastic deformation can broadly be classified as monotonic and cyclic loading. Both the deformation types produce unique kind of dislocation patterning or substructural evolution. At lower strain levels, dislocation substructures generated by both the modes are comparable for fcc crystals whereas noteworthy variances in the dislocation substructures are observed as deformation progresses [28]. The major difference between the two deformation

processes is configuration of dislocations – a dynamic equilibrium of dislocation substructure exists in cyclic loading due to the larger time and dislocation motion involved compared to monotonic loading [28]. Subsequent sub-sections discuss these deformation heterogeneities development for monotonic and cyclic deformation conditions. As the investigating material is Aluminum here, discussion on development of deformation microstructure is restricted to fcc materials.

2.2.1 Monotonic deformation and dislocation structure development

In a hierarchy of microstructural length scale, the deformed microstructure can be categorized as shear bands, deformation bands and dislocation boundaries (figure 2.7). Usually, shear bands are regions of strong localized shear (can be within a grain or over a span of many grains) which is generally extended to macroscopic dimensions [6, 21]. On the other hand, deformation bands are defined as the regions within the grains that deform comparatively homogeneously but with the different slip characteristics than the adjacent regions [6, 21]. Here it is important to note that slip characteristics and deformation behavior is crystal orientation dependent.

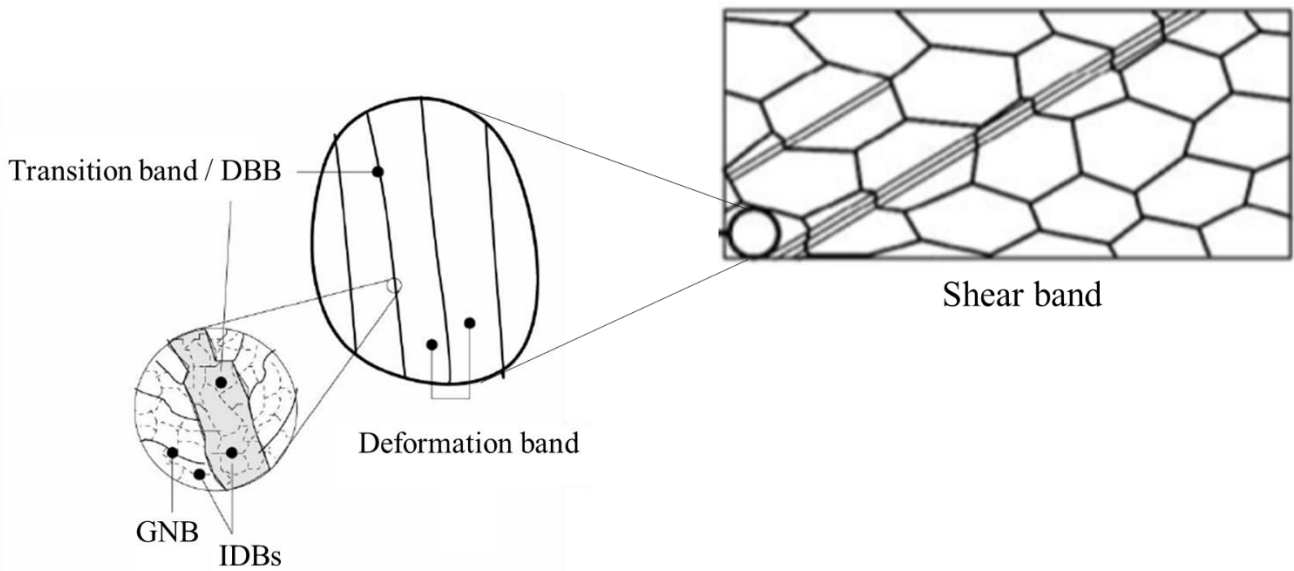


Figure 2.7: Schematic of different deformation heterogeneities in microstructural length scale. Courtesy [6, 29]

Deformation microstructure development is a dynamic evolution which can be interpreted from work hardening curve [30-34]. Before the failure of material, it undergoes various stages of work hardening as shown in figure 2.8. Most of the materials show 3 stages of work hardening, whereas the 4th stage is characteristic for higher deformation processes [6, 34].

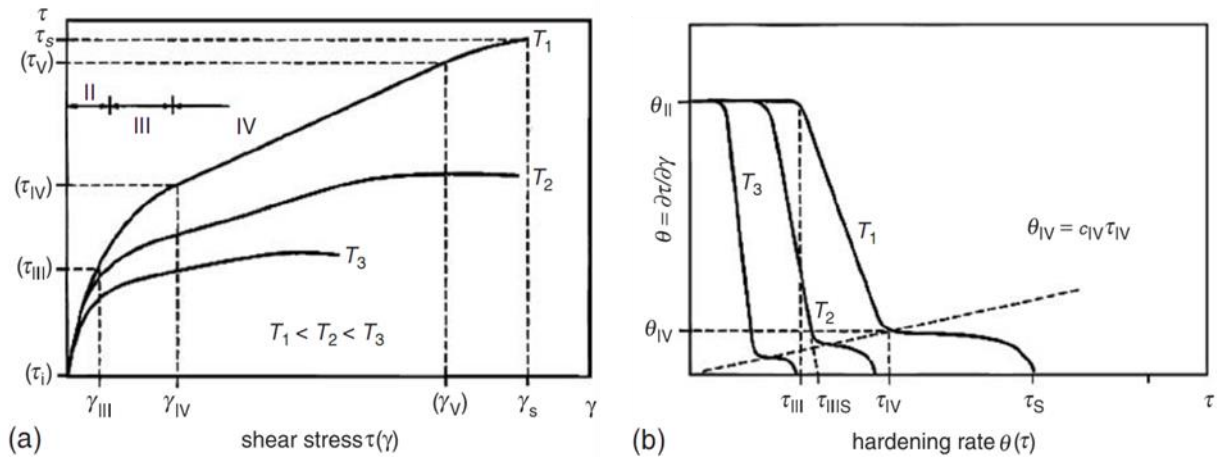


Figure 2.8: Schematic stress–strain $\tau(\gamma)$ and work hardening $(d\tau/d\gamma)(\tau)$ plots at three temperatures $T < 0.5T_m$. Courtesy [6, 34]

Stage I is commonly seen for single crystals oriented for single slip. This stage is characterized by initial part of the work hardening curve having low slope. In this stage, very little strain hardening occurs as dislocations do not get hindered by obstacles and can have long mean free path for movement. In polycrystalline material, grain boundary restricts the initial motion of dislocations acting as a “sink”. As the dislocations are confined to their slip planes without interacting with each other, this results in a very small hardening rate [33].

Application of increased strain activates the dislocation motion and their rapid multiplication enables a high and relatively constant hardening. This is referred as stage II. At this stage as a result of activation of different slip systems, lattice defects (primarily dislocations) start forming [6, 21]. Dislocation tangles starts to appear in microstructure which in due course forms dislocation cell structure. This local arrangement of dislocations actually causes the development of misorientation which increases till stage III starts.

Further deformation causes annihilation of dislocations of opposite sense which counterbalance the dislocation multiplication (stage III). At these two higher deformation levels, the strain heterogeneity at local scale is amplified by misorientation development. Microstructurally, the misorientation development is identified as significant number of dislocations organized into particular “patterns” within individual grains, composed of regions with almost free of dislocation (cell interior region) and high dislocation regions (cell walls) [21, 35]. Some free dislocations can also be present either randomly distributed inside the cells (between the dislocation walls), or more localized close to the grain boundaries to accommodate the strain incompatibilities between neighboring grains. Continuous escape of dislocations tend to make the cell walls into thinner, neater, boundaries [30] during stage III.

Stage IV, is generally seen at higher strains, mainly in many rolling and extrusion processes. Availability of unlimited cross slip due to higher strains makes the rate of hardening relatively low and constant [6, 31, 33, 34]. TEM study reveals that at this stage, material forms the banded structure of different orientations separated by transition zone and grain boundary as shown in figure 2.9.

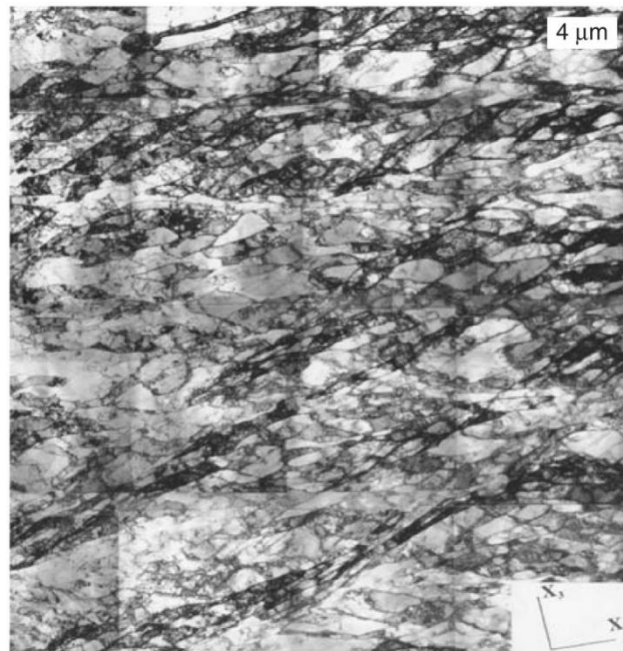


Figure 2.9: TEM micrograph reveals the dislocation cells and microbands in high purity iron after 80% cold reduction. Courtesy [6].

Based on the available reviews [23, 32, 36-38] and experimental observations [25, 39-41], there exists different terminologies to describe deformed microstructure. Within a common framework based on sub-division of grains, these deformation induced boundaries can be categorized as [23, 42]

- (a) Geometrically necessary boundaries or GNBs (dense dislocation walls (DDWs), microbands (MBs), lamellar boundaries (LBs), sub-grain boundaries)
- (b) Incidental dislocation boundaries or IDBs (ordinary cell boundaries)

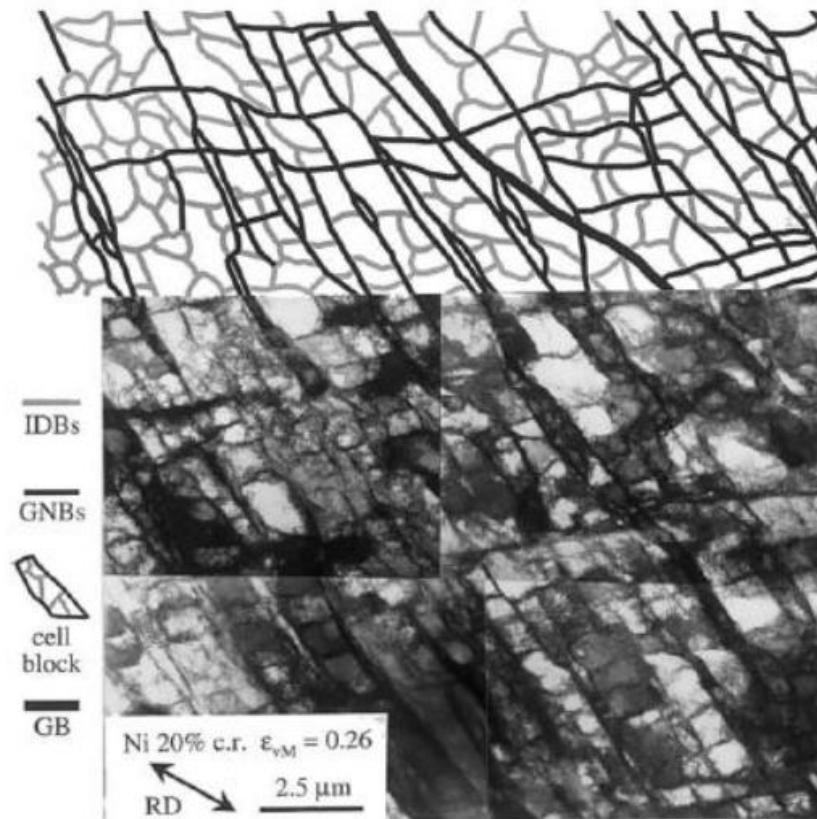


Figure 2.10: Figure represents the TEM micrograph of pure nickel following a reduction of 20% by cold rolling. It shows the dislocation microstructure and substructures, top part of the figure is a tracing of micrograph to demonstrate the cell block (CB) structure composed of GNBs and IDBs. The long GNBs are inclined to the rolling direction and almost parallel to the $\{111\}$ slip plane. Parts of two grains are separated by a grain boundary (GB). Image is taken in longitudinal section containing the normal and rolling direction (RD). Courtesy [36]

Figure 2.10 shows a transmission electron micrograph of these different dislocation boundaries. GNBs are assumed to develop by different slip activity on each side of boundary while IDBs tend to form by mutual entrapment of glide dislocations. It has been noted that misorientation across both the boundaries increase with increasing strain but the spacing decreases [22, 23, 43-46]. As a consequence of deformation, grain fragmentation happens and the substructure formed can be sub categorized as shown in figure 2.11 [47]. GNBs enclosed the many equiaxed cells and forms the blocks generally termed as cell block (CB) [21-23, 44-46, 48]. Depending upon strain, the GNBs are expressed as dense dislocation walls (DDWs) and micro-bands (MBs), based on appearance of boundaries whether single or paired [22, 23, 43, 45, 49, 50]. Instead of cell structure some alloys like Al-Mg, shows cell structures with the dislocations almost in two-dimensional walls and surrounding nearly dislocation-free regions [39].

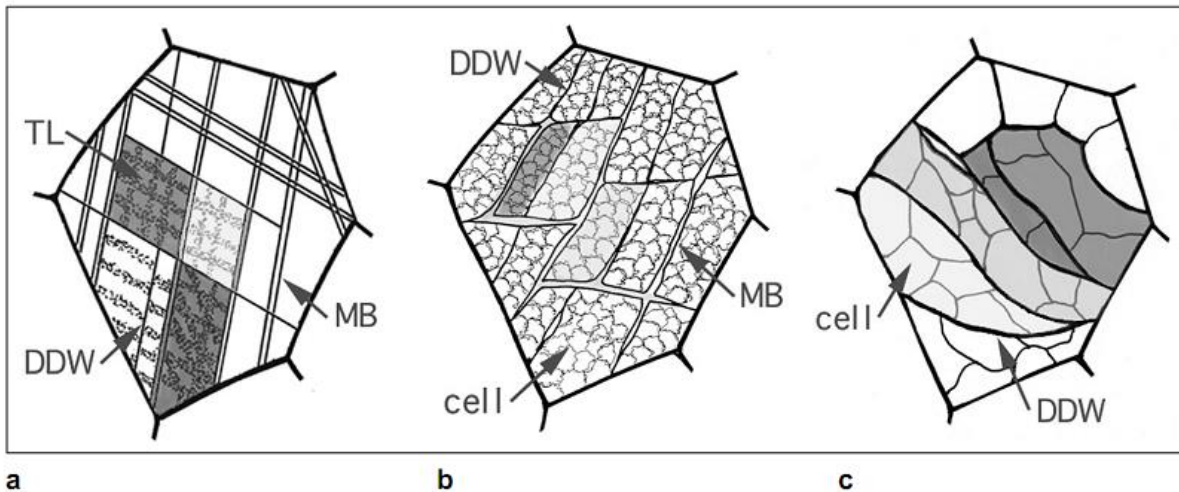
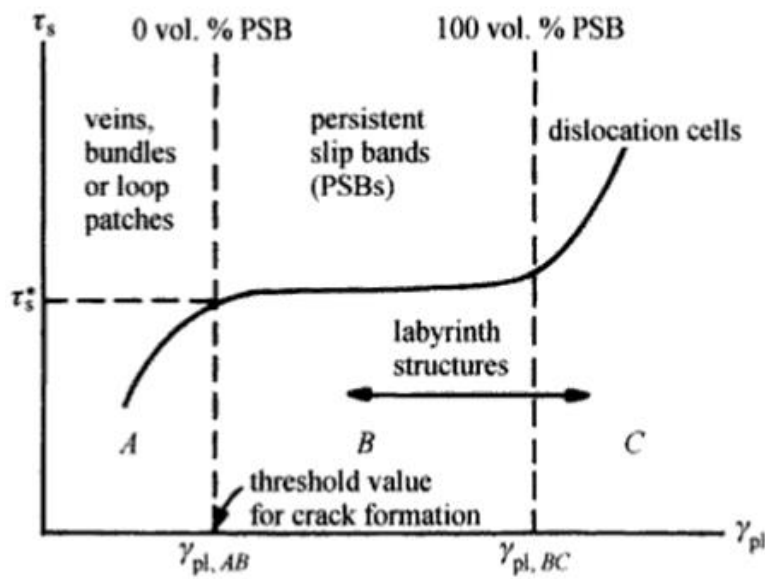


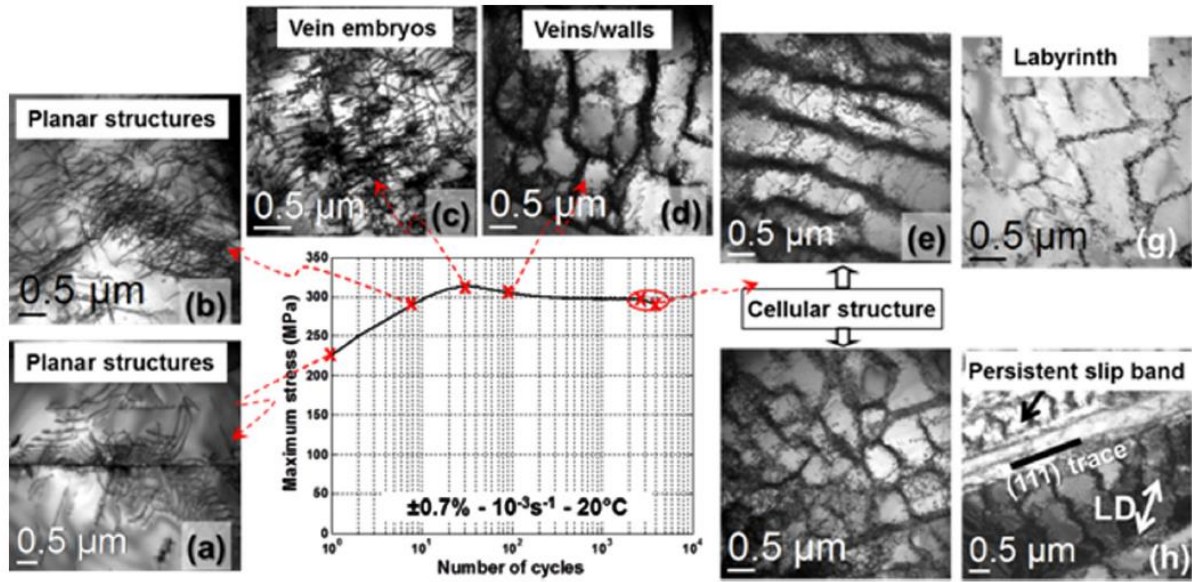
Figure 2.11: Schematic of different sub microstructural features of deformed microstructure. Courtesy [47]

2.2.2 Cyclic deformation and dislocation structure development

Unlike monotonic deformation, cyclic deformation may provide different substructural evolution. The back and forth movement of dislocations due to the cyclic reversal of load results in a microstructure that depends on degree of irreversibility of this movement. Correlation between these microstructural developments and mechanical properties offer an area of fundamental and industrial research. Microstructural evolution by cyclic deformation is also well studied [51-57]. For cyclic deformation of fcc single crystals with single slip orientation, the ‘cyclic stress-strain curve’ [58] shows three distinct regions (marked as A, B and C) as shown in figure 2.12(a) [28]. A general evolution of microstructure corresponding to these different regions is summarized in figure 2.12(b).



(a)



(b)

Figure 2.12: (a) Schematic representation of different regions of cyclic stress-strain curve. Courtesy [28], (b) Dislocation substructural evolution during cyclic deformation. Courtesy [59]

Region A refers to the work-hardening during cyclic loading. In general, alternating strain in initial cycles produce dislocations that get accumulated on primary glide plane and at later cycles it forms edge dislocation dipoles [57]. Further increase in cycles and below a threshold amplitude, the dislocation dipoles form a vein type structure (figure 2.13). The veins are elongated in shape and rich in dislocations (dislocation density $\sim 10^{15} \text{ m}^{-2}$). The veins are separated by channels which are comparatively dislocation free. This type of structure is known as matrix structure. At this stage, saturation of hysteresis loops happens following a dynamic equilibrium between the edge dislocations and screw dislocations.

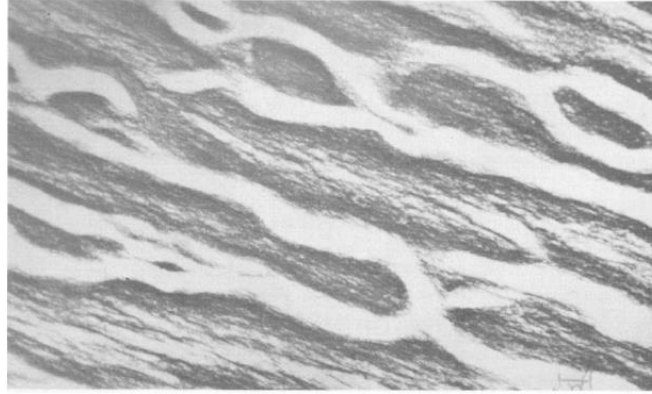


Figure 2.13: Vein structure in monocrystalline copper after cyclic loading at constant strain amplitude. Courtesy [55]

Towards the end of region A, a critical threshold amplitude is reached and the deformation becomes localized. That is the onset of region B which is identified as a ‘plateau’ region in the stress-strain curve showing a significant increase in plastic strain. At this stage, a ladder type structure is observed which is composed of a large number of slip planes (figure 2.14). This is known as persistent slip bands (PSBs), the term coined by Thompson et al. [60]. Dislocation substructure in PSBs are different as observed in matrix structure. In matrix type structure, veins consist almost 50% by volume and dense arrays of edge dislocations are observed. In contrary to this, mutual obstruction in glide dislocations results in PSBs where the ladder structure contains ~10% by volume. Ladder structure contains edge dislocations and screw dislocations are present in channels. A dynamic stability is attained where the ladder structure acts as source of new dislocation which goes to channel and further leave an edge dislocation in wall. This creation is counterbalanced by an annihilation which happens at walls of the ladder type structure.

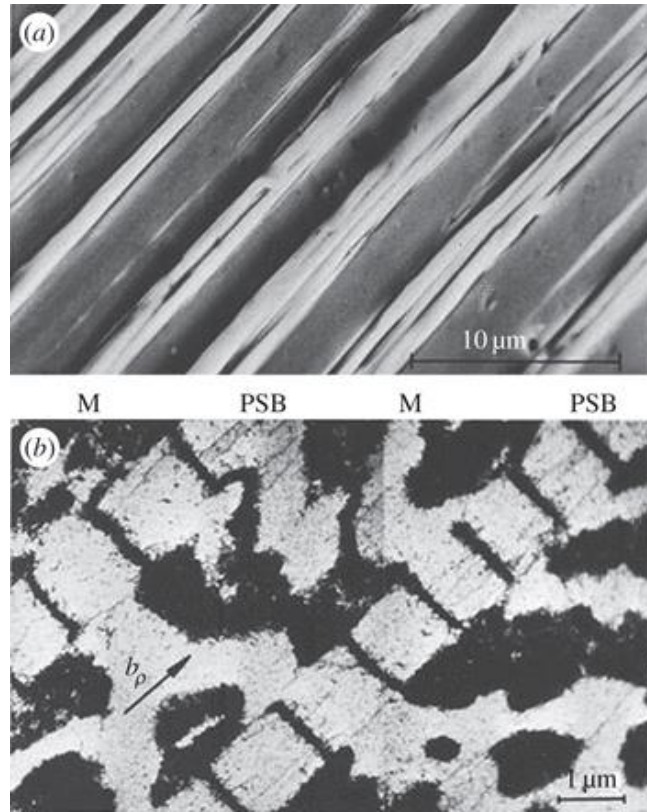


Figure 2.14: PSBs in fatigued copper – (a) appearance of PSBs under scanning electron microscope, (b) Transmission electron microscope image showing dislocation distribution in PSB and matrix of the same in single grain. Courtesy [61]

At much higher plastic strains, structure gets richer in dislocation at ladder wall side with channels almost dislocation free and ‘labyrinth’ and ‘cell’ structures are observed (region C). It has been suggested that the following sequence is seen at higher plastic strains involving microstructural changes matrix structure with labyrinth structure → PSBs and labyrinth structure → cell structure [62]. Figure 2.15 shows such examples.

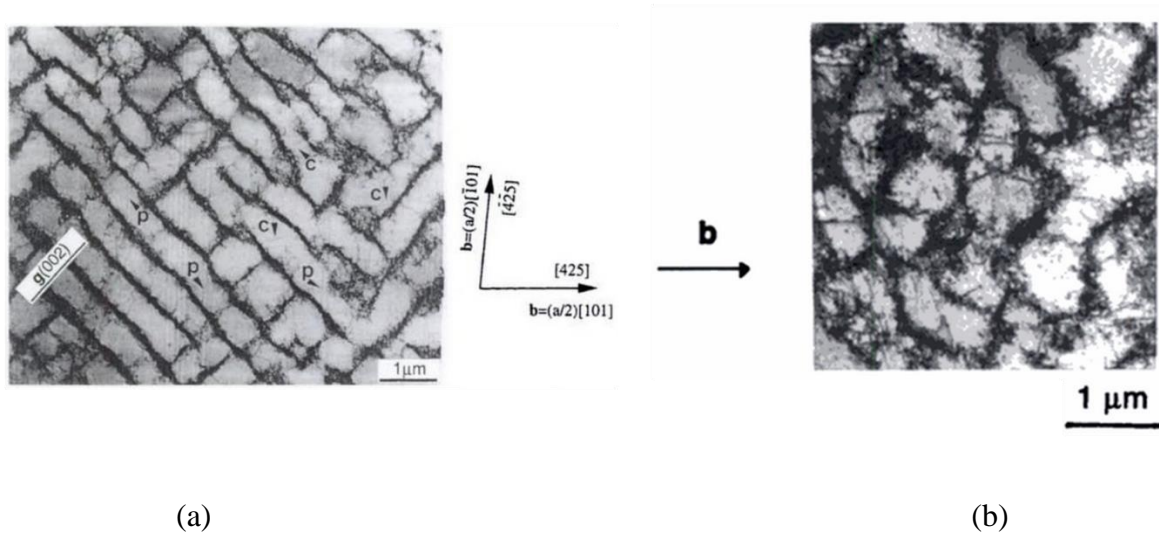


Figure 2.15: (a) Labyrinth structure formed in fatigued single crystal copper, (b) Cell structure formed at higher plastic strain in fatigued copper crystals. Courtesy [28]

2.2.3 Plastic deformation, dislocation structure and residual stress

The dislocation arrangement in plastic deformation is considered as dynamic instability as it starts well before the saturation stress level. Many classical theories were proposed to describe the science behind this substructure evolution and work hardening [63-65]. They mostly considered the dislocation movement due to the residual stress or a constant dislocation density which changes the pattern to minimize the strain energy. Also they considered dislocation movements due to single slip system. But with advance in knowledge, the theories are modified and a dynamic system is considered where local evolution criterion is considered. Sections 2.2.1 and 2.2.2 outlined a brief review on dislocation substructural evolution during plastic deformation.

When a polycrystalline material undergoes plastic deformation, compatibility between surrounding grains are needed. As the activation of slip systems and elastic stiffness tensor vary between grains, different grains experience different extent of work hardening. This naturally causes a non-uniform local stress distribution inside the microstructure: known as internal (or residual) stress and it can be varied with dislocation substructural modification/evolution [66]. In single phase metals and alloys, dislocation density and their arrangement influence magnitude of residual stress.

The literature on correlation between dislocation arrangement and residual stress dates back to '50s [65, 67-69]. It was considered that time the dislocation pile-ups are the classical source of residual stress. This was shown from slip line studies and theoretical calculations. Later in sixties, transmission electron microscopy (TEM) opened the door of dislocation arrangement observations. Classical studies from 1960-70 [70-72] showed the curved dislocation segments without external load, proving the existence of residual stresses. The well appreciated model on residual stress development considering dislocation configuration emerged out in '80s by Mughrabi, the "composite" model [73]. The model was first formulated for dislocation substructural changes associated with cyclic deformation, through it is applicable to all general cases where dislocations are distributed heterogeneously with a sharp contrast in dislocation populated regions such as dislocation "cell" structures. As a simplest case, let us consider dislocations (as an outcome of deformation) are distributed in the microstructure as 'cell' type microstructure. The boundary of the cells are pile-up of dislocations whereas the interiors are almost dislocation-free. When deformation is applied to this kind of structure, it behaves like a composite and the residual stress will generate to maintain the compatibility between the two different regions following 'rule of mixture'. Till now, this model is well applied in different studies to evaluate the connection between dislocation substructure and residual stress.

However, the orientation dependent residual stress and microstructural development still got open areas to research. Mostly, the studies performed till now are based on large grain single crystals or TEM observations. The drawback of these outcomes is primarily the statistical meaning of the data. Large grain specimens do not interpret the polycrystalline behavior or TEM observations are limited to few grains only. Hence a systematic study is needed which can fill out the gap of simultaneous observation of substructural development and residual stress as a function of crystallographic orientation during plastic deformation.

2.3 Thermal annealing of deformed material and dislocation substructure evolution

The deformed material possesses high stored energy. At elevated temperature, the instability in deformed state gets increased and ultimately the material gets softened and achieves the strain free state. This is known as annealing which has its own practical importance as well as fundamental significance in deformation behavior [21, 74]. Table 2.2 outlines a brief description of annealing related phenomenon. Based on the mechanisms involved these processes and driving forces, the stages observed in annealing can be distinguished as recovery, recrystallization and grain growth.

Table 2.2: Categorization of recovery, recrystallization and grain growth, based on mechanisms and driving forces involved. Courtesy [6].

Mechanism (kinetics)	Driving force (energies)			
	Point defects	Dislocations	Subgrain walls	Grain boundaries
Point defect diffusion	Low temperature			
Dislocation climb	Recovery			
Sub-boundary migration and coalascence	High temperature			
Grain boundary migration	Recrystallization			Grain growth

Recovery is considered as the initial stage of annealing which restores the material properties without significant changes in grain size and shape. Mainly the restoration happens through re-arrangement of dislocation substructure (and point defects annihilation also at low temperature: here low suggests $<0.3T_m$, T_m is melting temperature) towards low-energy configuration. The later step of recovery is recrystallization which is the alteration of deformed state to a strain free energy state. After the deformation signatures are removed through recrystallization, further application of temperature leads to grain growth. Figure 2.16 schematically illustrates dislocation annihilation

and rearrangement during thermal annealing. In this section, a brief understanding of recovery and the possible correlation with dislocation structural evolution and residual stress is described.

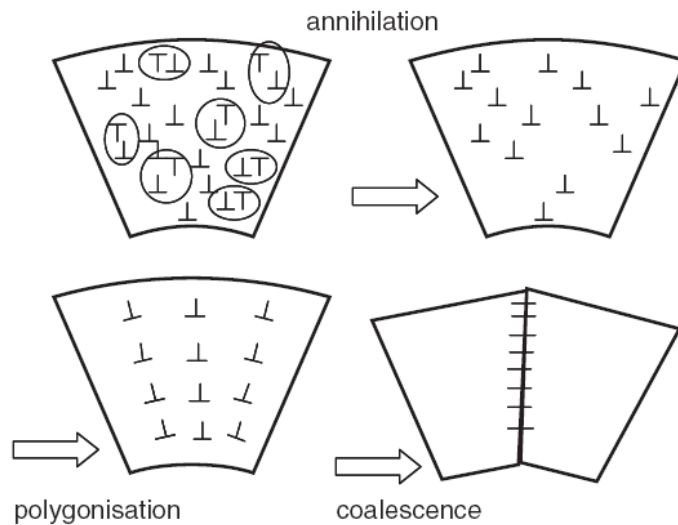


Figure 2.16: Schematic showing recovery mechanism by dislocation annihilation; cross-section of a bent crystal containing both free (edge) dislocations and dislocations which accommodate the orientation gradient. During annealing, some dislocations anneal out by climb of opposite sign segments (encircled pairs) then the remainder rearrange into sub-grain boundaries. Courtesy [6]

2.3.1 Dislocation substructure development during thermal recovery

Recovery is a part of annealing phenomenon where lowering of stored energy happens primarily by dislocation annihilation and rearrangement of dislocation structure prior to recrystallization. Recovery can also occur concurrently with deformation (known as dynamic recovery) – sometimes to such an extent, that dislocations are already in the form of well-developed subgrain structure [21, 75]. Post deformation annealing processes supply the necessary energy which minimizes total lattice distortion and strain energy created from plastic deformation. The thermal energy starts moving the free, random dislocations and it proceeds to a lower energy state either by rearrangement or annihilation of dislocations into dislocation walls or sub-boundaries forming low angle boundaries. The lower energy state has sub-grains which grows further with more energy supplied and reaches a recrystallized state [74]. Thus recovery is a series of microstructural changes, not just a single event of change which can be schematically shown as in figure 2.17 [21].

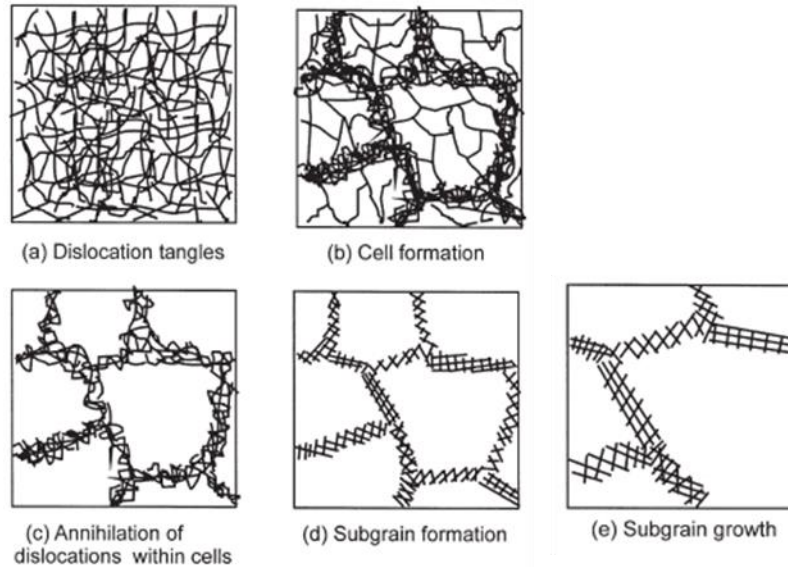


Figure 2.17: A schematic showing substructure evolution during Recovery. Courtesy [21]

Recovery kinetics is sensitive to crystal orientation [74-82], prior deformation, rate of deformation (strain rate) and temperature. Figure 2.18 shows the effect of strain rate and annealing time on the microstructure development. Attempts have been made to study the kinetic and mechanism of recovery [78, 83-89]. Extent of recovery is measured by direct measurement of release of stored (calorimetric method) or by indirect methods, which involves study of changes in some microstructure and properties of material. Later involves the measurement of hardness [78], X-ray peak broadening [90] or X-ray peak resolution [83], yield strength/flow stress [91]. All these measurements estimate the bulk recovery kinetics except the X-ray method. A significant amount of recovery (prior to recrystallization), lowers the driving force for subsequent recrystallization, which can influence the nature and kinetics of recrystallization. Recovery has long been considered as the primary mechanism responsible for the creation of recrystallized nuclei and thus the orientation dependent recovery can impact severely on the recrystallization and subsequent mechanical behavior. Classical example is the recovery of rolled cube (100) <001> orientation which shows faster recovery than other orientations [92]. Also because of microstructural modifications, misorientations change in recovery. Both increase [93, 94] and decrease [21] in misorientations have been observed in recovery. It is apprehended that the removal of orientation

gradient and the movements of ‘mobile’ dislocations play a major role in misorientation developments as well as the recovery kinetics.

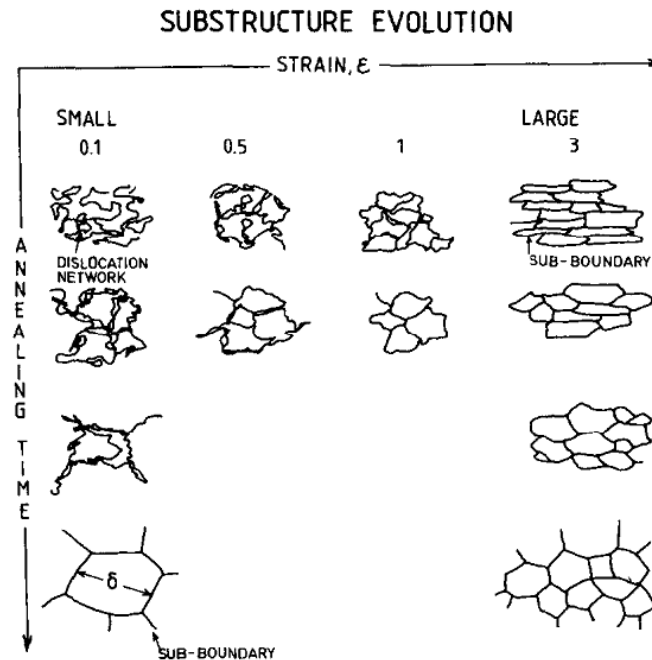


Figure 2.18: Schematic illustration of the substructure evolution with increasing strain and with annealing time. Courtesy [74]

2.3.2 Thermal annealing, dislocation structure and residual stress

Recovery is identified by the rearrangement to dislocation substructures due to thermal energy prior to recrystallization with subsequent and gradual decrease in stored energy. This thermal energy input also acts to relax the residual stresses. In fact, stress relaxation annealing is one of the major steps in industries to reduce the deformation induced stresses. This relaxation mechanisms include dislocation glide, dislocation climb, dislocation creep, grain boundary sliding and diffusional creep [6, 21, 75]. The mechanism in recovery at low temperatures (i.e. $< 0.3 T_m$) is condensation and annihilation of lattice defects preferably vacancies and interstitials. This involves dislocation climb and glide. At relatively higher temperatures, dislocation rearrangement and annihilation promotes the recovery process which may encounter cross-slip of dislocations, dislocation creep, grain boundary sliding and diffusional creep. It has been observed that for

randomly distributed dislocations, dislocation climb is a dominant mechanism of relaxation whereas bulk diffusion leads to stress relaxation in case of a stable configuration. All these mechanisms involve dislocation rearrangements to a lower energy dislocation structure (LEDS) and hence residual stress relaxation happens.

Researches were performed to look into the controlling mechanism of recovery: competition between dislocation glide and climb mechanism. It was hypothesized the activation energy (Q) is a decreasing function of residual stress and recovery kinetics can be expressed as

$$\frac{d\sigma}{dt} = -c \exp\left(\frac{-Q}{kT}\right) \text{-----}(2.9)$$

During thermal annealing, it is expected that the activation energy will increase, therefore a residual stress relief will occur. In other words, if there is residual stress gradient present in material, region with high dislocation density under favorable residual stress will promote recovery.

In another way, relaxation of residual stress by thermal annealing can be conveyed by the Zener-Wert-Avrami equation [17, 95]

$$\frac{\sigma^{T,t}}{\sigma^{t=0}} = \exp\left[-\left(A \exp\left(-\frac{\Delta H}{kT}\right)t\right)^m\right] \text{-----}(2.10)$$

whereas $\sigma^{T,t}$ and $\sigma^{t=0}$ denote residual stresses after and before annealing, respectively. T and t being the annealing temperature and time, ΔH and k are activation enthalpy and Boltzmann constant. Dominant relaxation mechanism is determined by ‘m’ which is also known as stress relaxation exponent.

It appears from the existing knowledge that thermal stress relief should have dislocation rearrangements as its origin. For example, a partially recrystallized structure of aluminum offered better stress relief than complete recrystallization. Observations are also present that a leaner alloy exhibited better stress relief as dislocation rearrangements are easy in less solute environment. However, due to lack of sufficient literature, it is not possible to completely understand the micro-mechanisms of thermal stress relief. The underlying difficulties could be the multiple micro-mechanisms that are active during recovery or the difficulty in quantifying the recovery behavior only as it is almost always difficult to differentiate between recovery and recrystallization. Also the measurement of micro residual stresses are not straight-forward experiments. Thus it is felt in

this present scope of thesis to understand the contribution of dislocation substructure on residual stress relief in recovery and its underlying micro-mechanisms.

2.4 Computational Plasticity

The mechanistic correlation between plasticity and dislocations was build up in 1930s when Orowan, Polanyi and Taylor [96-98] established the fact that ‘dislocations are the plasticity carriers’. During plastic deformation of crystalline materials, dislocations generate, move and multiply/react with one another heterogeneously. These heterogeneous regions are made of alternating regions of high and low local dislocation density, respectively. This process of forming dislocation patterns is 'self-organizing' in nature. It is observed that the formation of specific distributions of dislocations are characteristic of crystal structure of the material being deformed, temperature of deformation, strain and strain rate. Because these dislocation patterns are such general features occurring during the deformation process their influence on the mechanical behavior of the material is important. Thus modeling overall mechanical response during plasticity is basically governed by the underlying fact of dislocation motion and their interactions.

There are numerous computational techniques that have been developed to describe and predict the mechanics of material at different length and time scales (figure 2.19). Such methods span from atomistic scale such as quantum mechanics, molecular dynamics all the way up to macroscopic scale where continuum mechanics, finite element methods are the powerful tools to investigate. Figure 2.19 also describes the associated experimental techniques which are generally used to verify the outcome from the developed techniques. Each method has their applicability in certain range of length and time scales. With the advent of recent technologies, a thrust has come to bridge the different computational techniques which can predict the material behavior more accurately.

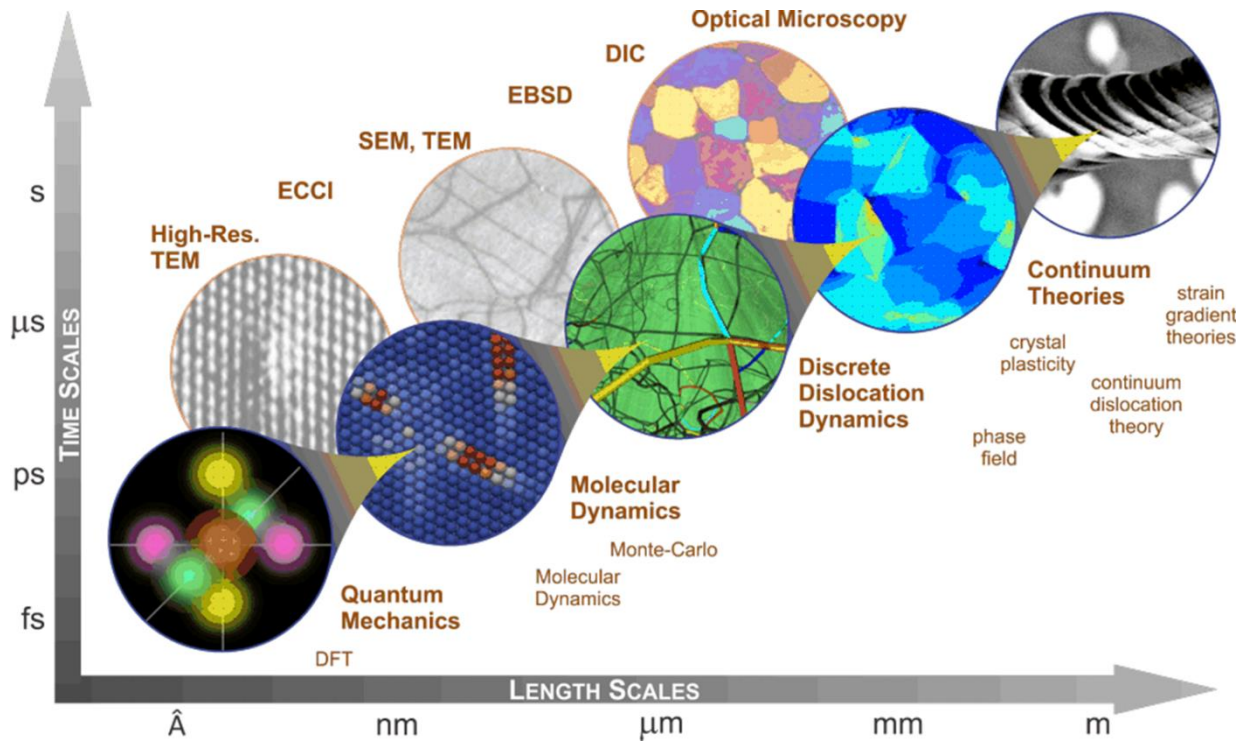


Figure 2.19: Computational and experimental techniques for a variety of length and time scales. Courtesy [99]

In the present thesis, objective is to understand the correlation between microscopic evolution and residual stress development. Amongst the available computational techniques, emphasis is given on discrete dislocation dynamics (DDD) and crystal plasticity methods in this literature review as these methods are used to validate/understand the aforementioned goal of present thesis. Length and time scale associated to DDD simulations are in order of microns and milliseconds respectively which are thousand times larger or smaller than atomistic models or macroscopic simulations. Thus they can be viewed as a bridge between these two scales with a great potential of making precise parameterization toward macroscopic models. On the other hand, crystal plasticity models are of macroscopic length and time scale of computational resources.

2.4.1 Discrete dislocation dynamics simulations

DDD simulations are devoted to the study of collective behavior of a large number of dislocations leading to the plasticity mechanisms. These simulation results are helpful for mapping out the underlying mechanisms of plasticity where “data” are not experimentally available or in-situ

experiments are cumbersome and limited. A large number of literature is present on DDD simulations of cubic systems on micromechanical response along with the dislocation substructure predictions [100-114]. The basic framework of DDD simulations is based on computing the motion of each dislocation based on a spatial and time discretization. Dislocations are represented as lines in a continuum elastic medium. Based on the discretization resolution of discrete line segments, the dynamics of dislocations can be reduced to the dynamics of individual segments maintaining the continuity of dislocation lines. Driving force for dislocation movements can come from local stress fields due to externally applied load (Peach – Koehler force) or the interaction with other dislocations. The operative driving force for dislocations is calculated for each segment based on the dislocation line tension, dislocation interaction forces and external loading. The dislocation segments respond to these forces by making discrete movement. These movements are performed according to the mobility function which is characteristic of the dislocation type and the specific material being simulated. The mobility functions can be calculated from experimental data or from atomistic simulations. This function also takes care of anisotropic dislocation motion as well as climb and cross slip mechanism. The important consideration in DDD simulations is the treatment of short range interactions. When two dislocations are at a close distance, their behavior is dominated by their mutual interactions and becomes less sensitive to the long range elastic stress field due to external loads, boundary conditions and the presence of other dislocations. Based on the type and arrangement of dislocations, two dislocations can annihilate or form dipole, a junction or a jog.

Discrete dislocation dynamics have been developed as 2D and 3D frameworks based on the method of superposition [100, 101, 103, 104, 110-117]. These frameworks have been successfully applied in various studies like inelastic behavior of material [114], bending and fracture of crystals [118-121], micro-pillar compression [122], residual stress evolution [123], effect of grain boundaries on mechanical behavior [124-126], dislocation – void interaction and void growth studies [127-129], study of mechanical behaviors which involve dislocation climb [130-133]. Also there exists frameworks that are extended to polycrystalline DDD [134-137] and large scale deformation prediction [138, 139]. In spite of increasing demand of DDD simulations for microstructural and micromechanical behavior predictions, it is important to note that the computational time associated with such simulations can be extremely large. Such large computational effort makes DDD simulations restricted mostly to single crystals or orientations and for small amount of applied

strain (typically ~10–15% plastic strain). One aspect of the present thesis is on orientation sensitivity of deformed microstructure. DDD simulations have been applied earlier to investigate the same. Such example exists for deformed microstructure development in hexagonal zircaloy-2 [140]. With similar starting dislocation structure, basal and non-basal orientations showed remarkable difference in dislocation structure as well as dislocation density (see figure 2.20).

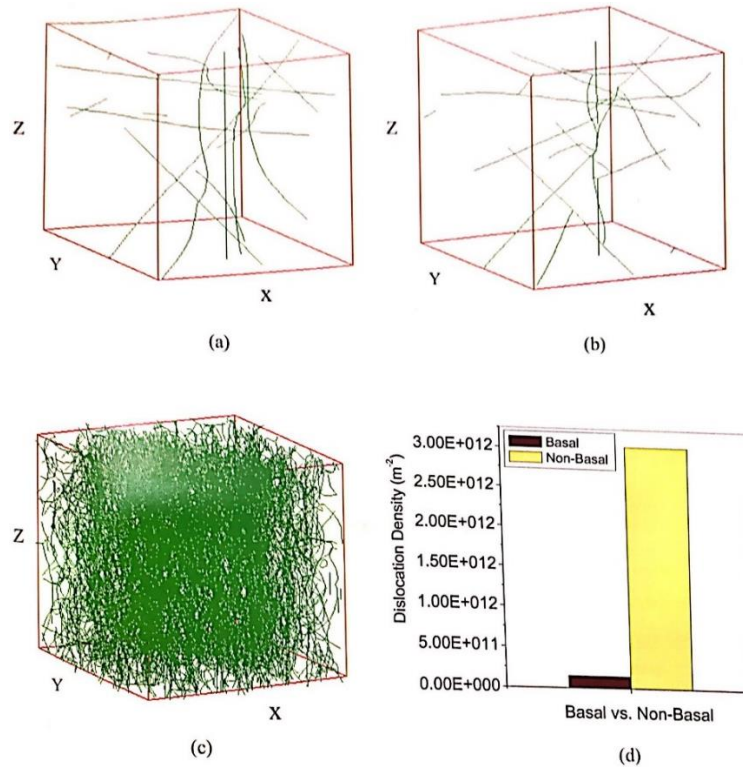


Figure 2.20: (a) Initial dislocation structure, (b) and (c) dislocation structure developments in basal and non-basal orientations, (d) dislocation density of those orientations after same duration of simulation time. Courtesy [140].

Also for cold-rolled grain-oriented (CRGO) steels, DDD simulations brought out such sensitivity [141]. Between (1 1 0) <0 0 1> and (1 1 0) <1-11> orientations, evolution of GND density and microstructure were significantly different (see figure 2.21).

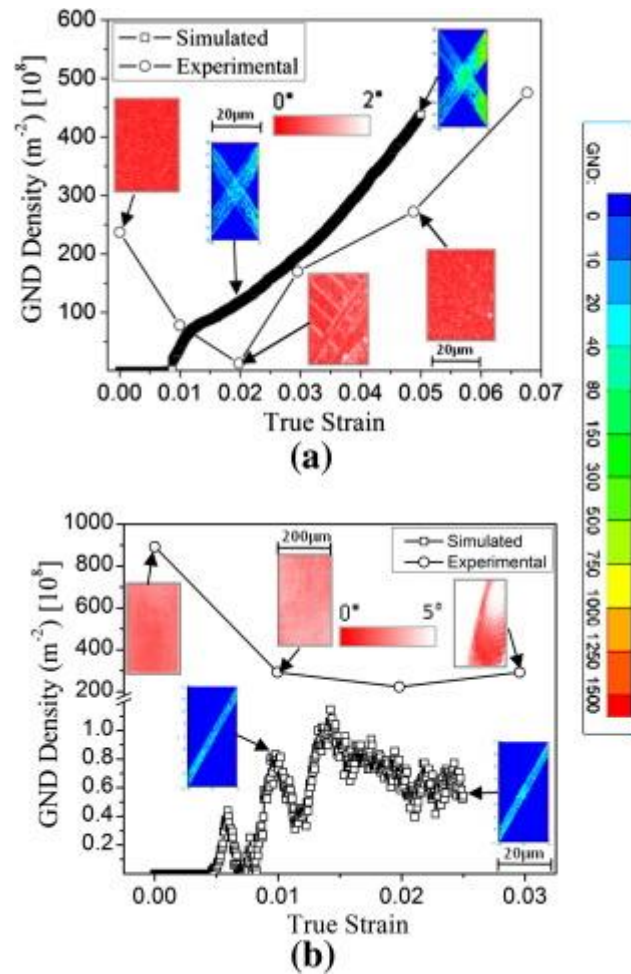


Figure 2.21: Simulated and experimental GND densities for (a) (1 1 0) <0 0 1> (b) (1 1 0) <1-11>. Simulations were obtained through 2-D DDD and experimental GND densities were calculated from EBSD data. Also included are images of simulated GND and experimental orientation gradients (gradient from average orientation: as estimated from EBSD data). The latter are expected to bring out slip bands and other forms of GNDs and strain localizations. Courtesy [141].

In deformed microstructure, residual stress is an immediate consequence of plastic deformation. In past, DDD has been used to analyze residual stress in a composite material. As DDD can bring out dislocation structure predictions using the orientation dependent input, post processing of data can bring out the residual stress which can be correlated with orientation. For example figure 4.17 shows the contour plots of (a) axial stress with superimposed dislocation structures, (b) the GND density and (c) lattice rotation [122].

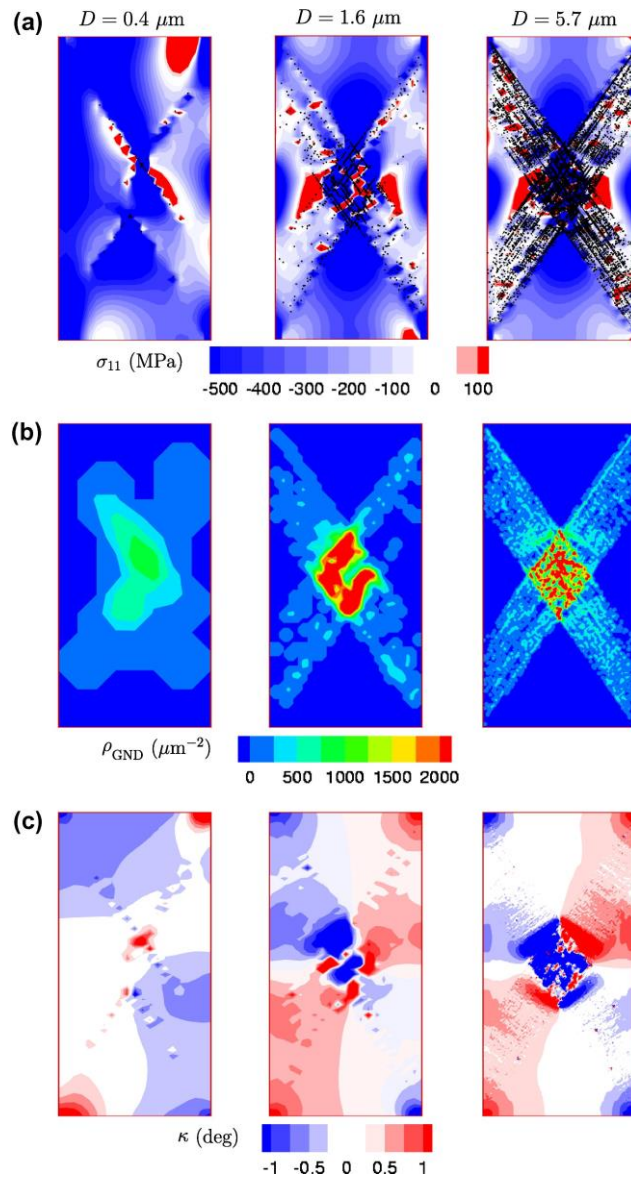


Figure 2.22: Contour plots of (a) axial stress, σ_{11} , with dislocation structure superimposed on crystal, (b) GND density, and (c) Lattice rotation. Courtesy [122]

2.4.2 Crystal plasticity simulations

Crystal plasticity models are a general framework to model the polycrystalline plasticity based on continuum mechanics. The modelling technique is designed to describe the kinematics of deformation depending on a set of constitutive equations needed to reproduce the physics of plasticity. Such constitutive equations contain analytical expressions to define the flow behavior. Amongst a wide range of numerical techniques to solve, finite element based methods have gained

the most popularity. These methods are commonly denoted as crystal plasticity finite element (CPFE) models. According to the method, continuum domain is discretized into discrete elements. Variational solution of the force equilibrium and displacement compatibility using a weak form of the principle of virtual work is imposed on such elements. Outcome of the model is based on the information gathered from the experimental studies of single crystal deformation and theoretical understanding from dislocation dynamics based models. For example it can capture the surface strain or roughness (figure 2.23) [142].

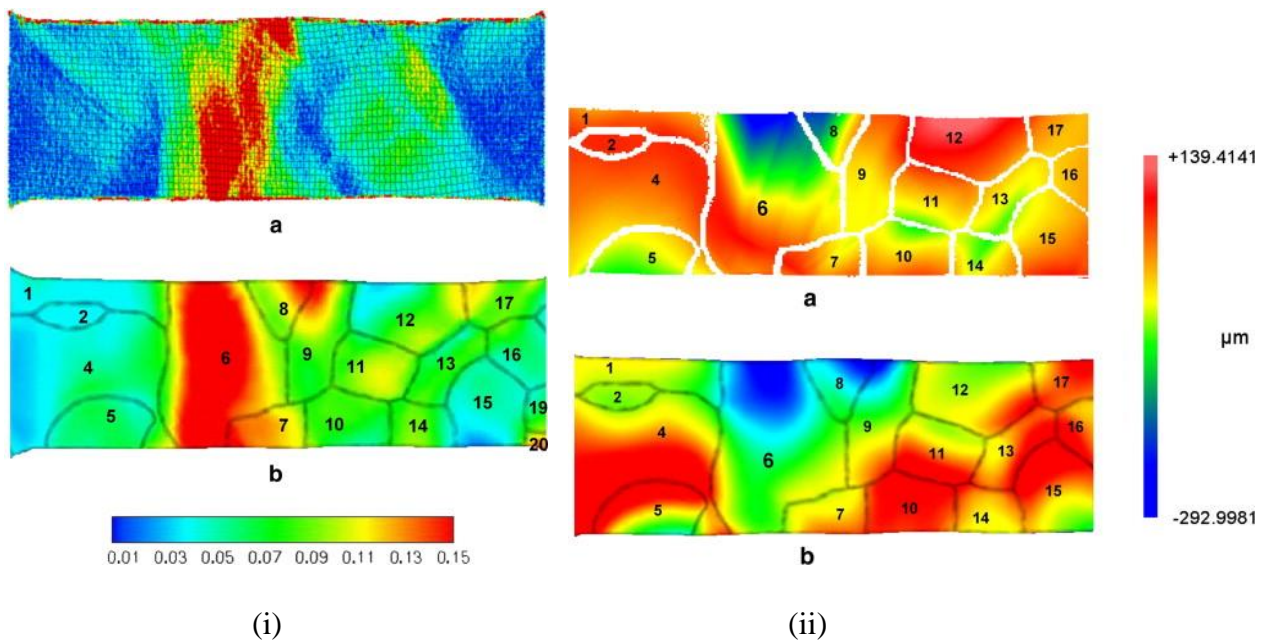


Figure 2.23: (i) Comparison of surface strain mapping between experimental (a) and simulation (b); (ii) Comparison of surface roughness between experimental (a) and simulation (b). Courtesy [142]

Detailed mathematical framework of crystal plasticity is beyond the scope of current thesis, the readers are referred to [143, 144] for an extensive review on the formulation of the same. Of specific interest to the framework is development of constitutive equations for hardening law. This involves in deriving a set of laws based on physical theory of deformation with the meaning parameters. Starting from 1960s until now, hardening laws are getting evolved by different research

groups. Deformation hardening for a given slip system is not only induced by plastic deformation cumulated on that slip system (known as self-hardening) but also from the accumulation on other slip systems (known as latent hardening). Based on the experimental knowledge with analytical solutions, hardening can be expressed mathematically as [143]

$$\tau^\alpha = \sum_{\beta=1}^n h_{\alpha\beta} d\gamma^\beta \quad \text{-----}(2.11)$$

Where $h_{\alpha\beta}$ is hardening matrix, γ and τ are shear strain and stress respectively, α is given as a function of shear rate, and β is the total number of slip systems. It has also been proposed that the hardening matrix can be divided into two independent hardening coefficients accounting for self and latent hardening. The self-hardening coefficients are identical for all slip systems while latent hardening matrix is shown to be anisotropic [105, 145, 146]. Both isotropic and anisotropic latent hardening of slip systems were considered in literature [147-150]. Such anisotropic consideration does not impact much on texture prediction compared to the isotropic case, but flow stress anisotropies get severely impacted [148].

Current CPFEE models either consider slip resistance [151-155] or dislocation density [142, 156-160] as internal state variable. Models based on slip resistance as internal state variable are able to predict stress-strain behavior, localized deformation or problems like surface roughening judiciously but they are incapable of predicting material behavior beyond certain limit of experimental data. However the other one is developed on microstructure dependent variable which can bring more physical understanding based evolution of properties. These models incorporate dislocation density evolution explicitly in their framework and the knowledge comes directly from the dislocation dynamics based studies. Thus they can bridge the two scales of computation techniques. However there are two methodologies for this multiscale modelling: (i) dislocation density and crystal plasticity take place independently *i.e.* parameters of constitutive equations in crystal plasticity comes from dislocation dynamics or atomistic simulation based studies [161, 162] and (ii) dislocation density and crystal plasticity happen together [159, 160, 163, 164]. Example and a comparison between phenomenological and dislocation based models is shown in figure 4.19 which shows a more accurate prediction of deformation by the physics based model compared to a visco-plastic formulation.

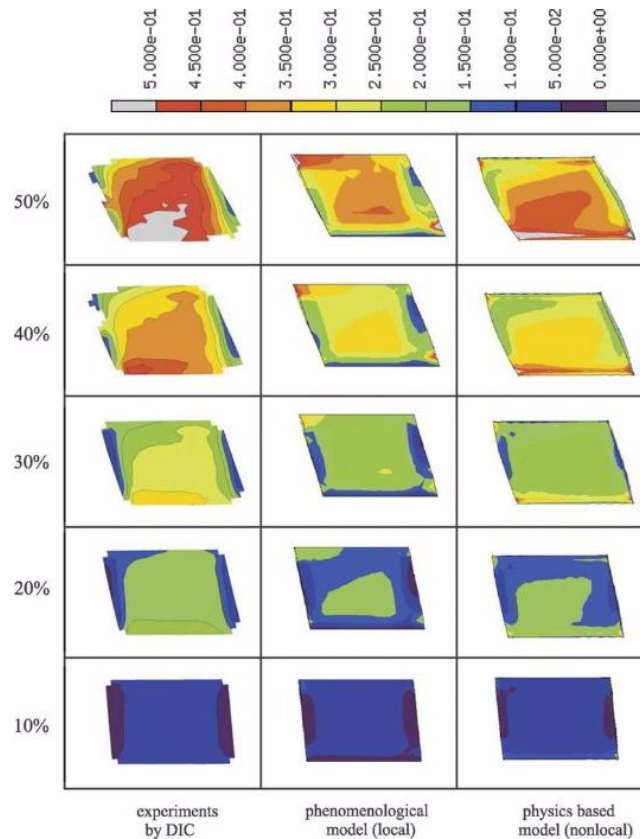


Figure 2.24: Comparison of von Mises strain on the surface of an aluminum single crystal – left column shows experimental measurement of strain from digital image correlation, the middle column shows the simulation results using conventional visco-plastic formulation whereas the right column is calculated using a dislocation based model which considers GNDs. Courtesy [163]

For plastically deformed materials, evolution of deformation texture can be considered as the “integral anisotropy of polycrystals in terms of the individual tensorial behavior of each grain and the orientation-dependent boundary conditions among the crystals” [143]. Thus deformation texture prediction using various forms of finite element approximation was the primary objective behind the CPFEM models [165, 166]. These models are further extended for studies like creep [167], high temperature deformation [168, 169], bulk textural evolution as well in grain texture formation [170], dislocation based constitutive modelling [142, 158-160, 171-173]. As these models are based on physics based formulations and less computationally expensive than DDD, they can involve large deformations and microstructure. However, the constitutive law prediction or development, which takes microstructure based input, is still a challenging task.

References

1. Bragg, W.H. and B. WL Bragg. *The reflection of X-rays by crystals*. in *Proc. R. Soc. Lond. A*. 1913. The Royal Society.
2. Joffe, A. and M. Kirpicheva, XVIII. *Röntgenograms of strained crystals*. The London, Edinburgh, and Dublin Philosophical Magazine and Journal of Science, 1922. **43**(253): p. 204-206.
3. Aksenov, G., *Measurement of elastic stress in a fine grained material*. *Appl. Phys.(USSR)*, 6 (1929) 3, 1929. **16**.
4. Drahekoupil, R., *Ermittlung von Eigenspannungen in metallischen Werkstücken mittels Röntgenstrahlen*. *VDI Z*, 1930. **74**: p. 1422.
5. Withers, P.J. and H.K.D.H. Bhadeshia, *Residual stress. Part 2 – Nature and origins*. *Materials Science and Technology*, 2001. **17**(4): p. 366-375.
6. Verlinden, B., et al., *Thermo-mechanical processing of metallic materials*. Vol. 11. 2007: Elsevier.
7. Heyn, E., *Internal strains in cold-wrought metals, and some troubles caused thereby*. *Journal of the Institute of Metals*, 1914. **12**(2): p. 1-37.
8. Hauk, V., *Structural and residual stress analysis by nondestructive methods: Evaluation-Application-Assessment*. 1997: Elsevier.
9. Noyan, I.C. and J.B. Cohen, *Residual stress: measurement by diffraction and interpretation*. 2013: Springer-Verlag.
10. Withers, P.J. and H. Bhadeshia, *Residual stress. Part 1–measurement techniques*. *Materials science and Technology*, 2001. **17**(4): p. 355-365.
11. Hauk, V. and E. Macherauch, *Residual stresses in science and technology*. 1987: DGM Informationsgesellschaft.
12. Van Houtte, P. and L. De Buyser, *The influence of crystallographic texture on diffraction measurements of residual stress*. *Acta metallurgica et materialia*, 1993. **41**(2): p. 323-336.
13. Rossini, N., et al., *Methods of measuring residual stresses in components*. *Materials & Design*, 2012. **35**: p. 572-588.
14. Cullity, B., *Elements of X-ray Diffraction, 2nd*. Adisson-Wesley Publishing. USA, 1978.
15. He, B.B., *Two-dimensional X-ray diffraction*. 2011: John Wiley & Sons.
16. <http://h-and-m-analytical.com/wp/residual-stress-app-note/>.

17. Kohli, D., et al., *Fabrication of simulated plate fuel elements: Defining role of stress relief annealing*. Journal of Nuclear Materials, 2014. **447**(1–3): p. 150-159.
18. Peng, J., et al., *Residual stress gradient analysis by the GIXRD method on CVD tantalum thin films*. Surface and Coatings Technology, 2006. **200**(8): p. 2738-2743.
19. Welzel, U., et al., *Stress analysis of polycrystalline thin films and surface regions by X-ray diffraction*. Journal of Applied Crystallography, 2005. **38**(1): p. 1-29.
20. Hutchings, M.T., et al., *Introduction to the characterization of residual stress by neutron diffraction*. 2005: CRC press.
21. Humphreys, F.J. and M. Hatherly, *Recrystallization and related annealing phenomena*. 1995: Elsevier.
22. Wert, J., Q. Liu, and N. Hansen, *Dislocation boundaries and active slip systems*. Acta metallurgica et materialia, 1995. **43**(11): p. 4153-4163.
23. Bay, B., et al., *Overview no. 96 evolution of f.c.c. deformation structures in polyslip*. Acta Metallurgica et Materialia, 1992. **40**(2): p. 205-219.
24. Delannay, L., et al., *Quantitative analysis of grain subdivision in cold rolled aluminium*. Acta materialia, 2001. **49**(13): p. 2441-2451.
25. Liu, Q. and N. Hansen, *Geometrically necessary boundaries and incidental dislocation boundaries formed during cold deformation*. Scripta Metallurgica et Materialia, 1995. **32**(8): p. 1289-1295.
26. Liu, Q., D. Juul Jensen, and N. Hansen, *Effect of grain orientation on deformation structure in cold-rolled polycrystalline aluminium*. Acta Materialia, 1998. **46**(16): p. 5819-5838.
27. Nakayama, Y. and K. Morii, *Microstructure and shear band formation in rolled single crystals of Al-Mg alloy*. Acta Metallurgica, 1987. **35**(7): p. 1747-1755.
28. Suresh, S., *Fatigue of materials*. 1998: Cambridge university press.
29. Mahesh, S. and C. Tomé, *Deformation banding under arbitrary monotonic loading in cubic metals*. Philosophical Magazine, 2004. **84**(33): p. 3517-3546.
30. Dieter, G.E. and D. Bacon, *Mechanical metallurgy*. Vol. 3. 1986: McGraw-Hill New York.
31. Rollett, A., et al., *Strain hardening at large strains*. 1988, Los Alamos National Lab., NM (USA).
32. Sevillano, J.G., P. Van Houtte, and E. Aernoudt, *Large strain work hardening and textures*. Progress in Materials Science, 1980. **25**(2): p. 69-134.

33. Kocks, U. and H. Mecking, *Physics and phenomenology of strain hardening: the FCC case*. Progress in materials science, 2003. **48**(3): p. 171-273.
34. Nes, E., *Modelling of work hardening and stress saturation in FCC metals*. Progress in Materials Science, 1997. **41**(3): p. 129-193.
35. Mughrabi, H., *Elektronenmikroskopische untersuchung der versetzungsanordnung verformter kupfereinkristalle im belasteten zustand*. The Philosophical Magazine: A Journal of Theoretical Experimental and Applied Physics, 1971. **23**(184): p. 897-929.
36. Hughes, D.A., *Microstructure evolution, slip patterns and flow stress*. Materials Science and Engineering: A, 2001. **319-321**: p. 46-54.
37. Ashby, M., *The deformation of plastically non-homogeneous materials*. Philosophical Magazine, 1970. **21**(170): p. 399-424.
38. Hansen, N., X. Huang, and D.A. Hughes, *Microstructural evolution and hardening parameters*. Materials Science and Engineering: A, 2001. **317**(1): p. 3-11.
39. Hughes, D.A., *Microstructural evolution in a non-cell forming metal: Al-Mg*. Acta Metallurgica et Materialia, 1993. **41**(5): p. 1421-1430.
40. Yi-Lin, L., et al., *Substructure development and mechanical properties in cold-rolled aluminium alloy 3004 I: Substructure development*. Materials Science and Engineering, 1987. **96**: p. 125-137.
41. Barker, I., N. Hansen, and B. Ralph, *The development of deformation substructures in face-centred cubic metals*. Materials Science and Engineering: A, 1989. **113**: p. 449-454.
42. Hughes, D., N. Hansen, and D. Bammann, *Geometrically necessary boundaries, incidental dislocation boundaries and geometrically necessary dislocations*. Scripta Materialia, 2003. **48**(2): p. 147-153.
43. Bay, B., N. Hansen, and D. Kuhlmann-Wilsdorf, *Deformation structures in lightly rolled pure aluminium*. Materials Science and Engineering: A, 1989. **113**: p. 385-397.
44. Hansen, N., *Cold deformation microstructures*. Materials Science and Technology, 1990. **6**(11): p. 1039-1047.
45. Hansen, N. and D.J. Jensen, *Flow stress anisotropy caused by geometrically necessary boundaries*. Acta Metallurgica et Materialia, 1992. **40**(12): p. 3265-3275.
46. Kuhlmann-Wilsdorf, D. and N. Hansen, *Geometrically necessary, incidental and subgrain boundaries*. Scripta Metallurgica et Materialia, 1991. **25**(7): p. 1557-1562.

47. Hughes, D.A., et al., *Metal forming at the center of excellence for the synthesis and processing of advanced materials*. JOM, 1998. **50**(6): p. 16-21.
48. Kuhlmann-Wilsdorf, D. and N. Comins, *Dislocation cell formation and work hardening in the unidirectional glide of fcc metals I: basic theoretical analysis of cell walls parallel to the primary glide plane in early stage II*. Materials Science and Engineering, 1983. **60**(1): p. 7-24.
49. Juul Jensen, D. and N. Hansen, *Flow stress anisotropy in aluminium*. Acta Metallurgica et Materialia, 1990. **38**(8): p. 1369-1380.
50. Kawasaki, Y. and T. Takeuchi, *Cell structures in copper single crystals deformed in the [001] and [111] axes*. Scripta Metallurgica, 1980. **14**(2): p. 183-188.
51. Laird, C., P. Charsley, and H. Mughrabi, *Low energy dislocation structures produced by cyclic deformation*. Materials Science and Engineering, 1986. **81**: p. 433-450.
52. Jin, N.Y., *Formation of dislocation structures during cyclic deformation of F.C.C. crystals—I. Formation of PSBs in crystals oriented for single-slip*. Acta Metallurgica, 1989. **37**(7): p. 2055-2066.
53. Jin, N.Y. and A.T. Winter, *Dislocation structures in cyclically deformed [001] copper crystals*. Acta Metallurgica, 1984. **32**(8): p. 1173-1176.
54. Rasmussen, K.V. and O.B. Pedersen, *Fatigue of copper polycrystals at low plastic strain amplitudes*. Acta Metallurgica, 1980. **28**(11): p. 1467-1478.
55. Kuhlmann-Wilsdorf, D. and C. Laird, *Dislocation behavior in fatigue*. Materials Science and Engineering, 1977. **27**(2): p. 137-156.
56. Kuhlmann-Wilsdorf, D. and C. Laird, *Dislocation behavior in fatigue V: Breakdown of loop patches and formation of persistent slip bands and of dislocation cells*. Materials Science and Engineering, 1980. **46**(2): p. 209-219.
57. Basinski, S., Z. Basinski, and A. Howie, *Early stages of fatigue in copper single crystals*. Philosophical magazine, 1969. **19**(161): p. 899-924.
58. Mughrabi, H., *The cyclic hardening and saturation behaviour of copper single crystals*. Materials Science and Engineering, 1978. **33**(2): p. 207-223.
59. Pham, M., et al., *Cyclic deformation response of AISI 316L at room temperature: mechanical behaviour, microstructural evolution, physically-based evolutionary constitutive modelling*. International Journal of Plasticity, 2013. **47**: p. 143-164.

60. Thompson, N., N. Wadsworth, and N. Louat, *Xi. The origin of fatigue fracture in copper*. The Philosophical Magazine: A Journal of Theoretical Experimental and Applied Physics, 1956. **1**(2): p. 113-126.
61. Mughrabi, H., *Dislocations in fatigue*. Dislocations and properties of real materials, 1984: p. 244-262.
62. Ackermann, F., et al., *The dependence of dislocation microstructure on plastic strain amplitude in cyclically strained copper single crystals*. Acta Metallurgica, 1984. **32**(5): p. 715-725.
63. Holt, D.L., *Dislocation cell formation in metals*. Journal of Applied Physics, 1970. **41**(8): p. 3197-3201.
64. Kuhlmann-Wilsdorf, D., *Theory of workhardening 1934-1984*. Metallurgical Transactions A, 1985. **16**(12): p. 2091-2108.
65. Mott, N.F., *CXVII. A theory of work-hardening of metal crystals*. The London, Edinburgh, and Dublin Philosophical Magazine and Journal of Science, 1952. **43**(346): p. 1151-1178.
66. Feaugas, X. and H. Haddou, *Effects of grain size on dislocation organization and internal stresses developed under tensile loading in fcc metals*. Philosophical Magazine, 2007. **87**(7): p. 989-1018.
67. Friedel, J., *CXXX. On the linear work hardening mate of face-centred cubic single crystals*. The London, Edinburgh, and Dublin Philosophical Magazine and Journal of Science, 1955. **46**(382): p. 1169-1186.
68. Seegar, A., S. Mader, and H. Kronmüller. *Electron microscopy and strength of crystals*. 1963. Interscience Publishers.
69. Hirsch, P. and T. Mitchell, *Stage II work hardening in crystals*. Canadian Journal of Physics, 1967. **45**(2): p. 663-706.
70. Mader, S., A. Seeger, and C. Leitz, *Work hardening and dislocation arrangement of FCC single crystals. I. Plastic deformation and slip line studies of nickel single crystals*. Journal of Applied Physics, 1963. **34**(11): p. 3368-3375.
71. Feltner, C., *Dislocation arrangements in aluminum deformed by repeated tensile stresses*. Acta Metallurgica, 1963. **11**(7): p. 817-828.
72. Essmann, U., *Die Versetzungsanordnung in plastisch verformten Kupfereinkristallen*. physica status solidi (b), 1963. **3**(5): p. 932-949.

73. Mughrabi, H., *Dislocation wall and cell structures and long-range internal stresses in deformed metal crystals*. Acta metallurgica, 1983. **31**(9): p. 1367-1379.
74. Nes, E., *Recovery revisited*. Acta Metallurgica et Materialia, 1995. **43**(6): p. 2189-2207.
75. Nes, E., K. Marthinsen, and Y. Brechet, *On the mechanisms of dynamic recovery*. Scripta Materialia, 2002. **47**(9): p. 607-611.
76. Humphreys, F., *Modelling microstructural evolution during annealing*. Modelling and Simulation in Materials Science and Engineering, 2000. **8**(6): p. 893.
77. Khatirkar, R., et al., *ND//< 111> recrystallization in interstitial free steel: the defining role of growth inhibition*. ISIJ international, 2012. **52**(5): p. 894-901.
78. Khatirkar, R., et al., *Orientation dependent recovery in interstitial free steel*. ISIJ international, 2012. **52**(5): p. 884-893.
79. Doherty, R.D., et al., *Current issues in recrystallization: a review*. Materials Science and Engineering: A, 1997. **238**(2): p. 219-274.
80. Albou, A., et al., *Orientation-dependent recovery in strongly deformed Al-0.1% Mn crystals*. Philosophical Magazine, 2011. **91**(31): p. 3981-4000.
81. Primig, S., et al., *Orientation dependent recovery and recrystallization behavior of hot-rolled molybdenum*. International Journal of Refractory Metals and Hard Materials, 2015. **48**: p. 179-186.
82. Xing, Q., X. Huang, and N. Hansen, *Recovery of heavily cold-rolled aluminum: Effect of local texture*. Metallurgical and materials transactions A, 2006. **37**(4): p. 1311-1322.
83. Mukunthan, K. and E. Hawbolt, *Modeling recovery and recrystallization kinetics in cold-rolled Ti-Nb stabilized interstitial-free steel*. Metallurgical and Materials Transactions A, 1996. **27**(11): p. 3410-3423.
84. Humphreys, F., *A network model for recovery and recrystallisation*. Scripta metallurgica et materialia, 1992. **27**(11): p. 1557-1562.
85. Belyakov, A., Y. Kimura, and K. Tsuzaki, *Recovery and recrystallization in ferritic stainless steel after large strain deformation*. Materials Science and Engineering: A, 2005. **403**(1-2): p. 249-259.
86. Desorbo, W. and D. Turnbull, *Kinetics of vacancy motion in high-purity aluminum*. Physical Review, 1959. **115**(3): p. 560.

87. Van Drunen, G. and S. Saimoto, *Deformation and recovery of [001] oriented copper crystals*. Acta metallurgica, 1971. **19**(3): p. 213-221.
88. Roumina, R. and C.W. Sinclair, *Recovery kinetics in the presence of precipitates: The softening response of an Al–Mg–Sc alloy*. Acta Materialia, 2010. **58**(1): p. 111-121.
89. Luton, M., R. Petkovic, and J. Jonas, *Kinetics of recovery and recrystallization in polycrystalline copper*. Acta Metallurgica, 1980. **28**(6): p. 729-743.
90. Himmel, L., *Recovery and recrystallization of metals*. 1963: Gordon and Breach.
91. Verdier, M., Y. Brechet, and P. Guyot, *Recovery of AlMg alloys: flow stress and strain-hardening properties*. Acta Materialia, 1998. **47**(1): p. 127-134.
92. Ridha, A. and W. Hutchinson, *Recrystallisation mechanisms and the origin of cube texture in copper*. Acta metallurgica, 1982. **30**(10): p. 1929-1939.
93. Furu, T., R. Ørsund, and E. Nes, *Subgrain growth in heavily deformed aluminium—experimental investigation and modelling treatment*. Acta Metallurgica et Materialia, 1995. **43**(6): p. 2209-2232.
94. Faivre, P. and R. Doherty, *Nucleation of recrystallization in compressed aluminium: studies by electron microscopy and Kikuchi diffraction*. Journal of Materials Science, 1979. **14**(4): p. 897-919.
95. Epp, J., et al., *Residual stress relaxation during heating of bearing rings produced in two different manufacturing chains*. Journal of Materials Processing Technology, 2011. **211**(4): p. 637-643.
96. Orowan, E., *The crystal plasticity. III: about the mechanism of the sliding*. Z Physik, 1934. **89**: p. 634-659.
97. Polanyi, M., *Über eine Art Gitterstörung, die einen Kristall plastisch machen könnte*. Zeitschrift für Physik, 1934. **89**(9-10): p. 660-664.
98. Taylor, G.I., *The mechanism of plastic deformation of crystals. Part I. Theoretical*. Proceedings of the Royal Society of London. Series A, 1934. **145**(855): p. 362-387.
99. http://www.mm.ethz.ch/research_OC.html.
100. Kubin, L.P., et al. *Dislocation microstructures and plastic flow: a 3D simulation*. in *Solid State Phenomena*. 1992. Trans Tech Publ.
101. Kubin, L. and G. Canova, *The modelling of dislocation patterns*. Scripta metallurgica et materialia, 1992. **27**(8): p. 957-962.

102. Devincre, B., T. Hoc, and L. Kubin, *Dislocation mean free paths and strain hardening of crystals*. Science, 2008. **320**(5884): p. 1745-1748.
103. Devincre, B. and L. Kubin, *Mesosopic simulations of dislocations and plasticity*. Materials Science and Engineering: A, 1997. **234**: p. 8-14.
104. Bulatov, V., et al., *Connecting atomistic and mesoscale simulations of crystal plasticity*. Nature, 1998. **391**(6668): p. 669.
105. Devincre, B., L. Kubin, and T. Hoc, *Physical analyses of crystal plasticity by DD simulations*. Scripta Materialia, 2006. **54**(5): p. 741-746.
106. Devincre, B., et al., *Mesosopic simulations of plastic deformation*. Materials Science and Engineering: A, 2001. **309**: p. 211-219.
107. Rhee, M., et al., *Models for long-/short-range interactions and cross slip in 3D dislocation simulation of BCC single crystals*. Modelling and Simulation in Materials Science and Engineering, 1998. **6**(4): p. 467.
108. Gómez-García, D., B. Devincre, and L. Kubin, *Dislocation patterns and the similitude principle: 2.5 D mesoscale simulations*. Physical review letters, 2006. **96**(12): p. 125503.
109. Zbib, H.M., M. Rhee, and J.P. Hirth, *On plastic deformation and the dynamics of 3D dislocations*. International Journal of Mechanical Sciences, 1998. **40**(2-3): p. 113-127.
110. Arsenlis, A., et al., *Enabling strain hardening simulations with dislocation dynamics*. Modelling and Simulation in Materials Science and Engineering, 2007. **15**(6): p. 553.
111. Benzerga, A., et al., *Incorporating three-dimensional mechanisms into two-dimensional dislocation dynamics*. Modelling and Simulation in Materials Science and Engineering, 2003. **12**(1): p. 159.
112. Guruprasad, P., W. Carter, and A. Benzerga, *A discrete dislocation analysis of the Bauschinger effect in microcrystals*. Acta Materialia, 2008. **56**(19): p. 5477-5491.
113. Guruprasad, P.J. and A.A. Benzerga, *A phenomenological model of size-dependent hardening in crystal plasticity*. Philosophical Magazine, 2008. **88**(30-32): p. 3585-3601.
114. Van der Giessen, E. and A. Needleman, *Discrete dislocation plasticity: a simple planar model*. Modelling and Simulation in Materials Science and Engineering, 1995. **3**(5): p. 689.
115. Zbib, H.M., et al., *3D dislocation dynamics: stress-strain behavior and hardening mechanisms in fcc and bcc metals*. Journal of Nuclear Materials, 2000. **276**(1-3): p. 154-165.

116. Bulatov, V. and W. Cai, *Computer simulations of dislocations*. Vol. 3. 2006: Oxford University Press on Demand.
117. Fivel, M.C., *Discrete dislocation dynamics: an important recent break-through in the modelling of dislocation collective behaviour*. Comptes Rendus Physique, 2008. **9**(3-4): p. 427-436.
118. Cleveringa, H., E. Van Der Giessen, and A. Needleman, *Comparison of discrete dislocation and continuum plasticity predictions for a composite material*. Acta Materialia, 1997. **45**(8): p. 3163-3179.
119. Cleveringa, H., E. Van der Giessen, and A. Needleman, *A discrete dislocation analysis of bending*. International Journal of Plasticity, 1999. **15**(8): p. 837-868.
120. Cleveringa, H., E. Van der Giessen, and A. Needleman, *A discrete dislocation analysis of mode I crack growth*. Journal of the Mechanics and Physics of Solids, 2000. **48**(6-7): p. 1133-1157.
121. Balint, D., et al., *Discrete dislocation plasticity analysis of crack-tip fields in polycrystalline materials*. Philosophical Magazine, 2005. **85**(26-27): p. 3047-3071.
122. Kiener, D., et al., *Work hardening in micropillar compression: In situ experiments and modeling*. Acta Materialia, 2011. **59**(10): p. 3825-3840.
123. Cleveringa, H., E.V. Giessen, and A. Needleman, *A discrete dislocation analysis of residual stresses in a composite material*. Philosophical Magazine A, 1999. **79**(4): p. 893-920.
124. Biner, S. and J. Morris, *A two-dimensional discrete dislocation simulation of the effect of grain size on strengthening behaviour*. Modelling and Simulation in Materials Science and Engineering, 2002. **10**(6): p. 617.
125. Biner, S. and J. Morris, *The effects of grain size and dislocation source density on the strengthening behaviour of polycrystals: a two-dimensional discrete dislocation simulation*. Philosophical Magazine, 2003. **83**(31-34): p. 3677-3690.
126. Balint, D., et al., *A discrete dislocation plasticity analysis of grain-size strengthening*. Materials Science and Engineering: A, 2005. **400**: p. 186-190.
127. Haghghat, S.H., et al., *Dislocation-void interaction in Fe: A comparison between molecular dynamics and dislocation dynamics*. Journal of Nuclear Materials, 2009. **386**: p. 102-105.

128. Segurado, J. and J. LLorca, *Discrete dislocation dynamics analysis of the effect of lattice orientation on void growth in single crystals*. International Journal of Plasticity, 2010. **26**(6): p. 806-819.
129. Segurado, J. and J. Llorca, *An analysis of the size effect on void growth in single crystals using discrete dislocation dynamics*. Acta Materialia, 2009. **57**(5): p. 1427-1436.
130. Mordehai, D., et al., *Introducing dislocation climb by bulk diffusion in discrete dislocation dynamics*. Philosophical Magazine, 2008. **88**(6): p. 899-925.
131. Keralavarma, S.M., et al., *Power-Law Creep from Discrete Dislocation Dynamics*. Physical Review Letters, 2012. **109**(26): p. 265504.
132. Haghghat, S.H., G. Eggeler, and D. Raabe, *Effect of climb on dislocation mechanisms and creep rates in γ' -strengthened Ni base superalloy single crystals: A discrete dislocation dynamics study*. Acta Materialia, 2013. **61**(10): p. 3709-3723.
133. Davoudi, K.M., L. Nicola, and J.J. Vlassak, *Dislocation climb in two-dimensional discrete dislocation dynamics*. Journal of Applied Physics, 2012. **111**(10): p. 103522.
134. Zhou, C. and R. LeSar, *Dislocation dynamics simulations of plasticity in polycrystalline thin films*. International Journal of Plasticity, 2012. **30-31**: p. 185-201.
135. Balint, D., et al., *Discrete dislocation plasticity analysis of the grain size dependence of the flow strength of polycrystals*. International Journal of Plasticity, 2008. **24**(12): p. 2149-2172.
136. Li, Z., et al., *Strengthening mechanism in micro-polycrystals with penetrable grain boundaries by discrete dislocation dynamics simulation and Hall–Petch effect*. Computational Materials Science, 2009. **46**(4): p. 1124-1134.
137. Nicola, L., et al., *Plastic deformation of freestanding thin films: experiments and modeling*. Journal of the Mechanics and Physics of Solids, 2006. **54**(10): p. 2089-2110.
138. Deshpande, V., A. Needleman, and E. Van der Giessen, *Finite strain discrete dislocation plasticity*. Journal of the Mechanics and Physics of Solids, 2003. **51**(11-12): p. 2057-2083.
139. Irani, N., J. Remmers, and V. Deshpande, *Finite strain discrete dislocation plasticity in a total Lagrangian setting*. Journal of the Mechanics and Physics of Solids, 2015. **83**: p. 160-178.
140. Sahoo, S.K., *Heterogeneous Deformation in Zirconium based alloys*. 2009, PhD Thesis, Indian Institute of Technology Bombay.

141. Shekhawat, S., et al., *Orientation-dependent plastic deformation in transformer steel: Experiments and dislocation dynamics simulations*. Acta Materialia, 2015. **84**: p. 256-264.
142. Zhao, Z., et al., *Investigation of three-dimensional aspects of grain-scale plastic surface deformation of an aluminum oligocrystal*. International Journal of Plasticity, 2008. **24**(12): p. 2278-2297.
143. Roters, F., et al., *Overview of constitutive laws, kinematics, homogenization and multiscale methods in crystal plasticity finite-element modeling: Theory, experiments, applications*. Acta Materialia, 2010. **58**(4): p. 1152-1211.
144. Roters, F., et al., *Crystal plasticity finite element methods: in materials science and engineering*. 2011: John Wiley & Sons.
145. Madec, R., et al., *The role of collinear interaction in dislocation-induced hardening*. Science, 2003. **301**(5641): p. 1879-1882.
146. Alankar, A., et al., *Determination of dislocation interaction strengths using discrete dislocation dynamics of curved dislocations*. Journal of engineering materials and technology, 2012. **134**(2): p. 021018.
147. Bertin, N., et al., *On the strength of dislocation interactions and their effect on latent hardening in pure Magnesium*. International Journal of Plasticity, 2014. **62**: p. 72-92.
148. Khadyko, M., et al., *Latent hardening and plastic anisotropy evolution in AA6060 aluminium alloy*. International Journal of Plasticity, 2016. **76**: p. 51-74.
149. Marin, E. and P. Dawson, *On modelling the elasto-viscoplastic response of metals using polycrystal plasticity*. Computer Methods in Applied Mechanics and Engineering, 1998. **165**(1-4): p. 1-21.
150. Marin, E.B., *On the formulation of a crystal plasticity model*. 2006, Sandia National Laboratories.
151. Beaudoin, A., et al., *Application of polycrystal plasticity to sheet forming*. Computer methods in applied mechanics and engineering, 1994. **117**(1-2): p. 49-70.
152. Kalidindi, S.R., C.A. Bronkhorst, and L. Anand, *Crystallographic texture evolution in bulk deformation processing of FCC metals*. Journal of the Mechanics and Physics of Solids, 1992. **40**(3): p. 537-569.
153. Asaro, R.J. and J. Rice, *Strain localization in ductile single crystals*. Journal of the Mechanics and Physics of Solids, 1977. **25**(5): p. 309-338.

154. Kumar, A. and P.R. Dawson, *Modeling crystallographic texture evolution with finite elements over neo-Eulerian orientation spaces*. Computer methods in applied mechanics and engineering, 1998. **153**(3-4): p. 259-302.
155. Delannay, L., P.J. Jacques, and S.R. Kalidindi, *Finite element modeling of crystal plasticity with grains shaped as truncated octahedrons*. International Journal of Plasticity, 2006. **22**(10): p. 1879-1898.
156. Cuitino, A.M. and M. Ortiz, *Computational modelling of single crystals*. Modelling and Simulation in Materials Science and Engineering, 1993. **1**(3): p. 225.
157. Roters, F., D. Raabe, and G. Gottstein, *Work hardening in heterogeneous alloys—a microstructural approach based on three internal state variables*. Acta materialia, 2000. **48**(17): p. 4181-4189.
158. Ma, A., F. Roters, and D. Raabe, *A dislocation density based constitutive model for crystal plasticity FEM including geometrically necessary dislocations*. Acta Materialia, 2006. **54**(8): p. 2169-2179.
159. Alankar, A., P. Eisenlohr, and D. Raabe, *A dislocation density-based crystal plasticity constitutive model for prismatic slip in α -titanium*. Acta Materialia, 2011. **59**(18): p. 7003-7009.
160. Alankar, A., I.N. Mastorakos, and D.P. Field, *A dislocation-density-based 3D crystal plasticity model for pure aluminum*. Acta materialia, 2009. **57**(19): p. 5936-5946.
161. Groh, S., et al., *Multiscale modeling of the plasticity in an aluminum single crystal*. International Journal of Plasticity, 2009. **25**(8): p. 1456-1473.
162. Shilkrot, L.E., R.E. Miller, and W.A. Curtin, *Multiscale plasticity modeling: coupled atomistics and discrete dislocation mechanics*. Journal of the Mechanics and Physics of Solids, 2004. **52**(4): p. 755-787.
163. Ma, A., F. Roters, and D. Raabe, *On the consideration of interactions between dislocations and grain boundaries in crystal plasticity finite element modeling—theory, experiments, and simulations*. Acta Materialia, 2006. **54**(8): p. 2181-2194.
164. Roters, F., et al., *DAMASK: the Düsseldorf Advanced Material Simulation Kit for studying crystal plasticity using an FE based or a spectral numerical solver*. Procedia IUTAM, 2012. **3**: p. 3-10.

165. Lebensohn, R.A. and C. Tomé, *A self-consistent anisotropic approach for the simulation of plastic deformation and texture development of polycrystals: application to zirconium alloys*. *Acta metallurgica et materialia*, 1993. **41**(9): p. 2611-2624.
166. Kalidindi, S.R., *Modeling anisotropic strain hardening and deformation textures in low stacking fault energy fcc metals*. *International Journal of Plasticity*, 2001. **17**(6): p. 837-860.
167. McHugh, P. and R. Mohrmann, *Modelling of creep in a Ni base superalloy using a single crystal plasticity model*. *Computational materials science*, 1997. **9**(1-2): p. 134-140.
168. Balasubramanian, S. and L. Anand, *Plasticity of initially textured hexagonal polycrystals at high homologous temperatures: application to titanium*. *Acta materialia*, 2002. **50**(1): p. 133-148.
169. Bower, A.F. and E. Wininger, *A two-dimensional finite element method for simulating the constitutive response and microstructure of polycrystals during high temperature plastic deformation*. *Journal of the Mechanics and Physics of Solids*, 2004. **52**(6): p. 1289-1317.
170. Asaro, R.J. and A. Needleman, *Overview no. 42 Texture development and strain hardening in rate dependent polycrystals*. *Acta metallurgica*, 1985. **33**(6): p. 923-953.
171. Ardeljan, M., I.J. Beyerlein, and M. Knezevic, *A dislocation density based crystal plasticity finite element model: application to a two-phase polycrystalline HCP/BCC composites*. *Journal of the Mechanics and Physics of Solids*, 2014. **66**: p. 16-31.
172. Arsenlis, A. and D.M. Parks, *Modeling the evolution of crystallographic dislocation density in crystal plasticity*. *Journal of the Mechanics and Physics of Solids*, 2002. **50**(9): p. 1979-2009.
173. Tóth, L.s.S., A. Molinari, and Y. Estrin, *Strain hardening at large strains as predicted by dislocation based polycrystal plasticity model*. *Journal of engineering materials and technology*, 2002. **124**(1): p. 71-77.

Chapter 3

Relating Residual Stress and Substructural Evolution during Tensile Deformation of an Aluminum-Manganese Alloy

3.1 Introduction

Aspects of polycrystalline plasticity offer an interesting challenge to the materials community. Typically in a metallic material, deformation induced crystallite imperfections, mainly dislocations, interact and a long range dislocation patterning or substructure evolution occurs [1-5]. As a consequence of this evolution, orientation gradients evolve inside individual grains, breaking it into small blocks [6]. This results in sub grain boundaries which contains excess dislocations that are necessary for accommodating the imposed curvatures (known as geometrically necessary dislocations or GNDs) [7-9]. As deformation progresses, the number of mobile dislocations increase as well as new dislocation sources are activated. Simultaneously, the grains do not undergo the same amount of deformation because the flow stress of an individual grain is a function of its crystallographic orientation [10]. When an external load is applied to a polycrystalline material, each grain experiences constraints from its neighboring grains, and thus tries to deform in a unique manner. This creates an incompatibility in the microscopic stress state. The result of this incompatibility, at the macroscopic scale, is the residual stress development inside the deforming material. The objective of this study is to correlate the evolution of the substructure during monotonic deformation with the development of residual stress.

In the context of this study, it is useful to distinguish between the different ‘residual stress’ nomenclatures [11-13]. The residual stress developed in a material can be divided into two categories depending on the length scale [1]: macro-residual stress and micro-residual stress. Macro-residual stress (often called as type-I or bulk residual stress) spans over a large number of grains and is of interest to design engineers. Micro-residual stress can be of two types: type-II (or intergranular residual stress), which varies from grain to grain due to heterogeneity and anisotropy of individual grains and are important as an indicator of strain hardening and damage to a material and type III (or intragranular residual stress) which exists inside a grain because of crystal

imperfections within it. In this study, the emphasis is placed on type I and type II stresses which will be referred as bulk and single-crystal residual stresses, respectively.

A large number of studies have been devoted to residual stress development during plastic deformation [14-32]. The microstructural observation scale spans from individual grains to polycrystalline material. Mostly the stresses were measured at the bulk scale, but there are studies where single-crystal stresses were also estimated. Crostack and Reimers [33] measured the residual stress in individual grains in the transition zone of a welded ferritic steel. The observed stress anisotropy was related to the thermal history of the welding process. Dupke and Reimers [34] investigated large grained as well as polycrystalline nickel (alloy IN 939) in the tensile mode of deformation. They showed that the strain variation amongst orientations can be as high as 30%. It was also shown that a grain in a polycrystalline environment, as opposed to a similar orientation in a single crystal, experiences an intermediate state of strain. A similar anisotropy in stress evolution was also observed during cyclic deformation [35]. Using synchrotron radiation and area detector, Margulies et al. [17] first presented the strain tensor of a grain embedded in a polycrystalline aluminium, and deformed in tension. Advancing this work, Martins et al. [36] measured 10 grains of different orientations. Developments in strain tensors were shown to be orientation dependent, which was stipulated to be by product of relative slip activation. Wang et al. [37] reported the “grain-orientation-dependent” residual stresses in a commercial 316 stainless steel, which they described using a stress orientation distribution function. Though there are several other examples of grain-scale stress measurements [15, 16, 18], they rarely talked about any microstructural changes or orientation effect.

Mughrabi [20] introduced the composite model for plastic deformation to highlight the presence of long-range residual stresses in deformed metals. Such stresses are, arguably, intimately linked to the dislocation substructure. Mughrabi’s model describes the heterogeneous distribution of dislocations and corresponding residual stresses in deformed metals by a simplified “rule of mixture”, with cell walls populated with dislocations and almost dislocation free cell interiors. There are many instances of application of this model [38-40]. Ungar et al. applied this to [001] oriented copper single crystals during monotonic deformation and found different local flow stresses which suggest the applied stress was redistributed during deformation based on the microscopic arrangements [28]. Biermann et al. [41] demonstrated the variation of residual stress

from grain to grain and concluded the spatial variation of residual stress must be taken into account for plasticity prediction of polycrystals. All the studies following this approach observed the development of microstructure using transmission electron microscopy (TEM).

In terms of describing the development of residual stress quantitatively, Corvasce et al. [42] proposed a self-consistent model to evaluate grain scale residual stress from a generic single phase FCC polycrystal during thermo-mechanical deformation. They showed substantial residual stress development with orientation sensitivity. Clausen et al. [43] also demonstrated a self-consistent model of FCC polycrystal deformation with different degrees of anisotropy and showed the $\{hkl\}$ dependence of lattice strain response to uniaxial deformation. Recent developments also demonstrate the possibility of mapping of plastic deformation and residual strain from electron back scattered diffraction [44-46]. Recent studies [47, 48] have used cross-correlation, from high resolution EBSD patterns, to probe intragranular residual stresses in monotonic and cyclic deformation. High resolution EBSD [49] has also been used to explore patterns of microstructural developments, especially evolution of the GND structures.

It is important to point out that most studies that concurrently observed microstructural changes and residual stresses are restricted to single-crystal or bulk stresses, and involved TEM measurements. The drawback of single crystal observation is the absence of the constraints from neighboring grains. The drawback of the bulk stress state is that it is potentially difficult to correlate with the micro-plasticity – the basis of macroscopic observations and failure. TEM offers high spatial resolution but it lacks statistics and may be limited to only a few grains. There exist several studies which observe the single-crystal residual stress in polycrystalline samples [17, 30, 33, 35, 50], but they were seldom correlated with microstructural evolution.

In this study, we investigated the development of residual stress in a polycrystalline aluminum-manganese alloy at both the bulk level and at the level of the individual grains. The concurrent microstructural development of the identical area was also monitored using electron back scattered diffraction (EBSD). The objective of this study was to bring out orientation dependence of microtexture and residual stress developments. Discrete dislocation dynamics (DDD) simulations were also conducted to rationalize the experimental observations.

3.2 Experimental Procedure

This study involved tensile deformation of a commercial Al-Mn alloy AA3003. Tensile samples were fabricated from a 5 mm thick cold rolled and annealed plate: chemical composition being listed in table 3.1. Analytical microscopy (in the form of WDS or wave length dispersive X-ray spectroscopy) revealed absence of long range composition gradients in the matrix. The original material was subjected to 603K (330°C) - 4h annealing. This was to increase the average grain size from 30 μm to 100 μm . It is to be noted that grain size of more than 50 μm was essential for single-crystal stress measurement.

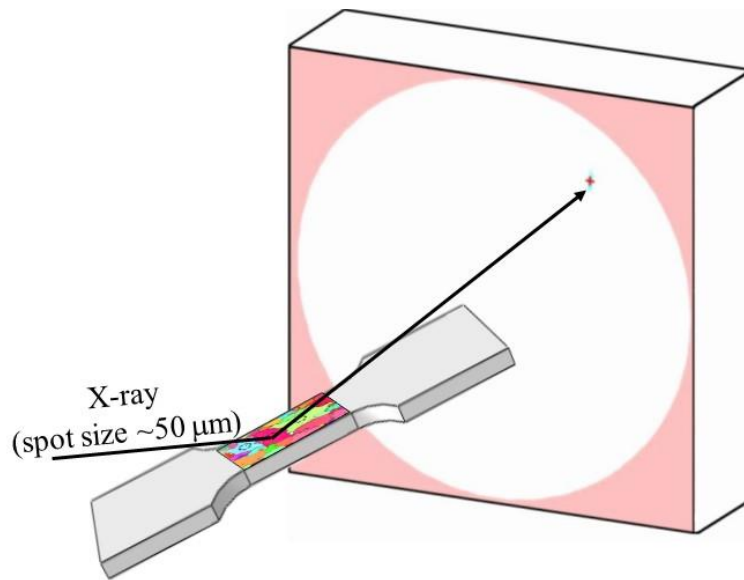
Table 3.1: Chemical composition (in wt% of alloying elements) of the alloy (AA3003)

Si	Cu	Fe	Mg	Zn	Ni	Mn	Ti	Al
0.25	0.05	0.40	<0.01	0.01	0.01	1.05	0.01	balance

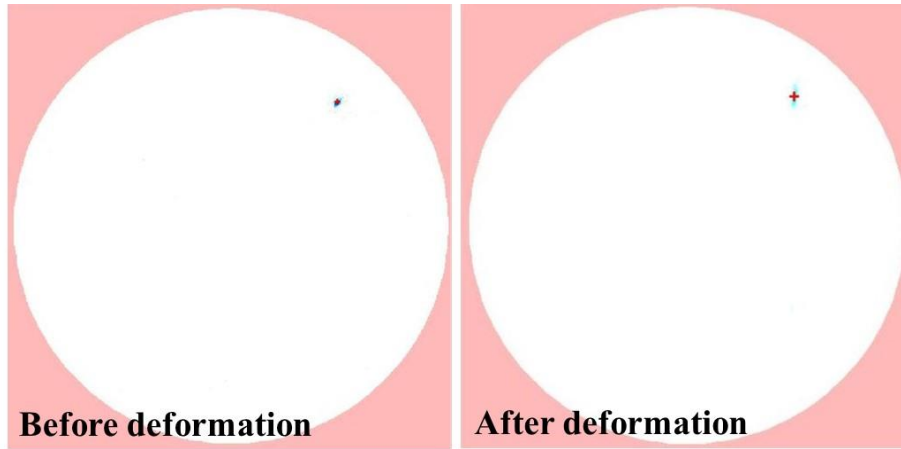
ASTM E8 sub-standard tensile samples were fabricated by electro-discharge machining (EDM). Following were the specimen dimensions: length = 100 mm, gauge length = 25 mm, gauge width = 6 mm and thickness = 5 mm. These specimens were deformed at a strain rate of 10^{-4} s^{-1} . The tensile samples were given interrupted, albeit incremental, strains. The exact strain values were decided based on the tensile strain hardening behavior (to be discussed later in section 3.3). At these strain increments, the microstructures and residual stress values were measured for identical region(s) and grain(s).

The measurements of residual stresses were performed at two different microstructural scales: type I (or bulk stress) and type II (or single-crystal) stresses. For the former, a PanalyticalTM X'Pert PRO MRD (Material Research Diffractometer) system was used. Measurements was performed using multiple {hkl} Grazing Incidence X-Ray Diffraction (GIXRD) [51-53]. It is to be noted that the samples were subjected to oscillations during the measurements, which covered the entire gauge length (several hundred grains).

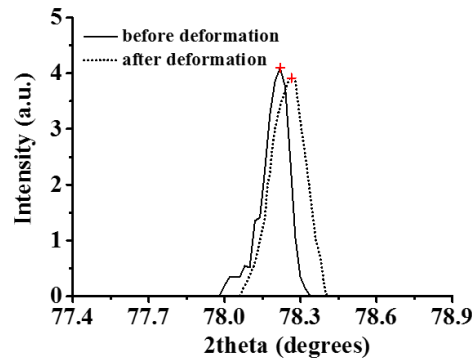
A Bruker D8 Discover™ system with Vantec™ area detector was used to measure single-crystal (or type II) residual stress. This exercise is non-trivial and demands a detailed explanation. As shown in figure 3.1a, micro-focused X-ray (of $\sim 50 \mu\text{m}$ spot size) was placed on a single grain of the tensile specimen. Appropriate video feed with laser tracking enabled accurate placement of the X-ray spot. It is to be noted that the orientation of these grains were measured, prior to X-ray diffraction (XRD), with EBSD. The EBSD data (or pole figure angles) were converted in XRD coordinates (Bragg angle and goniometer tilt/rotation). The conversion procedure is given in the appendix. As shown in the appendix, each set of pole figure angles can have several combinations of XRD coordinates, all giving rise to Laue diffraction (see figure 3.1a). For each Laue spot, iteration of the tilt and rotation angles were essential to obtain spot(s) of the highest intensity. The later typically accounted for measurement uncertainties (if any) in sample placement. With all these precautions, and as shown in figure 3.1b, Laue spots for the same grain were obtained before and after the tensile deformation. For each single-crystal residual stress matrix, at least six Laue spots were needed. Even with appropriate batch acquisition of data, each single-crystal residual stress measurement requires slightly more than 1 h of measurement time.



(a)



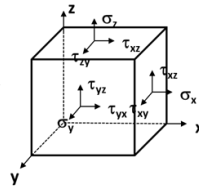
(b)



At least 6 sets of equation to solve the fundamental equation of strain



$$\sigma_{ij} = C_{ijkl} \epsilon_{kl}$$



(c)

Figure 3.1: (a) Schematic showing single-crystal stress measurement with micro-focus ($\sim 50 \mu\text{m}$ spot size) XRD and area detector. (b) Area detector image of Laue spot from the same grain before and after plastic deformation. Centroid position(s) of the spots were identified with an appropriate MatlabTM program and are shown as '+'. (c) From the respective centroid positions, intensity- 2θ plots were obtained and d-spacings were calculated. This exercise was repeated six times to solve strain tensors for individual grains.

To analyze the area detector data (or the Laue spot) a Matlab™ code was written. The computer program estimated the centroid position. Using the centroid position in Diffrac-Eva™ allowed measurements of the d-spacing for a particular Laue diffraction. This is referred as $d_{\psi\phi}$, or d-spacing of a single crystal at XRD angles of $\theta\psi\phi$. The strain ($\varepsilon_{\psi\phi}$) is then given as,

$$\varepsilon_{\psi\phi} = \frac{d_{\psi\phi} - d_0}{d_0} \quad \text{-----(3.1)}$$

where d_0 is the unstrained lattice parameter. This was obtained from annealed powder specimen of the same composition [12, 13]. $\varepsilon_{\psi\phi}$ is related to the average strains ε_{kl} in sample coordinate system [13],

$$\varepsilon_{\psi\phi} = \varepsilon_{11} \cos^2 \phi \sin^2 \psi + \varepsilon_{12} \sin 2\phi \sin^2 \psi + \varepsilon_{22} \sin^2 \psi \sin^2 \phi + \varepsilon_{33} \cos^2 \psi + \varepsilon_{13} \cos \phi \sin 2\psi + \varepsilon_{23} \sin \phi \sin 2\psi \quad \text{-----(3.2)}$$

Solution of equation 3.2 gives the residual strain tensor for an individual grain. It is to be noted that at least six Laue spots are required to establish the complete tensor. To convert the strain tensor into residual stress tensor, multiplication with appropriate stiffness tensor is needed [54]. This is based on a simple Hooke's law: $\sigma_{ij} = C_{ijkl}\varepsilon_{kl}$. The elastic constants of the stiffness matrix were assumed to be $C_{11}=108.2$ GPa, $C_{12}=61.3$ GPa and $C_{44}=28.5$ GPa [10, 13].

The microtexture was characterized using EBSD on a FEI Quanta™ Nova NanoSEM (scanning electron microscope). A TSL-OIM™ EBSD system was used. All scans were taken at 0.3 μm step size with identical beam and video conditions. For sample preparation, standard metallographic polishing was followed by electro polishing: 80:20 methanol:perchloric acid, 13 volts dc and -20° C.

GND densities were calculated, at all stages of tensile deformation, to quantify microstructural evolution. Presence of dislocations in a crystalline structure produces lattice curvatures, which appear as local misorientations in EBSD measurements [55]. The dislocation density tensor (α) is related [56] to dislocation network as,

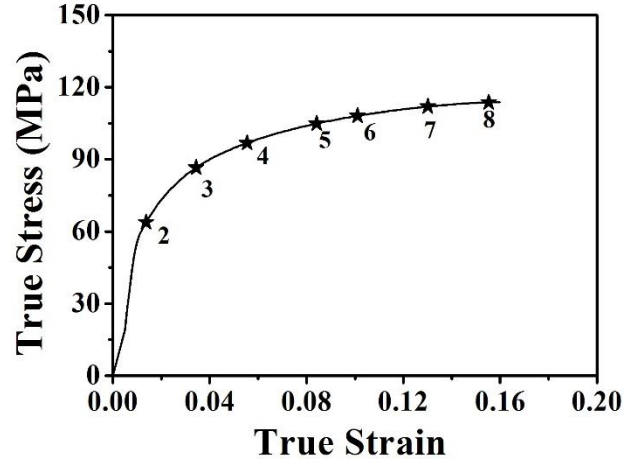
$$\alpha = \sum_{i=1}^k \rho^i (b^i \otimes z^i) \quad \text{-----(3.3)}$$

The dislocation dyadic represents a geometrical definition of dislocation i having Burgers vector b^i and slip plane normal direction z^i . ρ^i is a scalar quantity representing GND density. The EBSD data were analyzed, for estimating GND densities, through TSL-OIM™ software [57]. In this study, GND density was calculated for two different scales following the mentioned procedure. The bulk GND density was calculated over a large area covering many grains whereas the local GND density was calculated for a single grain or orientation covering a circular area having ~50 μm diameter.

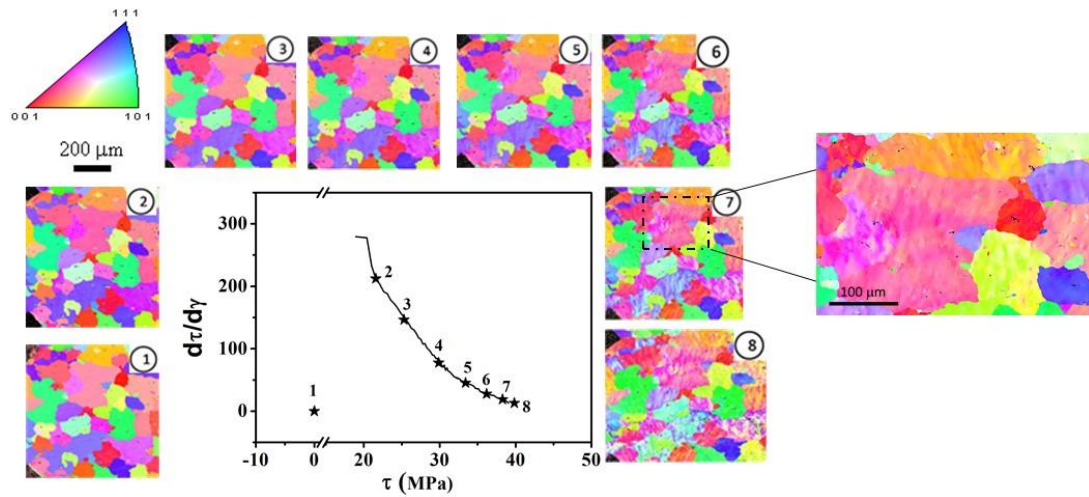
3.3 Results

Figure 3.2a is a true stress – true strain (σ - ϵ) curve for the AA3003 tensile specimen. The corresponding $\frac{d\tau}{d\gamma}$ versus τ plot is shown in figure 3.2b. The work hardening behavior can be represented as $\frac{d\sigma}{d\epsilon}$ versus σ (or ϵ) [58]. The same can also be converted to a single equivalent slip system to eliminate orientation effects. This is the so-called $\frac{d\tau}{d\gamma}$ versus τ plot [1], where $\sigma = \langle M \rangle \tau$ and $\gamma = \langle M \rangle \epsilon$. $\langle M \rangle$ is the average Taylor factor for a polycrystalline material, which was calculated as 2.8 from large area EBSD scans of the prior deformation specimen.

Figure 3.2b also includes progressive microtextural developments. The latter is shown in terms of ‘limited’ area EBSD IPF (inverse pole figure) maps. It is to be noted that very large areas (a total of 3mm × 3mm), and several tensile samples, were subjected to EBSD measurements. However, for brevity figure 3.2b includes only a small section of such scans. It is to be noted that the same tensile specimen(s) were subjected to progressive deformation. Samples were taken out at specific intervals (as points ‘1-8’ in figure 3.2) for measurements of microtexture and residual stresses. The selections of these points were based on the work hardening curve (figure 3.2b).



(a)



(b)

Figure 3.2: (a) Representative true stress – true strain behavior; (b) Microstructural developments at different locations of work hardening stages during tensile deformation (colors represent different orientations in inverse pole figure convention). In (b), enlarged region of ‘point 7’ shows the development of in-grain misorientations.

It is important to note that the microstructure evolution was non-monotonic. This is shown, qualitatively, in the EBSD images (figure 3.2b) and collated, quantitatively in table 3.2a. Table 3.2b tries to identify approximate regimes of microstructural evolution based on the EBSD

estimated parameter: densities of geometrically necessary dislocations (ρ_{GND}), low (ρ_{LAGB} : 1–15°) and high (ρ_{HAGB} : 15–62.8°) angle grain boundaries.

Table 3.2: (a) Applied stress (in MPa) versus EBSD estimated densities of geometrically necessary dislocations (ρ_{GND}), low (1–15°, ρ_{LAGB}) and high (15–62.8°, ρ_{HAGB}) angle grain boundaries. (b) Based on data from (a), different regimes of tensile deformation are identified.

(a)

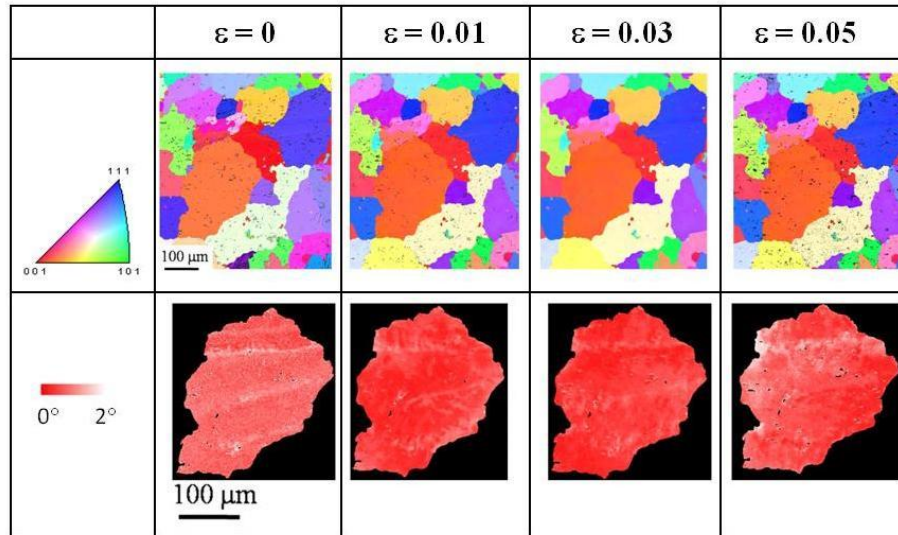
Applied stress (MPa)	Geometrically necessary dislocation density (ρ_{GND} in 10^{12} m^{-2})	Low angle (1–15°) boundary density (ρ_{LAGB} in μm^{-1})	High angle (15 –62.8°) boundary density (ρ_{HAGB} in μm^{-1})
0	26.45	0.17	0.0037
21.58	22.09	0.11	0.0034
25.38	20.47	0.10	0.0035
29.87	33.96	0.49	0.0042
33.41	28.17	0.24	0.0044
36.18	29.97	0.43	0.0057
38.29	32.63	0.42	0.0060
39.05	36.93	0.48	0.0065

(b)

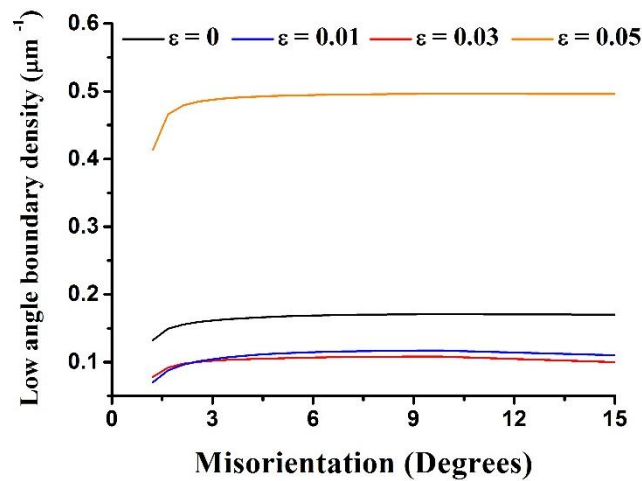
Applied stress (MPa)	Behavior of EBSD estimated parameters	Regimes of tensile deformation
0 to ~ 25	$\rho_{\text{GND}} \downarrow$ $\rho_{\text{LAGB}} \downarrow$ ρ_{HAGB} almost constant	Regime of mechanical stress relief
~ 25 to ~ 30	$\rho_{\text{GND}} \uparrow$ $\rho_{\text{LAGB}} \uparrow$ $\rho_{\text{HAGB}} \uparrow$	Work hardening
~ 30 to ~ 33	$\rho_{\text{GND}} \downarrow$ $\rho_{\text{LAGB}} \downarrow$ $\rho_{\text{HAGB}} \uparrow$	Beginning of grain fragmentation
~ 33 to ~ 39	$\rho_{\text{GND}} \uparrow$ $\rho_{\text{LAGB}} \uparrow$ $\rho_{\text{HAGB}} \uparrow$	Continuation of grain fragmentation

At the beginning (0 to ~25 MPa imposed stress), deformation induced annihilation of LAGB was observed. Although the initial microstructure came after annealing (603K - 4h), the grains contained both low angle boundaries and orientation gradients. This is shown in figure 3.3a. Introduction of tensile deformation, albeit minor, is expected (and observed) to produce significant near grain boundary mesoscopic shear (NGBMS). This has been reported earlier [59, 60]: a local shear strain exceeding > 1.2 , when the applied strain was only 0.01. The newly introduced NGBMS eliminated the earlier orientation gradients and removed low angle grain boundaries (LAGB) supporting such gradients. This is clearly seen in figures 3.3a and 3.3b: deformation induced annihilation of LAGB. It is to be noted than an earlier study [59], on semi-processed electrical steel made similar observations. Shekhawat et al [59] clearly showed that introduction of minor strains annihilated strain gradients and LAGBs, thus providing a mechanical stress relief. This study shows a similar mechanical stress relief, through elimination of LAGBs, in the present aluminum sample. Further stresses (~25 to ~30 MPa) led to work hardening, followed by (~30 to ~39 MPa) grain

fragmentation. Of course, any such microstructure evolution during different stages of work hardening is of interest. However, the objective is focused on evolution of residual stresses and its dependence, if any, on the developments of deformed microstructure.



(a)



(b)

Figure 3.3: (a) EBSD IPF maps of a cluster of grains for different ($\epsilon = 0, 0.01, 0.03$ and 0.05) true strains. 1 to 3° boundaries are shown as black lines. From a single grain, of the grain cluster, evolution of orientation gradients (grain average orientation and its deviations in 0-2° scale) was also shown. (b) shows the low angle boundary (1-15°) densities (boundary length per unit area) at the corresponding strain levels.

In the interrupted tensile tests, the bulk residual stress was measured. Measurements were made on the surface of the tensile specimen, and hence only σ_{11} and σ_{13} components of the overall residual stress tensor were measured [13]. Use of multiple $\{hkl\}$ GIXRD ensured measurement for all X-ray poles [52]. Figure 3.4 shows σ_{11} and σ_{13} versus τ . Both σ_{11} and σ_{13} show non-monotonic behavior with τ . In the case of σ_{11} , it increased initially and then fell at τ of ~ 30 MPa, Subsequently, σ_{11} increased again but dropped beyond a τ of ~ 35 MPa. σ_{13} exhibited the opposite trend of σ_{11} .

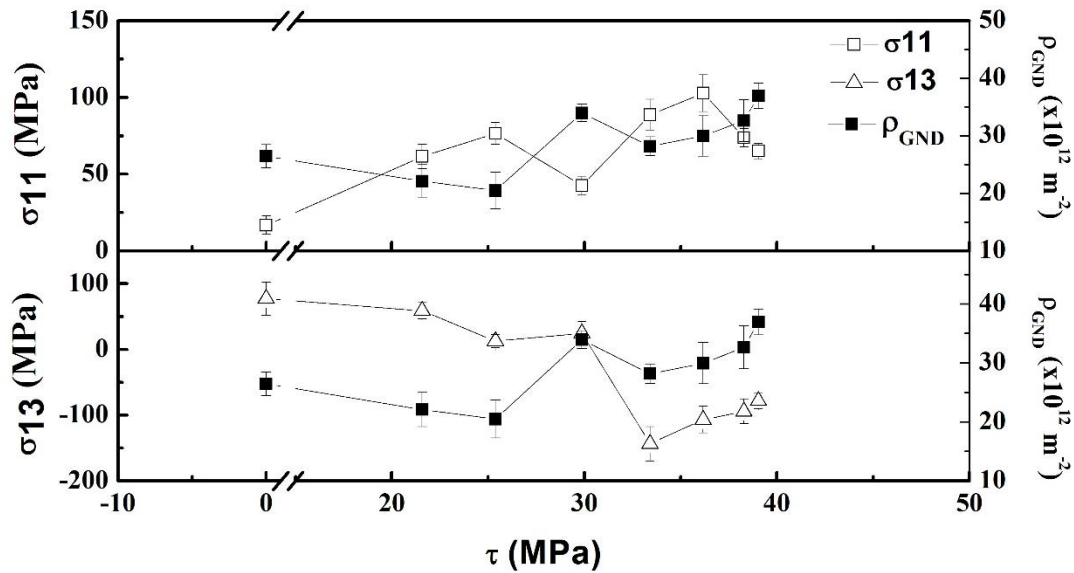


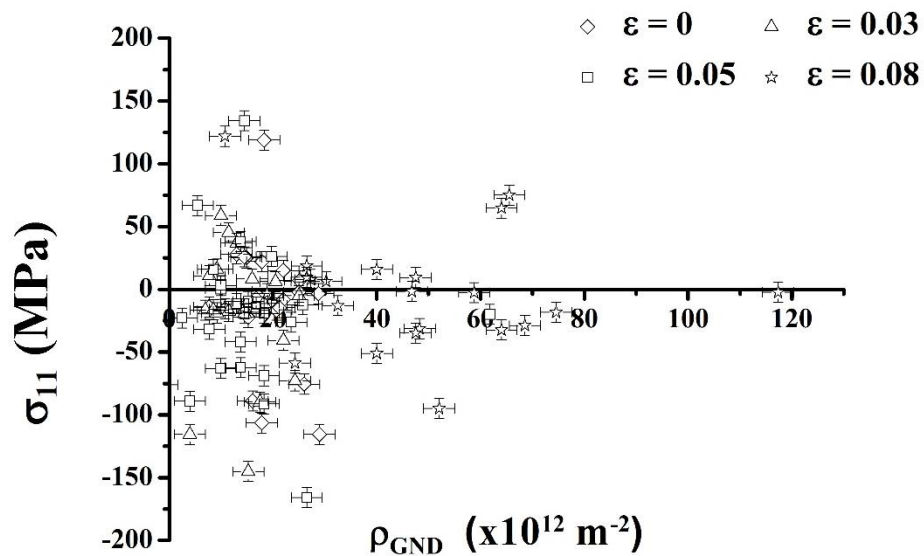
Figure 3.4: Correlation of Geometrically Necessary Dislocation density (ρ_{GND}) and normal residual stress (σ_{11}) and shear residual stress (σ_{13}) during each stage of tensile deformation. Y-axis includes appropriate error bars for residual stress and ρ_{GND} values.

For direct comparison with microtexture evolution, EBSD estimated ρ_{GND} (density of geometrically necessary dislocations) [57] values are also measured. These are shown in figure 3.4 as well. The ρ_{GND} evolution during tensile deformation followed the same trend as that of σ_{13} . However, deformation (or imposed τ) dependence σ_{11} and ρ_{GND} appeared to be exactly opposite.

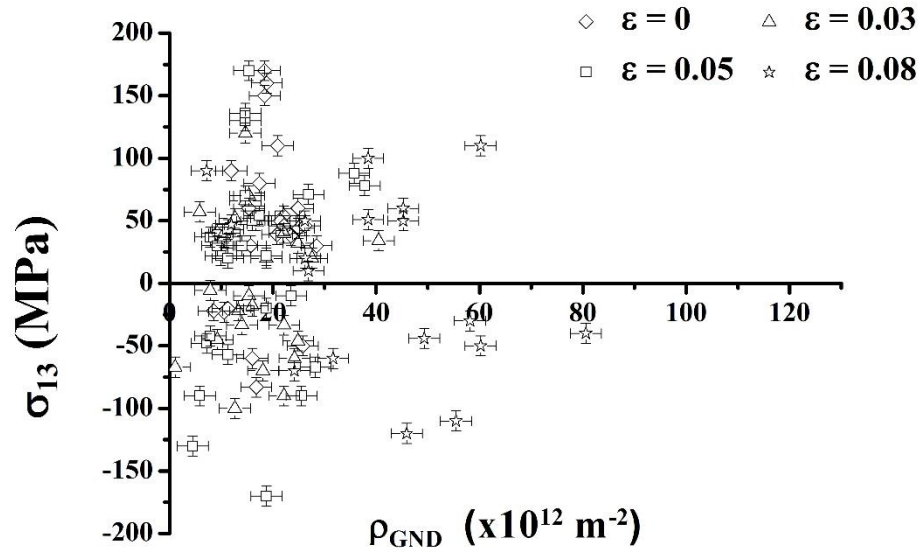
The non-monotonic changes in GND densities (figure 3.4) were above estimated measurement uncertainty ($3.5 \times 10^{12} \text{ m}^{-2}$). The latter was measured from multiple EBSD scans on the same

grain(s). The undeformed annealed microstructure had orientation gradients and LAGBs (see figure 3.3). Initial stages of plastic deformation eliminated them. At the later stages of plastic deformation, new orientation gradients, and corresponding near boundary mesoscopic shear strains, were introduced and grain fragmentation was initiated. All these different mechanisms appear to have contributed to the non-monotonic evolution of GND densities and residual stresses (both normal and shear). The objective was to explore possible linkage between GND density and residual stress evolution.

Single-crystal stress measurements were conducted in 25 grains, but at 5 stages of tensile deformation. Reason for this is simple, measurement at each stage involved at least 50 h of equipment time, and covering all 7 stages was not simply practical. XRD and EBSD measurements were taken from $\sim 50 \mu\text{m}$ spots. Average residual stress and ρ_{GND} values were then estimated from identical locations. Figure 3.5 plots σ_{11} and σ_{13} versus ρ_{GND} values (for the first four stages of tensile deformation). It is to be noted that the pattern did not change when all 5 stages were considered. Unlike the measurements of bulk residual stress, there was no obvious correlation between the local residual stress measurements and the local ρ_{GND} . This is indeed surprising, and will involve further deliberations in the discussion section.



(a)



(b)

Figure 3.5: For 25 grains, development of (a) normal (σ_{11}) and (b) shear (σ_{13}) residual stresses as a function of ρ_{GND} . The data is shown for first three stages of tensile deformation (imposed ϵ values are marked as respective legends). In both figures, measurement uncertainties are shown as appropriate error bars.

Von Mises stress is calculated from the residual stress tensor. Von Mises stress difference between two consecutive levels of strain under investigation is termed as $\Delta\text{RS}_{\text{VonMises}}$. In a similar way, the difference between geometrically necessary dislocation (GND) density is termed as $\Delta\rho_{\text{GND}}$. The figure 3.6 plots $|\Delta\text{RS}_{\text{VonMises}}|$ versus $|\Delta\rho_{\text{GND}}|$, [note: $||$ sign denotes the modulus value of the quantity] again for the first four stages of the tensile deformation. Measurement uncertainties (for $|\Delta\text{RS}_{\text{VonMises}}|$ and $|\Delta\rho_{\text{GND}}|$) were estimated from multiple measurements of the same grain(s). These were $\sim 20\text{MPa}$ for $|\Delta\text{RS}_{\text{VonMises}}|$ and $\sim 7.2 \times 10^{12} \text{ m}^{-2}$ for $|\Delta\rho_{\text{GND}}|$. These two are marked in figure 3.6 as dotted lines. Grains with $\Delta\rho_{\text{GND}}$ below measurement uncertainty were considered to be “elastic and negligibly plastically deforming grains” and showed small accumulation of residual stress. The remaining grains demonstrated significant changes in GND density and residual stress and were “elasto-plastically deforming grains”.

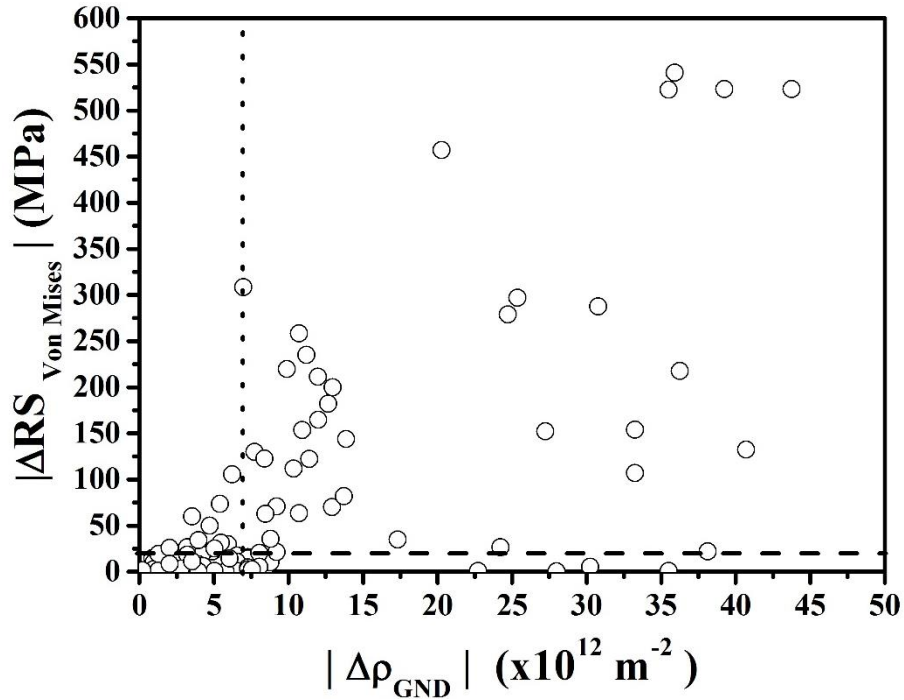
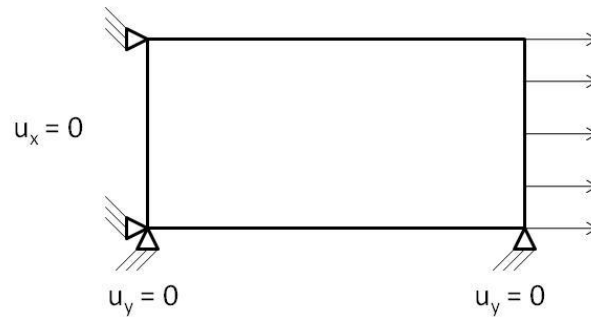


Figure 3.6: Change in Von Mises residual stress ($|\text{ARS}_{\text{VonMises}}|$) as a function of change in $|\rho_{\text{GND}}|$. The data is shown for first three stages of tensile deformation. Dotted lines indicate measurement uncertainties.

3.4 Discussion

The experimental results presented indicate an interesting contradiction. Bulk residual stress and ρ_{GND} had a clear relationship (figure 3.4). However, no such scaling was apparent in single-crystal residual stress measurements (figures 3.5 and 3.6). Arguably, the microstructure and residual stress evolution during plastic deformation originates from dislocation substructure and elastic incompatibilities (between neighboring grains). It was hence considered prudent to separate these two aspects. The residual stress developments in the “elastic and negligible plastic deforming grains” ($\rho_{\text{GND}} < 7.2 \times 10^{12} \text{ m}^{-2}$) were considered first. For this purpose a scientific shareware, OOF2 (OOF: object oriented finite element) developed by National Institute of Standards and Technology (NIST) [61], was used. Figure 3.7a shows the schematic view of the problem with the boundary conditions. The appropriate grains (~ 15 grains), see figure 3.7b, were considered in a 2-dimensional (2-d) finite element simulation. OOF2 imports EBSD data, including Euler angles and elastic tensors, and then imposes the necessary elastic deformation. Elastic constants of the stiffness

matrix of annealed Aluminum powder sample were used [12, 13]. The simulation space was applied the following boundary conditions: $u_x = 0$ on the left side and $u_y = 0$ on the bottom side of grain cluster. It is to be noted that macroscopically observed tensile strains were imposed on the right side of grain clusters, and the OOF2 2-d simulations allowed evaluation of σ_{11} values for the appropriate grains and grain clusters. Figure 3.7c shows the experimental (from single-crystal stress measurements) versus simulated (OOF2) σ_{11} values: and they had a linear scaling. The OOF2 simulations thus appear to capture the experimental trend. However, OOF2 predicted σ_{11} as GPa whereas experimental σ_{11} was in MPa. This was because the simulations were only elastic, while actual experiments were of elasto-plastic nature. A crystal plasticity finite element (CPFE) simulation may offer a better match. That was considered beyond the major objective of this study. The objective of this study is to relate evolution of dislocation substructure (ρ_{GND}) with single-crystal residual stresses. Hence discrete dislocation dynamics (DDD) simulations were preferred over CPFE in this present investigation. A separate study involving CPFE plus experimental measurements of residual stress distribution function [62, 63] for plane strain compressed aluminum is investigated later in chapter 5.



(a)

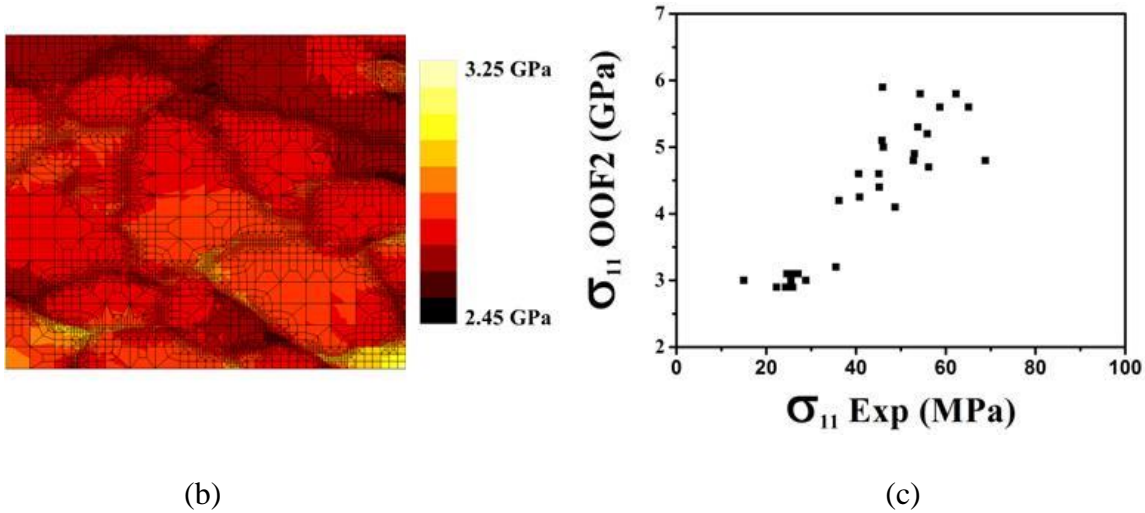


Figure 3.7: (a) Boundary condition of OOF2 geometry; (b) OOF2 simulation showing development of residual stress; (c) Comparison of normal residual stress (σ_{11}) between experiment and simulation.

There were ~25 “elasto-plastically deforming grains” (at all stages of tensile deformation). This data (figure 3.8) with many crystallographic orientations appear very confusing. It was hence decided to select few orientations for further study. The selection of common grains/orientations, for both experiments and DDD simulations, was tricky. Firstly, experimentally getting a large grain within 10° of an ideal orientation and then following it through stages of tensile deformation are non-trivial. The DDD simulations are also computationally exhaustive. Finally, the selected grains must have academic and applied interests (and are expected to have different deformation behavior). (Cube $\{100\} \langle 001 \rangle$, Cu $\{112\} \langle 111 \rangle$, B $\{011\} \langle 211 \rangle$) [1, 64] orientations, fit the second point perfectly well. Cube is expected to be unstable in deformation, though it can be a significant component of the recrystallization process [1, 6, 65-72]. Brass, on the other hand, happens at the beginning of plastic deformation or through extensive shear [1]. Cu is the final deformation texture component in fcc metallic materials, without extensive twinning. Both from deformation and recrystallization [1, 6, 65-72], these three ideal orientations have lots of significance and hence they were ‘preferentially’ selected. It may be noted that the ‘selection’ also involved a few other ideal, and random, fcc texture components. However, for brevity those data are not included here.

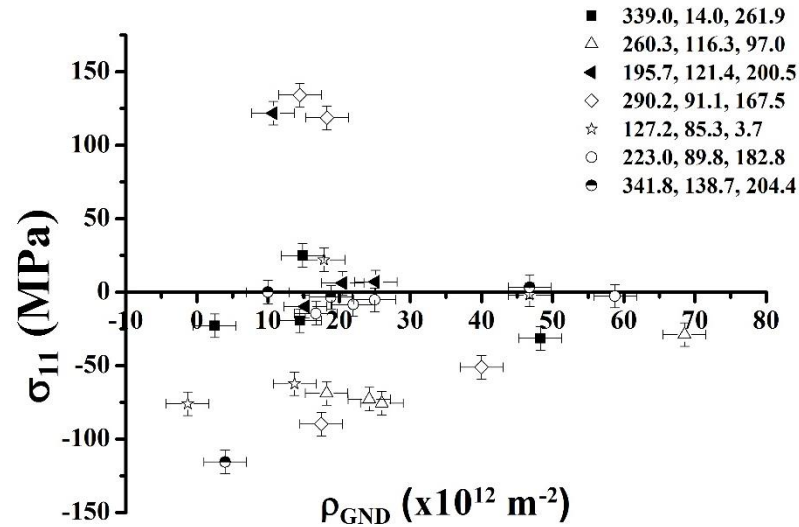
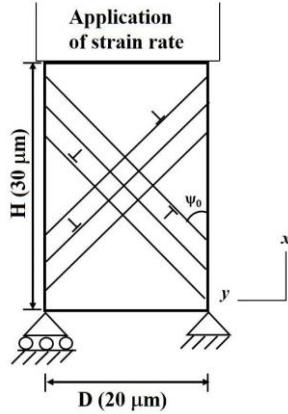
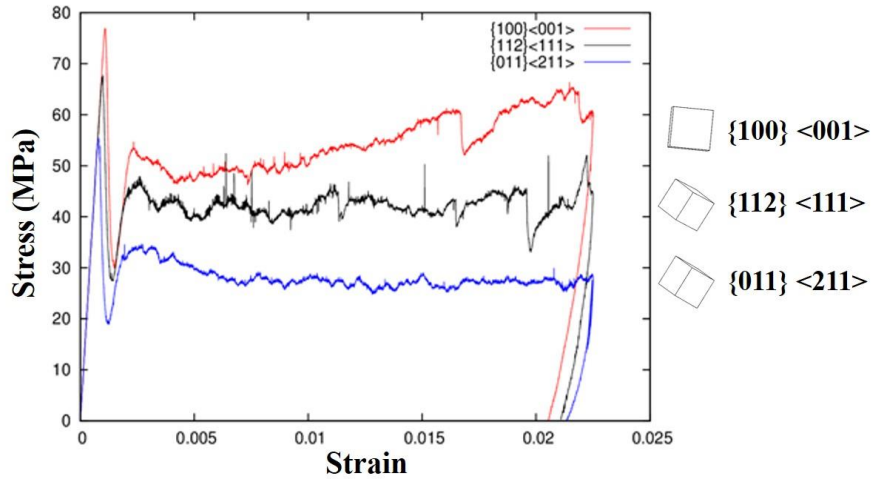


Figure 3.8: Development of normal (σ_{11}) residual stresses as a function of ρ_{GND} for different orientations. Measurement uncertainties are shown as appropriate error bars.

Many atomistic or discrete dislocation dynamics (DDD) based models [26, 73-82] have been used to describe substructure development during small scale deformation. This study used the DDD framework developed by Benzerga and co-workers [73, 77, 83], which captures the qualitative features of microstructural development with simultaneous mechanical response. DDD based simulations have been used in the past to study residual stress evolution in a composite material with crystalline matrix and elastic reinforcement [84]. In this study, we used DDD as a tool to mimic the tensile deformation of differently oriented crystals and thus to investigate quantitatively the orientation dependence of residual stress and ρ_{GND} evolution. The schematic shown in figure 3.9a illustrates the DDD simulation set up. The complete information about the formulation of DDD can be found in [73].



(a)



(b)

Figure 3.9: (a) Schematic of DDD simulation set up showing a plain strain model oriented for double slip where two slip systems are oriented at $\pm\psi_0$ from x axis, (b) Simulated stress-strain plot for the specimen during loading and unloading for three different orientations (orientations are shown as unit cells with $\{hkl\}\langle uvw \rangle$ notation at right side)

The simulations were carried out on single orientations considering as an elastic, homogeneous and isotropic rectangular box of size $30 \mu\text{m} \times 20 \mu\text{m}$, close to the experimental area of single-crystal stress measurement. A plane-strain condition was assumed with a constant axial displacement (U) rate along the x direction. The surfaces at $\pm D/2$ was traction free and zero shear stress at $\pm H/2$ were considered as boundary condition.

The initial configuration of simulation space was assumed to be dislocation free, but random distributions of Frank-Read sources and obstacles were considered. Two types of dislocation obstacles are considered in DDD modelling - initial stress-free point obstacles that represent precipitates and dynamic obstacles that represent forest dislocations. These act as the pinning agents. Random distribution of both the obstacles were assumed at the start of simulations. Dislocation loops were modelled as dipoles of edge dislocations of opposite sign and restricted to glide in their slip plane only. Probable slip systems were assumed to be oriented at $\pm\psi_0$ angle from the x -axis for an orientation. The Peach–Koehler force was accounted for their glide force and the dynamics was supposed to start when a dislocation dipole nucleated from a random source where the acting Peach–Koehler force exceeded a critical value for a prescribed time. The sign of the dislocation was dependent on the sign of the Peach–Koehler force. The nucleated dislocation interacted with other dislocations and might become pinned if it could not overcome the obstacle strength. Details of the input parameters used in the simulation are listed in table 3.3. Key input parameters related to mechanical property and microstructure were taken from experiments.

Table 3.3: Parameters used in the discrete dislocation dynamics simulations

Elastic Modulus (E)	66 GPa
Poisson's Ratio (ν)	0.3
Burgers Vector (b)	0.25E-3 μm
Slip plane spacing	50 nm
Drag coefficient (B)	1.0E-16 Pa-s
τ_{FR}	17 MPa
τ_{obs}	15 MPa
α	0.3
β_{bk}	0.5
β_{nu}	1
γ	0.1E4
Time increment	0.5E-8 s
Strain Rate	1000s ⁻¹
Schmid factor	Cube {100}<001>= 0.43 Cu {112}<111>= 0.40 Brass {011}<211>= 0.31

In this set of simulations, an average stress (σ) and applied strain (ε) is evaluated by:

$$\sigma = \frac{1}{H} \int_{-H/2}^{H/2} \sigma_{11}(\pm D/2, y) dy, \quad \varepsilon = \frac{U}{D} \quad \text{-----(3.4)}$$

where H is the height and D is the total length. U is the axial displacement rate along the x direction.

The deformation induced dislocation substructure evolution is quantified in terms of the evolution of the GND density (ρ_{GND}). The ρ_{GND} from the simulation was estimated [73, 85] by dividing the simulation space into small domains which were considered to be equivalent to the EBSD step size.

Within each sub-domain, the GND density was

$$\rho_{GND} = \sqrt{\left[\sum_k (\rho_+^{(k)} - \rho_-^{(k)}) \cos \phi^{(k)} \right]^2 + \left[\sum_k (\rho_+^{(k)} - \rho_-^{(k)}) \sin \phi^{(k)} \right]^2} \quad \text{-----}(3.5)$$

where $\rho_+^{(k)}$ and $\rho_-^{(k)}$ are positive and negative dislocation dipole densities and $\phi^{(k)}$ is the orientation of slip system k.

The GND density calculated in each domain was used to evaluate the effective GND density in simulation space as

$$\bar{\rho}_{GND} = \sum_{n=1}^m \frac{\Omega^n}{\Omega} \rho_{GND}(\Omega^n) \quad \text{-----}(3.6)$$

where Ω^n defines the element in structured grid and m is the number of elements in the unit cell.

As stated earlier, three different orientations (Cube {100} <001>, Cu {112} <111>, B {011} <211>) [1, 64] were selected from the experimental data (figure 3.8). DDD simulations were then carried out. Representative stress versus strain response for these specimens is shown in figure 3.9b. All the specimens were subjected to loading up to 2.25% strain and subsequently unloaded until the average macroscopic stress in the specimens was zero. All three specimens showed some amount of post yield hardening and upon unloading exhibited Bauschinger behavior. Similar loading-unloading simulations were carried out at the intermittent strains as well. Average stresses, only due to the presence of dislocations, were calculated at the ‘loading’ (after imposing appropriate stress-strain (figure 3.9b)) and ‘unloading’ (after imposing appropriate stress-strain and then unloading (figure 3.9b)) points. As DDD simulation was 2-dimensional, simulated σ_{11} component of the residual stress was available for comparison with experimental data.

The orientation dependent development of dislocation substructure and residual stress (σ_{11}) are shown in figure 3.10. In this figure, the network of dislocations is superimposed on the resultant σ_{11} contours for three different crystallographic orientations. The state of ‘loading’ showed regions of higher stresses where there were dislocation pileups at obstacles or junctions. The ‘unloading’ altered the dislocation assemble and the stress contours (see figure 3.10). At the initial stages of ‘unloading’, pinned dislocations were released and dislocation annihilations took place: leading to a reduction in ρ_{GND} . However, subsequent to this initial phase, where the unloading curve typically showed inelastic response, Bauschinger effect was observed accompanied by a reorganization of

the dislocation structure leading to increase in ρ_{GND} [77]. This substructure and residual stress (σ_{11}) evolution was found to be dependent on the specimen orientation, as highlighted in figure 3.10.

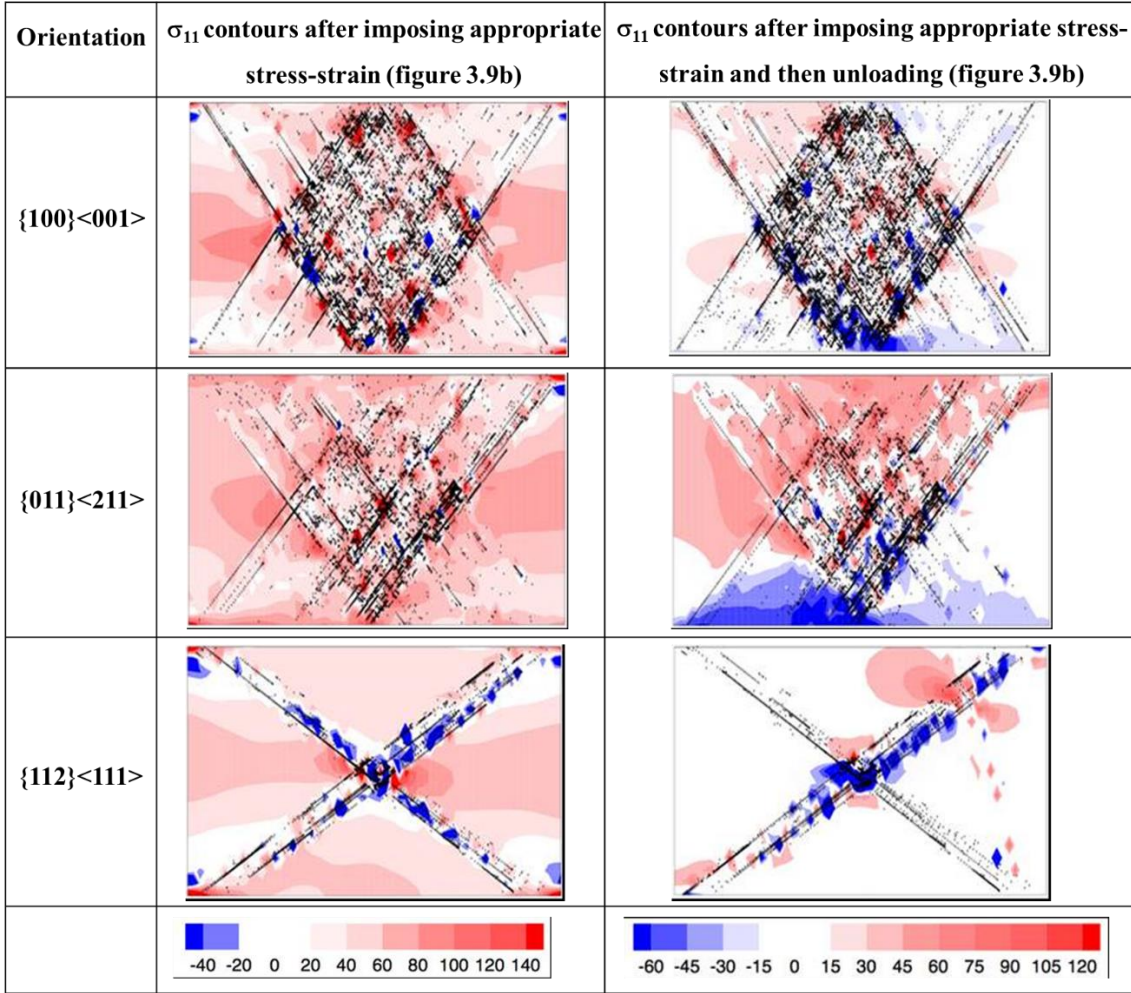


Figure 3.10: σ_{11} contours at $\epsilon_{11}=0.0225$. The data were obtained by imposing appropriate stress-strain, and then unloading, see figure 3.9b.

The DDD simulations were valid only for small strains, but the tensile deformations consisted of larger strains. The ρ_{GND} was naturally much higher in the experimental data. To overcome this discrepancy during the qualitative comparison between the experiments and simulations, both the experimental and simulated GND densities were scaled by dividing with the maximum value obtained in each case.

Figure 3.11 illustrates the comparison of σ_{11} versus ρ_{GND} , for three different crystallographic orientations, in the experiments and in the DDD simulations. Two sets of simulation data are shown, respectively after ‘loading’ (after imposing a tensile strain of 0.0225) and ‘unloading’ (zero macroscopic stress). The three orientation selected were the classical fcc texture components [1, 64] of (Cube $\{100\} \langle 001 \rangle$, Cu $\{112\} \langle 111 \rangle$, B $\{011\} \langle 211 \rangle$). Cube recrystallization has been a subject of text-books [1, 6], review [66, 67] and research [65, 68-72] articles. Recrystallized Cube grains are expected to form from deformed cube bands through frequency and/or size advantage [1]. It is clear that in polycrystalline aluminum recrystallized cube has a strong frequency advantage through lower stored energy of deformed cube and/or selective growth (presence of growth favorable $40^\circ \langle 111 \rangle$ boundaries) [65]. Though deformed cube has been reported to be heavily fragmented [65, 71], the deformed but recovered cube is expected to have lower stored energy [71]. The present DDD simulations also revealed clear indications of strain localizations in Cube. The higher residual stresses appear to be an outcome of such strain localizations. This observation is in contrast to the experimental findings that revealed lower stored energy in recovered Cube [71]. Ridha and Hutchinson [70] in their classical research had attributed lower stored energy in Cube orientations to the non-interaction of dislocations due to the higher recovery (as observed experimentally). The present experimental and DDD simulations did not account for the post-deformation recovery. In the absence of such recovery, experimental and simulation results on orientation sensitive build-up of GND and residual stress appear to be consistent and reproducible. They need to be extended to recovery experiments and simulations on similar orientations to investigate strain energy relief due to dislocation motion, in the absence of externally applied stress, leading to further changes in dislocation configurations.

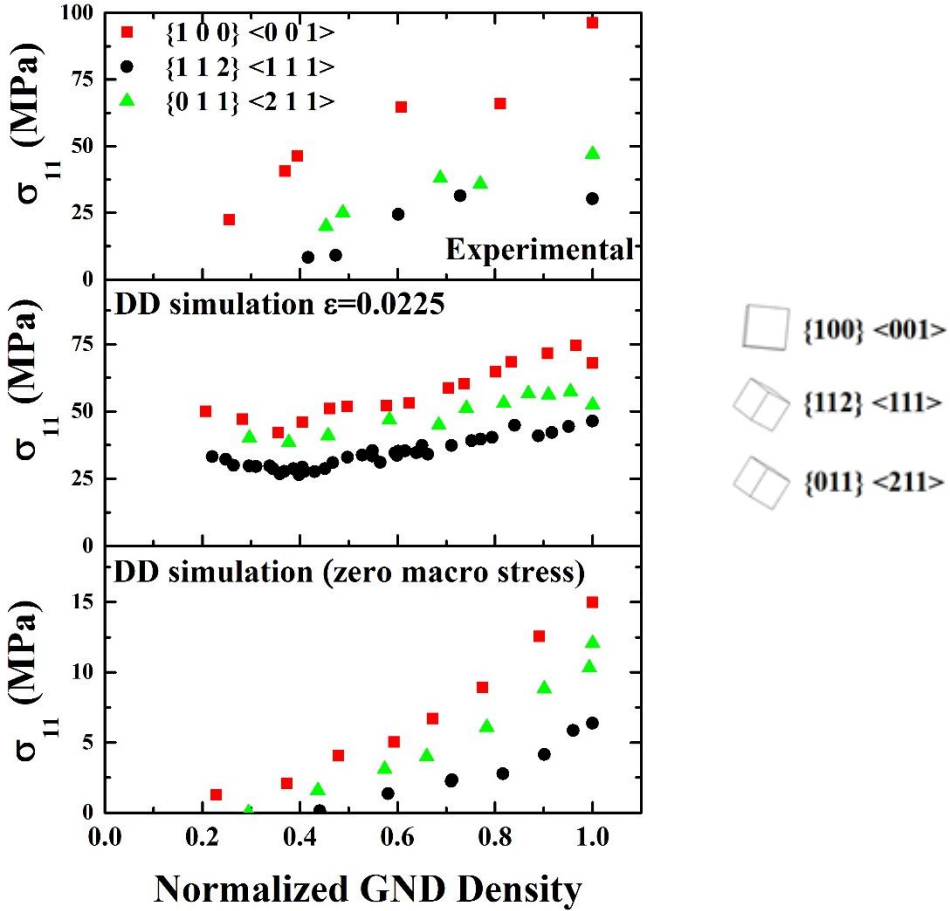


Figure 3.11: Comparison of experimental and DDD simulations, for three different orientations, showing developments in single-crystal σ_{11} as a function of normalized dislocation density (ρ_{GND}). DDD data are collated after imposing appropriate stress-strain and later by unloading (figure 3.9b and 3.10).

DDD simulation (figures 3.9b and 3.10) from ‘loading’ showed orientation dependent hardening and ρ_{GND} accumulation. There was also a direct correlation between the two. On a first glance, this is not unexpected. The ‘soft’ Cu/Brass (B) deformed more easily than ‘hard’ Cube, the latter accumulating more GND. The DDD simulations used Schmid factors (SF) for their orientation dependence. It is interesting to note that $\text{Cube}_{\text{SF}} > \text{Cu}_{\text{SF}} > \text{B}_{\text{SF}}$. Of course the Schmid factors are essential for single-crystal DDD simulations. In a poly-crystal environment, on the other hand, Taylor factors (M) need to be considered [1, 65, 86], where $\text{Cube}_{\text{M}} < \text{Cu}_{\text{M}} < \text{B}_{\text{M}}$ [86]. Classical DDD simulations are restricted [73, 77, 79, 80, 83, 85, 87-92] to single-crystals and present

simulations were 2-dimensional in nature. It will be interesting to explore how the present simulation results evolve in a stipulated poly-crystalline 3-dimensional environment. But a practical 3-dimensional DDD simulation (3-d DDD in a poly-crystalline environment with significant strains) remains unattainable at the present state of scientific and technological capabilities.

The stated limitations, however, do not dilute the present results. These results are novel, consistent and reproducible. In the macro-scale (figure 3.4), a scaling of σ_{11} with ρ_{GND} was shown. However, this was absent in the micro-scale (figures 3.5, 3.6, 3.11). There were two reasons. Firstly, there were “elastic and negligibly plastically deforming grains” and “elasto-plastically deforming grains”. Developments in σ_{11} (with ρ_{GND}) were naturally different between these two different classes of grains. Secondly, even for the “elasto-plastically deforming grains” the evolution of σ_{11} and ρ_{GND} was orientation dependent. Considering many orientations (figure 3.8) naturally gave a large scatter. Selecting three distinct, albeit near ideal, orientations offered a clear trend (see figure 3.11): orientation dependent evolution of σ_{11} and ρ_{GND} . The experiments and simulation showed a clear similarity (though DDD simulations were restricted to small strain values). They also conveyed the fact that residual stress evolved from the arrangements of geometrically necessary dislocations, an intuitive but interesting result.

3.5 Conclusions

This study started with an experimental report on the development of residual stress and microtexture in an aluminum alloy (AA3003). These were measured at different stages of interrupted tensile tests. Bulk residual stress showed a clear scaling with microtexture estimated density of geometrically necessary dislocation (ρ_{GND}). However, single-crystal residual stress did not show any such correlation. Experimental data showed two different sets of grains: “elastic and negligibly plastically deforming grains” and “elasto-plastically deforming grains”. The residual stress (σ_{11}) developments in the former did depend on the elastic constraints and incompatibilities, as simulated with an appropriate finite element tool (object oriented finite element simulation or OOF2 software).

The “elasto-plastically deforming grains” also presented a large scatter in the experiment data of σ_{11} versus ρ_{GND} . Selecting appropriate crystal orientations, and corresponding discrete dislocation dynamics (DDD) simulations, established clear trends in orientation dependent evolution of σ_{11} and ρ_{GND} . Experimental results and DDD simulations (which were at much lower strains) showed similar patterns. They also established the single-crystal residual stress evolved from the developments in dislocation substructure.

Appendix:

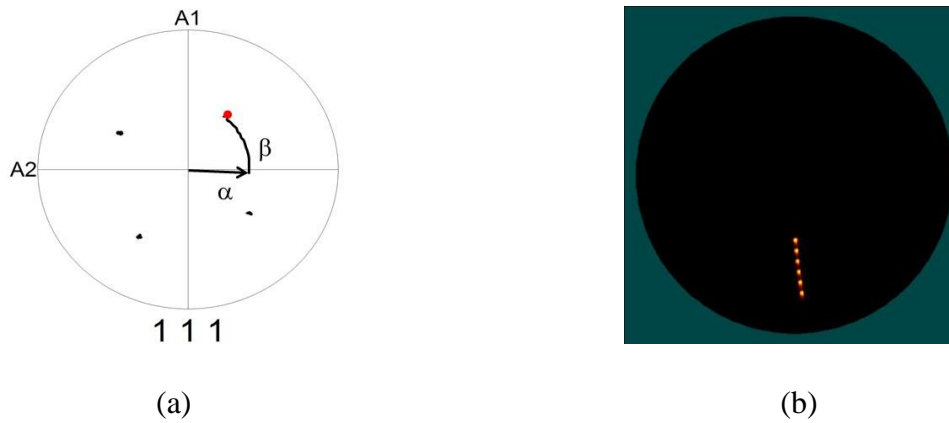


Figure 3.A12: (a) shows a typical (111) EBSD pole figure of a single-grain. (b) Laue diffraction spots at different goniometer tilt and rotation. The spot with highest intensity (as in figure 3.1c) was used for further processing

A single crystal x-ray diffraction captured by an area detector at different tilt (ψ) - rotation (φ) condition of goniometer is shown in figure 3.A1(a). The coordinates of the signal is in $\gamma - 2\theta$. For any particular combination of ($\psi, \varphi, \gamma, \theta, \omega$), the diffraction spot can be converted to the pole figure angles (α, β) as following [93]

$$\alpha = \sin^{-1}|h_3| = \cos^{-1} \sqrt{h_1^2 + h_2^2}$$

$$\beta = \pm \cos^{-1} \frac{h_1}{\sqrt{h_1^2 + h_2^2}} \quad \begin{array}{l} \beta \geq 0^\circ \text{ if } h_2 \geq 0 \\ \beta \geq 0^\circ \text{ if } h_2 < 0 \end{array} \quad \text{----- (3.a1)}$$

where h_1 , h_2 and h_3 are the unit vector components along the sample coordinates and can be deduced as

$$h_1 = \sin \theta (\sin \varphi \sin \psi \sin \omega + \cos \varphi \cos \omega) + \cos \theta \sin \varphi \cos \psi \cos \gamma \\ - \cos \theta \sin \gamma (\sin \varphi \sin \psi \cos \omega - \cos \varphi \sin \omega) \quad \text{----- (3.a2)}$$

$$h_2 = -\sin \theta (\cos \varphi \sin \psi \sin \omega - \sin \varphi \cos \omega) - \cos \theta \cos \varphi \cos \psi \cos \gamma \\ - \cos \theta \sin \gamma (\sin \varphi \sin \psi \cos \omega - \cos \varphi \sin \omega) \quad \text{----- (3.a3)}$$

$$h_3 = \sin \theta \cos \psi \sin \omega - \cos \theta \cos \omega \cos \psi \sin \gamma - \cos \theta \cos \gamma \sin \psi \quad \text{----- (3.a4)}$$

References

1. Verlinden, B., et al., *Thermo-mechanical processing of metallic materials*. Vol. 11. 2007: Elsevier.
2. Staker, M. and D. Holt, *The dislocation cell size and dislocation density in copper deformed at temperatures between 25 and 700 C*. *Acta Metallurgica*, 1972. **20**(4): p. 569-579.
3. Kubin, L.P., *Dislocation patterning*. *Materials science and technology*, 1993. **6**: p. 137-190.
4. Kubin, L., C. Fressengeas, and G. Ananthakrishna, *Collective behaviour of dislocations in plasticity*. *Dislocations in solids*, 2002. **11**: p. 101-192.
5. Brechet, Y. and C. Hutchinson, *Defect-induced dynamic pattern formation in metals and alloys*. *Solid State Physics*, 2006. **60**: p. 181-287.
6. Humphreys, F.J. and M. Hatherly, *Recrystallization and related annealing phenomena*. 1995: Elsevier.
7. Hansen, N., X. Huang, and D.A. Hughes, *Microstructural evolution and hardening parameters*. *Materials Science and Engineering: A*, 2001. **317**(1): p. 3-11.
8. Hughes, D.A., *Microstructure evolution, slip patterns and flow stress*. *Materials Science and Engineering: A*, 2001. **319-321**: p. 46-54.

9. Ashby, M., *The deformation of plastically non-homogeneous materials*. Philosophical Magazine, 1970. **21**(170): p. 399-424.
10. Dieter, G.E. and D.J. Bacon, *Mechanical metallurgy*. Vol. 3. 1986: McGraw-Hill New York.
11. Cullity, B., *Elements of X-ray Diffraction, 2nd*. Adisson-Wesley Publis hing. USA, 1978.
12. Hauk, V., *Structural and residual stress analysis by nondestructive methods: Evaluation-Application-Assessment*. 1997: Elsevier.
13. Noyan, I.C. and J.B. Cohen, *Residual stress: measurement by diffraction and interpretation*. 2013: Springer-Verlag.
14. James, M., et al., *Residual stresses and fatigue performance*. Engineering Failure Analysis, 2007. **14**(2): p. 384-395.
15. Lienert, U., et al., *In situ single-grain peak profile measurements on Ti-7Al during tensile deformation*. Materials Science and Engineering: A, 2009. **524**(1): p. 46-54.
16. Lienert, U., et al., *Investigating the effect of grain interaction during plastic deformation of copper*. Acta materialia, 2004. **52**(15): p. 4461-4467.
17. Margulies, L., et al., *Strain tensor development in a single grain in the bulk of a polycrystal under loading*. Acta Materialia, 2002. **50**(7): p. 1771-1779.
18. Miller, M., et al., *Measuring and modeling distributions of stress state in deforming polycrystals*. Acta materialia, 2008. **56**(15): p. 3927-3939.
19. Montross, C.S., et al., *Laser shock processing and its effects on microstructure and properties of metal alloys: a review*. International Journal of Fatigue, 2002. **24**(10): p. 1021-1036.
20. Mughrabi, H., *Dislocation wall and cell structures and long-range internal stresses in deformed metal crystals*. Acta metallurgica, 1983. **31**(9): p. 1367-1379.
21. Nakamura, T. and S. Suresh, *Effects of thermal residual stresses and fiber packing on deformation of metal-matrix composites*. Acta Metallurgica et Materialia, 1993. **41**(6): p. 1665-1681.
22. Oddershede, J., et al., *Grain-resolved elastic strains in deformed copper measured by three-dimensional X-ray diffraction*. Materials characterization, 2011. **62**(7): p. 651-660.

23. Oddershede, J., et al., *Determining grain resolved stresses in polycrystalline materials using three-dimensional X-ray diffraction*. Journal of Applied Crystallography, 2010. **43**(3): p. 539-549.
24. Oettel, H. and R. Wiedemann, *Residual stresses in PVD hard coatings*. Surface and coatings technology, 1995. **76**: p. 265-273.
25. Peyre, P., et al., *Laser shock processing of aluminium alloys. Application to high cycle fatigue behaviour*. Materials Science and Engineering: A, 1996. **210**(1–2): p. 102-113.
26. Shekhawat, S., et al., *Orientation-dependent plastic deformation in transformer steel: Experiments and dislocation dynamics simulations*. Acta Materialia, 2015. **84**: p. 256-264.
27. Turner, P. and C. Tomé, *A study of residual stresses in Zircaloy-2 with rod texture*. Acta Metallurgica et Materialia, 1994. **42**(12): p. 4143-4153.
28. Ungar, T., et al., *X-ray line-broadening study of the dislocation cell structure in deformed [001]-orientated copper single crystals*. Acta Metallurgica, 1984. **32**(3): p. 333-342.
29. Van Boven, G., W. Chen, and R. Rogge, *The role of residual stress in neutral pH stress corrosion cracking of pipeline steels. Part I: Pitting and cracking occurrence*. Acta Materialia, 2007. **55**(1): p. 29-42.
30. Wang, Y.-D., et al., *The development of grain-orientation-dependent residual stresses in a cyclically deformed alloy*. Nature Materials, 2003. **2**(2): p. 101-106.
31. Webster, G.A. and A.N. Ezeilo, *Residual stress distributions and their influence on fatigue lifetimes*. International Journal of Fatigue, 2001. **23**, **Supplement 1**: p. 375-383.
32. Wiklund, U., J. Gunnars, and S. Hogmark, *Influence of residual stresses on fracture and delamination of thin hard coatings*. Wear, 1999. **232**(2): p. 262-269.
33. Crostack, H.-A. and W. Reimers. *Residual stress profile from grain to grain in a welding zone*. in *International Conference on Residual Stresses*. 1989. Springer.
34. Dupke, R. and W. Reimers, *X-ray diffraction investigations on individual grains in the polycrystalline Ni-base superalloy IN 939 during cyclic loading. Pt. 2. Residual stresses*. Zeitschrift für Metallkunde, 1995. **86**(10): p. 665-670.
35. Reimers, W., et al., *Investigations of large grained samples—examples*, in *Measurement of residual and applied stress using neutron diffraction*. 1992, Springer. p. 263-276.

36. Martins, R.V., et al., *Simultaneous measurement of the strain tensor of 10 individual grains embedded in an Al tensile sample*. *Materials Science and Engineering: A*, 2004. **387**: p. 84-88.
37. Wang, Y.D., R.L. Peng, and R.L. McGreevy, *A novel method for constructing the mean field of grain-orientation-dependent residual stress*. *Philosophical Magazine Letters*, 2001. **81**(3): p. 153-163.
38. Mughrabi, H., *Dislocation clustering and long-range internal stresses in monotonically and cyclically deformed metal crystals*. *Revue de physique appliquée*, 1988. **23**(4): p. 367-379.
39. Estrin, Y., et al., *A dislocation-based model for all hardening stages in large strain deformation*. *Acta materialia*, 1998. **46**(15): p. 5509-5522.
40. Levine, L.E., et al., *X-ray microbeam measurements of individual dislocation cell elastic strains in deformed single-crystal copper*. *Nature materials*, 2006. **5**(8): p. 619-622.
41. Biermann, H., et al., *Local variations of lattice parameter and long-range internal stresses during cyclic deformation of polycrystalline copper*. *Acta metallurgica et materialia*, 1993. **41**(9): p. 2743-2753.
42. Corvasce, F., P. Lipinski, and M. Berveiller. *Intergranular residual stresses in plastically deformed polycrystals*. in *International Conference on Residual Stresses*. 1989. Springer.
43. Clausen, B., T. Lorentzen, and T. Leffers, *Self-consistent modelling of the plastic deformation of fcc polycrystals and its implications for diffraction measurements of internal stresses*. *Acta Materialia*, 1998. **46**(9): p. 3087-3098.
44. Brewer, L.N., D.P. Field, and C.C. Merriman, *Mapping and Assessing Plastic Deformation Using EBSD*, in *Electron Backscatter Diffraction in Materials Science*, J.A. Schwartz, et al., Editors. 2009, Springer US: Boston, MA. p. 251-262.
45. Kamaya, M., A.J. Wilkinson, and J.M. Titchmarsh, *Measurement of plastic strain of polycrystalline material by electron backscatter diffraction*. *Nuclear engineering and design*, 2005. **235**(6): p. 713-725.
46. Wilkinson, A. and D. Dingley, *Quantitative deformation studies using electron back scatter patterns*. *Acta metallurgica et materialia*, 1991. **39**(12): p. 3047-3055.
47. Jiang, J., T.B. Britton, and A.J. Wilkinson, *Mapping type III intragranular residual stress distributions in deformed copper polycrystals*. *Acta Materialia*, 2013. **61**(15): p. 5895-5904.

48. Jiang, J., T.B. Britton, and A.J. Wilkinson, *Evolution of intragranular stresses and dislocation densities during cyclic deformation of polycrystalline copper*. *Acta Materialia*, 2015. **94**: p. 193-204.
49. Jiang, J., T.B. Britton, and A.J. Wilkinson, *The orientation and strain dependence of dislocation structure evolution in monotonically deformed polycrystalline copper*. *International Journal of Plasticity*, 2015. **69**: p. 102-117.
50. Dupke, R. and W. Reimers, *X-ray diffraction investigations on individual grains in the polycrystalline Ni-base superalloy IN 939 during cyclic loading II: residual stresses*. *Zeitschrift für Metallkunde*, 1995. **86**(10): p. 665-670.
51. Welzel, U., et al., *Stress analysis of polycrystalline thin films and surface regions by X-ray diffraction*. *Journal of Applied Crystallography*, 2005. **38**(1): p. 1-29.
52. Kohli, D., et al., *Fabrication of simulated plate fuel elements: Defining role of stress relief annealing*. *Journal of Nuclear Materials*, 2014. **447**(1-3): p. 150-159.
53. Peng, J., et al., *Residual stress gradient analysis by the GIXRD method on CVD tantalum thin films*. *Surface and Coatings Technology*, 2006. **200**(8): p. 2738-2743.
54. Dieter, G.E. and D. Bacon, *Mechanical metallurgy*. Vol. 3. 1986: McGraw-Hill New York.
55. Wright, S.I., M.M. Nowell, and D.P. Field, *A review of strain analysis using electron backscatter diffraction*. *Microscopy and microanalysis*, 2011. **17**(03): p. 316-329.
56. Nye, J., *Some geometrical relations in dislocated crystals*. *Acta metallurgica*, 1953. **1**(2): p. 153-162.
57. Field, D., et al., *Analysis of local orientation gradients in deformed single crystals*. *Ultramicroscopy*, 2005. **103**(1): p. 33-39.
58. Kocks, U. and H. Mecking, *Physics and phenomenology of strain hardening: the FCC case*. *Progress in materials science*, 2003. **48**(3): p. 171-273.
59. Shekhawat, S., et al., *Direct Experimental Observations on Concurrent Microstructure and Magnetic Property Developments in Non-Grain Oriented Electrical Steel*. *Metallurgical and Materials Transactions A*, 2014. **45**(9): p. 3695-3698.
60. Keskar, N., et al., *Quantifying the mesoscopic shear strains in plane strain compressed polycrystalline zirconium*. *Acta Materialia*, 2014. **69**: p. 265-274.
61. Reid, A.C., et al., *Modelling microstructures with OOF2*. *International Journal of Materials and Product Technology*, 2009. **35**(3-4): p. 361-373.

62. Rajmohan, N., et al., *Neutron diffraction method for stored energy measurement in interstitial free steel*. Acta Materialia, 1997. **45**(6): p. 2485-2494.
63. Kallend, J. and Y. Huang, *Orientation dependence of stored energy of cold work in 50% cold rolled copper*. Metal science, 1984. **18**(7): p. 381-386.
64. Hirsch, J. and K. Lücke, *Overview no. 76*. Acta Metallurgica, 1988. **36**(11): p. 2863-2882.
65. Albou, A., et al., *Direct correlation of deformation microstructures and cube recrystallization nucleation in aluminium*. Scripta Materialia, 2010. **62**(7): p. 469-472.
66. Doherty, R., et al., *Current issues in recrystallization: a review*. Materials Science and Engineering: A, 1997. **238**(2): p. 219-274.
67. Doherty, R.D., *Recrystallization and texture*. Progress in Materials Science, 1997. **42**(1-4): p. 39-58.
68. Duggan, B., et al., *On the origin of cube texture in copper*. Acta metallurgica et materialia, 1993. **41**(6): p. 1921-1927.
69. Jensen, D.J., *Growth of nuclei with different crystallographic orientations during recrystallization*. Scripta metallurgica et materialia, 1992. **27**(5): p. 533-538.
70. Ridha, A. and W. Hutchinson, *Recrystallisation mechanisms and the origin of cube texture in copper*. Acta metallurgica, 1982. **30**(10): p. 1929-1939.
71. Samajdar, I. and R. Doherty, *Cube recrystallization texture in warm deformed aluminum: understanding and prediction*. Acta materialia, 1998. **46**(9): p. 3145-3158.
72. Vatne, H., R. Shahani, and E. Nes, *Deformation of cube-oriented grains and formation of recrystallized cube grains in a hot deformed commercial AlMgMn aluminium alloy*. Acta materialia, 1996. **44**(11): p. 4447-4462.
73. Guruprasad, P. and A. Benzerga, *Size effects under homogeneous deformation of single crystals: a discrete dislocation analysis*. Journal of the Mechanics and Physics of Solids, 2008. **56**(1): p. 132-156.
74. Lee, M., et al., *A dislocation density-based single crystal constitutive equation*. International Journal of Plasticity, 2010. **26**(7): p. 925-938.
75. Kumar, M.A. and S. Mahesh, *Banding in single crystals during plastic deformation*. International Journal of Plasticity, 2012. **36**: p. 15-33.
76. Roters, F., D. Raabe, and G. Gottstein, *Calculation of stress—strain curves by using 2 dimensional dislocation dynamics*. Computational materials science, 1996. **7**(1): p. 56-62.

77. Guruprasad, P., W. Carter, and A. Benzerga, *A discrete dislocation analysis of the Bauschinger effect in microcrystals*. *Acta Materialia*, 2008. **56**(19): p. 5477-5491.
78. Wang, Z. and I. Beyerlein, *An atomistically-informed dislocation dynamics model for the plastic anisotropy and tension–compression asymmetry of BCC metals*. *International Journal of Plasticity*, 2011. **27**(10): p. 1471-1484.
79. Van der Giessen, E. and A. Needleman, *Discrete dislocation plasticity: a simple planar model*. *Modelling and Simulation in Materials Science and Engineering*, 1995. **3**(5): p. 689.
80. Kubin, L.P., et al. *Dislocation microstructures and plastic flow: a 3D simulation*. in *Solid State Phenomena*. 1992. Trans Tech Publ.
81. Zbib, H.M., M. Rhee, and J.P. Hirth, *On plastic deformation and the dynamics of 3D dislocations*. *International Journal of Mechanical Sciences*, 1998. **40**(2): p. 113-127.
82. Arsenlis, A., et al., *Enabling strain hardening simulations with dislocation dynamics*. *Modelling and Simulation in Materials Science and Engineering*, 2007. **15**(6): p. 553.
83. Benzerga, A., et al., *Incorporating three-dimensional mechanisms into two-dimensional dislocation dynamics*. *Modelling and Simulation in Materials Science and Engineering*, 2003. **12**(1): p. 159.
84. Cleveringa, H., E.V. Giessen, and A. Needleman, *A discrete dislocation analysis of residual stresses in a composite material*. *Philosophical Magazine A*, 1999. **79**(4): p. 893-920.
85. Guruprasad, P.J. and A.A. Benzerga, *A phenomenological model of size-dependent hardening in crystal plasticity*. *Philosophical Magazine*, 2008. **88**(30-32): p. 3585-3601.
86. Samajdar, I. and R.D. Doherty, *Role of $S [(123) \langle 634 \rangle]$ orientations in the preferred nucleation of cube grains in recrystallization of FCC metals*. *Scripta metallurgica et materialia*, 1995. **32**(6): p. 845-850.
87. Cleveringa, H., E. Van Der Giessen, and A. Needleman, *Comparison of discrete dislocation and continuum plasticity predictions for a composite material*. *Acta Materialia*, 1997. **45**(8): p. 3163-3179.
88. Cleveringa, H., E. Van der Giessen, and A. Needleman, *A discrete dislocation analysis of bending*. *International Journal of Plasticity*, 1999. **15**(8): p. 837-868.
89. Cleveringa, H., E. Van der Giessen, and A. Needleman, *A discrete dislocation analysis of mode I crack growth*. *Journal of the Mechanics and Physics of Solids*, 2000. **48**(6-7): p. 1133-1157.

90. Kubin, L. and G. Canova, *The modelling of dislocation patterns*. Scripta metallurgica et materialia, 1992. **27**(8): p. 957-962.
91. Zbib, H.M., et al., *3D dislocation dynamics: stress–strain behavior and hardening mechanisms in fcc and bcc metals*. Journal of Nuclear Materials, 2000. **276**(1-3): p. 154-165.
92. Zbib, H.M., M. Rhee, and J.P. Hirth, *On plastic deformation and the dynamics of 3D dislocations*. International Journal of Mechanical Sciences, 1998. **40**(2-3): p. 113-127.
93. He, B.B., *Two-dimensional X-ray diffraction*. 2011: John Wiley & Sons.

Chapter 4

Microstructural Origin of Residual Stress relief in Aluminum

4.1 Introduction

Deformed aluminum typically shows [1-7] a hierarchy of dislocation substructures: from deformation bands and strain localizations to cell blocks and dislocation cells. Such substructure is also expected [8-12] to be associated with evolution of residual stresses. Post deformation annealing often modifies the substructure [3, 5, 13-20] and enables residual stress relief [21-23]. This is the so-called thermal stress relief: a subject of both applied and academic interest. However, correlating substructure evolution with residual stress relief is a tedious experimental task that has rarely been attempted. Furthermore, the physics underlying any such correlations cannot be fully revealed on the sole basis of experiments. The present study thus sets out to address possible correlations by combining experimental measurements with discrete dislocation dynamics (DDD) simulations. The DDD simulations are expected to account for key processes believed to drive microstructure evolution during annealing.

The residual stress can be viewed both mechanistically and from an atomistic perspective [5, 24], the latter being more appropriate to the present work. This happens as the stress-free equilibrium lattice spacing (d_0) is changed to a non-equilibrium value, and constraints allow retention (fully or in part) of such non-equilibrium value after the external stresses are removed. Naturally, the constraints are important to the subsequent stress relief. In a deformed material, the dislocation substructures may provide such constraints [5]. Annealing, on the other hand, modifies the dislocation substructures and thus enables a stress relief.

In general, annealing involves both recovery and partial recrystallization. Recovery is driven by the stored energy of cold work [25] and does not involve movement of high angle grain boundaries [3, 18]. The actual mechanisms include low temperature point defect annihilation to relatively higher temperature sub-boundary movement and coalescence [3, 5]. Recrystallization, on the other hand, incorporates movement of high angle boundaries [3, 5]. Any large, and strain-free, sub-grain is potential recrystallized nuclei. It becomes active in presence of growth favorable boundary.

Movement of such growth favorable boundaries, or the growth of a recrystallized grain, may not eliminate all dislocations in the substructure, but may remove the misorientation [5].

Several authors [10, 11, 13] related internal stresses (and possible stress relief) with changes in dislocation substructures. Examples can be drawn from the work of Hasegawa and Kocks [26] or from Borbèly et al. [27]. The latter argued that long range internal stresses were caused by a mismatch between soft cell interior and hard cell walls – the composite model for residual stresses based on geometrically necessary and incidental dislocation boundaries [10]. The state of residual stress may be determined by the total dislocation density [14] and/or by the dislocation substructure [10]. On one hand, *mechanical* stress relief has been related [12, 28] to the elimination of pre-existing low angle boundaries and associated lattice curvatures. On the other hand, the effectiveness of *thermal* stress relief in recovery and recrystallization remains unclear. Wierzbanski et al. [29] had shown accelerated stress relief at the beginning of recrystallization. By way of contrast, Kumar et al. [30] indicated that recovery enabled the most significant part of the thermal stress relief. Another recent work by Kohli et al. [21] on simulated fabrication of plate-fuel (with aluminum clad) showed fastest recovery kinetics at some intermediate annealing temperature. Elimination of strain localizations appeared to be more effective for residual stress relief than near complete recrystallization. The findings in [21] were for a specific material system and further motivate the work undertaken in this study in the context of a broader family of alloys.

Thus, residual stress relief, eventually of thermal origin, should be associated with rearrangement of dislocation substructures. Furthermore, recovery and its associated stress relief have been hypothesized to be orientation sensitive, as reported in the classical work of Ridha and Hutchinson [31]. Experimental observation, on the higher recovery in deformed Cube $\{100\}\langle 001\rangle$, was justified in terms of dislocation interactions: the possibility that edge dislocations with orthogonal Burgers vectors, in deformed Cube, do not interact and hence result in stronger recovery.

Monte Carlo simulations have been used effectively in the past [32-35] to capture various aspects of microstructural evolution during recovery. However, such simulations cannot directly provide the state of residual stresses. On the other hand, methods of discrete dislocation dynamics (DDD) have been developed over the past few decades with increasing levels of refinement [36-45]. These methods, which may be viewed as coarse-grained molecular dynamics of plasticity [46], have enabled simulations providing key insights into a variety of plasticity phenomena in strain

hardening [45, 47, 48], energy storage [49], thermal stresses in thin films [50], indentation [51], and size effects [52-56]. An important recent development in DDD has consisted of incorporating dislocation climb following various paradigms [57-60]. While the basic formulation is three-dimensional [44] few implementations have been attempted in 3D using various approximations [61, 62]. Although still in their infancy, such developments have demonstrated the predictive character of the framework in analyzing creep as emergent behavior [58], in particular in geophysics [63, 64], as well as stress relief in thin films [57] and composites [65].

Here, deformed (50% cold rolled) commercial purity aluminum (AA1050) was subjected to laboratory annealing at 473, 523 and 573 K. The annealing involved mostly recovery, but also partial (fraction recrystallized ~ 0.29) recrystallization. The residual stress relief and substructure evolution were measured from these specimens: the so-called indirect measurements. This was later followed by direct measurements, involving micro-Laue diffraction [12] and site-specific electron diffraction [21]. DDD simulations were then carried out to gain insight into the microstructural origins of stress relief. The simulations were carried out using the framework of high-temperature discrete dislocation plasticity [44]. Within this framework, the effects of temperature and orientation dependence of stress relief were also investigated.

4.2 Experimental Methods

This study involved fully recrystallized commercial purity aluminum (AA1050), chemical composition being listed in Table 4.1. The material was cold rolled to 50% thickness reduction in a laboratory rolling mill. The rolled specimens, from the mid-width and mid thickness sections, were then annealed in a laboratory muffle furnace at 473, 523 and 573 K (and for 15 and 30 minutes). These constituted the test matrix of the specimens.

Table 4.1: Chemical composition, in wt% alloying elements, of the AA1050 used in this study.

Alloy	Si	Cu	Fe	Mg	Mn	Al
AA1050	0.25	0.05	0.40	0.05	0.05	balance

Samples were prepared by standard metallography plus electro polishing. The latter involved an electrolyte of 80:20 methanol and perchloric acid, 13 volts dc and 253 K temperature. To define the annealing induced softening, at least 10 Vickers hardness (with 300 gm load) were taken in each specimen. A Bruker™ D8 Discover system, with Vantec-500™ area detector, was used for the measurements of stress and dislocation density ODFs (orientation distribution function). The procedure of measurement, plus analysis, is explained in the appendix. The same unit was also used for micro-Laue diffraction or measurements of single crystal residual stress matrix. Chapter 3, section 3.2 described the methodology involved. Bulk residual stresses, both normal and shear stress components, were also measured with multiple {hkl} GIXRD (grazing incident X-ray diffraction) in a PANalytical™ MRD system. For details on this technique, it can be found elsewhere [12, 21, 66-68]. Appropriate convention was followed for residual stress components where σ_{ij} ($i, j = 1, 2, 3$) denotes stress components.

Microstructural characterization was done using FEI™ Quanta-3D FEG (field emission gun) SEM (scanning electron microscope) equipped with TSL-EDX™ electron backscattered diffraction (EBSD) system. All EBSD scans used identical step size (0.1 μ m) and beam/video conditions. As the annealing involved partial recrystallization, a combined criterion of grain size plus in-grain misorientation was used to identify the recrystallized grains. More specifically, and as described elsewhere [69-71], recrystallized grain were considered to be above 3 μ m in size and below 0.75° grain orientation spread (GOS). For representation of the EBSD images, standard inverse pole figure (IPF) [72] combined with the image quality (IQ) maps were used. IQ represents the number of detected Kikuchi bands [72], and has been used in the past [73] to effectively represent substructural evolution. EBSD data were further analyzed for GND (geometrical necessary dislocation) density, boundary density, GOS and GAM (grain average misorientation). For GND density measurement, methodology can be found in [12, 74]. Grain boundaries, with different misorientation angles, were measured per unit area: and these constituted the boundary density plots. It is to be noted that 0-1° boundaries were neglected as measurement uncertainty. A grain was defined by the continuous presence of >5° boundary. Average point-to-point misorientation of such grain represented GAM. GOS, on the other hand, is based on an average (quaternion average) grain orientation, and average misorientation of other measurement points (inside that grain) with respect to the aforementioned average orientation. Formulations for GAM and GOS, as used in this study, are given in eq. (4.1) and (4.2) respectively.

$$GAM = \frac{1}{N} \frac{1}{n} \sum_{j=1}^N \sum_{i=1}^n (g_i g_j^{-1}) \quad \text{-----(4.1)}$$

$$GOS = \frac{1}{N} \sum_{i=1}^N (g_{av} g_i^{-1}) \quad \text{-----(4.2)}$$

where a grain orientation contains N data points with g_i and g_j representing orientations of two consecutive points i and j. g_{av} is the quaternion average of grain orientation for all data points and ‘n’ denotes total number of nearest neighbor data points in a grain.

The sub-grain size (or dislocation cell size) was also measured using an image analysis method. It is based on the EBSD misorientation and image quality maps as developed by Barou et al. [73]. The method first traced the sub grain boundaries after application of a convolution filter to the image quality maps. The linear intercept method [75] was then used to estimate the sub-grain sizes.

4.3 Simulations

Two-dimensional (2D) discrete dislocation dynamics (DDD) simulations were performed to uncover the underlying mechanisms of recovery and associated stress relief. More specifically, focus was laid on single crystals so as to explore the contribution of dislocation glide and climb processes to the stress relief during annealing. The simulations were carried out in two steps. The first step involved deforming a crystal, of a given crystallographic orientation, to a predefined compressive strain at a low homologous temperature ($T/T_m \ll 1/3$). This step mimicked the cold rolling operation in the experiments and generated dislocation-populated microstructure(s). The second step consisted of an annealing simulation, where the pre-deformed specimen was subjected to a “heat treatment” at some temperature $T/T_m > 1/3$ and no external stress.

The “cold deformation” simulations were carried out using the so-called 2.5D framework: first developed in [45] and later enhanced by Guruprasad and coworkers [52, 53, 62]. Initially homogeneous and elastically isotropic single crystalline specimens, oriented for double slip, were subjected to compressive loading along the x_1 -axis. The rectangular specimens had dimensions 30 x 20 microns. The slip systems were specified at an angle $\pm \psi_0$ to the loading x_1 -axis. Three crystal orientations (as described later) were considered. In the 2.5D model this was achieved

approximately by varying the angle ψ_0 , which was related to the Schmid factor of the respective orientations.

All simulations were carried out by deforming the specimen under displacement-controlled loading along a boundary at a nominal strain rate of 10^3 s^{-1} . Lateral surfaces were traction free. In the model, dislocation pairs of opposite signs were used to represent dislocation loops, which were restricted to glide in their slip planes. Line tension effects were modeled as in [45]. Material parameters of Aluminum were used with shear modulus $\mu = 26 \text{ GPa}$, Burgers vector $b = 0.25 \text{ nm}$ and Poisson's ratio $\nu = 0.3$. The specimen was initially assumed to be dislocation free with a randomly distributed source density ($\rho_0 = 10^{12} \text{ m}^{-2}$). When active, each point source emitted a pair of opposite signed dislocations and thus mimicked a Frank-Read process. The value of the critical stress represented the strength of the source ($\tau_{nuc} = 15 \text{ MPa}$ for Goss $\{110\}\langle 001 \rangle$ orientation, $\tau_{nuc} = 17 \text{ MPa}$ for Brass $\{110\}\langle \bar{1}12 \rangle$ orientation and $\tau_{nuc} = 19 \text{ MPa}$ for S $\{123\}\langle 63\bar{4} \rangle$ orientation), with a standard deviation of 0.5 MPa for all. In order for the source to emit a fresh dipole, the Peach-Koehler force at the location of the source had to exceed a nucleation threshold, $\tau_{nuc} b$, and stay above the critical value for a sufficient amount of time ($t_{nuc} = 10 \text{ ns}$), termed as nucleation time. A mobile dislocation might encounter obstacles, for instance precipitates or dislocation junctions. Static obstacles, such as precipitates, were represented by point obstacles. These obstacles acted as pinning points up to a certain value of stress, beyond which the dislocations broke free. An obstacle density, of about $\rho_{obs} = 10^{12} \text{ m}^{-2}$, and a constant obstacle strength, $\tau_{obs} = 150 \text{ MPa}$, were used.

The formulation was based on a linear elastic approximation. The superposition principle was used to calculate the long-range stress fields in the finite-size specimens. The dislocations glide, under the influence of the Peach-Koehler force (f_g^i), did arise due to the state of stress at the position of the dislocation. Glide velocity (v_g^i) of a dislocation i was calculated based on a mobility law given as follows:

$$Bv_g^i = f_g^i + \mathcal{L}^i b^i \quad \text{-----}(4.3)$$

where B is the drag factor (a value of $1.0 \times 10^{-5} \text{ Pa}\cdot\text{s}$ was used at room temperature and assumed to vary linearly with temperature [76]), \mathcal{L}^i is the line tension, and b^i is the Burgers vector of the dislocation. Since the nonlinear effects were not considered in a linear elastic approximation, they were accounted through a set of rules describing the short-range dislocation interactions. These

included the rules for dislocation mobility as given above, annihilation at a critical distance, etc. Further, short range interactions such as junction formation, acting either as dynamic obstacles or as sources, were also accounted for in terms of constitutive rules. The deformation was simulated by integrating the equations of motion for a time (t), required for achieving a particular amount of strain using a fine time step ($dt = 0.5$ ns), which represented typical time scale for dislocation glide. Further details can be found elsewhere [12]. The stress-strain responses (forward and unloading), obtained from this first step, were reported in Ref. [12]. All specimens were compressed to 2% strain. Specimen sizes were large enough to avoid size effect [52, 53, 62] and limited plastic activity upon unloading [12].

The “annealing” simulations were carried out using a recently developed framework of high-temperature discrete dislocation plasticity [44, 58]. Unloaded specimens, from step 1, were taken as the initial state. In step 2, the compressive force in the x_1 -direction was held fixed at zero, and a spatially uniform value of the homologous temperature ($T/T_m > 1/3$) was prescribed. In addition to the dislocations from step 1, the specimen was assumed to contain a distribution of vacancies modeled using a continuous concentration field $c(\mathbf{x}, t)$, dependent on the spatial position \mathbf{x} and time t . The driving forces for dislocation motion at elevated temperatures were obtained from the gradients of the Gibbs free energy functional, considered to depend on the vacancy field as well as the elastic stored energy of the dislocations. The configurational force on a dislocation i was,

$$\mathbf{f}^i = -\frac{\partial G}{\partial \mathbf{x}^i}, \quad G = G(c(\mathbf{x}, t), \mathbf{x}^i(t)) \quad \text{-----}(4.4)$$

where \mathbf{x}^i denotes the position vector of dislocation i . Accurate evaluation of the field $c(\mathbf{x}, t)$ is prohibitively expensive computationally. This is due to the presence of strong gradients at the scale of the dislocation cores, which act as sources/sinks for vacancies during climb. Therefore, the field $c(\mathbf{x}, t)$ was interpreted as a coarse-grained quantity defined as the spatial average of the actual vacancy field over a meso-scale volume element containing many dislocations. The evolution of c was obtained by solving the modified continuity equation,

$$\dot{c} = -\nabla \cdot \mathbf{j} + \dot{c}_{src} \quad \text{-----}(4.5)$$

where \mathbf{j} denotes the volumetric flux of vacancies arising from the gradients in the chemical potential of vacancies, μ_v , according to the diffusive law,

$$\mathbf{j} = -\bar{D}\nabla\mu_v, \quad \bar{D} = \frac{D\Omega c(1-c)}{kT} \quad \text{-----(4.6)}$$

In the above equation, D is the vacancy diffusion coefficient, Ω is the atomic volume and k is the Boltzmann constant. The source term \dot{c}_{src} , in eq. (4.5), denotes the contribution to the coarse-grained vacancy field c due to climb of all dislocations within a meso-scale volume element. Detailed expressions for \dot{c}_{src} , the chemical potential μ_v and the Gibbs free energy functional G in terms of the stresses, dislocation positions and the vacancy field c can be found in [44]. Eqs. (4.5)-(4.6) were linearized assuming $c \ll 1$ and solved using the finite element method and an implicit ODE solver to determine the evolution of the vacancy field in the specimen. Boundary conditions for the above problem corresponded to vanishing chemical potential for the vacancies on all boundaries, consistent with the traction-free conditions in the annealing simulations.

The configurational force \mathbf{f}^i on dislocation i , computed using (4), in general, had components along the glide and the climb directions (see [44]). However, the glide mobilities of the dislocations were, in general, much higher than their climb mobilities. Hence, it was computationally challenging to resolve unit events at the fast time scale of glide while performing the simulations for sufficient time to allow appreciable climb and recovery to take place. This was achieved by using an adaptive time stepping procedure. Glide simulations were performed using a sufficiently small value of the time step until the dislocation microstructure evolved to a quasi-equilibrium state as defined by the strain rate remaining zero within a specified tolerance over a fixed interval of time. When this condition was attained, further glide of dislocations was suspended and climb simulations were performed using a much larger (temperature dependent) value of the time step. When any dislocation in the system climbed to a neighboring slip plane, the system was assumed to be “activated” from its local equilibrium state. Then only the glide simulations were resumed using the smaller time step until the next quasi-equilibrium state was again achieved. This procedure, where glide and climb simulations were performed sequentially using an adaptive time stepping procedure, enabled us to perform simulations of creep [45] and recovery (as in the present study) over realistic time scales.

During the climb steps, the climb velocity (v_c^i) was calculated using an approximate analytical solution for steady state climb of an edge dislocation in an ambient vacancy field c [59].

$$v_c^i = -\eta \frac{D}{b^i} \left[c_0 \exp\left(\frac{f_c^i \Omega}{b^i k T}\right) - c \right] \text{-----(4.7)}$$

where c_0 is the equilibrium vacancy concentration at temperature T and zero stress, f_c^i is the climb component of the Peach-Koehler force, b^i is the modulus of the Burgers vector, c is the ambient vacancy concentration away from core and the dimensionless pre-factor η is assumed to be unity. Note that climb could occur even in the absence of a component of the Peach-Koehler force f_c^i in the climb direction, if the ambient vacancy concentration c was different from its thermal equilibrium value c_0 . This contribution to the driving force for dislocation climb was called the osmotic force due to the vacancy field. Dislocation positions were updated incrementally using a forward Euler algorithm in both the glide and climb steps. Values of the material parameters used in the recovery simulations are listed in Table 4.2.

Table 4.2: Parameters used in the discrete dislocation dynamics simulations for recovery

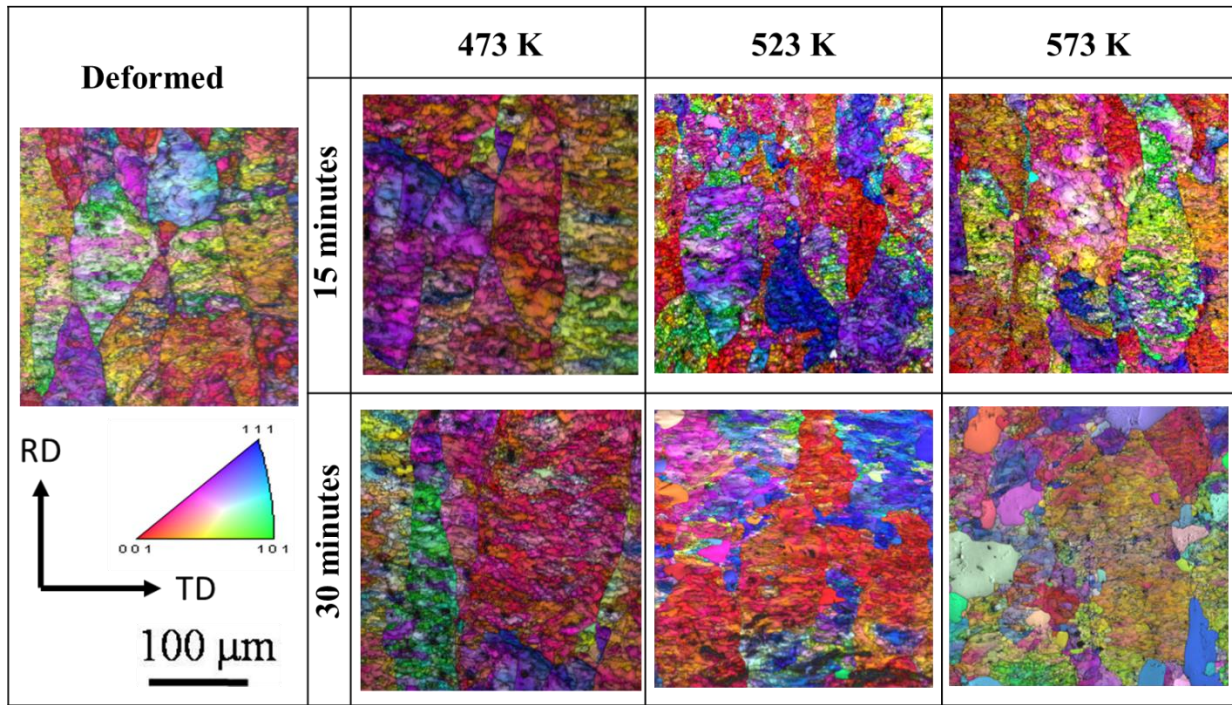
Parameter	Value considered in simulation
Elastic Modulus (E)	66 GPa
Poisson's Ratio (ν)	0.3
Burgers Vector (b)	0.25E-3 μm
Slip plane spacing	50b nm
Schmid factor	$\left\{ \begin{array}{l} \text{S } \{123\}\langle 63\bar{4} \rangle = 0.43 \\ \text{Goss } \{110\}\langle 001 \rangle = 0.40 \\ \text{Brass } \{110\}\langle \bar{1}12 \rangle = 0.31 \end{array} \right.$
Drag coefficient (B)	$\left\{ \begin{array}{l} 5.32\text{E-}17 \text{ Pa}\cdot\text{s at T=473 K} \\ 5.52\text{E-}17 \text{ Pa}\cdot\text{s at T=523 K} \\ 5.75\text{E-}17 \text{ Pa}\cdot\text{s at T=573 K} \end{array} \right.$
Glide time step (Δt_{glide})	5E-10 s
Climb time step (Δt_{climb})	10E2 s
Atomic Volume (Ω)	16.3 \AA^3
Vacancy Diffusion coefficient pre-exponential (D_0)	1.51E-5 m^2/s

The GND density was determined at any strain level in the “cold deformation” simulations or at any instant in the “annealing” simulations following a resolution-sensitive procedure, as outlined by Guruprasad and co-workers [52, 53]. At elevated temperatures, the GND density was a direct measure of polygonization of the lattice during recovery.

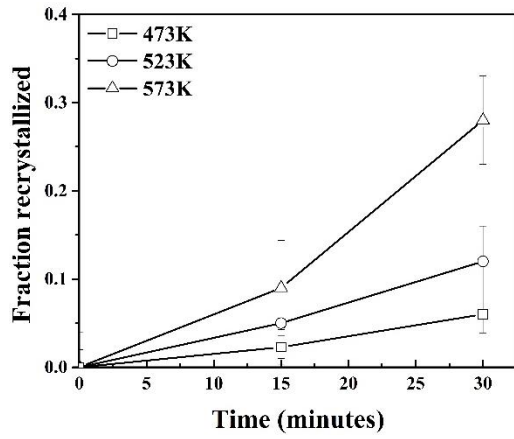
4.4 Results

4.4.1 Basic Experimental Facts

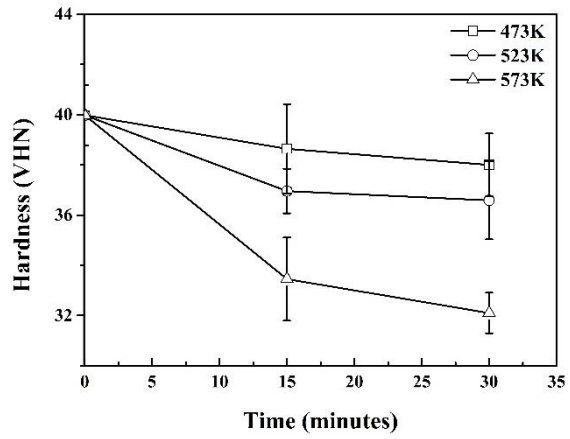
Figure 4.1a summarizes the microstructural developments during the annealing process. As deformed microstructure had ~ 70 μm elongated grains, with ~ 2 μm dislocation cells. It also had clear in-grain misorientations, as GOS (grain orientation spread) and GAM (grain average misorientation). Annealing involved recovery and, especially at the higher annealing temperatures, partial recrystallization – see figure 4.1b. The fraction recrystallized (F_R) was estimated using the twin criteria of minimum grain size and GOS [42-44]. F_R was ~ 0.05 after 473 K annealing, but increased to a more noticeable value of ~ 0.29 after 573 K treatment. Combined effects of the recovery and the recrystallization naturally reduced the hardness (figure 4.1c). More relevant to this study, annealing also brought in substructural changes. As listed in Table 4.2, the EBSD estimated values of sub-grain size was increased as a function of annealing temperature and time. Exactly opposite effect was noted (figure 4.1d) for in-grain misorientations (GOS and GAM): they decreased with annealing. All these measurements were made with multiple EBSD scans on an area of at least $1 \text{ mm} \times 1 \text{ mm}$. Such scans were also used to estimate the boundary density (BD: boundary length per unit area). The respective BD values for low ($1-15^\circ$, see figure 4.1e) and high ($>15^\circ$, see figure 4.1f) angle boundaries were estimated for different annealing time and temperature. They showed an interesting trend. They indicate a temperature dependent drop in the boundary densities. Later in this study, experimental microtexture data are further exploited to relate microstructural evolution (or rate of change in boundary density) with the apparent kinetics of thermal stress relief.



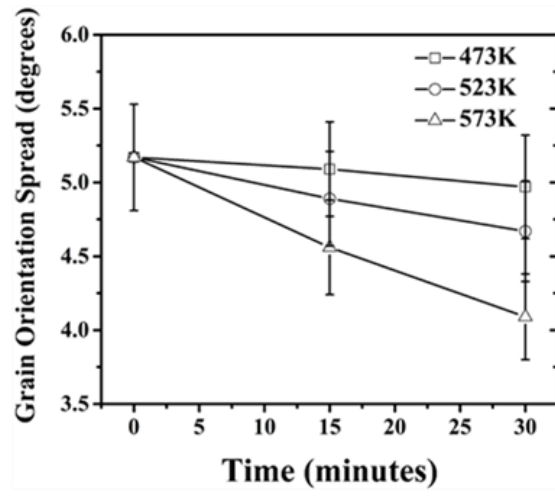
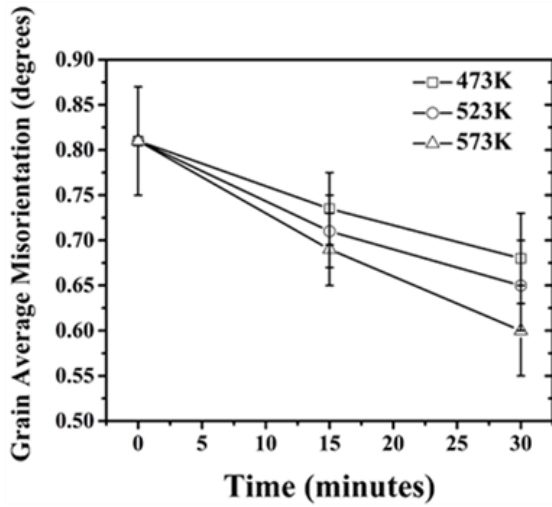
(a)



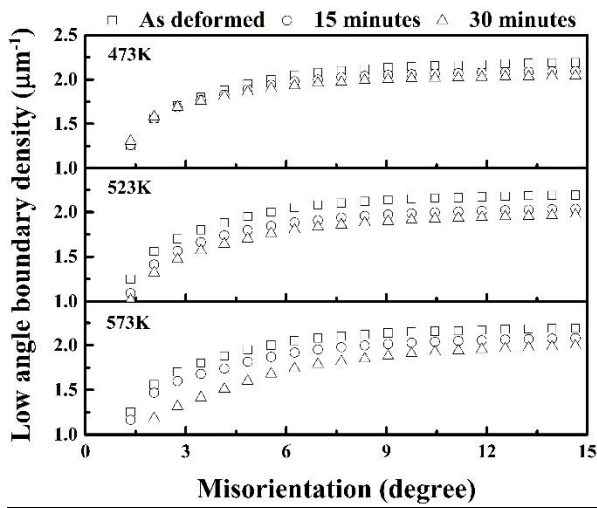
(b)



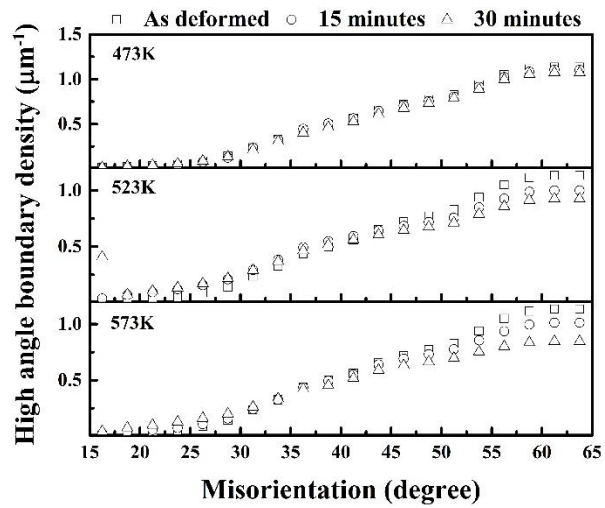
(c)



(d)



(e)



(f)

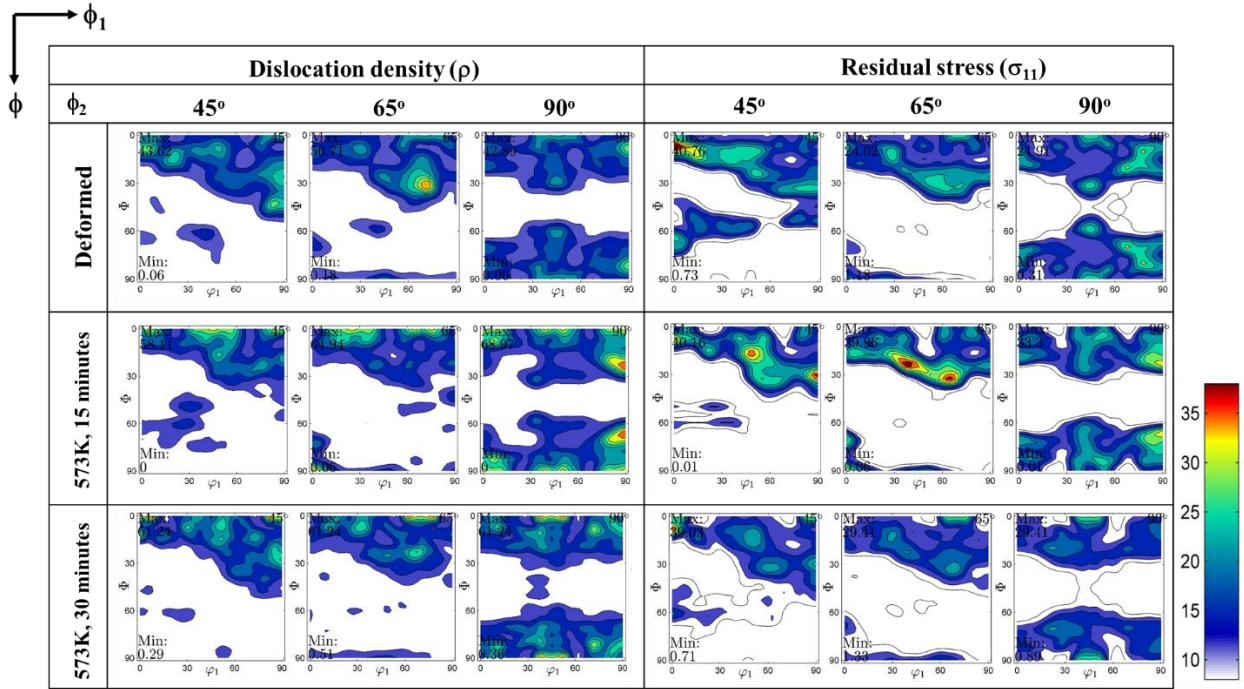
Figure 4.1: (a) EBSD microstructures, combination of IPF (inverse pole figure) and IQ (image quality) maps, showing microstructural changes during annealing. (b) Fraction recrystallized and (c) hardness versus time at different annealing temperatures. (d) Brings out quantification of microstructural changes in terms GAM and GOS. (e) and (f) show the low (1-15°) and high (>15°) angle boundary density (boundary length per unit area) during annealing.

Table 4.3: Average dislocation cell or sub-grain size at different annealing temperature/time. These values were measured from EBSD-IQ maps and image analysis – based on a method described elsewhere [46].

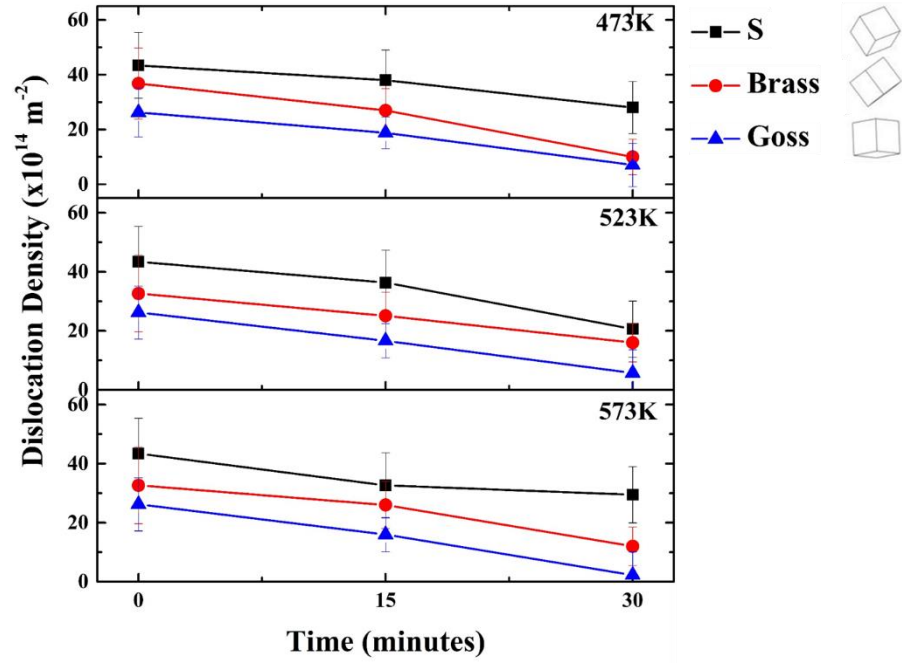
Temp. \ Time	0 minutes	15 minutes	30 minutes
473 K	2.16±0.52	2.59±0.32	3.10±0.41
523 K		2.80±0.89	3.27±0.33
573 K		2.96±0.91	3.73±0.60

X-ray measurements in the Euler space has been exploited, in the past, to plot appropriate ODFs (orientation distribution function) involving stored energy of cold work [77-80] and even residual strain/stress [81-84]. The former is based on X-ray peak broadening, while residual strain/stress measurements used peak shifts. It needs to be pointed out, at this stage, that X-ray line profiles offer better estimates of defect characterization than relatively simpler measures based on full-width-half-maxima [85, 86]. This study used dislocation density measurements from X-ray line profiles, while normal residual stresses along x -axis were measured from peak shifts with respect to an annealed powder. The exact algorithm used for these measurements/analysis is given in the appendix. The output is shown, in appropriate [72] ODF sections, in figure 4.2a. The figure shows a qualitative match between high intensity regions of dislocation density and stress ODFs. In other words, orientations with higher dislocation density appeared to contain higher residual stresses as well. The last point is expanded further with three ideal orientations: S {123} $\langle \bar{6}3\bar{4} \rangle$, Brass {110} $\langle \bar{1}12 \rangle$ and Goss {110} $\langle 001 \rangle$. From the respective ODFs (figure 4.2a) dislocation densities (figure 4.2b) of these orientations (within $\pm 15^\circ$ deviation) were estimated and plotted as a function of annealing temperature and time. Figure 4.2b thus established orientation sensitive drop in dislocation density: Goss being the lowest, followed by Brass and S. An earlier study [12] had shown the developments in residual stresses were sensitive to both orientation and GND (geometrically necessary dislocation) density. Figure 4.2c thus plots the residual stress versus dislocation density, and again an orientation plus dislocation density sensitivity of residual stresses, albeit in samples subjected to annealing, appeared to emerge. To exploit this point further, Figure

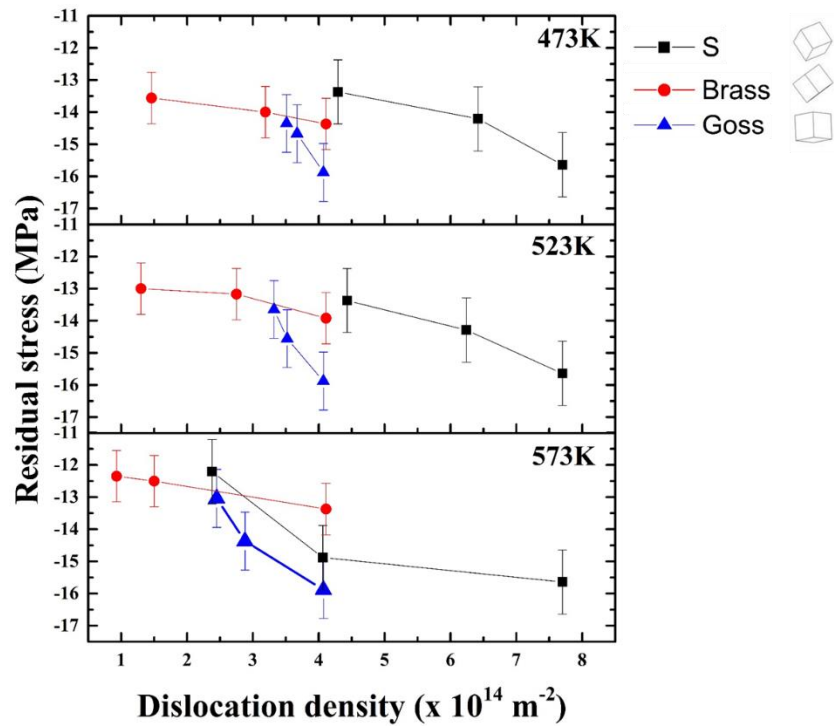
4.2d plots changes in residual stress versus changes in dislocation density ($\frac{d\sigma_{11}}{d\rho}$) for all three ideal orientations and annealing temperatures. The figure of course shows orientation dependence, but except for Goss orientation, no such temperature-dependent rate of stress relaxation with dislocation density ($\frac{d\sigma_{11}}{d\rho}$) is observed.



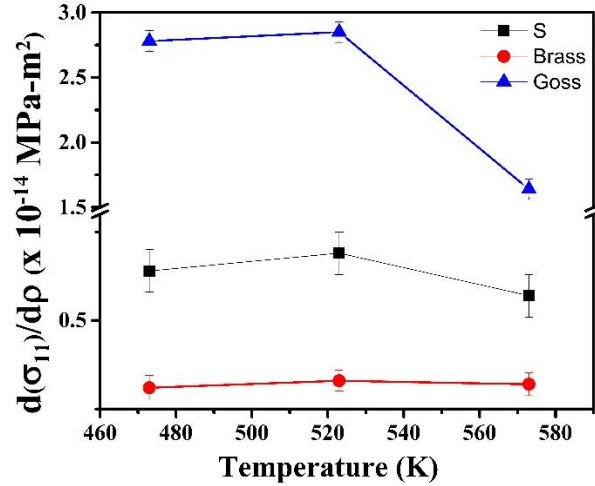
(a)



(b)



(c)



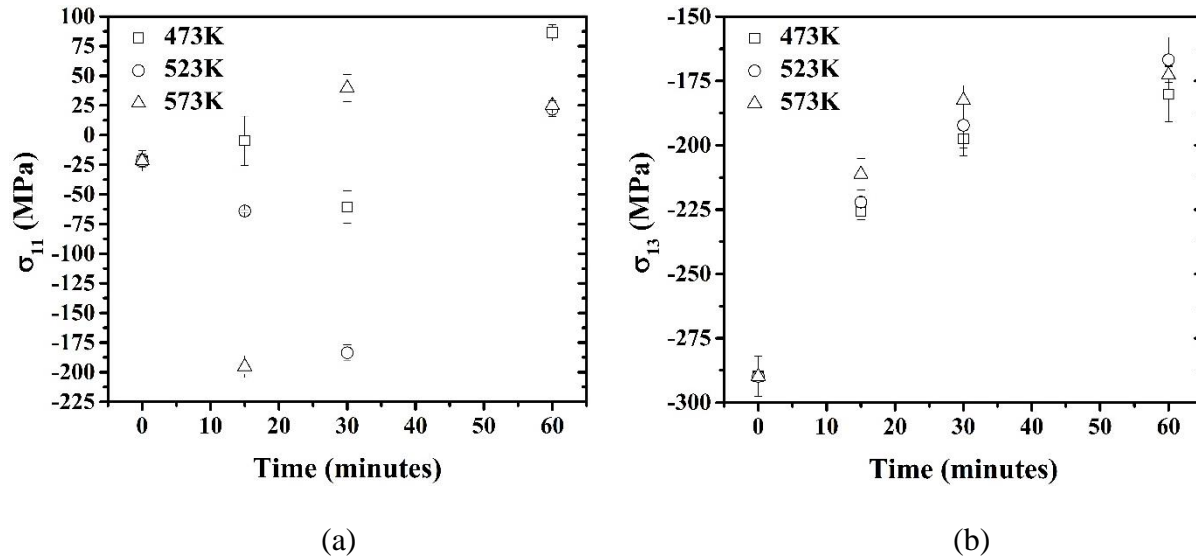
(d)

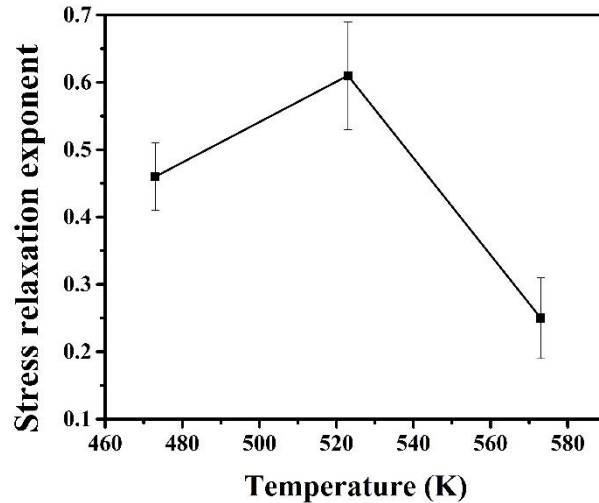
Figure 4.2: (a) Effects of recovery on dislocation density (ρ) and residual Stress (σ_{11} component). These are shown for recovery at 573 K (for 15 and 30 minutes) using standard [45] ODF (orientation distribution function) sections of $\varphi_2 = 45^\circ, 65^\circ, 90^\circ$. (b) Evolution of dislocation density with recovery time and (c) Residual Stress (σ_{11}) versus dislocation density. (b) and (c) were taken from the respective ODFs (as in figure 4.2a), with error bars indicating the data from symmetric positions of the ideal (S $\{123\} \langle \bar{6}34 \rangle$, Brass $\{110\} \langle \bar{1}12 \rangle$ and Goss $\{110\} \langle 001 \rangle$) orientations with $\pm 15^\circ$ deviation. (d) Rate of stress relief with dislocation density as a function of recovery temperatures as estimated from slopes of figure 4.2c.

Residual stress (both normal, σ_{11} , and shear, σ_{13}) is often measured, in XRD, from the standard $d\text{-}\sin^2\psi$ [87, 88]. However, such measurements are valid only for individual X-ray poles. An alternative is to measure residual stresses from multiple $\{hkl\}$ GIXRD [12, 21, 67] where all poles are considered and an orientation-independent σ_{11} and σ_{13} components can be estimated. Figures 3a and 3b show the GIXRD measured σ_{11} and σ_{13} components, respectively, as a function of annealing time and temperature. In this study the σ_{11} component changed with annealing time non-monotonically (figure 4.3a), while σ_{13} (figure 4.3b) showed a progressive stress relief. A progressive stress relief (as in figure 4.3b) can be used to estimate stress relaxation exponent m [21]. The Zener-Wert-Avrami equation [21, 89] states,

$$\frac{\sigma^{T,t}}{\sigma^{t=0}} = \exp\left[-\left(A \exp\left(-\frac{\Delta H}{kT}\right)t\right)^m\right] \quad \text{-----(4.8)}$$

whereas $\sigma^{T,t}$ and $\sigma^{t=0}$ denote residual stresses after and before annealing, respectively. T and t being the annealing temperature and time, ΔH and k are activation enthalpy and Boltzmann constant. Stress relaxation exponent (m) was measured from the multiple {hkl} GIXRD data of σ_{13} , see figure 4.3c, and clearly showed highest stress relaxation at the intermediate annealing temperature of 523 K. It is curious to observe a non-monotonic dependence of stress relaxation with temperature even though the bulk hardness data shows a monotonic drop in values. In the next paragraphs, an effort will be made to seek a microstructural justification.





(c)

Figure 4.3: Residual stress components of (a) σ_{11} and (b) σ_{13} as a function of annealing time. The multiple $\{hkl\}$ GIXRD measurements for residual stresses were taken at different annealing temperatures. (c) Progressive stress relief for σ_{13} was used to calculate Zener–Wert–Avrami exponent (stress relaxation exponent m : see eq. (4.8)) for all three recovery temperatures.

Though the statistics of the X-ray measurements are substantial ($5 \text{ mm} \times 5 \text{ mm}$), they have two shortcomings. Firstly, such measurements did not distinguish between recovered and recrystallized regions (and the highest annealing temperature-time led to a F_R of ~ 0.29). More importantly, a large orientation spread ($\pm 15^\circ$) was used to achieve meaningful statistics. Direct observations [12, 21] on the concurrent microstructural and residual stress measurements provided a clear alternative. As shown in figure 4.4, respective orientations (within 5° of the ideal component) were obtained in the as deformed state. They were then subjected to progressive annealing. And at different stages of the annealing simultaneous measurements of EBSD and residual stresses were made. The high resolution IQ maps, figure 4.4, brought out annihilation and reconstruction of dislocation substructures, while micro-Laue diffraction [12] measured the entire stress matrix.

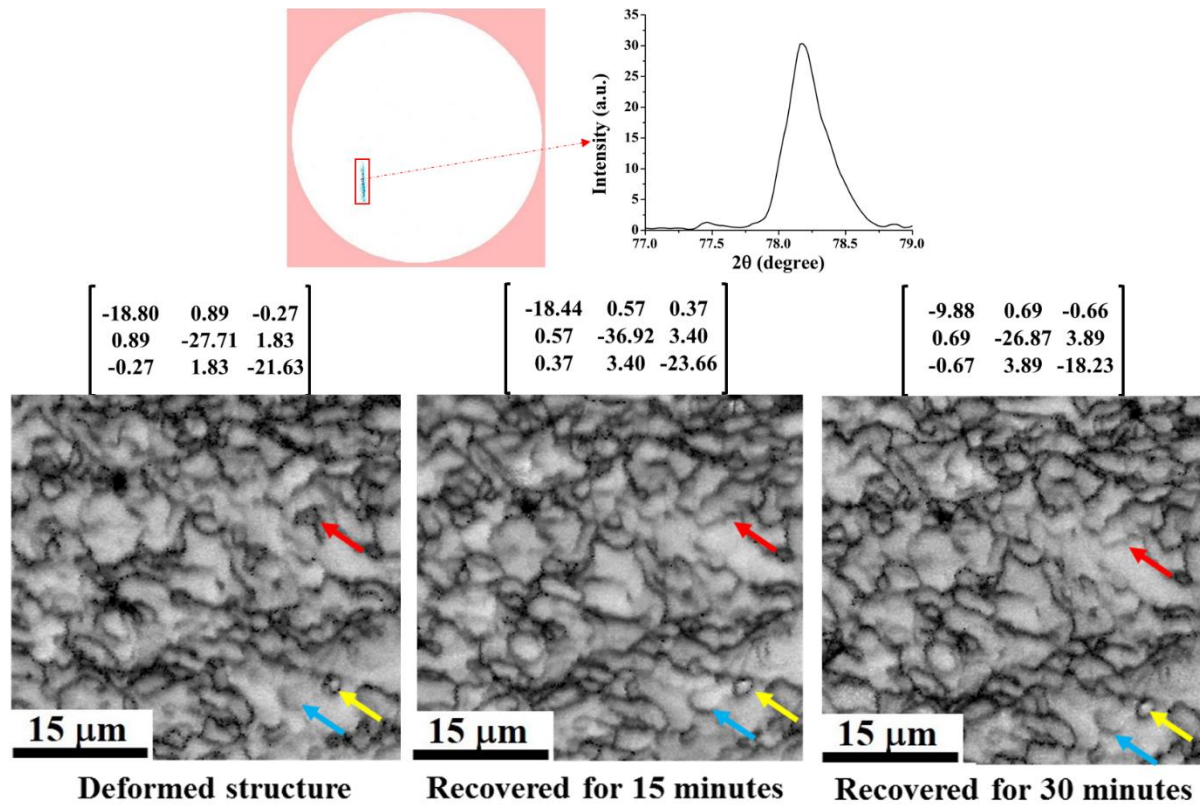


Figure 4.4: EBSD IQ (image quality) maps showing changes in dislocation cell or sub-grain structures. These are taken from the same grain or orientation during different recovery stages (or time periods) of 473 K annealing. They show both annihilation (‘red’ arrow) and creation (‘blue’ and ‘yellow’ arrows) of dislocation boundaries. Residual stress measurements, with micro-Laue diffraction, are taken at each stage, and the entire stress matrix was estimated.

4.4.2 Comparison between experiments and simulations

From such direct experimental measurements, temperature dependent drop in GND densities (see figure 4.5a) and the associated evolution of residual stresses (figure 4.6a) were captured for three ideal texture components. Further, direct experimental measurements also obtained $\frac{d\sigma_{11}}{d\rho_{GND}}$ (rate of stress relief with change in GND density) against temperature, see Fig. 4.7a. The figure showed: (i) highest $\frac{d\sigma_{11}}{d\rho_{GND}}$ at the intermediate annealing temperature of 523 K and (ii) a clear orientation sensitivity ($S > \text{Goss} > \text{Brass}$). All these were also simulated numerically. The simulations showed

the recovery of the microstructure: reflected in change in GND density with recovery time (see figure 4.5b-d). They also captured the residual stress relief through reduction in GND density (figure 4.6b), and the patterns of $\frac{d\sigma_{11}}{d\rho_{GND}}$ (figure 4.7b). The results from experiments and simulations thus predicted, qualitatively, fall in GND density and consequently residual stress relief with annealing time. There were some quantitative differences between the experimental observations and simulation predictions. For example, the fall in GND density and residual stress predictions from simulations did not follow the same orientation dependence (as that of the experiments). The simulations, however, captured the orientation effect in rate of stress relief with change in GND density (see figure 4.7b).

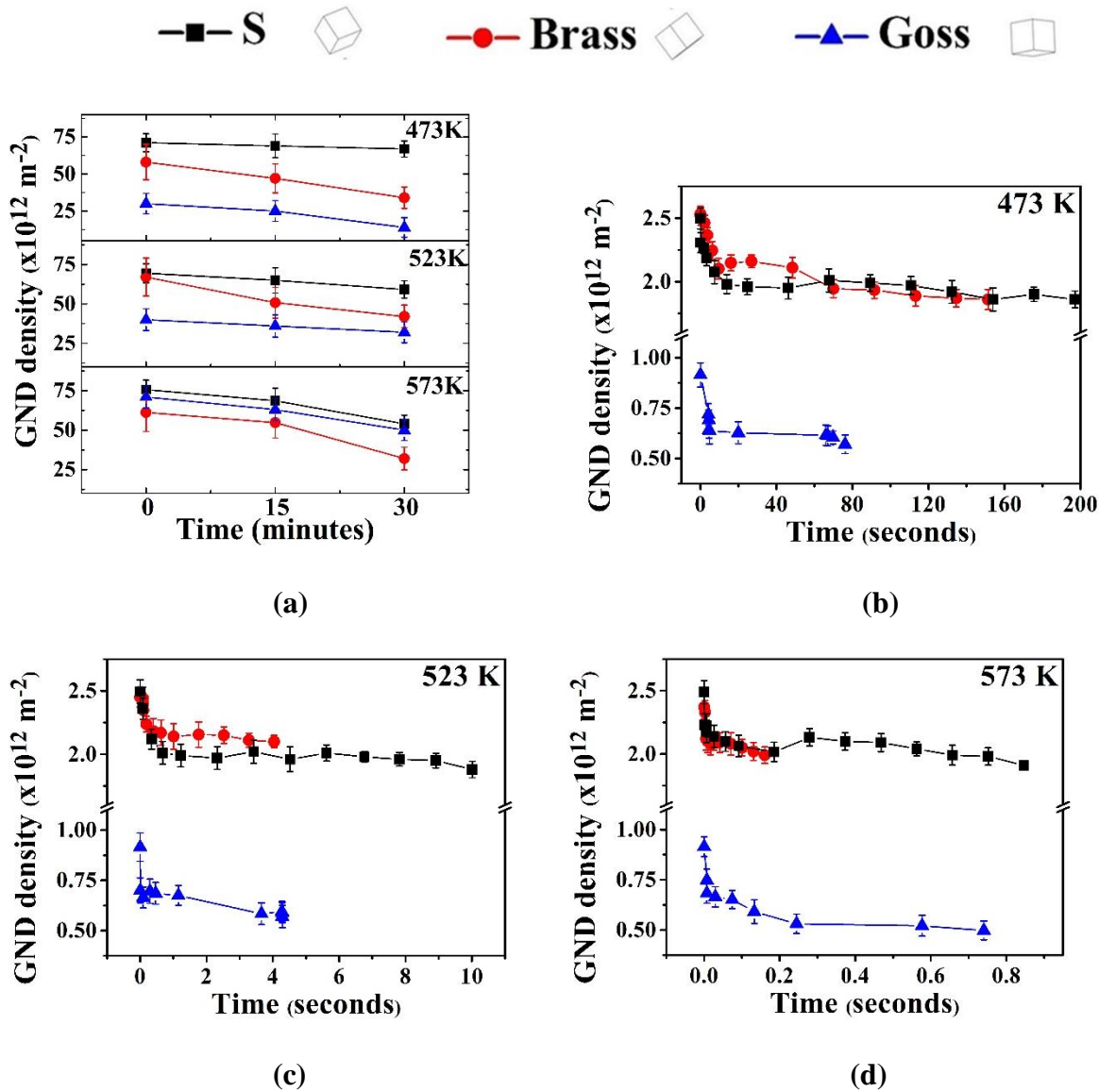
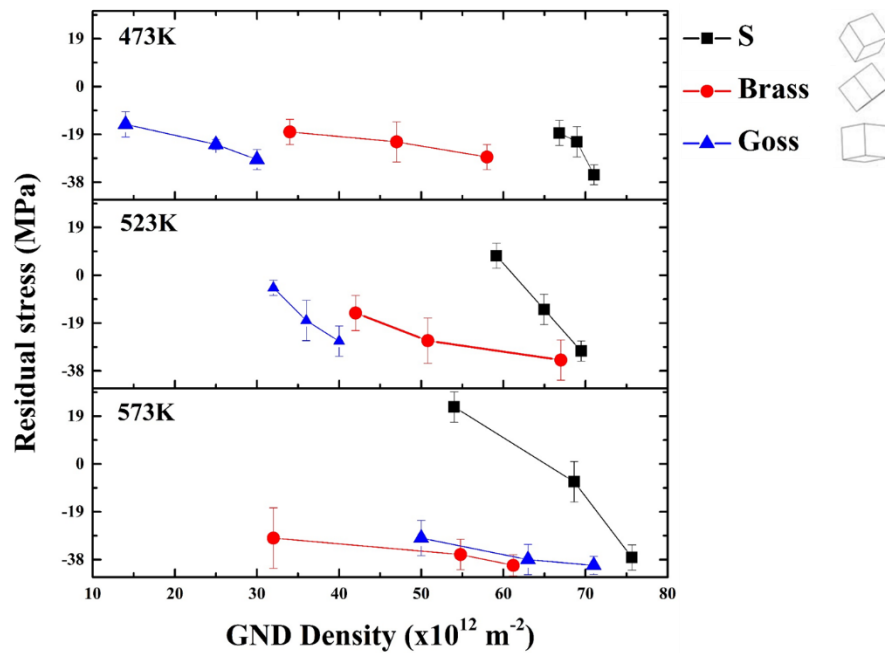


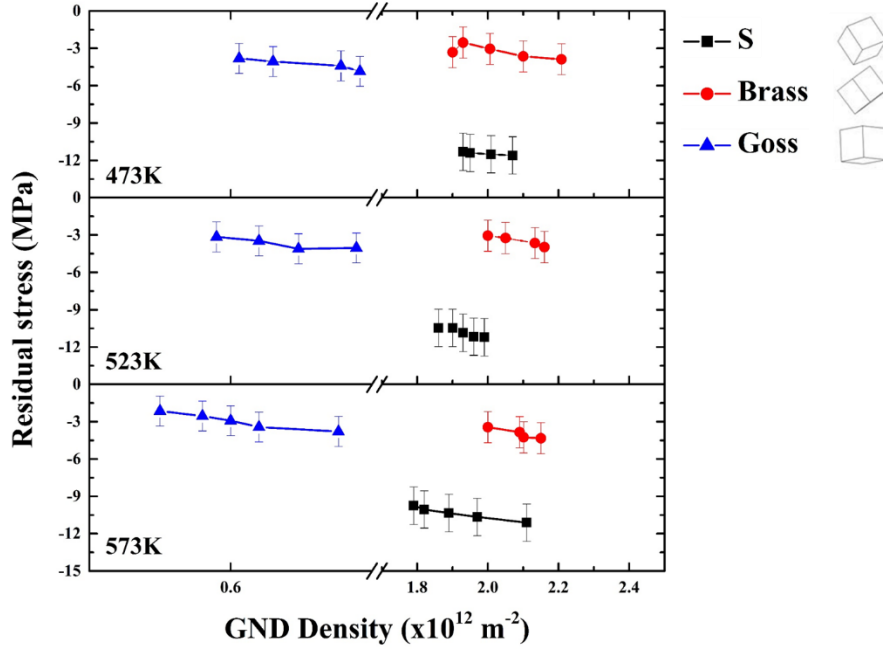
Figure 4.5: GND density versus annealing time as (a) measured from EBSD and (b) simulated from DDD. The measurements were taken from regions within 5° from ideal S $\{123\} \langle \bar{6}34 \rangle$, Brass $\{110\} \langle \bar{1}12 \rangle$ and Goss $\{110\} \langle 001 \rangle$ orientations. The orientations are shown with their respective unit cells.

It has been hypothesized, implicitly in this study, that temperature and orientation dependent residual stress relief (figure 4.7a) has its origin in the concurrent evolution of dislocation substructure. In other words, thermal stress relief is enabled by the annihilation of subgrain

boundaries [24]. To test this argument, the data on boundary density (figure 4.1e and 4.1f) were further exploited (see figure 4.8a). The rate of change of high ($>15^\circ$) angle boundary density increased with annealing temperature, while for the low ($1-15^\circ$) boundaries the maximum rate of change was at the intermediate temperature. The pattern of temperature and orientation dependent change in low angle boundaries (figure 4.8b) was similar in nature as that the experimental $\frac{d\sigma_{11}}{d\rho_{GND}}$ (figure 4.7a). Much of the subsequent discussion is aimed at possible explanation: an explanation based on dislocation dynamics.

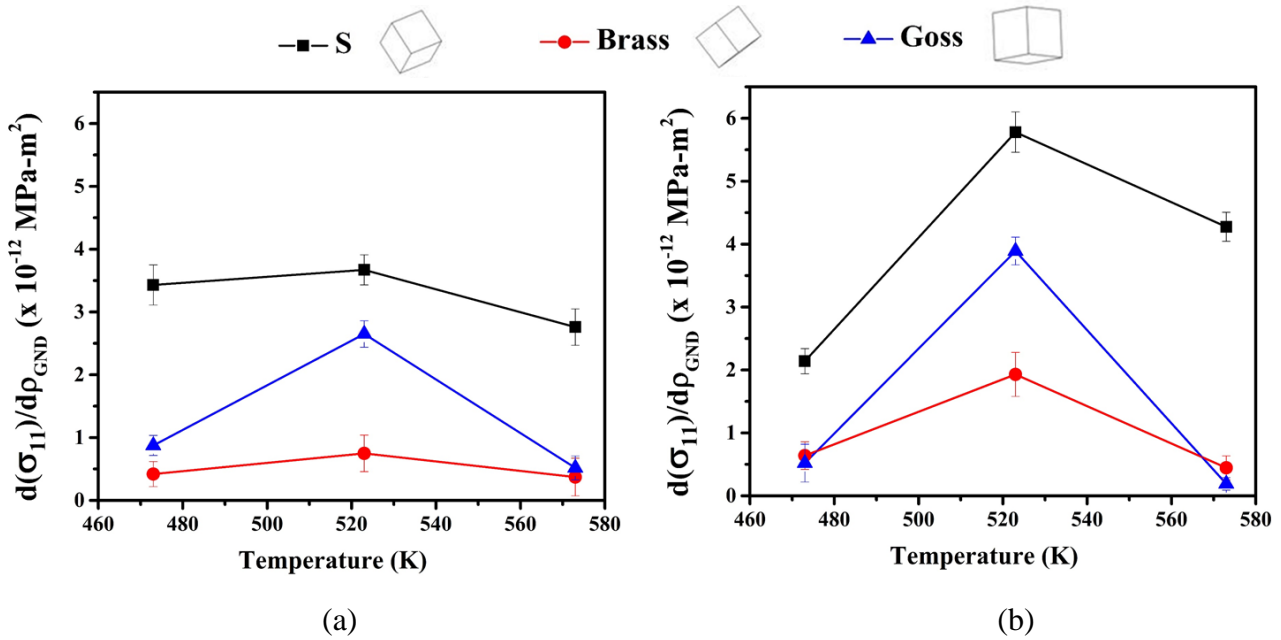


(a)



(b)

Figure 4.6: Residual Stress versus GND density as (a) measured experimentally from the direct observations (figure 4.4) and (b) simulated with DDD. These observations were made for three ideal orientations (as in figure 4.5).



(a)

(b)

Figure 4.7: Rate of stress relief with GND density ($\frac{d\sigma_{11}}{d\rho_{\text{GND}}}$) for three different orientations as a function of temperature as observed from (a) direct observations and (b) DDD simulations.

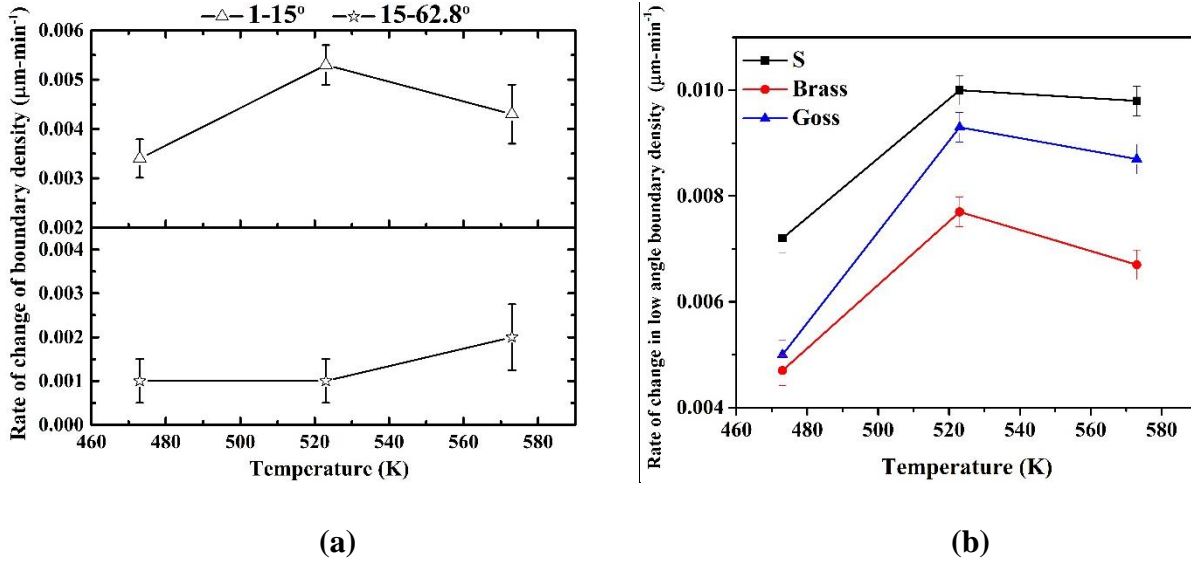
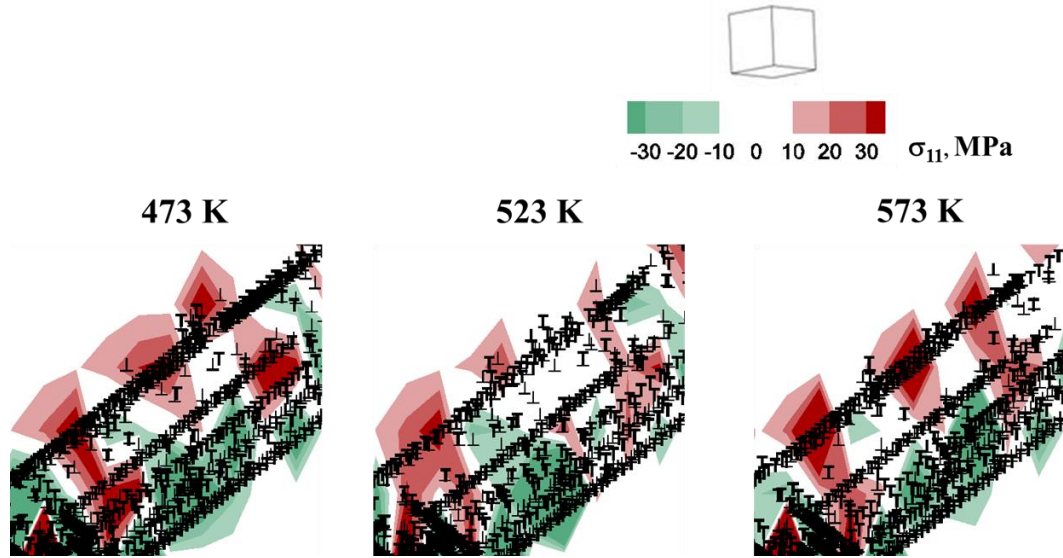


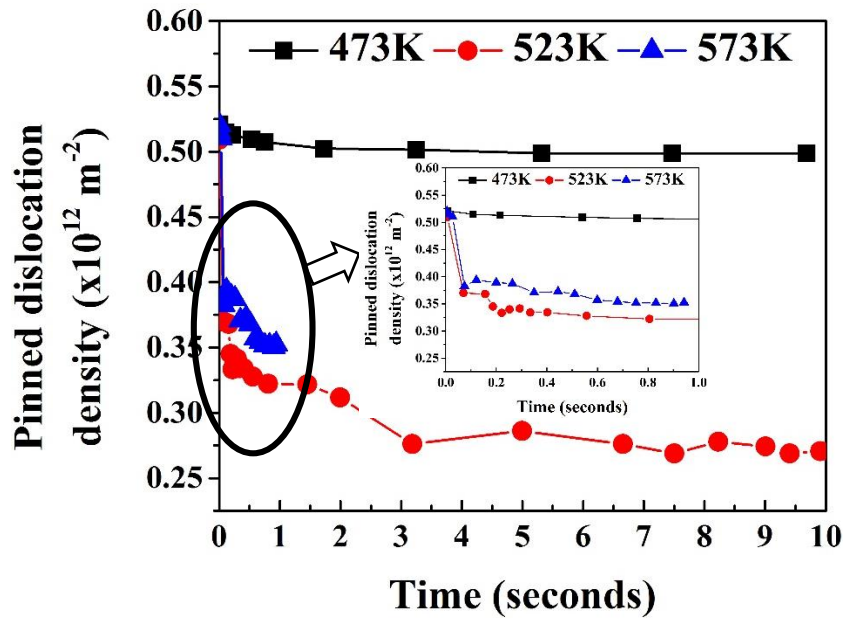
Figure 4.8: Rate of change of (a) low (1-15°) and high (>15°) angle boundaries with annealing temperature. Rate of change of low (1-15°) angle boundaries for different (see figure 4.5) ideal orientations. The data were obtained from large area EBSD scans.

4.5 Discussion

The experimental results have uncovered a counter-intuitive observation: fastest stress relief and associate decrease in low angle boundary concentration at the intermediate annealing temperature. The discrete dislocation dynamics (DDD) simulations were performed to rationalize this observation. In figure 4.9a, the dislocation structure is shown, superposed onto contours of the σ_{11} stress component, for all three annealing temperatures. The same single crystal specimen with a Goss {110}<001> orientation was subjected to 2% plane strain compression and subsequently unloaded and annealed at these temperatures. A similar study was undertaken for S and Brass orientations as well. It was observed that the post recovery substructures, especially the density of pinned dislocations, were temperature dependent.



(a)



(b)

Figure 4.9: (a) Enlarged view of DDD simulations on substructure and residual stress evolution after achieving steady state dislocation density during recovery. Deformed ($\sim 2\%$ plastic strain) Goss $\{110\}\langle 001 \rangle$ grain was subjected to recovery at 473, 523 and 573 K. Steady state of dislocation densities were obtained at 80 seconds, 4.6 seconds and 1 second for 473, 523 and 573 K temperatures, respectively. (b) Evolution of pinned dislocation density over the recovery time for orientation S $\{123\}\langle 63\bar{4} \rangle$ showing saturation for three recovery temperatures.

Figure 4.9b shows, for instance, the evolution of pinned density with time for the S orientation, which also showed the highest stress relief amongst the orientations studied. After a transient of a few seconds, the decreasing pinned dislocation density leveled off to a temperature-dependent value (see inset). This temperature dependence is summarized in figure 4.10a for the same S orientation, and in figure 4.10b for the Goss orientation. The results presented in figures 4.9b and 4.10a-4.10b bring out two important findings. Firstly, the reduction in pinned dislocation density was orientation sensitive. More importantly, the reduction was maximum at some intermediate annealing temperature. These are indeed in agreement with the experimental results (see figure 4.8).

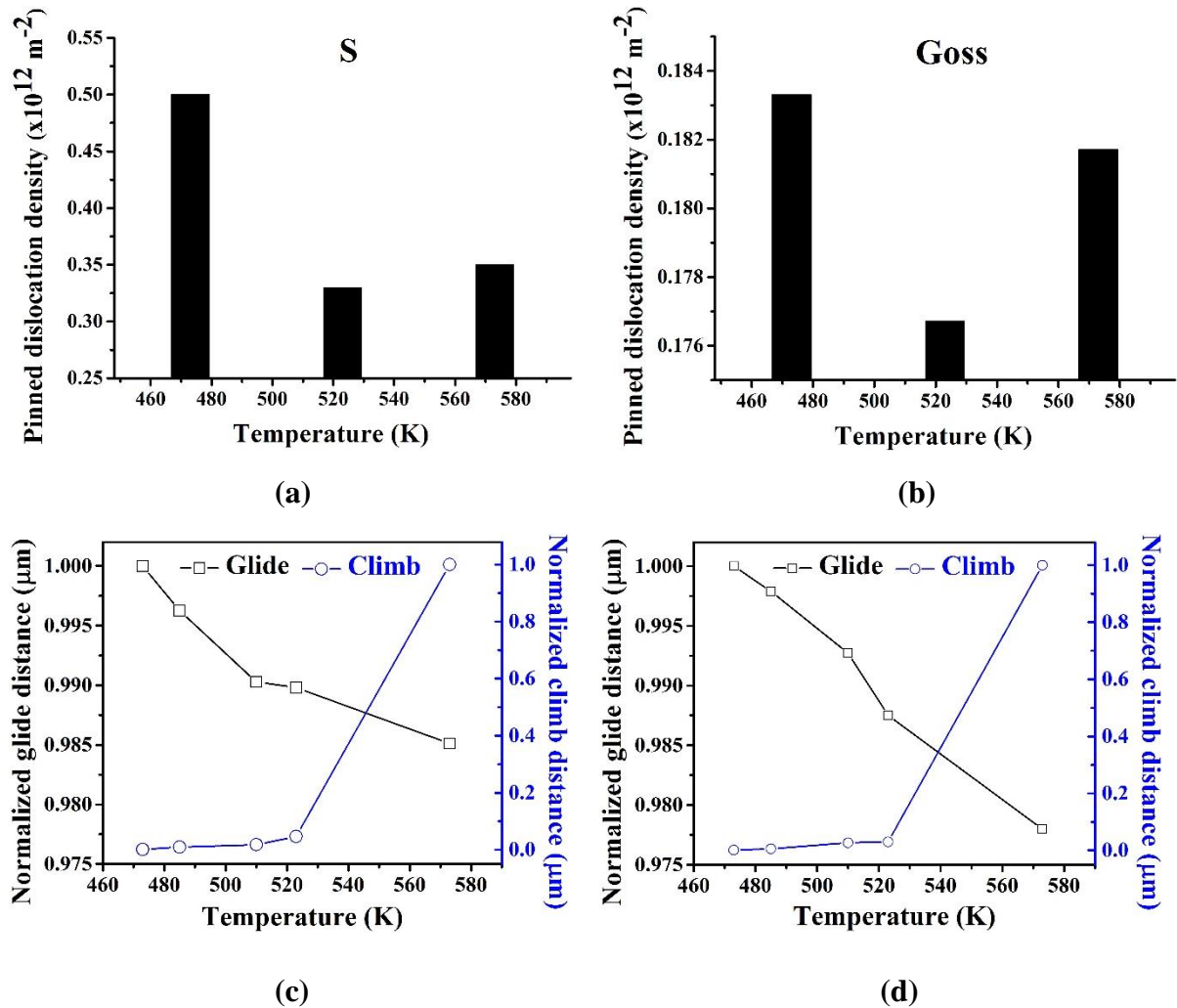


Figure 4.10: Saturated pinned dislocation density for the three annealing temperature and two ideal orientations: (a) S $\{123\}\{63\bar{4}\}$ and (b) Goss $\{110\}\{001\}$. For the two ideal orientations (c) S and (d) Goss, normalized glide and climb distances traveled are plotted as a function of recovery temperature.

The simulations, reported in this study, hint at possible underlying mechanisms. Figure 4.10c-4.10d shows the normalized average glide (L_{Glide}) and climb (L_{Climb}) distances, for S and Goss orientations, and for all three recovery temperatures. The distance traveled by all dislocations during a simulation time step was calculated for both glide and climb, by summing up the incremental distances travelled by each dislocation. The process was repeated for multiple time steps and the average values for total glide and climb distances were calculated. In all the cases,

the standard deviation was found to be less than 10%. For ease of comparison, the estimated average glide and climb distances were then normalized by the maximum distance travelled. Figures 4.10c and 4.10d show a drop in L_{Glide} and a corresponding increase in L_{Climb} as the annealing temperature increased. It is thus apparent that a balance between glide and climb provided the maximum recovery at the intermediate temperature for the DDD simulations. The experimental data, on the other hand, showed an identical pattern in terms of low angle boundary density (see figure 4.8b).

While the simulations presented here provided some insight into the stress relief process by means of dislocation glide/climb mechanisms, they rely on a formulation that has limitations in a number of respects. For instance, grain-boundary-mediated processes have not been taken into consideration when these likely play a key role in experiments. Accounting for GBs as preferred pathways for vacancy diffusion would require further development of the presently available framework. It is worth noting that Shishvan et al. [66] have simulated the formation of dislocation cell patterns under high-temperature deformation using a framework that bears some connection with that used here. One possible avenue of investigation would thus consist of analyzing the evolution of low-angle boundaries initially included in the computer model in order to mimic better experimental conditions.

This work provided experimental observations, both indirect and direct, on orientation dependent recovery and stress relief. The first set of data, those from indirect measurements, were statistically robust: but, as discussed earlier, had limitations from partial recrystallization and higher orientations spread in the Euler space. Direct experimental measurements, with high resolution EBSD and micro-Laue diffraction, resolved these issues. Both indirect and direct measurements provided a qualitatively similar trend of accelerated stress relief at the intermediate temperature. This trend appeared counterintuitive, at least at first glance, but was also captured in the DDD simulations as a competition between climb-mediated de-pinning of dislocations from obstacles and subsequent glide-induced rearrangements of dislocation ensembles. The manuscript thus proposes a unique perspective to the *microstructural origin of residual stress relief*: a perspective supported by theoretical postulation of a balance between dislocation glide and climb mechanisms.

4.6 Conclusions

This study dealt with both experimental measurements, indirect and direct, and DDD simulations on the microstructural origin of residual stress relief in Aluminum. Following are the main observations:

- ✓ 50% cold rolled commercial purity aluminum was subjected to annealing at three different temperatures (473, 523 and 573 K). Higher annealing temperature/time led to partial recrystallization: highest fraction recrystallized being ~0.29. Otherwise, microstructural changes were primarily through recovery. A near monotonic increase in sub-grain size and decrease in in-grain misorientation were observed with annealing temperature/time.
- ✓ Residual stress and dislocation density were measured in the Euler space and plotted as appropriate ODFs (orientation distribution function). An orientation dependent drop in dislocation density. GIXRD measurements showed *highest* stress relief at the intermediate annealing temperature.
- ✓ Direct experimental measurements, with high resolution EBSD and micro-Laue diffraction, also confirmed, qualitatively, the earlier trend of bulk measurements. Such measurements, conducted on the same deformed/recovered grain or orientation, revealed that $\frac{d\sigma_{11}}{d\rho_{GND}}$ (change in residual stress versus change in geometrically necessary dislocation density) was orientation sensitive and *highest* at the intermediate annealing temperature. It was also clear that the elimination of low angle (1-15°) boundaries was most efficient at the intermediate temperature.
- ✓ DDD simulations revealed that the fastest reduction of pinned dislocation density and highest $\frac{d\sigma_{11}}{d\rho_{GND}}$ occurred at the intermediate annealing temperature. From the simulations, it was observed that the average dislocation glide decreased and the average dislocation climb increased with increase in annealing temperature. Competition between dislocation glide and climb emerged as the enabling mechanism for the thermal recovery and associated residual stress relief.

Appendix:

Method to estimate residual stress and dislocation density orientation distribution function from x-ray diffraction

A Bruker™ D8 Discover system, with micro-focus (~50 μm minimum spot size) x-ray and Vantec™ area detector, was used for the XRD measurements. The measurements involved were dislocation density and residual stress as respective ODFs (orientation distribution function). X-ray texture measurements are a well-established technique discussed elsewhere [72]. The ODFs of residual stress (normal stress or σ_{11}) and dislocation density needs further deliberation. As shown in figure 4.A1a, pole figure angles can be represented as α and β . The area detector data provides diffraction frames in $\gamma - 2\theta$ (azimuthal angle and Bragg angle [90]) coordinate for different goniometer angles (ω, ψ, ϕ), see figure 4.A1b. Pole figure angles can be calculated from the goniometer angles ($\omega, \psi, \phi, \gamma$) as [90],

$$\alpha = \sin^{-1}|h_3| = \cos^{-1} \sqrt{h_1^2 + h_2^2}$$

$$\beta = \pm \cos^{-1} \frac{h_1}{\sqrt{h_1^2 + h_2^2}} \quad \begin{array}{l} \beta \geq 0^\circ \text{ if } h_2 \geq 0 \\ \beta \geq 0^\circ \text{ if } h_2 < 0 \end{array} \quad \text{----- (4.a1)}$$

where h_1, h_2 and h_3 are the unit vector components along the sample coordinates and can be deduced as

$$h_1 = \sin \theta (\sin \varphi \sin \psi \sin \omega + \cos \varphi \cos \omega) + \cos \theta \sin \varphi \cos \psi \cos \gamma$$

$$- \cos \theta \sin \gamma (\sin \varphi \sin \psi \cos \omega - \cos \varphi \sin \omega) \quad \text{----- (4.a2)}$$

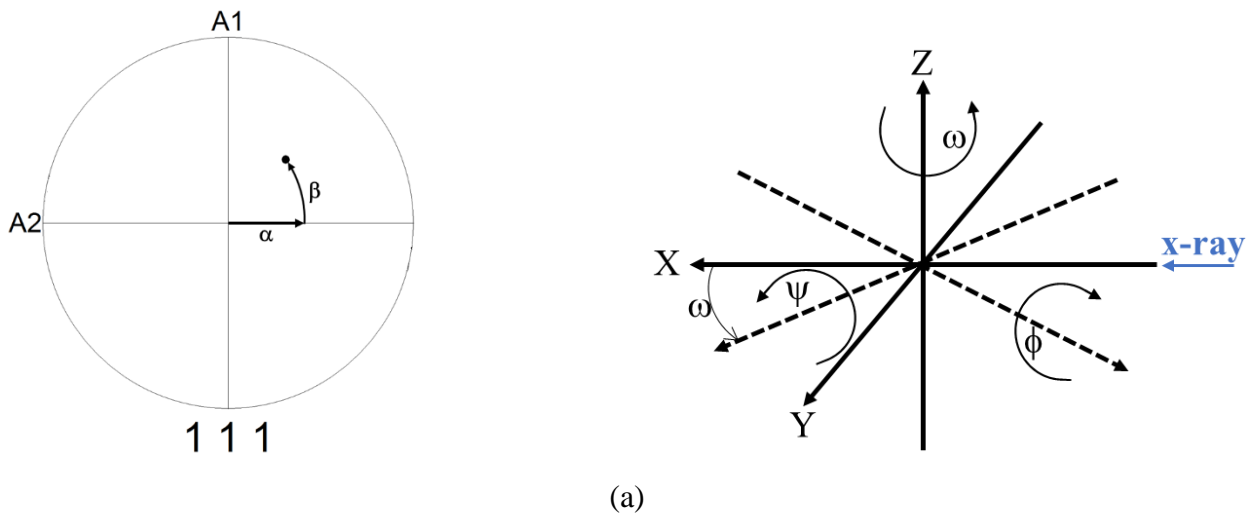
$$h_2 = -\sin \theta (\cos \varphi \sin \psi \sin \omega - \sin \varphi \cos \omega) - \cos \theta \cos \varphi \cos \psi \cos \gamma$$

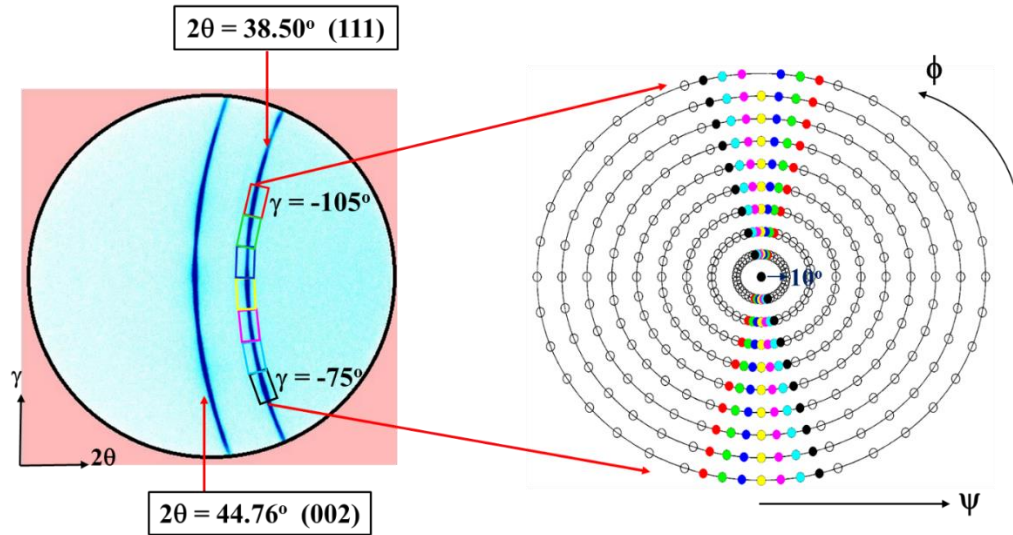
$$- \cos \theta \sin \gamma (\sin \varphi \sin \psi \cos \omega - \cos \varphi \sin \omega) \quad \text{----- (4.a3)}$$

$$h_3 = \sin \theta \cos \psi \sin \omega - \cos \theta \cos \omega \cos \psi \sin \gamma - \cos \theta \cos \gamma \sin \psi \quad \text{----- (4.a4)}$$

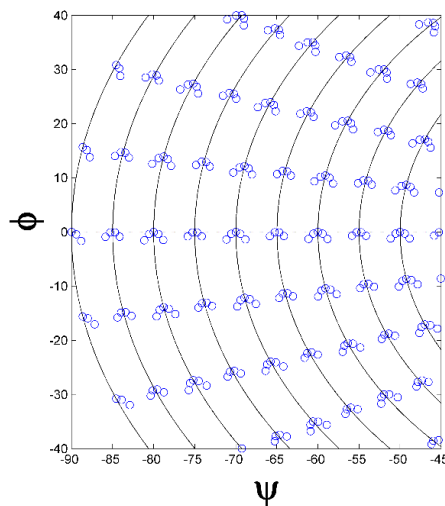
Figure 4.A1b shows a typical area detector measurement. Such measurements provided the peak positions and the peak profiles for different values of γ . As shown in figure 4.A1b (and also

described in eq. (4.a1)-(4.a4)), each γ did correspond to ψ - ϕ values on the pole figure scheme. There were two ambiguities: (i) area detector signal of a specific γ -value had a spread of θ and (ii) multiple combinations of goniometer angles provided same pole figure angles (see figure 4.A1c). Taking average values resolved both these issues. Residual strains, at different angular locations, were calculated from shifts in peak position – actual deformed specimen versus annealed powder sample. Residual stresses were then calculated from the Hooke's law using an isotropic elastic constant of 70.3 GPa. Dislocation density, on the other hand, was calculated from each peak profile by second order variance method [27] using an in-house MATLABTM code. From the experimentally measured dislocation density and residual stress pole figures, the respective ODFs (orientation distribution function) were then calculated/plotted using MTEXTM software.





(b)



(c)

Figure 4.A1: Extraction of area detector data for plotting dislocation density (DD) and residual stress (RS) orientation distribution function (ODF). (a) Representation of pole figure angles (α and β) in a schematic pole figure (left side) and the goniometer angles (ω , ψ , ϕ) in XYZ coordinate system (right side). (b) Area detector (VantecTM) data (on peak profile and peak shift) were taken at different γ angles (azimuthal angle, in the anti-clockwise direction, from the diffraction plane [90]). These correspond to different positions in the measurement scheme in ψ - ϕ axes. (c) Several data points (on DD and RS) were obtained at each pole figure position (in ψ - ϕ axes), and the average values were considered for subsequent ODF calculation.

References

- [1] A. Akef, J.H. Driver, Orientation splitting of cube-oriented face-centred cubic crystals in plane strain compression, *Mater. Sci. Eng., A* 132(Supplement C) (1991) 245-255.
- [2] L. Delannay, O. Mishin, D.J. Jensen, P. Van Houtte, Quantitative analysis of grain subdivision in cold rolled aluminium, *Acta Mater.* 49(13) (2001) 2441-2451.
- [3] F.J. Humphreys, M. Hatherly, *Recrystallization and related annealing phenomena*, second ed., Pergamon Materials Series, Elsevier, Oxford 2004.
- [4] Y. Nakayama, K. Morii, Microstructure and shear band formation in rolled single crystals of Al-Mg alloy, *Acta Metall.* 35(7) (1987) 1747-1755.
- [5] B. Verlinden, J. Driver, I. Samajdar, R.D. Doherty, *Thermo-mechanical processing of metallic materials*, first ed., Pergamon Materials Series, Elsevier, Oxford 2007.
- [6] B. Bay, N. Hansen, D.A. Hughes, D. Kuhlmann-Wilsdorf, Overview no. 96 evolution of f.c.c. deformation structures in polyslip, *Acta Metall. Materlia* 40(2) (1992) 205-219.
- [7] Q. Liu, D. Juul Jensen, N. Hansen, Effect of grain orientation on deformation structure in cold-rolled polycrystalline aluminium, *Acta Mater.* 46(16) (1998) 5819-5838.
- [8] L.E. Levine, B.C. Larson, W. Yang, M.E. Kassner, J.Z. Tischler, M.A. Delos-Reyes, R.J. Fields, W. Liu, X-ray microbeam measurements of individual dislocation cell elastic strains in deformed single-crystal copper, *Nature mater.* 5(8) (2006) 619-622.
- [9] T. Ungar, H. Mughrabi, D. Rönnpapel, M. Wilkens, X-ray line-broadening study of the dislocation cell structure in deformed [001]-orientated copper single crystals, *Acta Metall.* 32(3) (1984) 333-342.
- [10] H. Mughrabi, Dislocation wall and cell structures and long-range internal stresses in deformed metal crystals, *Acta Metall.* 31(9) (1983) 1367-1379.
- [11] H. Mughrabi, T. Ungár, W. Kienle, M. Wilkens, Long-range internal stresses and asymmetric X-ray line-broadening in tensile-deformed [001]-orientated copper single crystals, *Philos. Mag. A* 53(6) (1986) 793-813.
- [12] A. Lodh, T.N. Tak, A. Prakash, P.J. Guruprasad, C. Hutchinson, I. Samajdar, Relating Residual Stress and Substructural Evolution During Tensile Deformation of an Aluminum-Manganese Alloy, *Metall. Mater. Trans. A* 48(11) (2017) 5317-5331.
- [13] M. Verdier, Y. Brechet, P. Guyot, Recovery of AlMg alloys: flow stress and strain-hardening properties, *Acta Mater.* 47(1) (1998) 127-134.

- [14] M. Verdier, M. Janecek, Y. Bréchet, P. Guyot, Microstructural evolution during recovery in Al–2.5%Mg alloys, *Mater. Sci. Eng., A* 248(1) (1998) 187-197.
- [15] Q. Xing, X. Huang, N. Hansen, Recovery of heavily cold-rolled aluminum: Effect of local texture, *Metall. Mater. Trans. A* 37(4) (2006) 1311-1322.
- [16] T. Furu, R. Ørsund, E. Nes, Subgrain growth in heavily deformed aluminium—experimental investigation and modelling treatment, *Acta Metall. Materlia* 43(6) (1995) 2209-2232.
- [17] O.V. Mishin, A. Godfrey, T. Yu, N. Hansen, D.J. Jensen, Evolution of microstructure and texture during recovery and recrystallization in heavily rolled aluminum, *IOP Conference Series: Mater. Sci. Eng.* 82(1) (2015) 012083.
- [18] E. Nes, Recovery revisited, *Acta Metall. Materlia* 43(6) (1995) 2189-2207.
- [19] D. Raabe, 23 - Recovery and Recrystallization: Phenomena, Physics, Models, Simulation A2 - Laughlin, David E, in: K. Hono (Ed.), *Physical Metallurgy (Fifth Edition)*, Elsevier, Oxford, 2014, pp. 2291-2397.
- [20] C.Y. Yu, P.L. Sun, P.W. Kao, C.P. Chang, Evolution of microstructure during annealing of a severely deformed aluminum, *Mater. Sci. Eng., A* 366(2) (2004) 310-317.
- [21] D. Kohli, R. Rakesh, V.P. Sinha, G.J. Prasad, I. Samajdar, Fabrication of simulated plate fuel elements: Defining role of stress relief annealing, *J. Nucl. Mater.* 447(1–3) (2014) 150-159.
- [22] M. Verdier, F. Bley, M. Janecek, F. Livet, J.P. Simon, Y. Bréchet, Characterization of dislocation structures and internal stresses in Al-Mg alloys during recovery by synchrotron radiation, *Mater. Sci. Eng., A* 234-236(Supplement C) (1997) 258-262.
- [23] O. Vohringer, Relaxation of residual stresses by annealing or mechanical treatment, Pergamon Press, *Advances in Surface Treatments. Technology--Applications--Effects.* 4 (1987) 367-396.
- [24] P.J. Withers, H.K.D.H. Bhadeshia, Residual stress. Part 2 – Nature and origins, *Mater. Sci. Technol.* 17(4) (2001) 366-375.
- [25] M.B. Bever, D.L. Holt, A.L. Titchener, The stored energy of cold work, *Prog. Mater Sci.* 17 (1973) 5-177.
- [26] T. Hasegawa, U.F. Kocks, Thermal recovery processes in deformed aluminum, *Acta Metall.* 27(11) (1979) 1705-1716.
- [27] A. Borbély, G. Hoffmann, E. Aernoudt, T. Ungár, Dislocation arrangement and residual long-range internal stresses in copper single crystals at large deformations, *Acta Mater.* 45(1) (1997) 89-98.

- [28] S. Shekhawat, V. Basavaraj, V. Hiwarkar, R. Chakrabarty, J. Nemade, P. J. Guruprasad, K. Suresh, R. Doherty, I. Samajdar, Direct Experimental Observations on Concurrent Microstructure and Magnetic Property Developments in Non-Grain Oriented Electrical Steel, *Metall. Mater. Trans. A* 45(9) (2014) 3695-3698.
- [29] K. Wierzbowski, A. Baczyński, R. Wawszczak, J. Tarasiuk, P. Gerber, B. Bacroix, A. Lodini, Residual stress and stored energy during recrystallisation in polycrystalline copper, *Mater. Sci. Technol.* 21(1) (2005) 46-52.
- [30] G. Kumar, R. Singh, J. Singh, D. Srivastava, G.K. Dey, I. Samajdar, Defining the stages of annealing in a moderately deformed commercial Zirconium alloy, *J. Nucl. Mater.* 466 (2015) 243-252.
- [31] A. Ridha, W. Hutchinson, Recrystallisation mechanisms and the origin of cube texture in copper, *Acta Metall.* 30(10) (1982) 1929-1939.
- [32] O.M. Ivasishin, S.V. Shevchenko, N.L. Vasiliev, S.L. Semiatin, A 3-D Monte-Carlo (Potts) model for recrystallization and grain growth in polycrystalline materials, *Mater. Sci. Eng., A* 433(1) (2006) 216-232.
- [33] P. Peczak, M.J. Luton, A Monte Carlo study of the influence of dynamic recovery on dynamic recrystallization, *Acta Metall. Materlia* 41(1) (1993) 59-71.
- [34] B. Radhakrishnan, G.B. Sarma, T. Zacharia, Modeling the kinetics and microstructural evolution during static recrystallization—Monte Carlo simulation of recrystallization, *Acta Mater.* 46(12) (1998) 4415-4433.
- [35] D.J. Srolovitz, G.S. Grest, M.P. Anderson, Computer simulation of recrystallization—I. Homogeneous nucleation and growth, *Acta Metall.* 34(9) (1986) 1833-1845.
- [36] A. Arsenlis, W. Cai, M. Tang, M. Rhee, T. Opperstrup, G. Hommes, T.G. Pierce, V.V. Bulatov, Enabling strain hardening simulations with dislocation dynamics, *Modell. Simul. Mater. Sci. Eng.* 15(6) (2007) 553.
- [37] L.P. Kubin, G. Canova, M. Condat, B. Devincere, V. Pontikis, Y. Bréchet, Dislocation microstructures and plastic flow: a 3D simulation, *Solid State Phenom., Trans Tech Publ*, 1992, pp. 455-472.
- [38] E. Van der Giessen, A. Needleman, Discrete dislocation plasticity: a simple planar model, *Modell. Simul. Mater. Sci. Eng.* 3(5) (1995) 689.

- [39] T.D. de la Rubia, H.M. Zbib, T.A. Khraishi, B.D. Wirth, M. Victoria, M.J. Caturla, Multiscale modelling of plastic flow localization in irradiated materials, *Nature* 406(6798) (2000) 871.
- [40] N. Ghoniem, S.-H. Tong, L. Sun, Parametric dislocation dynamics: a thermodynamics-based approach to investigations of mesoscopic plastic deformation, *Phys. Rev. B* 61(2) (2000) 913.
- [41] D. Weygand, L. Friedman, E. Van der Giessen, A. Needleman, Aspects of boundary-value problem solutions with three-dimensional dislocation dynamics, *Modell. Simul. Mater. Sci. Eng.* 10(4) (2002) 437.
- [42] A. Vattré, B. Devincere, F. Feyel, R. Gatti, S. Groh, O. Jamond, A. Roos, Modelling crystal plasticity by 3D dislocation dynamics and the finite element method: the discrete-continuous model revisited, *J. Mech. Phys. Solids* 63 (2014) 491-505.
- [43] N. Irani, J. Remmers, V. Deshpande, Finite strain discrete dislocation plasticity in a total Lagrangian setting, *J. Mech. Phys. Solids* 83 (2015) 160-178.
- [44] S. M. Keralavarma, A. A. Benzerga, High-temperature discrete dislocation plasticity, *J. Mech. Phys. Solids* 82 (2015) 1-22.
- [45] A. A. Benzerga, Y. Bréchet, A. Needleman, E. Van der Giessen, Incorporating three-dimensional mechanisms into two-dimensional dislocation dynamics, *Modell. Simul. Mater. Sci. Eng.* 12(1) (2003) 159.
- [46] V. Bulatov, F.F. Abraham, L. Kubin, B. Devincere, S. Yip, Connecting atomistic and mesoscale simulations of crystal plasticity, *Nature* 391(6668) (1998) 669.
- [47] V.V. Bulatov, L.L. Hsiung, M. Tang, A. Arsenlis, M.C. Bartelt, W. Cai, J.N. Florando, M. Hiratani, M. Rhee, G. Hommes, Dislocation multi-junctions and strain hardening, *Nature* 440(7088) (2006) 1174.
- [48] H. Fan, S. Aubry, A. Arsenlis, J.A. El-Awady, The role of twinning deformation on the hardening response of polycrystalline magnesium from discrete dislocation dynamics simulations, *Acta Mater.* 92 (2015) 126-139.
- [49] A. A. Benzerga, Y. Brechet, A. Needleman, E. Van der Giessen, The stored energy of cold work: Predictions from discrete dislocation plasticity, *Acta Mater.* 53(18) (2005) 4765-4779.
- [50] L. Nicola, E. Van der Giessen, A. Needleman, Discrete dislocation analysis of size effects in thin films, *J. Appl. Phys.* 93(10) (2003) 5920-5928.
- [51] H. Kreuzer, R. Pippan, Discrete dislocation simulation of nanoindentation: indentation size effect and the influence of slip band orientation, *Acta Mater.* 55(9) (2007) 3229-3235.

- [52] P. J. Guruprasad, A. A. Benzerga, Size effects under homogeneous deformation of single crystals: a discrete dislocation analysis, *J. Mech. Phys. Solids* 56(1) (2008) 132-156.
- [53] D. Kiener, P.J. Guruprasad, S.M. Keralavarma, G. Dehm, A.A. Benzerga, Work hardening in micropillar compression: In situ experiments and modeling, *Acta Mater.* 59(10) (2011) 3825-3840.
- [54] M.D. Uchic, P.A. Shade, D.M. Dimiduk, Plasticity of micrometer-scale single crystals in compression, *Annu Rev Mater. Res.* 39 (2009) 361-386.
- [55] A.A. Benzerga, Micro-pillar plasticity: 2.5 D mesoscopic simulations, *J. Mech. Phys. Solids* 57(9) (2009) 1459-1469.
- [56] J.A. El-Awady, Unravelling the physics of size-dependent dislocation-mediated plasticity, *Nature Commun.* 6 (2015) 5926.
- [57] K.M. Davoudi, L. Nicola, J.J. Vlassak, Dislocation climb in two-dimensional discrete dislocation dynamics, *J. Appl. Phys.* 111(10) (2012) 103522.
- [58] S.M. Keralavarma, T. Cagin, A. Arsenlis, A.A. Benzerga, Power-Law Creep from Discrete Dislocation Dynamics, *Phys. Rev. Lett.* 109(26) (2012) 265504.
- [59] D. Mordehai, E. Clouet, M. Fivel, M. Verdier, Introducing dislocation climb by bulk diffusion in discrete dislocation dynamics, *Philos. Mag.* 88(6) (2008) 899-925.
- [60] K. Danas, V. Deshpande, Plane-strain discrete dislocation plasticity with climb-assisted glide motion of dislocations, *Modell. Simul. Mater. Sci. Eng.* 21(4) (2013) 045008.
- [61] S.H. Haghghat, G. Eggeler, D. Raabe, Effect of climb on dislocation mechanisms and creep rates in γ' -strengthened Ni base superalloy single crystals: A discrete dislocation dynamics study, *Acta Mater.* 61(10) (2013) 3709-3723.
- [62] P. J. Guruprasad, W. Carter, A. A. Benzerga, A discrete dislocation analysis of the Bauschinger effect in microcrystals, *Acta Mater.* 56(19) (2008) 5477-5491.
- [63] R. Reali, F. Boioli, K. Gouriet, P. Carrez, B. Devincere, P. Cordier, Modeling plasticity of MgO by 2.5D dislocation dynamics simulations, *Mater. Sci. Eng., A* 690 (2017) 52-61.
- [64] F. Boioli, P. Carrez, P. Cordier, B. Devincere, K. Gouriet, P. Hirel, A. Kraych, S. Ritterbex, Pure climb creep mechanism drives flow in Earth's lower mantle, *Sci. Adv.* 3(3) (2017).
- [65] S.S. Shishvan, R.M. McMeeking, T.M. Pollock, V.S. Deshpande, Discrete dislocation plasticity analysis of the effect of interfacial diffusion on the creep response of Ni single-crystal superalloys, *Acta Mater.* 135 (2017) 188-200.

- [66] J. Peng, V. Ji, W. Seiler, A. Tomescu, A. Levesque, A. Bouteville, Residual stress gradient analysis by the GIXRD method on CVD tantalum thin films, *Surf. Coat. Technol.* 200(8) (2006) 2738-2743.
- [67] G. Kumar, S. Balo, A. Dhoble, J. Singh, R. Singh, D. Srivastava, G.K. Dey, I. Samajdar, Through-Thickness Deformation Gradient in a Part-Pilgered Zirconium Tube: Experimental Measurements and Numerical Validation, *Metall. Mater. Trans. A* 48(6) (2017) 2844-2857.
- [68] U. Welzel, J. Ligot, P. Lamparter, A.C. Vermeulen, E.J. Mittemeijer, Stress analysis of polycrystalline thin films and surface regions by X-ray diffraction, *J. Appl. Crystallogr.* 38(1) (2005) 1-29.
- [69] S. Raveendra, S. Mishra, K.V. Mani Krishna, H. Weiland, I. Samajdar, Patterns of Recrystallization in Warm- and Hot-Deformed AA6022, *Metall. Mater. Trans. A* 39(11) (2008) 2760.
- [70] S. Raveendra, H. Paranjape, S. Mishra, H. Weiland, R. Doherty, I. Samajdar, Relative stability of deformed cube in warm and hot deformed AA6022: possible role of strain-induced boundary migration, *Metall. Mater. Trans. A* 40(9) (2009) 2220-2230.
- [71] M.H. Alvi, S.W. Cheong, J.P. Suni, H. Weiland, A.D. Rollett, Cube texture in hot-rolled aluminum alloy 1050 (AA1050)—nucleation and growth behavior, *Acta Mater.* 56(13) (2008) 3098-3108.
- [72] O. Engler, V. Randle, Introduction to texture analysis: macrotexture, microtexture, and orientation mapping, CRC press 2009.
- [73] F. Barou, C. Maurice, J.-M. Feppon, J. Driver, Sub-grain boundary mobilities during recovery of binary Al–Mn alloys, *Int. J. Mater. Res.* 100(4) (2009) 516-521.
- [74] D. Field, P. Trivedi, S. Wright, M. Kumar, Analysis of local orientation gradients in deformed single crystals, *Ultramicroscopy* 103(1) (2005) 33-39.
- [75] H. Abrams, Grain size measurement by the intercept method, *Metallography* 4(1) (1971) 59-78.
- [76] S. Groh, E. Marin, M. Horstemeyer, H. Zbib, Multiscale modeling of the plasticity in an aluminum single crystal, *Int. J. Plast.* 25(8) (2009) 1456-1473.
- [77] J. Kallend, Y. Huang, Orientation dependence of stored energy of cold work in 50% cold rolled copper, *Metal science* 18(7) (1984) 381-386.

- [78] N. Rajmohan, Y. Hayakawa, J. Szpunar, J. Root, Neutron diffraction method for stored energy measurement in interstitial free steel, *Acta Mater.* 45(6) (1997) 2485-2494.
- [79] N. Rajmohan, J. Szpunar, Stored energy in can body aluminium alloy after cold rolling and stress relieving, *Mater. Sci. Technol.* 15(11) (1999) 1259-1265.
- [80] D.D. Sam, B.L. Adams, Orientation and strain dependence of stored energy of cold work in axisymmetric copper, *Metall. Mater. Trans. A* 17(3) (1986) 513-517.
- [81] H. Behnken, Strain-Function Method for the Direct Evaluation of Intergranular Strains and Stresses, *Phys. Status Solidi (A)* 177(2) (2000) 401-418.
- [82] P. Van Houtte, L. De Buyser, The influence of crystallographic texture on diffraction measurements of residual stress, *Acta Metall. Materlia* 41(2) (1993) 323-336.
- [83] Y.D. Wang, R.L. Peng, R.L. McGreevy, A novel method for constructing the mean field of grain-orientation-dependent residual stress, *Philos. Mag. Lett.* 81(3) (2001) 153-163.
- [84] Y.D. Wang, X.-L. Wang, A.D. Stoica, J.W. Richardson, R. Lin Peng, Determination of the stress orientation distribution function using pulsed neutron sources, *J. Appl. Crystallogr.* 36(1) (2003) 14-22.
- [85] I. Groma, X-ray line broadening due to an inhomogeneous dislocation distribution, *Phys. Rev. B* 57(13) (1998) 7535.
- [86] T. Ungár, Microstructural parameters from X-ray diffraction peak broadening, *Scripta Mater.* 51(8) (2004) 777-781.
- [87] B. Cullity, *Elements of X-ray Diffraction*, 2nd, Adisson-Wesley Publishing USA (1978).
- [88] I.C. Noyan, J.B. Cohen, *Residual stress: measurement by diffraction and interpretation*, Springer-Verlag 2013.
- [89] J. Epp, H. Surm, T. Hirsch, F. Hoffmann, Residual stress relaxation during heating of bearing rings produced in two different manufacturing chains, *J. Mater. Process. Technol.* 211(4) (2011) 637-643.
- [90] B.B. He, *Two-dimensional X-ray diffraction*, John Wiley & Sons 2011.

Chapter 5

Orientation Dependent Developments in Misorientation and Residual Stress in Rolled Aluminum: The Defining Role of Dislocation Interactions

5.1 Introduction

Evolution of the deformed microstructures may differ in scale and also in details [1-2], but such evolution is expected to be orientation dependent [3-5]. Part of the deformed microstructure developments may originate from dislocation dynamics within the individual single-crystals, while additional contributions are also expected from interactions between the neighboring grains. Decoupling these two effects, on the orientation sensitive evolution of deformed microstructure, may not be practical experimentally. This is where appropriate modelling may make a critical impact.

Plastic deformation, in single and polycrystalline material, can be viewed both in terms of dislocation dynamics [6-8] and continuum plasticity [9-11]. A combined (or hybrid) approach has also been proposed in the last two decades [11]. In a generic crystal plasticity framework, the self and latent hardening of the respective slip systems are considered to be isotropic [12-13]. In other words, strain hardening is identical for any interaction between two dissimilar slip systems. In reality, however, strain hardening is strongly dependent on type of dislocation interactions and junctions formed [14-16]. Orientation sensitive dislocation interactions, or appropriate constitutive laws accounting for the same, can be incorporated [11, 17-19] in the CPFPE. This has been termed as CPFPE with DIBH (dislocation interaction based hardening). Such a model may not offer better solution for overall deformation texture development, but was shown to be extremely effective in capturing flow stress anisotropy [20-21].

This study first quantified experimental patterns of orientation dependent deformed microstructure (misorientation, dislocation density and residual stress) evolution in rolled commercial purity aluminum. Once the hierarchy of orientation sensitivity was established statistically, CPFPE (with and without DIBH) and DDD simulations were used to capture the experimentally observed orientation sensitivity. It was hypothesized that relative success of such numerical simulations

would indicate importance of single-crystal dislocation interactions versus polycrystalline slip-transfer as the governing mechanism for orientation dependent microstructure evolution.

5.2 Experimental Details

A fully recrystallized (with mean grain size of ~50 μm) commercial purity AA1050 alloy (chemical composition listed in Table 5.1) was cold rolled to different thickness reductions (true strains of 0.22, 0.51 and 0.92) in a laboratory rolling mill. Controlled near plane strain deformation (~0.04 true strain) was also imposed in a split channel die plane strain compression (SCDPSC) set-up [22]. Samples (for details on sample preparation, please refer chapter 3.2) were taken from the mid-width and mid-thickness sections for microstructural characterization. The latter involved XRD (X-ray diffraction: in a BrukerTM D8 Discover with micro-focus plus VantecTM area-detector) and EBSD (electron backscattered diffraction: in a FEITM Quanta 3D-FEG (field emission gun) scanning electron microscope (SEM) equipped with TSL-OIMTM system).

Table 5.1: Chemical composition, in wt% alloying elements, of the AA1050 used in this study.

Alloy	Si	Cu	Fe	Mg	Mn	Al
AA1050	0.25	0.05	0.40	0.05	0.05	balance

The XRD measurements were made as single-crystal micro-Laue diffraction [4], capable of establishing residual stress matrix in individual grains. In addition, the X-ray peak shift and peak profile were also measured as four incomplete pole figures and plotted as appropriate [2, 23] ODF (orientation distribution function) sections: the so-called dislocation density and residual stress ODFs [5, 24]. Large area EBSD scans (at least 1000 $\mu\text{m} \times 1000 \mu\text{m}$) were performed at a step size of 0.3 μm , keeping beam and video conditions identical between the scans. Other than standard inverse pole figure (IPF) mapping, the EBSD data was also used to capture in-grain misorientation, GOS (grain orientation spread) and KAM (kernel average misorientation), developments. These can be written as,

$$GOS = \frac{1}{N} \sum_{i=1}^N (g_{av} g_i^{-1}) \quad \text{-----(5.1)}$$

$$KAM = \frac{1}{N} \sum_k g_i g_j^{-1} \quad \text{-----(5.2)}$$

where a grain orientation contains N data points with g_i and g_j representing orientations of two consecutive points i and j. g_{av} is the quaternion average of grain orientation for all data points. In calculation on KAM, misorientation between points i and any of its neighbor j did not exceed 5° . In other words, careful experiments, with XRD and EBSD, established orientation dependent development in deformed microstructures.

5.3 Model Description

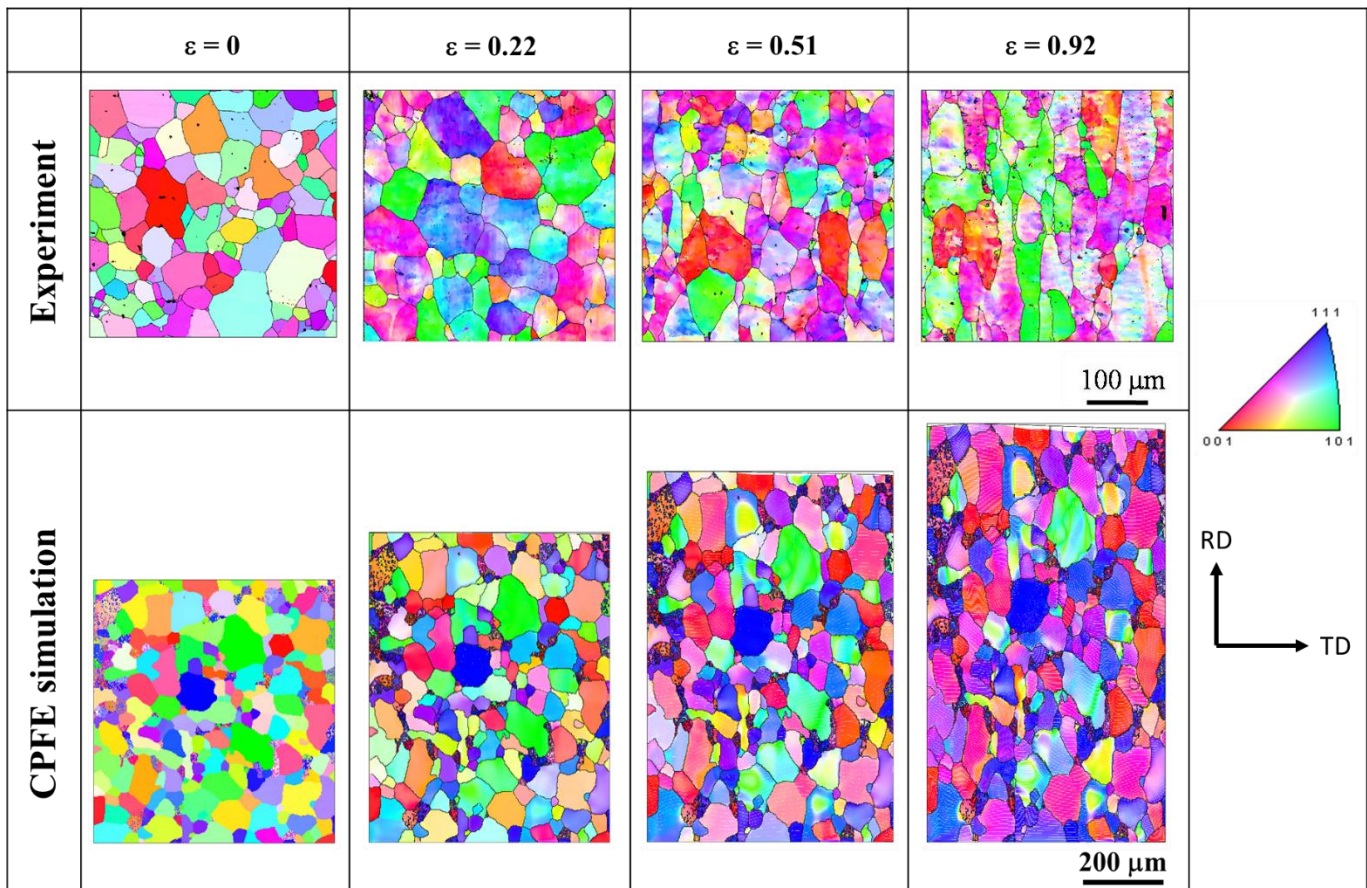
The CPFE model used a user subroutine interface, UMAT, developed by Marin et al. [12]. MTEX™ [25] was used to discretize EBSD data, of the undeformed state, into a C3D8R element (based on EBSD step size). Each grain was represented as one single (quaternion average) orientation. The undeformed microstructure for the CPFE was a pseudo 2D mesh with only one element thickness in z direction. CPFE simulations were conducted, but without and with DIBH. Without DIBH represented isotropic latent-hardening of all slip systems. The introduction of DIBH, on the other hand, uses dislocation interaction based latent hardening matrix [14]. Hardening on all latent slip systems is not identical when dislocation interactions are accounted for. Other material parameters used for the CPFE simulations are shown in Table 5.2. For details of the DDD simulation, please refer chapter 3.

Table 5.2: Material parameters and hardening coefficients [14] for different junctions used in this study.

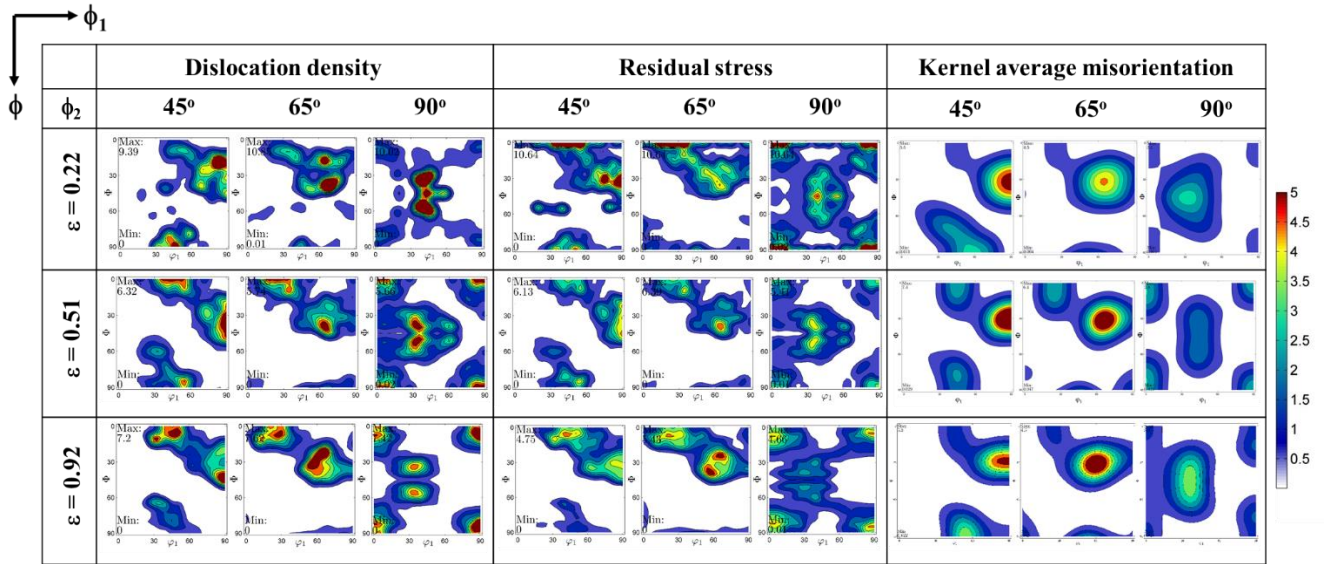
h_0^α	$\kappa_{s,0}^\alpha$	$\kappa_{s,S}^\alpha$	m	$\dot{\gamma}^0$	Hirth (g_2)	Collinear (g_3)	Glissile (g_4)	Lomer (g_5)
50 MPa	20.50 MPa	55.80 MPa	0.03	$5E10 \text{ s}^{-1}$	0.0454 ± 0.003	$0.625 \pm$ 0.044	$0.137 \pm$ 0.014	$0.122 \pm$ 0.012

5.4 Results

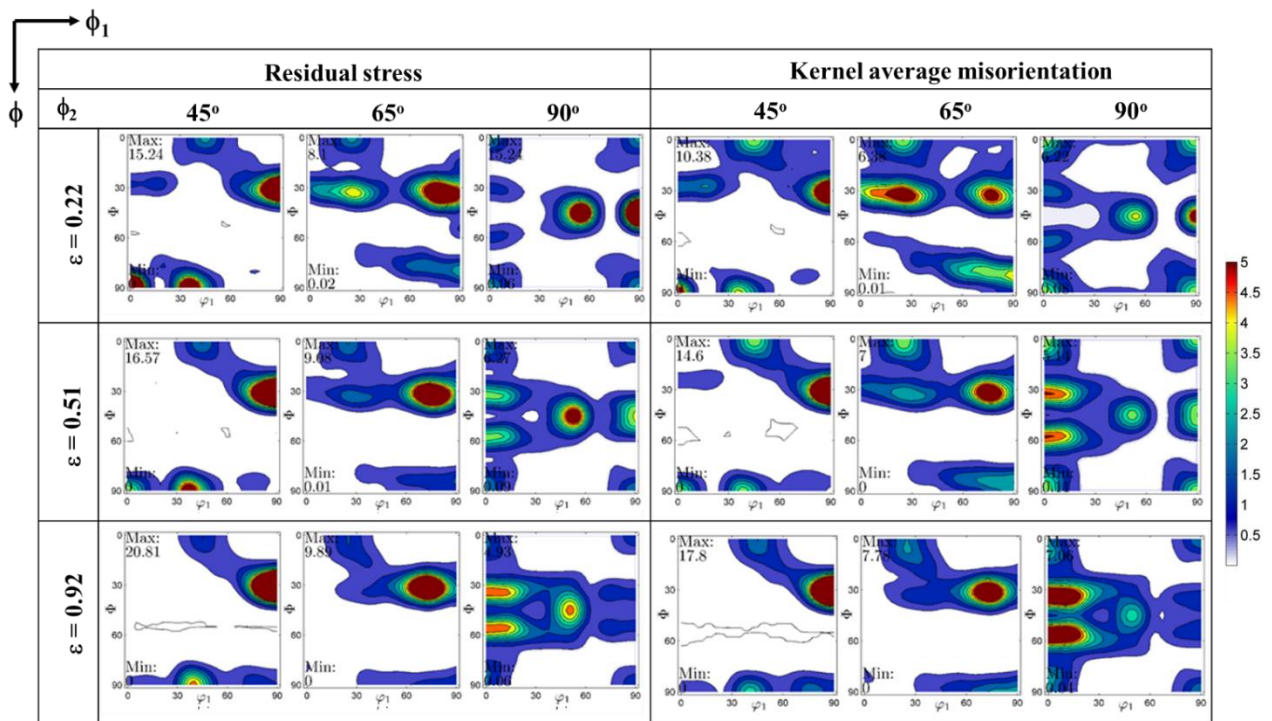
As shown in figure 5.1a, progressive deformation, in both experiments and simulations, led to grain elongation and developments in orientation gradients. However, elongation and in-grain orientation gradients were, arguably, more uniform in the simulated microstructures. Both the experiments (figure 5.1b) and the CPFЕ simulations (figure 5.1c) were also successful in quantifying the orientation dependent microstructure evolution as appropriate ODF sections. Experimental data were exploited to plot ODFs of dislocation density, residual stress (σ_{11}) and KAM (see figure 5.1b). The residual stress and KAM ODFs (figure 5.1c), on the other hand, were obtained from the CPFЕ data. They showed qualitative match between experiments and simulation, and also an apparent trend that orientations with higher KAM and dislocation density also had higher σ_{11} .



(a)



(b)



(c)

Figure 5.1: (a) Microtexture, in inverse pole figure (IPF) notation, evolution of rolled aluminum: as observed experimentally and simulated with crystal plasticity finite element (CPFE incorporating DIBH (dislocation interaction based hardening)). (b) Experimental ODFs (orientation distribution function) of dislocation density, residual stress (σ_{11}) and kernel average misorientation (KAM). (c) CPFE, with DIBH, simulated ODFs of σ_{11} and KAM.

As indicated in the earlier paragraph, the simulations appeared to reflect lower in-grain orientation gradients (see figure 5.1a). This translated into the quantitative values of GOS (figure 5.2a). The CPFE simulations, with and without DIBH, clearly underpredicted the GOS. Local point-to-point misorientations, or the KAM values were, however, overpredicted in the CPFE. Interestingly, experimental orientation dependence of KAM, GOS and σ_{11} evolutions were captured remarkably well by CPFE simulations with DIBH (see figure 5.3). However, this was not the case for CPFE simulations without DIBH. In a word, though both CPFE simulations did not quantitatively capture exact experimental values of in-grain misorientation developments (see figure 5.2): CPFE with DIBH was remarkably successful in simulating the experimental orientation dependence (see figure 5.3).

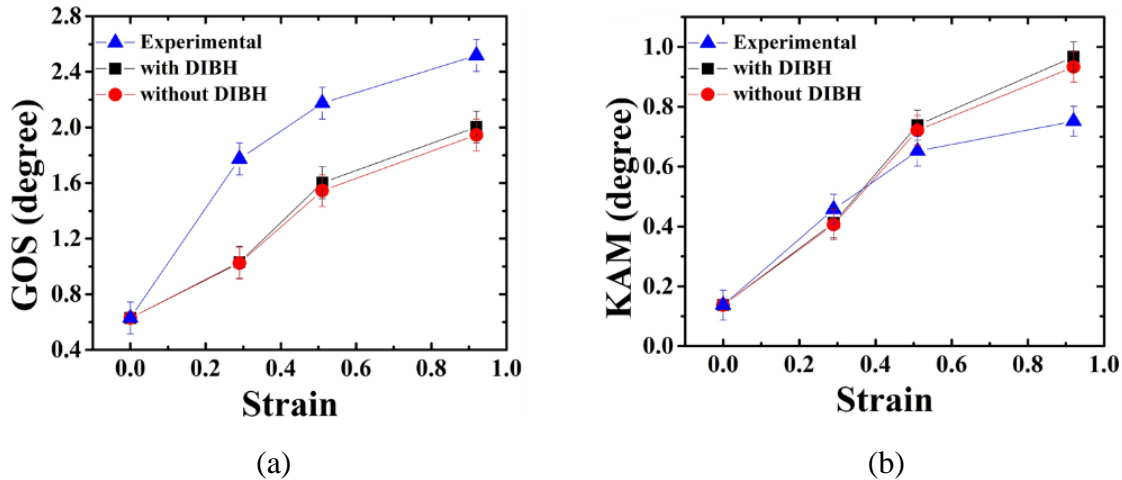


Figure 5.2: Evolution of (a) grain orientation spread (GOS) and (b) KAM with plastic strain. These are shown for experimental and simulated (CPFE simulations with and without the dislocation interaction based hardening (DIBH)) data. Error bars indicate standard deviations from multiple EBSD scans and simulations.

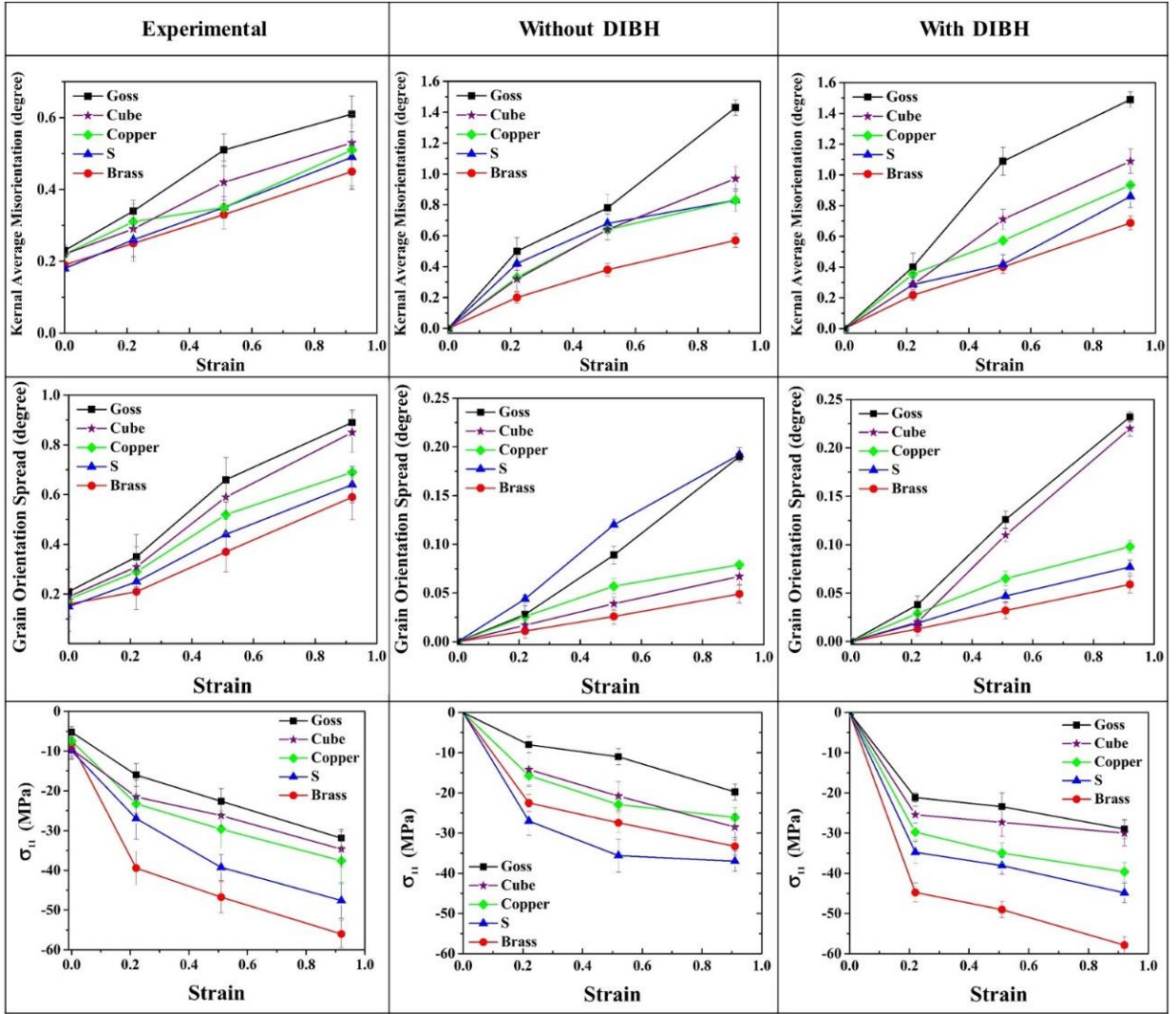
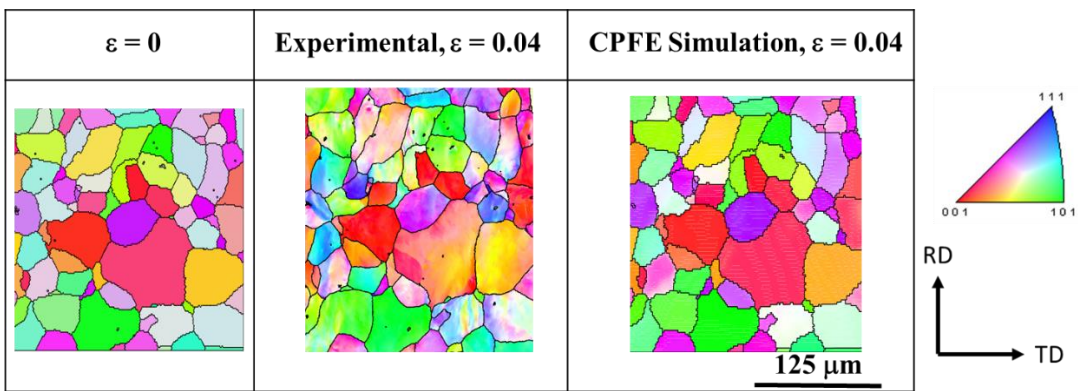


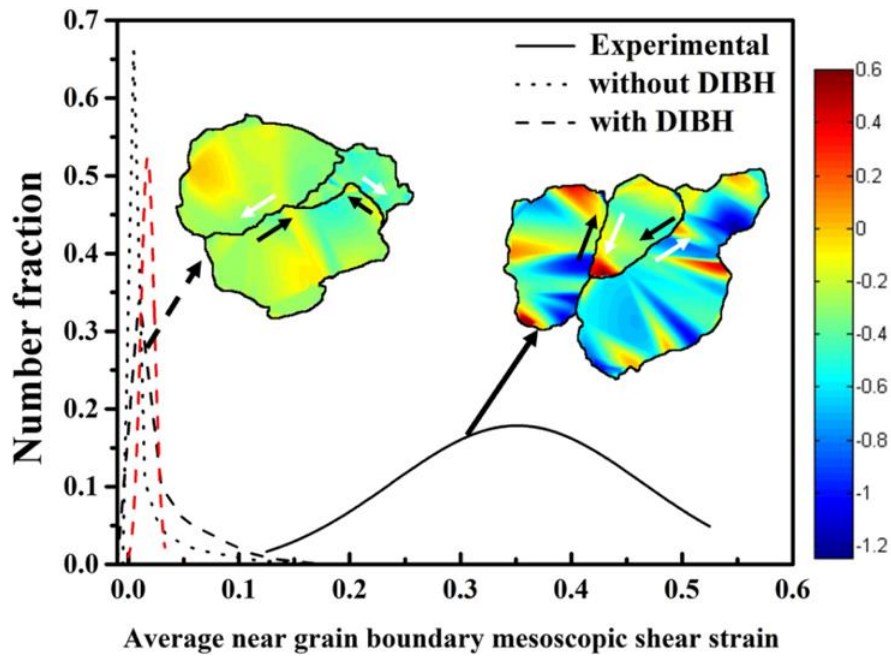
Figure 5.3: Orientation dependent evolution of KAM, GOS and σ_{11} : as obtained experimentally and simulated with CPFЕ (with and without DIBH). These are shown for Goss $\{110\}\{001\}$, Cube $\{100\}\{001\}$, Copper $\{112\}\{111\}$, S $\{123\}\{63\bar{4}\}$ and Brass $\{110\}\{1\bar{1}2\}$ [23]. Error bars indicate standard deviations from multiple EBSD scans and simulations.

To compare between experiments and simulations further, direct observations were made through SCDPSC specimens. As shown in figure 5.4a, the simulation did not exactly reproduce the experimental microstructures. First, the shapes of the deformed grains were often different in the experiments and the simulations. And the simulations appeared to have lower orientation gradients. Using an algorithm described elsewhere [22], the near boundary mesoscopic shear (NBMS) strains

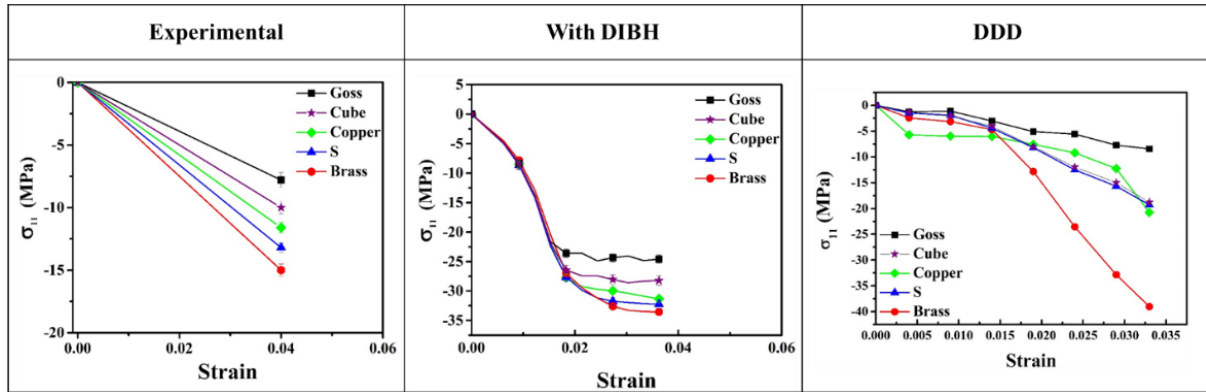
were calculated. As shown in figure 5.4b, the simulated structures had insignificant NBMS, which was comparable with the measurement uncertainty. The NBMS in the experiments, on the other hand, were substantial. It is hence clear that the CPFЕ simulations did not consider near-neighbor interactions and associated slip-transfer. However, and as shown in figure 5.4c, the CPFЕ simulations with DIBH successfully captured the experimental trends (direct *ex-situ* measurements) in the orientation dependence of σ_{11} evolution. It is also clear (as in figure 5.4c) the same hierarchy of orientation sensitivity was also captured with single-crystal DDD.



(a)



(b)



(c)

Figure 5.4: (a) Direct observation on microstructural evolution in split channel die plane strain compression (SCDPSC). The same microstructure was also simulated with CPFEE incorporating DIBH. (b) Near boundary mesoscopic shear (NBMS) strains were measured [18] from the appropriate microstructures (both experimental and simulated): and are shown for a representative grain cluster. Average NBMS, for ~ 50 randomly selected grains, are plotted from the experimental and simulated grain structures. Also included is the estimated measurement uncertainty as red dotted line. (c) Residual stress evolution were measured experimentally and simulated numerically for different ideal orientations: Goss $\{110\}\langle 001\rangle$, Cube $\{100\}\langle 001\rangle$, Copper $\{112\}\langle 111\rangle$, S $\{123\}\langle 63\bar{4}\rangle$ and Brass $\{110\}\langle \bar{1}12\rangle$ [23].

5.5 Discussion and summary

This study thus established, experimentally, a clear hierarchy of orientation dependent microstructure (misorientation and residual stress) evolution. An orientation sensitive deformed microstructure is also expected [4, 26-28] from existing literature. The problem has often been to relate such experimental orientation dependence with crystal plasticity. The experimental values of stored energy [29-31], for example, were not conclusively related to the Taylor factor: a scalar index of poly-crystalline plasticity. It was stipulated that changes in crystallographic orientations, during plastic deformation, may not allow such a simplified relationship. Though residual stresses were also measured in the Euler space [32], the experimentally measured stress ODFs were never compared to values emerging from plasticity simulations. It is important, at this point, to refer that chapter 3 established clear patterns of orientation dependent evolution of dislocation density and residual stress, and simulated the same with DDD. Hansen et al. [26] also differentiated the

dislocation substructure evolution based on crystallographic orientations in an IPF space. This has been extended by Feaugas and Haddou [33] in clear regimes of dislocation interactions and corresponding domains of residual stresses. It thus appears that the in-grain residual stresses are decided by a hierarchy of dislocation arrangement [4, 33].

Modelling dislocation interactions, analytically or as DDD simulations [6-8], has certain limitations. Firstly, only limited strains can be imposed [34]. More importantly, the DDD is typically valid for single crystals [34]. Though there are enough indications [11, 19, 35] that CPFE may capture the experimental patterns of microstructural evolution, rarely such simulations were compared with quantitative data of orientation dependent microstructural evolution. And that is exactly what was attempted in this study. The CPFE with DIBH was successful, both at lower (0.04) and higher (0.22-0.92) strains, in reproducing the experimental hierarchy of orientation sensitivity. And these simulations were conducted without near-neighbor interactions (figure 5.4b) and associated slip-transfer. Though slip transfer or strain partitioning between the neighbors may still determine the exact magnitude of in-grain orientation gradients, the orientation dependent developments in misorientation and residual Stress are clearly controlled by in-grain dislocation interactions.

References

1. Frederick John Humphreys and Max Hatherly: *Recrystallization and related annealing phenomena*. second ed. (Pergamon Materials Series, Elsevier, Oxford 2004).
2. Bert Verlinden, Julian Driver, Indradev Samajdar and Roger D Doherty: *Thermo-mechanical processing of metallic materials*. first ed. (Pergamon Materials Series, Elsevier, Oxford 2007).
3. Niels Hansen, Xiaoxu Huang and Grethe Winther, *Materials Science and Engineering: A* 2008, vol. 494, pp. 61-67.
4. Arijit Lodh, Tawqeer Nasir Tak, Aditya Prakash, P. J. Guruprasad, Christopher Hutchinson and Indradev Samajdar, *Metallurgical and Materials Transactions A* 2017, vol. 48, pp. 5317-5331.
5. CC Merriman, DP Field and P Trivedi, *Materials Science and Engineering: A* 2008, vol. 494, pp. 28-35.
6. LP Kubin and G Canova, *Scripta metallurgica et materialia* 1992, vol. 27, pp. 957-962.

7. Ladislav P Kubin, G Canova, M Condat, Benoit Devincere, V Pontikis and Yves Bréchet, In *Solid State Phenomena*, (Trans Tech Publ: 1992), pp 455-472.
8. Hussein M Zbib, Moono Rhee and John P Hirth, *International Journal of Mechanical Sciences* 1998, vol. 40, pp. 113-127.
9. L. Anand and M. Kothari, *Journal of the Mechanics and Physics of Solids* 1996, vol. 44, pp. 525-558.
10. D. Peirce, R. J. Asaro and A. Needleman, *Acta Metallurgica* 1982, vol. 30, pp. 1087-1119.
11. Franz Roters, Philip Eisenlohr, Luc Hantcherli, Denny Dharmawan Tjahjanto, Thomas R Bieler and Dierk Raabe, *Acta Materialia* 2010, vol. 58, pp. 1152-1211.
12. EB Marin and PR Dawson, *Computer Methods in Applied Mechanics and Engineering* 1998, vol. 165, pp. 1-21.
13. Esteban B Marin, Sandia National Laboratories 2006.
14. Benoît Devincere, Ladislav Kubin and Thierry Hoc, *Scripta Materialia* 2006, vol. 54, pp. 741-746.
15. P Shanthraj and MA Zikry, *Acta materialia* 2011, vol. 59, pp. 7695-7702.
16. Tamás Ungár, Alexandru D Stoica, Géza Tichy and Xun-Li Wang, *Acta Materialia* 2014, vol. 66, pp. 251-261.
17. Halle Abrams, *Metallography* 1971, vol. 4, pp. 59-78.
18. Alankar Alankar, Ioannis N Mastorakos and David P Field, *Acta materialia* 2009, vol. 57, pp. 5936-5946.
19. Athanasios Arsenlis and David M Parks, *Journal of the Mechanics and Physics of Solids* 2002, vol. 50, pp. 1979-2009.
20. N Bertin, CN Tomé, IJ Beyerlein, MR Barnett and L Capolungo, *International Journal of Plasticity* 2014, vol. 62, pp. 72-92.
21. Mikhail Khadyko, Stephane Dumoulin, Georges Cailletaud and Odd Sture Hopperstad, *International Journal of Plasticity* 2016, vol. 76, pp. 51-74.
22. N Keskar, S Mukherjee, KV Mani Krishna, D Srivastava, GK Dey, P Pant, RD Doherty and I Samajdar, *Acta Materialia* 2014, vol. 69, pp. 265-274.
23. Olaf Engler and Valerie Randle: *Introduction to texture analysis: microtexture, microtexture, and orientation mapping*. (CRC press, 2009).

24. Y. D. Wang, R. Lin Peng and R. L. McGreevy, *Philosophical Magazine Letters* 2001, vol. 81, pp. 153-163.
25. R Hielscher and Helmut Schaeben, *Journal of Applied Crystallography* 2008, vol. 41, pp. 1024-1037.
26. Niels Hansen, Xiaoxu Huang, Wolfgang Pantleon and Grethe Winther, *Philosophical Magazine* 2006, vol. 86, pp. 3981-3994.
27. Xiao-xu Huang and Grethe Winther, *Philosophical Magazine* 2007, vol. 87, pp. 5189-5214.
28. Jun Jiang, T Ben Britton and Angus J Wilkinson, *International Journal of Plasticity* 2015, vol. 69, pp. 102-117.
29. JS Kallend and YC Huang, *Metal science* 1984, vol. 18, pp. 381-386.
30. N Rajmohan and JA Szpunar, *Materials science and technology* 1999, vol. 15, pp. 1259-1265.
31. David D Sam and Brent L Adams, *Metallurgical and Materials Transactions A* 1986, vol. 17, pp. 513-517.
32. YD Wang, R Lin Peng and RL McGreevy, *Philosophical magazine letters* 2001, vol. 81, pp. 153-163.
33. Xavier Feaugas and H Haddou, *Philosophical Magazine* 2007, vol. 87, pp. 989-1018.
34. Erik Van der Giessen and Alan Needleman, *Modelling and Simulation in Materials Science and Engineering* 1995, vol. 3, p. 689.
35. Franz Roters, Philip Eisenlohr, Thomas R Bieler and Dierk Raabe: *Crystal plasticity finite element methods: in materials science and engineering*. (John Wiley & Sons, 2011).

Chapter 6

Defining the Orientation Dependent Microstructure Evolution through Cyclic Deformation in an Aluminum Alloy

Abstract

Fully recrystallized commercial Al-Mn alloy (AA3003) was subjected to cyclic deformation, with two different strain amplitudes ($\Delta\varepsilon_p$: 0.0001 and 0.0025) and three different temperatures (300, 323 and 348K). X-ray diffraction, with area detector, and high resolution EBSD measurements provided two novel experimental observations on orientation dependent microstructure evolution. $\{001\}$ and $\{111\}$ were shown to develop compressive stresses, while tensile stresses were noted for $\{110\}$. Equally interesting was the observation on kernel average misorientation (KAM) evolution. Dependence of KAM on crystallographic orientation was significantly more at the highest cyclic deformation temperature.

6.1 Introduction

The past chapters showed orientation dependent residual stress evolution in tensile deformation (chapter 3) and during laboratory rolling (chapter 5). Chapter 4, on the other hand, provided results on concurrent evolution of microstructure and residual stress during thermal recovery. All these incorporated niche experimental tools, especially micro-Laue diffraction for single crystal residual stress measurements and stress ODFs, and also involved appropriate numerical simulations, discrete dislocation dynamics (DDD) and crystal plasticity finite element (CPFE), to provide critical theoretical inputs.

An important implication of residual stress is towards the fatigue life of a metallic material [1, 2]. In aluminum alloys, the story goes back to the Comet disaster [3, 4] and continues today in designing alloys and microstructure for fatigue resistance [5, 6]. Though the microstructure evolution during cyclic deformation is a well-studied subject (also covered in chapter 2.2.2 of the literature review), literature is largely silent on the orientation dependent residual stress and misorientation evolution during cyclic deformation. This is the reason for designing the last chapter

of this thesis: *Defining the Orientation Dependent Microstructure Evolution through Cyclic Deformation in an Aluminum Alloy*.

Though this chapter presents two novel aspects of experimental microstructure evolution; the numerical DDD simulations, expanding on these aspects, remain incomplete (at this stage). Equally significant are absence of some critical (albeit planned) experimental data on transmission Kikuchi diffraction (TKD) and transmission electron microscopy (TEM). In the next few paragraphs, the existing results are summarized and a brief discussion is presented.

6.2 Experimental Details

The cyclic deformation involved samples of 16 mm gauge length and 6 mm × 5 mm cross section area. The deformations were conducted in a MTS-858 table-top machine with two different strain amplitudes ($\Delta\varepsilon_p$: 0.0001 and 0.0025) and three different temperatures (300, 323 and 348K). The corresponding flow stress versus number of cycles are plotted in figure 6.1. The figure shows cyclic hardening behavior for $\Delta\varepsilon_p$: 0.0025 and softening, for both strain amplitudes, with increase in temperature. Samples were collected after different number of cycles (200, 500 and 1000 cycles) and then subjected to detailed characterization.

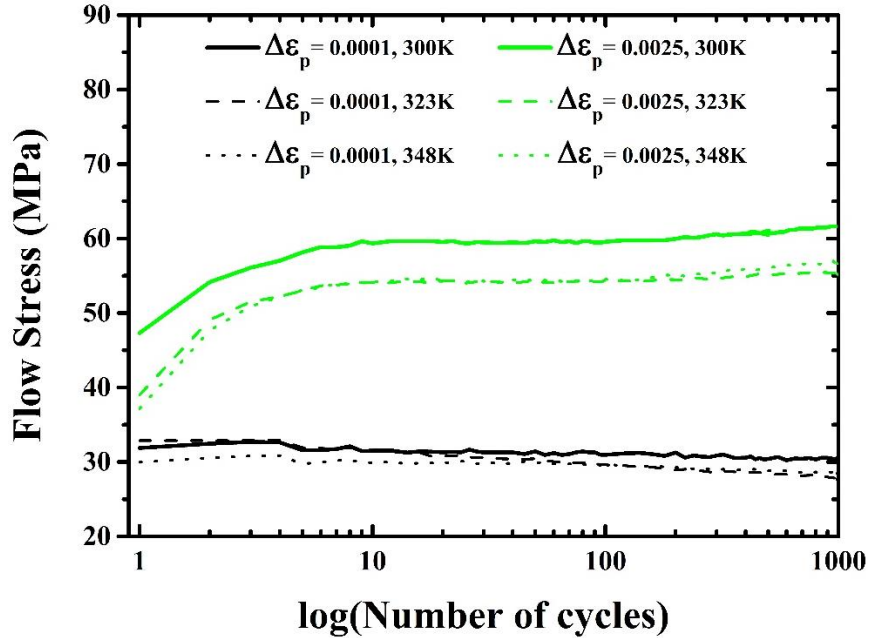


Figure 6.1: Flow stress versus number of cycles. These are shown for cyclic deformation with two different strain amplitudes ($\Delta\epsilon_p$: 0.0001 and 0.0025) and three different temperatures (300, 323 and 348K)

6.3 Results and Discussion

For details on the sample preparation, please refer chapters 3-5. The deformed samples were subjected to X-ray diffraction. A BrukersTM D8-Discover system with micro-focus X-ray and VantecTM area detector was used. A typical area detector signal is shown in figure 6.2a. The Debye-Scherrer rings represent different orientation families: generalized in the inverse pole figure, or in the detector signal image, as {111}, {001}, {110} and {113}. These are the different poles or the plane normal. Cyclic deformation brought (see figure 6.2b) clear peak shifts and changes in peak profile. In other words, though the strain amplitudes were relatively small: cyclic deformation appeared to enforce changes in dislocation density (or peak profile) and residual stress (or peak shift). Finally, it is to be noted that for cyclic deformation, with alternating strain mode, plane normal (figure 6.2a) appears more representative than the exact crystallographic orientations. Experimental measurements had also shown that differences between ideal orientations of the same family (Goss and Brass for example: both as {110}<uvw>) of plane normal had nearly identical evolution of residual stress and misorientation.

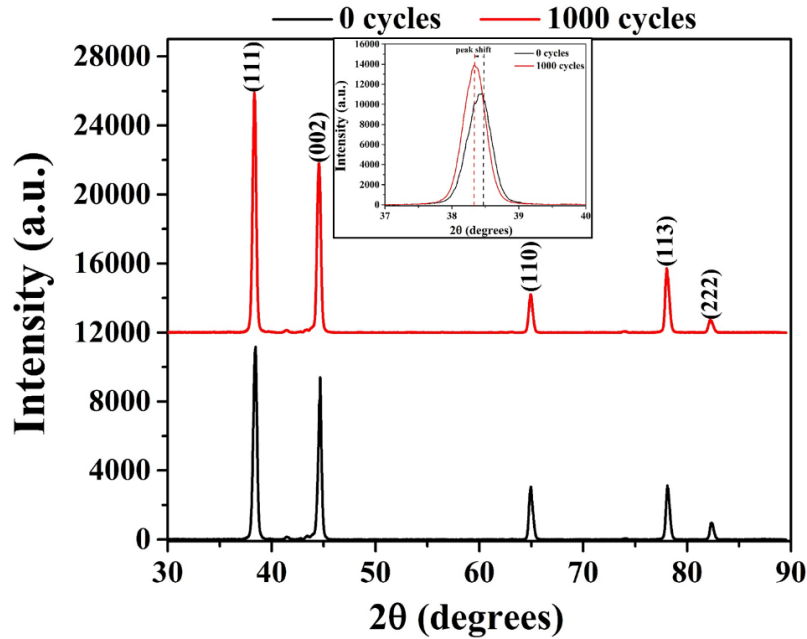
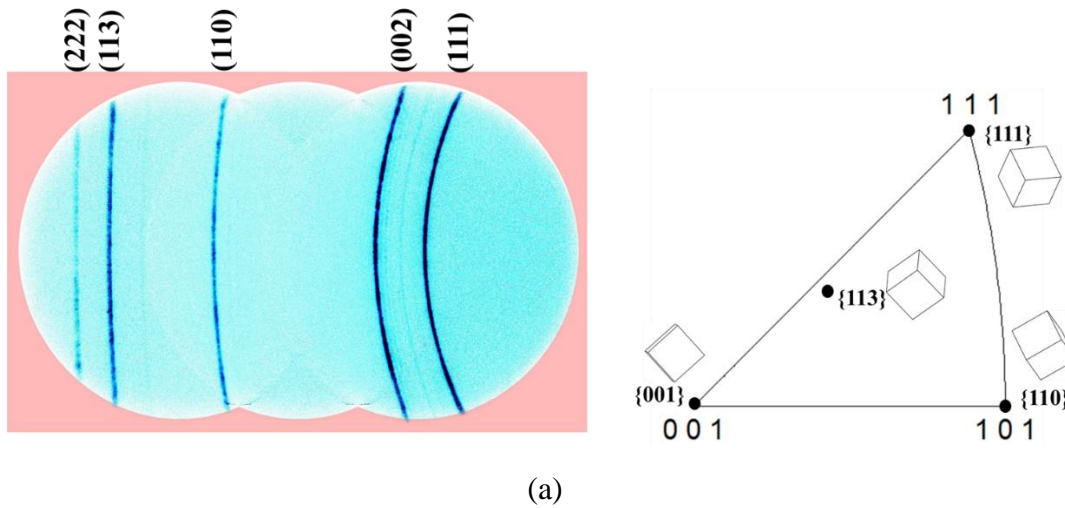
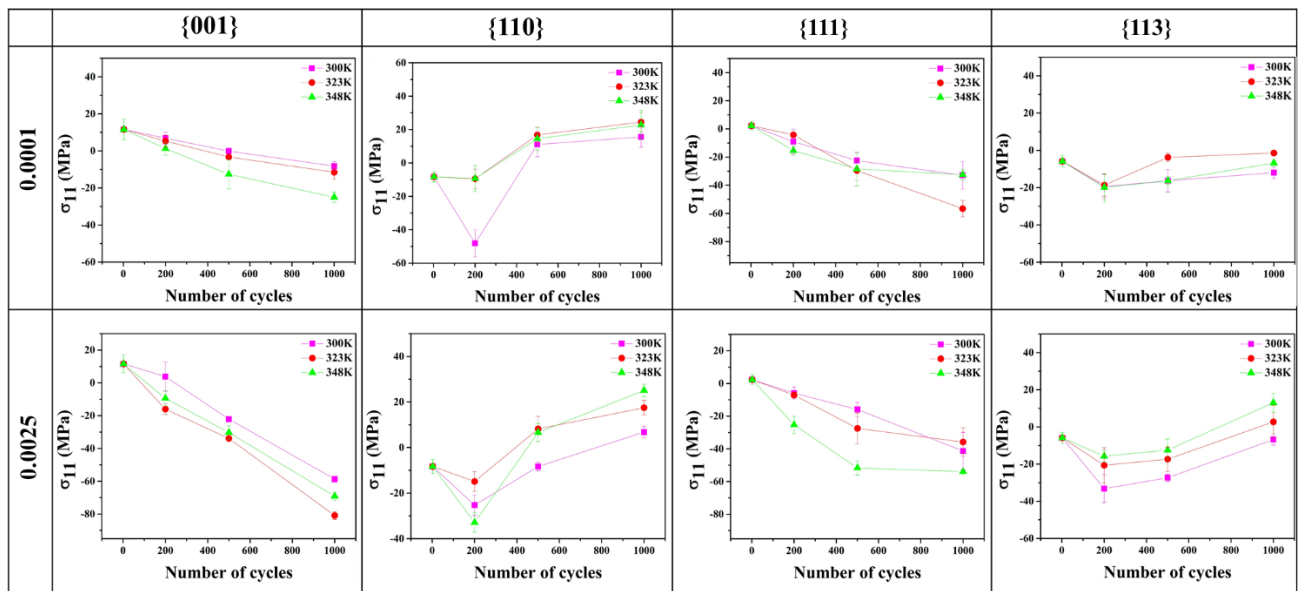


Figure 6.2: (a) X-ray diffraction with an area detector: showing different poles or family of orientations. The latter can be represented in an inverse pole figure (IPF) as orientations with different plane normal ($\{111\}$, $\{001\}$, $\{110\}$ and $\{113\}$). (b) Intensity versus 2θ plots were extracted from the area detector data (figure 6.2a) to show changes in peak profile and peak shift with cyclic deformation.

Standard $d\text{-sin}^2\psi$ measurements, albeit using extensive area detector data and a commercial software LeptosTM, was used to estimate the normal stress or σ_{11} component (see chapter 3 for stress convention) of the residual stress matrix. The results, summarized in figure 6.3a, shows a consistent (independent of $\Delta\varepsilon_p$ and temperature) but orientation dependent development in residual stress. $\{001\}$ and $\{111\}$ developed compressive stresses, while $\{110\}$ had tensile stress. It is to be noted that the accuracy of the residual stress measurements, involving an automated peak-positioning of the area detector data, is excellent: as represented by the nominal errors bars or standard deviations of residual stress data. The residual stress measurements were also conducted in the Euler space: for details on the methodology please refer chapters 4-5. Figure 6.3b shows the respective stress ODFs in IPF (inverse pole figure) notation. The IPFs, plotted for both tensile and compressive stresses, confirm the earlier patterns of the orientation dependent residual stresses. It is also clear that these results on residual stresses (figure 6.3) may have significant implications in designing fatigue-resistant microstructure or texture.



(a)

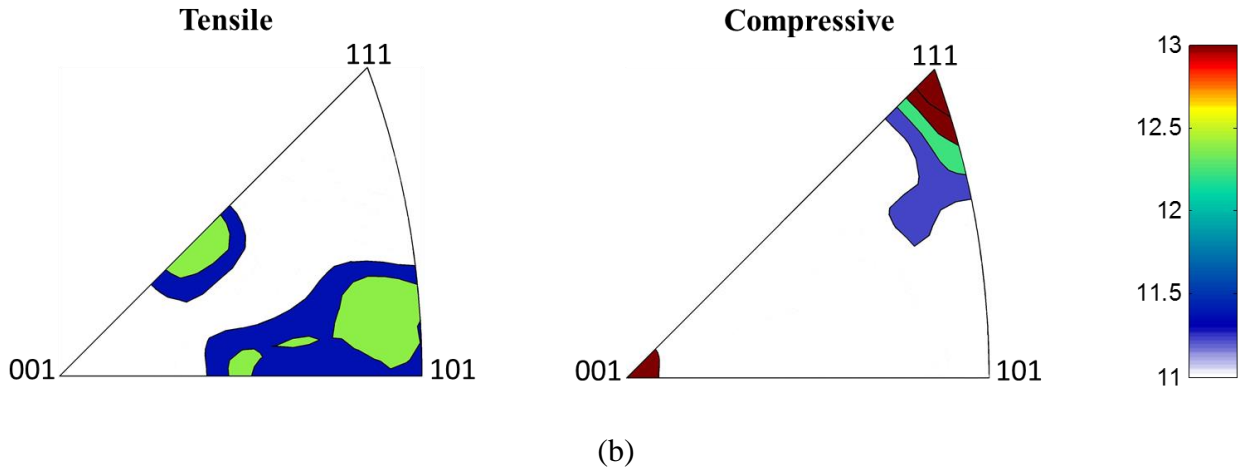
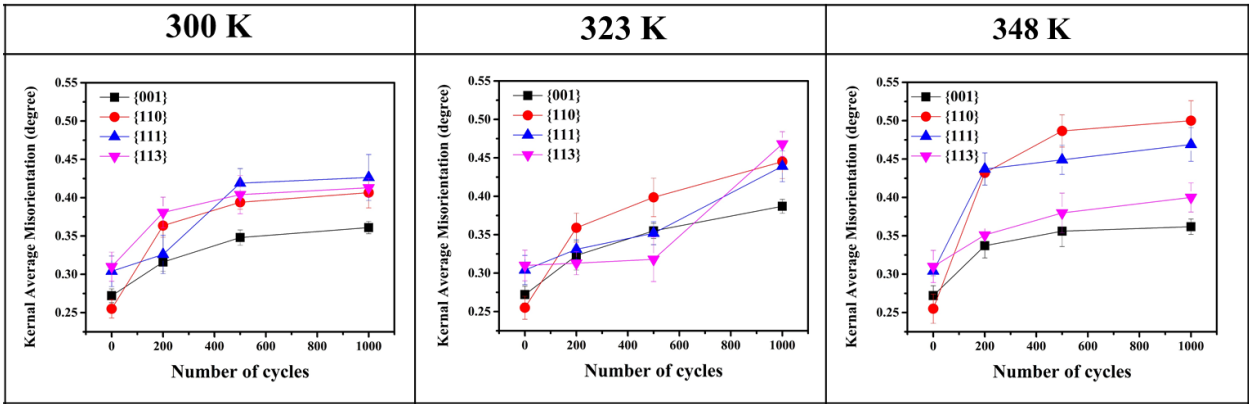
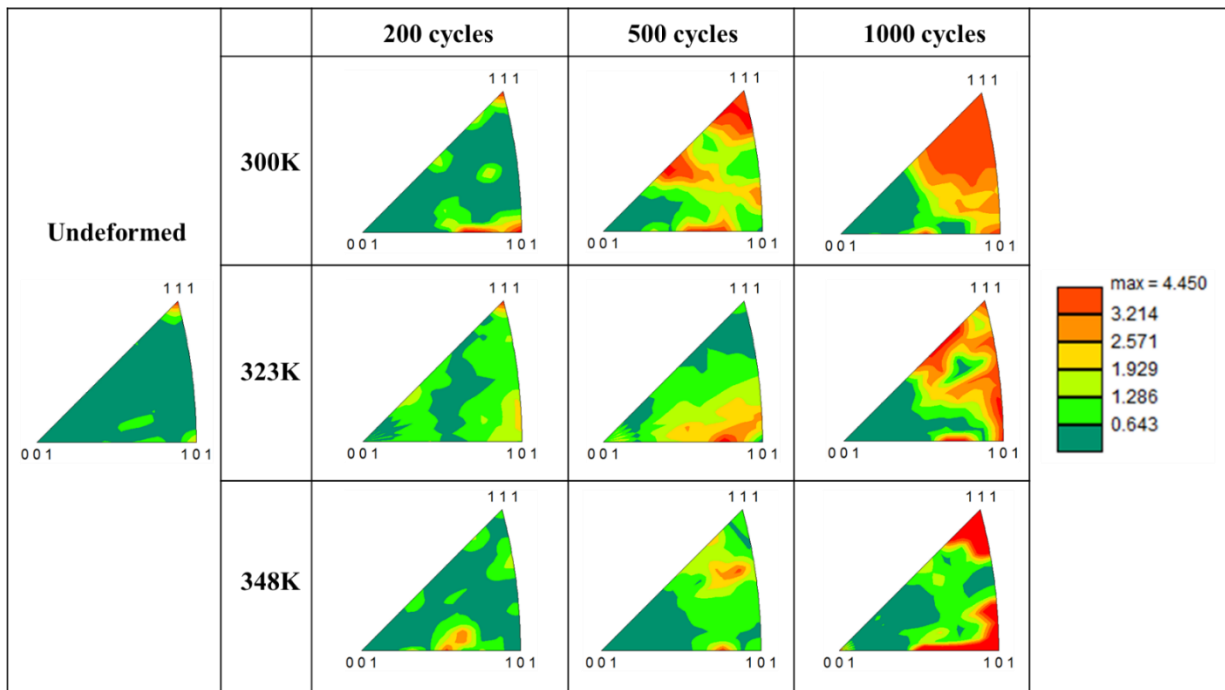


Figure 6.3: (a) $d\text{-sin}^2\psi$ stress measurements, with area detector, for the normal (σ_{11}) component of the residual stress matrix. It shows that $\{001\}$ and $\{111\}$ to develop compressive stresses. Tensile stresses, on the other hand, was noted in $\{110\}$. These observations, on orientation dependent residual stress evolution, were valid for all stress amplitudes and deformation temperatures. (b) Inverse pole figure representing tensile and compressive residual stresses for sample subjected to cyclic deformation at 300K ($\Delta\epsilon_p = 0.0025$ and 1000 cycle). (a) - (b) provide a clear picture of orientation (plane normal – see figure 6.1a) dependent residual stress development

Another important observation was on orientation dependence of the misorientation development. As shown in figure 6.4a, 300K deformation showed lower KAM for $\{100\}$. Misorientation developments for the other plane normals, however, appeared similar. The same trend continued for 323K cyclic deformation. For 348K, a clear difference between the plane normals appeared: $\{001\} < \{113\} < \{111\} < \{110\}$. The IPFs constituted of the KAM, the so-called scalar texture: see figure 6.4b, also shows the same trend in a more representative/pictorial way. It shows wider distribution in the scalar texture, or more anisotropy, at the highest cyclic deformation temperature. The data presented in figure 6.4 were obtained over very large area ($1\text{mm} \times 1\text{mm}$) scans of $0.3\ \mu\text{m}$ resolution. Of course, EBSD resolution has certain intrinsic limitations. TKD measurements, with significantly higher spatial and angular resolution and corresponding TEM imaging are planned to conclusively support the experimental data presented in figure 6.4.



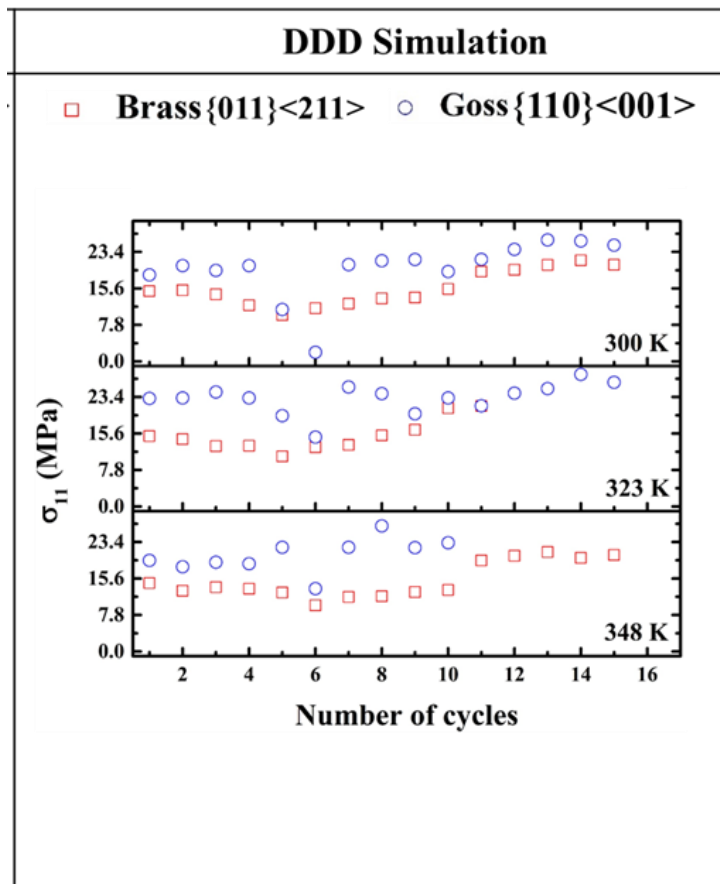
(a)



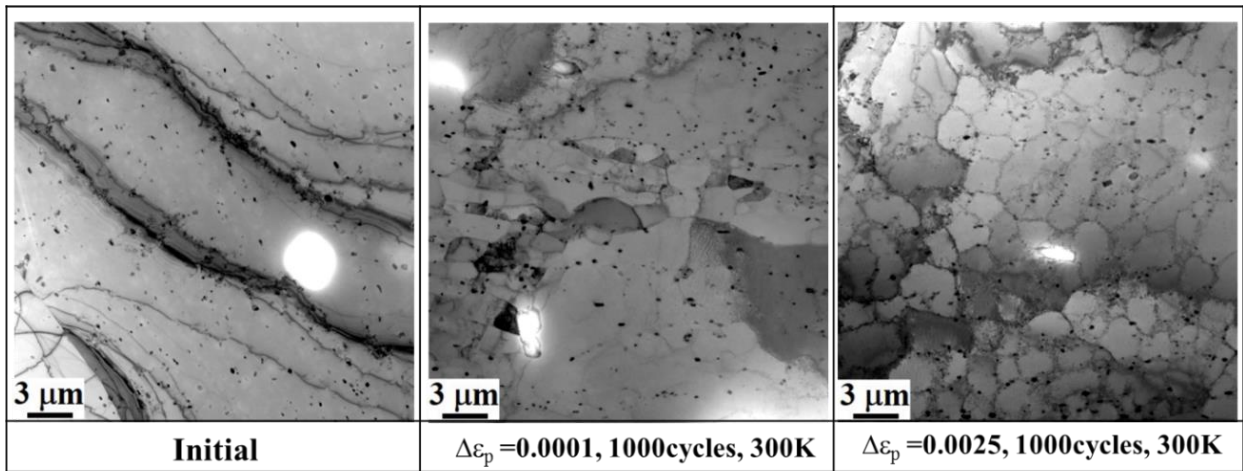
(b)

Figure 6.4: EBSD measured kernel average misorientation (KAM) for different plane normal (as in figure 1a). (b) EBSD estimated KAM plotted in an IPF for different cyclic deformations. (a) and (b) show a greater magnitude of orientation dependence for the higher temperatures of cyclic deformation.

Several issues remain unresolved. Initial DDD simulations (figure 6.5a), for example, indicated that residual stress evolution is nearly identical with the same plane normal (Goss and Brass in figure 6.5a). These simulations involve significant computation resources and needs to be brought to logical conclusions. The question remains if DDD can capture the experimental patterns of orientation dependent microstructure evolution (figures 6.4 and 6.5). The other interesting aspect of cyclic deformation is the evolution of dislocation substructures (figure 6.5b). The misorientation between the neighboring cells are often insignificant even to be captured with high resolution EBSD. This is where TKD, plus TEM, is thought to be more effective and are currently being planned and executed. Preliminary data indicates that orientation with similar GND (geometrically necessary dislocation) density may have differences in dislocation substructure and hence significant differences in residual stress. This point remains to be reproducibly substantiated and numerically simulated.



(a)



(b)

Figure 6.5: Examples of (a) DDD simulations of single-crystal residual stress development during cyclic deformation and (b) TEM imaging showing substructure formation.

References

1. Dieter, G.E. and D. Bacon, *Mechanical metallurgy*. Vol. 3. 1986: McGraw-Hill New York.
2. Webster, G. and A. Ezeilo, *Residual stress distributions and their influence on fatigue lifetimes*. International Journal of Fatigue, 2001. **23**: p. 375-383.
3. Withey, P.A., *Fatigue failure of the de Havilland comet I*. Engineering Failure Analysis, 1997. **4**(2): p. 147-154.
4. Schijve, J., *Fatigue damage in aircraft structures, not wanted, but tolerated?* International Journal of Fatigue, 2009. **31**(6): p. 998-1011.
5. Zolotarevsky, V.S., N.A. Belov, and M.V. Glazoff, *Casting aluminum alloys*. Vol. 12. 2007: Elsevier Amsterdam.
6. McDowell, D., et al., *Microstructure-based fatigue modeling of cast A356-T6 alloy*. Engineering Fracture Mechanics, 2003. **70**(1): p. 49-80.

Chapter 7

Concluding Remarks and Scope for Future Research

This thesis started on a fundamental premise. As shown in the introduction itself (figure 1.2), the energy potential well dictates that any crystalline material to have an equilibrium lattice parameter (r_0). A shift in the r_0 naturally violates the equilibrium and is the source of residual stress. Interestingly, even a body with residual stress is at equilibrium with its surrounding [1]. This is achieved with appropriate constraints. For mesoscopic in-grain residual stresses (type II stress, see figure 2.2), the dislocation substructure (figure 1.3) was hypnotized to provide such constraints. And this hypothesis provided the basis for the present PhD thesis.

A natural corollary of the aforementioned hypothesis is the possibility of ‘concurrent developments of microstructure and residual stresses’. And relating such concurrent developments became the natural thesis objective. To reach the overall objective, the thesis used certain niche experimental and simulation tools. The classical, albeit routine, $d\text{-sin}^2\psi$ measurements [2-5] of bulk residual stresses were avoided. After all, such measurements are specific to a crystallographic pole. Instead, bulk measurements involved multiple $\{hkl\}$ GIXRD (grazing incident X-ray diffraction) [1, 6-13]. Such measurement involves all crystallographic poles and hence can be taken as an orientation independent representative measurement of the normal and shear stress (figure 3.1c) components [14]. More involved were micro-Laue measurements of single crystal residual stress (see figures 3.1 and 4.4). This technique, rarely [15, 16] exploited in routine experimental stress measurements, was critical in establishing orientation dependent in-grain stresses during plastic deformation and also during thermal stress relief. However, micro-Laue measurements were restricted to a spot or grain size of $\sim 50 \mu\text{m}$. For microstructures involving finer grains and especially for better statics, this PhD thesis extensively used residual stress ODFs (orientation distribution function): again, a niche experimental measurement technique [17, 18].

The patterns of experimental data, on residual stresses and in-grain misorientations, were then compared to appropriate numerical simulations. This was not to blindly simulate the experiment data, but to bring out the underlying metal physics. The two simulation tools (discrete dislocation dynamics (DDD) and CPFE (crystal plasticity finite element)), in conjecture with experimental

data, were remarkably successful in this endeavor. And following were main combined, experimental and simulation, thesis findings.

- ✓ During tensile deformation, concurrent developments in GND (geometrical necessary dislocation) density and in-grain residual stresses were established. And such developments were effectively captured with DDD. In other words, slip-system activation and dislocation interactions in single crystals appeared to account for the evolution of both in-grain lattice curvatures and residual stresses.
- ✓ During thermal recovery, evolution in residual stress and in-grain misorientations were also shown to be orientation and temperature dependent. It was indeed interesting to show, with both experiments and numerical simulations, that maximum recovery happened at the intermediate temperature. DDD recovery simulations clearly attributed the non-monotonic thermal stress relief to a balance between dislocation glide and climb mechanisms.
- ✓ As DDD simulations are inherently restricted to lower strains, the thesis also used CPFEM to capture orientation dependent microstructural evolution to samples subjected to laboratory cold rolling. CPFEM considering anisotropic latent hardening of the appropriate slip systems, but insignificant interactions between neighboring grains, did produce the experimental hierarchy of orientation dependent microstructural evolution. The same was also observed, albeit at much lower strains, for the single crystal DDD simulations. In other words, it appears that the patterns of orientation dependence emerged primarily from single-crystal plasticity.
- ✓ During cyclic deformation, on the other hand, residual stress evolution appeared to be strongly orientation dependent. $\{001\}$ and $\{111\}$ were shown to develop compressive stresses, while tensile stresses were noted for $\{110\}$. Though this chapter remains partially complete, the chapter has significant technological implications for tailoring fatigue-resistant microstructures. This, plus the fact that additional experiments and simulations are expected to be completed before the thesis defense, encouraged the author to include this chapter in the thesis.

The combined experimental and numerical studies and the overall novelty makes this thesis extremely interesting. However, there are limitations: both experimentally and on the numerical simulations. For example,

- Residual stress measurements were restricted to $\sim 50 \mu\text{m}$, unavoidable given the present experimental limitations on micro-focusing of laboratory X-ray. However, such limitations can be reduced significantly with synchrotron radiation and with brighter X-ray source like Metal-Jet. More importantly, the newly emerging technique of cross-correlation (or EBSD based residual stress measurements) can provide unique opportunities.
- Higher computation power to extend the DDD simulations, possibilities of using 3D-DDD or DDD taking more accurate inputs of metal physics, DDD incorporating grain boundaries and CPFE + DDD are also possibilities of extending the numerical modelling used in this thesis.

In summary, it can be stated that though the observations from the present thesis remain interesting and novel today, all these can be off-setted in future with better experimental tools and computational power. However, what will remain pioneering, and a matter of just pride, is the effort of this thesis to effectively use residual stress as a feature of microstructural characterization. And a clear possibility of better understanding of the microstructural evolution through incorporation of local residual stress as an appropriate microstructural parameter.

References

1. Withers, P.J. and H.K.D.H. Bhadeshia, *Residual stress. Part 2 – Nature and origins*. Materials Science and Technology, 2001. **17**(4): p. 366-375.
2. Cullity, B., *Elements of X-ray Diffraction*. 1978.
3. Hauk, V. and E. Macherauch, *Residual stresses in science and technology*. 1987: DGM Informationsgesellschaft.
4. He, B.B., *Two-dimensional X-ray diffraction*. 2011: John Wiley & Sons.
5. Noyan, I.C. and J.B. Cohen, *Residual stress: measurement by diffraction and interpretation*. 2013: Springer-Verlag.

6. Kohli, D., et al., *Fabrication of simulated plate fuel elements: Defining role of stress relief annealing*. Journal of Nuclear Materials, 2014. **447**(1–3): p. 150-159.
7. Kumar, G., et al., *Through-Thickness Deformation Gradient in a Part-Pilgered Zirconium Tube: Experimental Measurements and Numerical Validation*. Metallurgical and Materials Transactions A, 2017. **48**(6): p. 2844-2857.
8. Peng, J., et al., *Residual stress gradient analysis by the GIXRD method on CVD tantalum thin films*. Surface and Coatings Technology, 2006. **200**(8): p. 2738-2743.
9. Welzel, U., et al., *Stress analysis of polycrystalline thin films and surface regions by X-ray diffraction*. Journal of Applied Crystallography, 2005. **38**(1): p. 1-29.
10. Holy, V., T. Baumbach, and U. Pietsch, *High-resolution X-ray scattering from thin films and multilayers*. 1999: Springer.
11. Lim, G., et al., *Grazing incidence synchrotron x-ray diffraction method for analyzing thin films*. Journal of Materials Research, 1987. **2**(4): p. 471-477.
12. Ma, C.-H., J.-H. Huang, and H. Chen, *Residual stress measurement in textured thin film by grazing-incidence X-ray diffraction*. Thin Solid Films, 2002. **418**(2): p. 73-78.
13. Levine, J.R., et al., *Grazing-incidence small-angle X-ray scattering: new tool for studying thin film growth*. Journal of Applied Crystallography, 1989. **22**(6): p. 528-532.
14. Dieter, G.E. and D. Bacon, *Mechanical metallurgy*. Vol. 3. 1986: McGraw-Hill New York.
15. Martins, R.V., et al., *Simultaneous measurement of the strain tensor of 10 individual grains embedded in an Al tensile sample*. Materials Science and Engineering: A, 2004. **387**: p. 84-88.
16. Margulies, L., et al., *Strain tensor development in a single grain in the bulk of a polycrystal under loading*. Acta Materialia, 2002. **50**(7): p. 1771-1779.
17. Wang, Y., R.L. Peng, and R. McGreevy, *A novel method for constructing the mean field of grain-orientation-dependent residual stress*. Philosophical magazine letters, 2001. **81**(3): p. 153-163.
18. Wang, Y.D., et al., *Determination of the stress orientation distribution function using pulsed neutron sources*. Journal of Applied Crystallography, 2003. **36**(1): p. 14-22.

List of Publications

From this thesis

Serial No	Details	Status
1	Relating Residual Stress and Substructural Evolution During Tensile Deformation of an Aluminum - Manganese Alloy, Arijit Lodh , Tawqeer N. Tak , Aditya Prakash, P.J. Guruprasad, Christopher R. Hutchinson, Indradev Samajdar, Metallurgical and Materials Transactions A , 2017. 48(11): p. 5317-5331	Published
2	Microstructural Origin of Residual Stress Relief in Aluminum, Arijit Lodh, Tawqeer N. Tak, Aditya Prakash, P.J. Guruprasad, Shyam M. Keralavarma, A. Amine Benzerga, Christopher R. Hutchinson, Indradev Samajdar	Communicated to Acta Materialia
3	Orientation Dependent Developments in Misorientation and Residual Stress in Rolled Aluminum: The Defining Role of Dislocation Interactions, Arijit Lodh, Ujjal Tewary, Ram Pratap Singh, Tawqeer N. Tak, Aditya Prakash, Alankar Alankar, P.J. Guruprasad, Indradev Samajdar	Communicated to Metallurgical and Materials Transactions A

From other's work/collaborations

Serial No	Details	Status
1	Experimental characterization and finite element modeling of through thickness deformation gradient in a cold rolled zirconium sheet, G Kumar, A Lodh, J Singh, R Singh, D Srivastava, GK Dey, I Samajdar, CIRP Journal of Manufacturing Science and Technology 19, 176-190	Published
2	Hot-rolled and continuously cooled bainitic steel with good strength–elongation combination, S Das, S Sinha, A Lodh, AR Chintha, M Krugla, A Haldar, Materials Science and Technology 33 (8), 1026-1037	Published
3	Effect of Thermal Exposure on the Charpy Impact Properties of Thermo-Mechanically Treated Reinforcement Steel Bar, M Sk, B Syed, A Chatterjee, A Lodh, S Kundu, D Chakrabarti, Steel Research International 88 (5)	Published
4	Burst Ductility of Zirconium Clads: The Defining Role of Residual Stress, Gulshan Kumar, AK Kanjarla, Arijit Lodh, Jaiveer Singh, Ramesh Singh, D Srivastava, GK Dey, N Saibaba, RD Doherty, Indradev Samajdar, Metallurgical and Materials Transactions A 47 (8), 3882-3896	Published
5	Plastic Deformation and Corrosion in Austenitic Stainless Steel: A Novel Approach Through Microtexture and Infrared Spectroscopy, N Srinivasan, V Kain, N Birbilis, B. Sunil Kumar, M.N. Gandhi, P.V. Sivarprasad, Guocai Chai, A Lodh, P.M. Ahmedabadi, I. Samajdar, Corrosion Science , Volume 111, October 2016, Pages 404-413	Published